



University  
of Glasgow

Harris, Rachel (2022) *Investigating the metabolic and therapeutic effects of combined glutaminase and mutant-BRAF inhibitors in melanoma*. PhD thesis.

<https://theses.gla.ac.uk/83354/>

Copyright and moral rights for this work are retained by the author

A copy can be downloaded for personal non-commercial research or study, without prior permission or charge

This work cannot be reproduced or quoted extensively from without first obtaining permission in writing from the author

The content must not be changed in any way or sold commercially in any format or medium without the formal permission of the author

When referring to this work, full bibliographic details including the author, title, awarding institution and date of the thesis must be given

Enlighten: Theses

<https://theses.gla.ac.uk/>  
[research-enlighten@glasgow.ac.uk](mailto:research-enlighten@glasgow.ac.uk)

Investigating the metabolic and  
therapeutic effects of combined  
glutaminase and mutant-BRAF inhibitors  
in melanoma

Rachel Harris (BSc, MRes)

Submitted in fulfilment of the requirements of  
the degree of Doctor of Philosophy (Cancer  
Sciences)

CRUK Beatson Institute Garscube Estate,  
Switchback Road, Bearsden, Glasgow

Institute of Cancer Science

College of Medical, Veterinary and Life Sciences  
University of Glasgow

September 2022

## Key Findings

- Glutaminase inhibition decreases the growth of BRAF inhibitor resistant cells in combination with a BRAF inhibitor both *in vitro* and *in vivo*.
- Glutaminase inhibition causes a reduction in glutamine derived aspartate *in vitro*, which is essential for cell growth.
- Supplementing aspartate or compounds that can regenerate NAD<sup>+</sup> can rescue growth from glutaminase inhibition.
- Glutaminase inhibition *in vivo* affects levels of ornithine, citrulline and glutamine in the serum independently of its effect on the tumour.
- BRAF inhibition *in vivo* increases levels of tumour aspartate and glutamine, demonstrating that BRAF mutant melanoma undergoes metabolic rewiring under BRAF inhibition.
- PLX4032 and CB839 cause a decrease in the HIF1 $\alpha$  target genes and a reduction in the ATP/AMP ratio, which is exacerbated by CB839 treatment.
- PLX4032 decreases citrulline *in vivo* and increases the expression of the urea cycle enzyme argininosuccinate lyase *in vivo*.

## Abstract

Metastatic melanoma is a deadly form of skin cancer and the leading cause of skin cancer deaths. For patients with stage three and four melanomas, an adjuvant therapy known as Vemurafenib is used as a first line therapy for all patients whose tumour harbours a BRAF mutation. This treatment is an inhibitor of the mutant BRAF oncoprotein and prevents the constitutive activation of the RAS-RAF-MEK-ERK signalling cascade. This treatment allows remarkable clinical success, but BRAF inhibitor resistance invariably develops, however previous studies showed that acquisition of BRAF inhibitor resistance causes increased dependence on glutamine.

Therefore, in this study I investigated the use of the clinically relevant glutaminase inhibitor, CB839 in mutant BRAF melanoma. I demonstrated that glutaminase inhibition selectively reduces growth of cells *in vitro* and tumours *in vivo* under long term BRAF inhibition. However, I found that the presence of BRAF inhibition itself sensitizes some of these models to glutaminase inhibition. BRAF inhibitor resistant cells under BRAF inhibition *in vitro* had reduced generation of glutamine derived glutamate. In addition, BRAF inhibition *in vivo* resulted in decreased transcription of genes encoding for glycolytic enzymes and transporters. These transcriptional changes were associated with decreased pyruvate and ATP/AMP ratio when BRAF inhibition was coupled with glutaminase inhibition.

*In vitro*, glutaminase inhibition caused decreased the production of glutamine derived aspartate, which was shown to be essential for the growth of these cells. *In vivo*, tumour aspartate levels were

decreased by glutaminase inhibition, but unexpectedly increased by BRAF inhibition, demonstrating that aspartate levels obtained under CB839 treatment do not limit the growth of melanoma xenografts.

Further investigation *in vivo* revealed that BRAF inhibition causes metabolic rewiring, increasing the tumour levels of glutamine and decreasing those of citrulline. Furthermore, BRAF inhibition increased the tumour expression of argininosuccinate lyase (ASL), and decreased the levels of systemic ammonia, suggesting that BRAF inhibition may affect the activity of the urea cycle. *In vivo*, an untargeted metabolomic approach found several metabolic features whose levels were altered by combined CB839 and PLX4032 treatment. Further studies to confirm their identities and their role in the antitumour effect of CB839 and PLX4032 treatment may yield useful insights into the use of the combination of these two clinically relevant treatments.

## Lay summary

Melanoma is the deadliest form of skin cancer, leading to over 2,000 deaths a year in the UK. Whilst surgical removal of a melanoma may be curative if performed early, late-stage melanomas that have spread to other organs usually require further pharmaceutical treatment. Two main treatments are currently used in melanoma, which are known as Ipilimumab and Vemurafenib. Vemurafenib is the best treatment option for patients who have a genetic change gene, BRAF within their tumour (around half of all patients). Whilst this treatment prolongs the survival of melanoma patients, the tumour usually develops resistance to this treatment within about 2 years. Therefore, treatment strategies for tumours that are resistant to Vemurafenib are needed.

The biological process of metabolism - encapsulating all the chemical reactions that take place in a living organism - has been extensively studied in cancer since the 1950's. More recently, advances in this field have shown that changes in the metabolism occur when melanoma becomes resistant to Vemurafenib. More specifically, the reaction that converts a molecule called glutamine to another called glutamate was shown to be more essential for the growth of melanoma cells once they have become resistant to Vemurafenib. CB839 is a pharmaceutical treatment which inhibits this reaction, which we used in combination with Vemurafenib on melanoma tumours. We showed that CB839 and Vemurafenib can be given simultaneously in animal models, without detrimental effects to health - demonstrating the safety of this combination. Furthermore, we showed that addition of CB839 to Vemurafenib treatment can reduce the growth of melanoma if both treatments are given simultaneously at an early stage. We showed that in tumours, both

CB839 and Vemurafenib cause changes in the metabolism. Going forward, deciphering which metabolic reactions targeted by both these pharmaceutical treatments may better inform their use and improve the survival of melanoma patients.

# Contents

|   |    |
|---|----|
| Key Findings .....  | 2  |
| Abstract .....  | 3  |
| Lay summary.....  | 5  |
| List of Figures .....   | 12 |
| Authors Declaration .....   | 22 |
| Acknowledgements .....  | 22 |
| Abbreviations .....   | 23 |
| Chapter 1: Introduction.....  | 29 |
| 1.1 Melanoma: Pathogenesis and Diagnosis.....   | 29 |
| 1.1.1 Epidemiology .....  | 29 |
| 1.1.2 Melanocytes: Location and Function.....   | 30 |
| 1.1.3 Molecular Pathogenesis of Melanoma.....   | 33 |
| 1.1.4 Diagnosis of Melanoma.....  | 37 |
| 1.2 Melanoma Treatment and BRAF Inhibitor Resistance.....                                     | 42 |
| 1.2.1 The RAS-RAF-MEK-ERK Pathway and its Dysregulation.....                                  | 42 |
| 1.2.2 Vemurafenib.....  | 43 |
| 1.2.3 Treatment of Melanoma .....   | 45 |
| 1.2.4 Mechanisms of BRAF Inhibitor Resistance.....  | 50 |
| 1.3 Metabolism in Cancer and Strategies to Target it.....                                     | 53 |
| 1.3.1 Metabolism in Cancer .....  | 53 |
| 1.3.2 Metabolic Changes Induced by BRAF Mutation in Melanoma<br>.....                         | 55 |
| 1.3.3 Metabolic Changes Induced by Mutant BRAF Inhibition and<br>Resistance in Melanoma ..... | 57 |

|                         |  |    |
|-------------------------|--|----|
| 1.3.4                   | Glutamine Addiction in Cancer.....                               | 61 |
| 1.4                     | Methods to Study Cancer Metabolism.....                          | 72 |
| 1.4.1                   | Cell Culture and Media .....                                     | 72 |
| 1.4.2                   | Mouse Models of Mutant BRAF Melanoma .....                       | 74 |
| 1.4.3                   | Studying Cancer Metabolism with Metabolomics .....               | 77 |
| 1.4.4                   | Processing of LC-MS Data for Metabolomics.....                   | 81 |
| 1.5.1                   | Study Aims.....  | 88 |
| Chapter 2: Methods..... |  | 89 |
| 2.1                     | Cell culture and Treatment .....                                 | 89 |
| 2.2                     | <i>In vitro</i> Assays .....                                     | 89 |
| 2.2.1                   | Experimental Media.....  | 89 |
| 2.2.2                   | Supplementation of Metabolites & Glutaminase Inhibition          | 90 |
| 2.2.1                   | Growth Response Experiment by Lowry Assay .....                  | 91 |
| 2.2.2                   | Growth Assays by Cell Counting.....                              | 91 |
| 2.2.3                   | SDS-PAGE Western Blot.....                                       | 92 |
| 2.2.4                   | Glutamine and Glutamate Uptake/Secretion by Bioanalyser<br>..... | 93 |
| 2.2.5                   | Extraction of Intracellular Metabolites .....                    | 94 |
| 2.3                     | <i>In vivo</i> Models of Melanoma .....                          | 95 |
| 2.3.1                   | Transplantation of Cells.....                                    | 95 |
| 2.3.2                   | Analysis of Tumour volume .....                                  | 96 |
| 2.3.3                   | Treatment regimes.....   | 96 |
| 2.3.4                   | Dissection.....  | 96 |
| 2.3.5                   | Preparation of Tissue Samples for Metabolomic Analysis ..        | 97 |
| 2.3.5                   | Preparation of Serum for Metabolomic Analysis .....              | 97 |

|  |     |
|--|-----|
| 2.3.6 Quantification of Serum Ammonia .....  | 98  |
| 2.3.6 Immunohistochemistry.....  | 98  |
| 2.3.7 RNAseq Preparation .....   | 99  |
| 2.3.8 RNAseq Analysis.....   | 100 |
| 2.4 Metabolomic Analysis.....  | 101 |
| 2.4.1 pHILIC Chromatography.....   | 101 |
| 2.4.2 QE and QE+ Acquisition .....   | 102 |
| 2.4.3 Targeted Analysis.....   | 103 |
| 2.4.5 Untargeted Analysis .....  | 104 |
| Chapter 3: Results .....   | 106 |
| 3.1 BRAF Inhibition Results in Greater Growth Inhibition, and<br>Depletion of Glutamate and Aspartate in Response to Glutaminase<br>Inhibition. .... | 106 |
| 3.1.1 Greater Growth Inhibition in Response to Glutaminase<br>Inhibition Occurs Under BRAF Inhibition .....  | 106 |
| 3.1.2 Plasmax™ Reduces Glutamine Consumption and Glutamate<br>Secretion Compared to DMEM.....  | 114 |
| 3.1.3 TCA cycle activity is More Dependent on Glutaminase Activity<br>in BRAF Inhibitor Resistant Cells .....  | 117 |
| 3.1.4 Glutaminase Inhibition Results in Depletion of Aspartate and<br>Nucleotide Synthesis in BRAF Inhibitor Resistant Cells.....                    | 121 |
| 3.1.5 Growth Inhibition by Glutaminase Inhibition Can be Reduced<br>by Supplementing Aspartate or NAD+ Regenerating Metabolites .                    | 128 |
| 3.2 Generating <i>in vivo</i> models of BRAF Inhibitor Resistant Melanoma<br><i>in vivo</i> to Determine CB839 Therapeutic Efficacy .....            | 139 |

|  |     |
|--|-----|
| 3.2.1 Treatment with CB839 causes changes in serum metabolites .....   | 139 |
| 3.2.2 Intraperitoneal PLX4032 Treatment Decreases the Growth of Naïve Melanoma Xenografts.....   | 142 |
| 3.3 Glutaminase Inhibition Reduces the Growth of BRAF Mutant Melanoma when Given in Combination with BRAF Inhibitors .....                           | 146 |
| 3.3.1 Combined Glutaminase Inhibition and BRAF Inhibition Causes Significantly Reduced Growth of Xenograft Tumours from BRAF Mutant Cell Lines ..... | 146 |
| 3.3.2 The Acquisition of BRAF Inhibitor Resistance <i>in vivo</i> does not Increase Sensitivity to Glutaminase Inhibition .....                      | 151 |
| 3.4 PLX4032 and CB839 Rewire the Metabolism of A375 Derived Tumours and Change Glutamine and Citrulline Levels.....                                  | 156 |
| 3.4.1 Several Metabolic Features are Altered in Response to PLX4032 and CB839.....   | 156 |
| 3.4.2 PLX4032 Causes Metabolic Rewiring, Resulting in Changes in Aspartate, Glutamine and Citrulline.....  | 162 |
| 3.4.3 PLX4032 Reduces Expression of HIF1a targets .....  | 173 |
| Chapter 4: Discussion .....  | 186 |
| 4.1 Inhibition of Glutaminase Causes Greater Growth Inhibition for Cells under BRAF Inhibition .....   | 186 |
| 4.2 <i>In Vivo</i> CB839 Treatment Changes Serum Metabolites which has the Potential to Affect its Efficacy .....                                    | 188 |
| 4.3 BRAF Inhibition Reduces the Expression of Glycolytic Genes and Increases Dependence on Glutaminolysis .....                                      | 189 |
| 4.4 Glutaminase Activity is Required for Aspartate Synthesis and Maintenance of NAD <sup>+</sup> /NADH Homeostasis.....                              | 192 |

|   |     |
|---|-----|
| 4.5 BRAF and Glutaminase Inhibition Affect the expression of the Urea Cycle Enzyme, Argininosuccinate Lyase ..... | 195 |
| 4.5 Overveiw .....  | 200 |
| 4.7 Future work .....   | 203 |
| 4.7.1 Determination of the direct metabolic effects of BRAF inhibition.....                                       | 203 |
| 4.7.2 Determination of the systemic effects of CB839 .....  | 204 |
| 4.7.3 Determination of metabolic changes caused by combined CB839 and PLX4032 treatment .....                     | 205 |
| References .....  | 206 |

## List of Figures

Figure 1.1.2-1: Diagram depicting the location of melanocytes in the skin.

Figure 1.1.2-2: Diagram depicting the mechanisms inducing melanin production in melanocytes.

Figure 1.1.3-1: Diagram depicting the main molecular pathways driving the pathogenesis of melanoma.

Table 1.1.4-1 (a) Tumour category based on depth and ulceration of a tumour

Table 1.1.4-1 (b) Nodal metastases category based on number of regional lymph nodes infiltrated

Table 1.1.4-1 (c) Distant metastases category based on presence of metastases

Table 1.1.4-1 (d) Melanoma staging criteria based on tumour depth, lymph node metastases and distant metastases.

Figure 1.2.3-1: (above) Diagram depicting the location of BRAF mutation within the BRAF gene and the structure of BRAF kinase in complex with PLX4720.

Figure 1.2.4-1: Schematic diagram showing resistance mechanisms of melanoma cells to BRAF inhibition.

Figure 1.3.2-1: A schematic diagram showing changes in proteins associated with metabolism in association with BRAF mutation.

Figure 1.3.4-1: Schematic diagram showing the contribution of glutamine derived carbon and nitrogen to TCA cycle intermediates, aspartate, asparagine, argininosuccinate, proline and ornithine.

Figure 1.3.4-2: Schematic diagram depicting the Malate-Aspartate shuttle allowing the transfer of electrons into the mitochondria to be used by the electron transport chain to make ATP.

Figure 1.3.4-3: A schematic diagram depicting the use of glutamine, glycine and aspartate derived nitrogen in purine synthesis.

Figure 1.3.4-4: A schematic diagram depicting the use of glutamine and aspartate derived nitrogen in purine synthesis.

Figure 1.3.4-5: A schematic depicting the use of glutamine derived glutamate in the ROS buffering system.

Table 1.4.1-1: Chart depicting the concentrations of 20 proteogenic amino acids in Plasmix™ and DMEM with high glucose and the normal concentration range for human serum.

Figure 1.4.2-1: A schematic diagram depicting three different types of mouse models available to study BRAF mutant melanoma and their advantages and limitations.

Figure 1.4.3-1: A diagram depicting a cross sectional diagram of the basic components of an orbitrap mass spectrometer.

Figure 1.4.3-2: A diagram depicting the main concepts of pHILIC chromatography.

Figure 1.4.4-1: Diagram depicting the generation of an XIC trace from successive MS scans.

Figure 1.4.4-2: Schematic diagram representing the use of <sup>13</sup>C labelled glutamine in glutamine anaplerosis and the TCA cycle.

Figure 1.4.4-3: A diagram showing pre and post processing steps of an untargeted metabolomic analysis from a list of chromatographic peaks produced from raw LC-MS data.

Table 2.2.1-1: Table showing the volumes of MEM media in which cells were seeded in for 24 hours.

Table 2.4.2: Scan filters and their timing windows used in a SIM to detect intermediates of nucleotide synthesis.

Figure 3.1.1-1: dose-response of melanoma cell lines, as well as their BRAF inhibitor resistant sub-clones A375R and COLO829R to the BRAF inhibitor PLX4720.

Figure 3.1.1-2: A representative western blot of glutaminase in BRAF inhibitor resistant and sensitive melanoma cell lines.

Figure 3.1.1-3: Graphs showing the growth response of melanoma cells to CB839 treatment relative to untreated cells.

Figure 3.1.1-4: Graphs showing the growth response of BRAF inhibitor resistant melanoma cells to CB839 and PLX4720 treatment as indicated, relative to untreated cells.

Figure 3.1.2-1: Graphs depicting the glutamine and glutamate consumption and secretion rates of melanoma cell lines in Plasmax and DMEM media with or without CB839.

Figure 3.1.2-2: Graphs depicting the isotopologue distribution of glutamate and  $\alpha$ -ketoglutarate in melanoma cells after a 48-hour incubation in 8mL 0.65mM  $^{13}\text{C}_5$  glutamine in Plasmax<sup>TM</sup> or in 8mL 5mM  $^{13}\text{C}_5$  glutamine in DMEM.

Figure 3.1.3-1: Graphs depicting the intracellular levels of glutamine, glutamate and  $\alpha$ -ketoglutarate in melanoma cells in Plasmax<sup>TM</sup>, in response to a 24 hour treatment with 1 $\mu\text{M}$  of CB839.

Figure 3.1.3-2: Graphs depicting the isotopologue distribution of glutamate in melanoma cells after a 48-hour incubation in 8mL 0.65mM  $^{13}\text{C}_5$  glutamine in Plasmax<sup>TM</sup>.

Figure 3.1.3-3: Graphs depicting the isotopologue distribution of  $\alpha$ -ketoglutarate melanoma cells after a 48 hour incubation in 8mL 0.65mM  $^{13}\text{C}_5$  Glutamine in Plasmax<sup>TM</sup>.

Figure 3.1.4-1: Volcano plots showing the  $\log_2$  fold change and  $-\log_{10}$  p value for an unpaired t test comparing the intracellular levels of 66 metabolites between vehicle and CB839 treated BRAF inhibitor resistant melanoma cells in vitro.

Figure 3.1.4-2: Graphs depicting the intracellular levels of aspartate in melanoma cells in Plasmax<sup>TM</sup>, in response to a 24-hour treatment with  $1\mu\text{M}$  of CB839.

Figure 3.1.4-3: Graphs depicting the intracellular levels of pyrimidine synthesis intermediates in BRAF inhibitor resistant melanoma cells in Plasmax<sup>TM</sup>, in response to a 24-hour treatment with  $1\mu\text{M}$  of CB839.

Figure 3.1.4-5: Graphs depicting the number of BRAF inhibitor resistant melanoma cells after supplementation of 1mM dihydroorotate, 1mM carbamoyl aspartate or a mixture of  $100\mu\text{M}$  each of adenosine, guanosine, cytosine, thymidine, uridine, and inosine (AGCTUI) and treatment with 100nM CB839, relative to cells grown in Plasmax<sup>TM</sup>.

Figure 3.1.5-1: Graphs depicting the isotopologue distribution of aspartate in melanoma cells after a 48 hour incubation in 8mL 0.65mM  $^{13}\text{C}_5$  Glutamine in Plasmax<sup>TM</sup>.

Figure 3.1.5-2: Graphs depicting the number of BRAF inhibitor resistant melanoma cells after supplementation of 10mM aspartate and treatment with 100nM CB839, relative to cells grown in Plasmax<sup>TM</sup>.

Figure 3.1.5-3: Graphs depicting the ratio of NAD<sup>+</sup> to NADH in melanoma cells in Plasmax™, in response to a 24-hour treatment with 1 μM of CB839.

Figure 3.1.5-4: Graphs depicting the number of BRAF inhibitor resistant melanoma cells after supplementation of 5mM dimethyl-s-malate, 5mM oxaloacetate and treatment with 100nM CB839, relative to cells grown in Plasmax™.

Figure 3.1.5-5: Graphs depicting the number of BRAF inhibitor resistant melanoma cells after supplementation of 5mM lactate and 1mM Pyruvate and treatment with 100nM CB839, relative to cells grown in Plasmax™.

Figure 3.1.5-6: Graphs depicting the number of BRAF inhibitor resistant melanoma cells after supplementation of 5mM dimethyl-α-ketoglutarate (DMαKG) and treatment with 100nM CB839, relative to cells grown in Plasmax™.

Figure 3.1.5-7: Graphs depicting the ratio of NAD<sup>+</sup> to NADH, as well as the level of malate, aspartate and glutamate in COLO829R cells in Plasmax™, in response to a 24-hour treatment with 1 μM of CB839.

Figure 3.2.1-1: Graph depicting the weight of NSG mice and percent of start weight in response to 200mg/kg CB839 and a vehicle for PLX4032 treatment over 2 weeks of treatment.

Figure 3.2.1-2: Volcano plots showing the log<sub>2</sub> fold change and -log<sub>10</sub> p value for an unpaired t test comparing the serum levels of 66 metabolites between vehicle and CB839 treated NSG mice.

Figure 3.2.1-3: Graphs depicting the level of aspartate, asparagine, glutamine, citrulline and ornithine in the serum of vehicle and CB839 treated NSG mice.

Figure 3.2.2-1: Graph depicting the weight of each mouse since start of treatment with 10mg/kg PLX4032 or a vehicle and the % change in the weight of each mouse since treatment start.

Figure 3.2.2-2: Graph depicting the weight of each mouse since start of treatment with 10mg/kg PLX4032 and 200mg/kg CB839 or a vehicle and the % change in the weight of each mouse since treatment start.

Figure 3.2.2-3: Figure depicting the growth of each tumour since the subcutaneous injection of 1 million A375, COLO829 or YUMM1.7 cells into the flank of mice under PLX4032 treatment.

Figure 3.2.2-4: Volcano plots showing the log<sub>2</sub> fold change and -log<sub>10</sub> p value for an unpaired t test comparing the serum levels of 66 metabolites between vehicle and PLX4032 treated NSG mice.

Figure 3.3.1-1: Growth of tumours derived from A375 cells injected subcutaneously into the flank of an NSG mouse treated with 200mg/kg CB839 and/or 10mg/kg PLX4032 as indicated.

Figure 3.3.1-2: Growth of tumours derived from COLO829 cells injected subcutaneously into the flank of an NSG mouse treated with 200mg/kg CB839 and/or 10mg/kg PLX4032 as indicated.

Figure 3.3.1-3: Growth of tumours derived from YUMM1.7 cells injected subcutaneously into the flank of an C57BL/6 mouse treated with 200mg/kg CB839 and/or 20mg/kg PLX4032 as indicated.

Figure 3.3.2-1: Volume of tumours derived from A375 cells injected subcutaneously into the flank of an NSG mouse treated with 10mg/kg PLX4032 until tumours reached >200mm<sup>3</sup>, before being switched to 200mg/kg CB839 and/or 10mg/kg PLX4032 as indicated.

Figure 3.3.2-2: Growth of tumours derived from YUMM1.7 cells injected subcutaneously into the flank of a C57BL/6 mouse treated with 20mg/kg PLX4032 until tumours reached >200mm<sup>3</sup>, before being switched to 200mg/kg CB839 and/or 20mg/kg PLX4032 as indicated.

Figure 3.4.1-1: Volcano plot showing the -log<sub>10</sub> adjusted p value and log<sub>2</sub> fold change in a comparison between combination treatment and vehicle treatment.

Figure 3.4.1-2: Venn diagram showing the number of hits that were significant between combination treatment against vehicle treatment, combination against CB839 treatment and combination against PLX4032 treatment.

Table 3.4.1-1: Table depicting 41 metabolic features significantly different between vehicle and combination treated tumours and not between vehicle and PLX4032 or to CB839 treated tumours.

Figure 3.4.1-3: Heatmap showing the Log<sub>2</sub> fold change of 8 features changing significantly between vehicle and combination treated tumours and not between vehicle and PLX4032 or to CB839 treated tumours.

Figure 3.4.2-1: Aspartate levels measured from tumour tissue or serum taken from NSG mice that were subcutaneously injected with A375 cells and treated with PLX4032, CB839 or a combination of the two.

Figure 3.4.2-2: Glutamine and glutamate levels measured from tumour tissue taken from NSG mice that were subcutaneously injected with A375 cells and treated with PLX4032, CB839 or a combination of the two.

Figure 3.4.2-3: Glutamine and citrulline levels measured from serum taken from NSG that were subcutaneously injected with A375 cells and treated with PLX4032, CB839 or a combination of the two.

Figure 3.4.2-4: Volcano plot showing the log<sub>2</sub> fold change and -log<sub>10</sub> p value of a comparison of the levels of 66 metabolites measured in tumour samples between PLX4032 treatment and vehicle treatment.

Figure 3.4.2-5: Citrulline levels measured from tumour tissue or serum taken from NSG mice that were subcutaneously injected with A375 cells and treated with PLX4032, CB839 or a combination of the two.

Figure 3.4.2-6: Ornithine, Arginine and Argininosuccinate levels measured from tumour tissue or serum taken from NSG mice that were subcutaneously injected with A375 cells and treated with PLX4032, CB839 or a combination of the two.

Figure 3.4.2-7: Microscope images of ASS1 immunohistochemical staining in tumours generated from a subcutaneous injection of A375 cells in an NSG mouse and treated with PLX4032, CB839 or a combination of the two.

Figure 3.4.2-8: Serum ammonia levels from NSG mice that were subcutaneously injected with A375 cells and treated with PLX4032, CB839 or a combination of the two.

Figure 3.4.3-1: Reads of GLS, GLUD1, ASS1 and ASL as measured by RNAseq in A375 derived tumours treated with the indicated treatment and taken at endpoint.

Figure 3.4.3-2: Plot depicting principal component 1 (PC1) and principal component 2 (PC2) of a principal component analysis performed on the reads from 21,508 genes measured in tumours

treated with PLX4032, CB839 or a combination of the two, by RNAseq.

Figure 3.4.3-3: Venn Diagram showing the number of genes that had significantly different expression in the comparisons of PLX4032, CB839 or Combination treatment vs Vehicle.

Figure 3.4.3-4: heatmap showing the 43 genes significantly changed in a comparison of combination treatment vs PLX4032 treatment.

Table 3.4.3-1: Table showing the gene names for genes that had a significant difference in their expression between PLX4032 and combination treatment.

Figure 3.4.3-5: Results of an enrichment analysis performed on genes measured by RNAseq and ranked by their  $\pi$  value in a comparison of PLX4032 against vehicle and combination against vehicle treatment in A375 derived tumours.

Figure 3.4.3-6: A heatmap of the 29 genes significantly regulated by the combination treatment and attributed to “transcription of HIF1 $\alpha$  targets” in an enrichment analysis.

Figure 3.4.3-7: Levels of Glucose, Lactate, Glucose-6-Phosphate and Pyruvate levels measured from tumour tissue taken from NSG mice that were subcutaneously injected with A375 cells and treated with PLX4032, CB839 or a combination of the two.

Figure 3.4.3-8: The ratio of ATP to AMP measured from tumour tissue taken from NSG mice that were subcutaneously injected with A375 cells and treated with PLX4032, CB839 or a combination of the two.

Figure 4.3-1: Diagram depicting how glucose and glutamine derived carbons contribute to the function of the TCA cycle and allow the production of glutamate.

Figure 4.4-1: A diagram depicting the generation of NAD<sup>+</sup> by oxaloacetate, pyruvate, and  $\alpha$ -ketoglutarate.

Figure 4.5-2: Diagram depicting the urea cycle and the use of aspartate derived carbon and nitrogen.

Figure 4.5-1: A diagram showing the links between redox homeostasis and aspartate synthesis.

## Authors Declaration

I hereby testify that all the work presented in this thesis is my own, unless otherwise stated. I confirm that this work has not been previously submitted for consideration of any other degree.

Rachel Harris

## Acknowledgements

No successful scientific project is a one-person feat, and as such I would like to thank several people for their contribution, assistance and support with this project. Firstly, I would like to thank my supervisors David Sumpton and Saverio Tardito, as well as my former supervisor Gillian Mackay for the opportunity to do this project, as well as their support, discussion, and patience through every step of the way. I would like to thank Ruhi Deshmukh for her guidance and mentoring throughout the *in vivo* aspects of the project, as well as in helping me learn to navigate a scientific project. I would also like to thank lab members Tobias Ackerman, Maria-Francesca Allega, Victor Villars, Engy Shokry, Alejandro Huerta Uribe and former lab member Giovanni Rodriguez-Blanco, as well as my project reviewers Oliver Maddocks and Jim Norman for the insightful discussion and technical support.

I would like to thank Karen Blyth for the use of her project licence in the *in vivo* aspects of this work, as well as her discussion and mentoring in the project. Also, to the staff of the Beatson animal unit, especially Evarest Onwubiko and Barbara Ann Hughes for performing treatments and measurements on the mice. I would like to thank Colin Nixon and the rest of the Beatson histology services for their help with slide preparation, and Gemma Thompson for her help with imaging. Also, to Graeme Clark and Robin Shaw performing

the RNAseq analysis. I would like to thank Franziska Baenke, formerly from the Marais lab for the cell lines used for most of this project. Also, to Calithera Biosciences for their contribution of CB839.

I would like to thank Cancer Research UK for providing the funding for this PhD. Finally, I would like to thank my friends and family - in particular Irene Caldera-Quevedo and Adiba Khan for their reassurance and encouragement throughout the PhD.

## Abbreviations

|               |  |
|---------------|--|
| $\alpha$ -MSH | $\alpha$ -melanocyte stimulating hormone                   |
| ACO           | aconitase  |
| ACTH          | adrenocorticotropic hormone                                |
| ADI-PEG20     | arginine deiminase (pegylated ADI)                         |
| AGC           | automatic gain control                                     |
| AKT           | Ak mouse Thymoma - serine/threonine kinase 1               |
| AML           | acute myeloid leukemia                                     |
| AMP           | adenosine 5'-monophosphate                                 |
| ASL           | argininosuccinate lyase                                    |
| ASNS          | asparagine synthetase                                      |
| ASS1          | argininosuccinate synthase                                 |
| ATM           | Ataxia-telangiectasia mutated serine/threonine kinase      |
| ATP           | adenosine 5'-triphosphate                                  |
| BCL2          | B-cell lymphoma 2  |
| BPTES         | bis-2-5-phenylacetamido-1,3,4-thiadiazol-2-ylethyl sulfide |

|         |   |
|---------|---|
| BRAF    | murine sarcoma viral oncogene homolog B     |
| C57BL/6 | C57 black 6                                 |
| cAMP    | 3',5'-cyclic adenosine monophosphate        |
| CD80    | cluster of differentiation 80               |
| CD86    | cluster of differentiation 86               |
| CDH2    | cadherin 2                                  |
| CDK2NA  | cyclin dependent kinase inhibitor 2A        |
| CDK4    | cyclin dependent kinase 4                   |
| CGGC    | compare groups of growth curves             |
| CMP     | cytidine 5'-monophosphate                   |
| CoA     | coenzyme A                                  |
| CPD     | cyclobutane pyrimidine dimers               |
| CRAF    | murine sarcoma viral oncogene homolog C     |
| CREB    | cAMP responsive element binding protein     |
| CS      | citrate synthase                            |
| CTLA-4  | cytotoxic T-lymphocyte associated protein 4 |
| CYSR    | cystine reductase                           |
| DMEM    | Dulbecco's Modified Eagle Medium            |
| DNA     | deoxyribonucleic acid                       |
| EGFR    | epidermal growth factor receptor            |
| ERK     | extracellular signal-regulated kinase       |
| ESI     | electrospray ionization                     |

|          |   |
|----------|---|
| ETC      | electron transport chain  |
| FH       | fumarate hydratase  |
| Foxn1    | forkhead box N1   |
| GAC      | Glutaminase C   |
| GCL      | glutamate-cysteine ligase   |
| GDP      | guanosine 5'-diphosphate  |
| GEMM     | genetically engineered mouse model                                  |
| GLS      | glutaminase   |
| GLUD     | glutamate dehydrogenase   |
| GMP      | guanosine 5'-monophosphate  |
| GOT      | glutamic-oxaloacetic transaminase                                   |
| GPCR     | G protein-coupled receptor  |
| GRB2     | growth factor receptor bound protein 2                              |
| GSH      | glutathione   |
| GSS      | glutathione synthetase  |
| GSSG     | glutathione disulfide   |
| GTP      | guanosine 5'-triphosphate   |
| HGF      | human growth factor   |
| HILIC    | Hydrophilic interaction chromatography                              |
| HIV/AIDS | human immunodeficiency virus and acquired immunodeficiency syndrome |
| HMGCL    | 3-hydroxy-3-methylglutaryl-CoA lyase                                |

|        |   |
|--------|---|
| HMGCS1 | 3-hydroxy-3-methylglutaryl-CoA synthase 1 |
| IDH    | isocitrate dehydrogenase                  |
| IGF    | insulin-like growth factor 1              |
| IL2ry  | interleukin 2 receptor subunit gamma      |
| KGA    | K-type mitochondrial glutaminase          |
| LC-MS  | liquid chromatography-mass spectrometry   |
| MC1R   | melanocortin 1 receptor                   |
| MDH    | malate dehydrogenase                      |
| MDM2   | Mouse double minute 2                     |
| MEK    | mitogen-activated protein kinase kinase 1 |
| MITF   | melanocyte inducing transcription factor  |
| MS2    | MS/MS                                     |
| Mtorc1 | mammalian target of rapamycin complex 1   |
| NRAS   | Neuroblastoma RAS viral oncogene homolog  |
| NSCLC  | non-small cell lung cancer                |
| NSG    | NOD-scid gamma                            |
| OAT    | ornithine aminotransferase.               |
| Oct-01 | Octamer transcription factor 1            |
| OGDH   | 2-oxoglutarate dehydrogenase              |
| P5CS   | pyrroline-5-carboxylate synthase          |
| PCA    | principal component analysis              |
| PD-1   | Programmed cell death protein 1           |

|               |  |
|---------------|--|
| PDGFR         | platelet-derived growth factor receptor                                |
| PGC1 $\alpha$ | peroxisome proliferator-activated receptor gamma coactivator 1-alpha   |
| PI3K          | phosphatidylinositol-4,5-bisphosphate 3-kinase                         |
| PI3KCA        | phosphatidylinositol-4,5-bisphosphate 3-kinase catalytic subunit alpha |
| PIP2          | phosphatidylinositol 4,5-bisphosphate                                  |
| PIP3          | phosphatidylinositol (3,4,5)-trisphosphate                             |
| PKA           | protein kinase A   |
| PLS-DA        | partial least squares discriminant analysis                            |
| Prkdc         | protein kinase, DNA-activated, catalytic subunit                       |
| PRODH         | proline dehydrogenase  |
| PTEN          | Phosphatase And Tensin Homolog   |
| PYCR          | pyrroline-5-carboxylate reductase                                      |
| RAS           | Rat sarcoma virus  |
| Rb            | retinoblastoma   |
| RF lens       | Radio Frequency Lens   |
| ROS           | reactive oxygen species  |
| RT            | room temperature   |
| RTK           | Receptor tyrosine Kinase   |
| SCS           | succinyl CoA synthase  |
| SDH           | succinate dehydrogenase  |

|        |  |
|--------|--|
| SIM    | Selective Ion Monitoring                                 |
| SLC1A5 | solute carrier family 1 member 5                         |
| SOS1   | Son of sevenless guanine nucleotide exchange factor 1    |
| SREBP1 | sterol regulatory element-binding transcription factor 1 |
| TCA    | tricarboxylic acid                                       |
| TMP    | thymidine 5'-monophosphate                               |
| TNM    | Tumour, Nodes, Metastasis                                |
| TRP1   | tyrosinase   |
| ULK1   | Unc-51 like autophagy activating kinase 1                |
| UMP    | uridine 5'-monophosphate                                 |
| UV     | ultraviolet  |
| xCT    | cystine/glutamate antiporter                             |
| XIC    | extracted ion chromatograms                              |

# Chapter 1: Introduction

## 1.1 Melanoma: Pathogenesis and Diagnosis

Melanoma is a form of skin cancer, derived from melanocytes. Whilst several oncogenes are known to drive the growth of melanoma, the high proportion of cases harbouring the BRAF V600E mutation have made it a focus for targeted BRAF inhibitor therapies such as Vemurafenib. Despite the success of such targeted therapies, BRAF inhibitor resistance is a common occurrence. This section will introduce the molecular pathophysiology of melanoma, as well as an overview of its diagnosis and treatment.

### 1.1.1 Epidemiology

Melanoma is the deadliest form of skin cancer, accounting for less than 5% of skin cancer cases, but being the cause of 75% of skin cancer deaths (Davis, Shalin and Tackett, 2019). In the UK, melanoma is the 5<sup>th</sup> most common cancer with 16,200 new cases and 1,300 deaths in 2017 (Memon *et al.*, 2021). It is a disease commonly attributed to excessive UV exposure, with an estimated 86% of all melanomas in the UK thought to be caused by excessive UV radiation (DM Parkin, D Mesher and P Sasieni, 2011; Memon *et al.*, 2021). As with most cancer types of cancer, age is also associated with risk factor for developing melanoma. A steady increase in incidence rates occurs with age until the age of 60-70, when incidence rates plateau (Natalie H. Matthews *et al.*, 2017). Sex has also been linked to melanoma risk, with a higher worldwide incidence of melanoma in

males than females, although it is not known whether this association is due to behavioural differences in sun exposure or hormonal differences (Bellenghi *et al.*, 2020).

Aside from factors associated with UV exposure, genetic evidence also suggests that hereditary factors independent of ethnicity may also be involved in melanoma risk. For example, mutations in the *CDKN2A* gene have been identified in 20-40% of families with a high number of melanoma cases (Rossi *et al.*, 2019). Furthermore, the *CDK4* gene has been linked to melanoma susceptibility, although germline mutations in this gene have so far only been found to occur in 3 families worldwide (Goldstein and Tucker, 2001). Furthermore, immune activity is a risk factor in melanoma, as melanoma incidence is higher in individuals who are prescribed immunosuppressive medications after organ transplant or contracting HIV/AIDS (Grulich *et al.*, 2007).

### 1.1.2 Melanocytes: Location and Function

Melanoma is a cancer derived from melanocytes, which are found in the basal epidermis, hair follicles, meninges, and choroidal layer of the eye (Leonardi *et al.*, 2018) (Figure 1.1.2-1). Melanocytes are derived from the neural crest, meaning they are differentiated along the same lineage as neurons, glial cells, the adrenal medulla, and cardiac cells (Lin and Fisher, 2007). Their main function is to produce the pigment - melanin, which is produced by the oxidation and polymerisation of tyrosine in response to UV induced DNA damage (Leonardi *et al.*, 2018). As with any specialised cell types, molecular characteristics of melanocytes are regulated by transcription factors

specific to this cell type. The primary transcription factor responsible for maintaining the melanocyte lineage is MITF, which can bind the DNA in association with other transcription factors. MITF can cause the transcription of genes such as *TRP1* which allows the conversion of tyrosine into melanin (Figure 1.1.2-2) (Kawakami and Fisher, 2017). For the ability of the MITF protein to enable transcription of pro-survival genes *BCL2* and *CDK2*, the *MITF* gene has been identified as an oncogene, and some melanoma cells retain their dependence on MITF (Hartman and Czyz, 2015).

*MITF* expression can be induced by the melanocortin-1 receptor (MC1R). This is a G-protein coupled receptor (GPCR) found on the surface of melanocytes, responsible for translating signals from  $\alpha$ -melanocyte stimulating hormone ( $\alpha$ -MSH) and adrenocorticotrophic hormone (ACTH) to cause the transcription of genes associated with melanin synthesis (Hartman and Czyz, 2015) (Figure 1.1.2-2). Aside from  $\alpha$ -MSH and ACTH mediated control of melanin synthesis, UV radiation stimulates the production of melanin. UVB light (280-315nm wavelength) can directly cause DNA damage, generating either cyclobutane pyrimidine dimers (CPDs) or 6-4 photoproducts (6-4 PPs) (Clancy, 2008) in two adjacent DNA bases. In addition, UVB and UVC light can alter the  $H_2O_2$  binding site in the catalase enzyme, allowing water molecules to access the heme iron and generate protons, which interact with oxygen and generate ROS (de Jager *et al.*, 2017). This form of UV light causes more damage but is less able to penetrate the skin deeply than UVA light. Despite this, UVA is also able to generate superoxide (de Jager *et al.*, 2017). The oxygen radicals produced by UVA can thereby lead to extensive DNA damage by reacting with the DNA, both in melanocytes and keratinocytes (Jhappan, Noonan and Merlino, 2003). UVA exposure can therefore

trigger a “DNA damage response” to genetic insult. This is largely mediated by the tumour suppressor, p53. When released from its ubiquitin ligase (MDM2), p53 can accumulate in the nucleus and promote the transcription of DNA damage response proteins such as  $\alpha$ MSH and ACTH, as well as TRP1 (Jhappan, Noonan and Merlino, 2003) (Figure 1.1.2-2). The resultant p53-dependant expression of melanin producing enzymes can increase the production of melanin pigment, which are able to absorb UV photons and free radicals to prevent further DNA damage (Jhappan, Noonan and Merlino, 2003). Therefore, whilst melanocytes exist as part of a defence system to prevent DNA damage caused by UV light, they can also be subject to UV-induced DNA damage, thus initiating cancer.

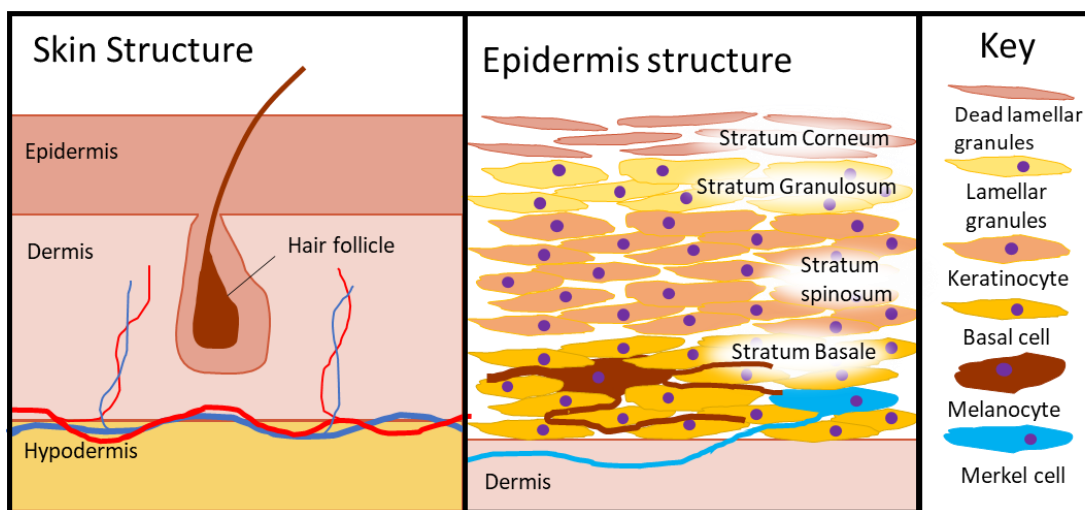


Figure 1.1.2-1: Diagram depicting the location of melanocytes in the skin. Figure based on and adapted from Anatomy & Physiology, 1<sup>st</sup> edition(Lindsay M. Biga *et al.*, 2019)). The epidermis is the outer most layer of the skin, with the dermis underneath perfused with blood, lymph, nerves, and other structures such as hair follicles and sweat glands. The hypodermis is tightly attached to the dermis and is made up of well vascularised connective tissue and adipose tissue (left). Diagram showing the cellular structure of the epidermis. Melanocytes are dispersed with protrusions around the basal cells within the stratum basale (right).

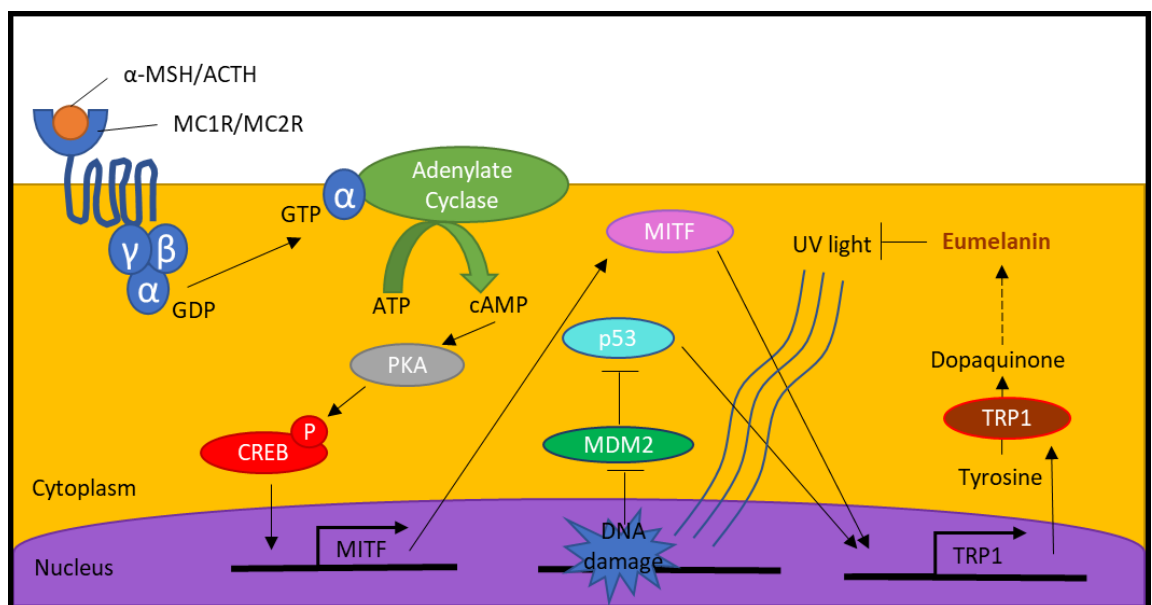


Figure 1.1.2-2: Diagram depicting the mechanisms inducing melanin production in melanocytes. Melanin production is mediated partially via the expression of the *TRP1* gene and the activity of the TRP1 enzyme and can be induced by both endocrine signals as well as DNA damage.

### 1.1.3 Molecular Pathogenesis of Melanoma

The transformation of melanocytes into melanoma is caused by the dysregulation of signalling pathways involved in controlling cellular homeostasis(David Polsky and Carlos Codon-Cardo, 2003). In a

healthy cell, these signalling pathways are tightly regulated to maintain the normal function and replication of the cell. However, mutations in genes encoding factors of these signalling pathways can cause their aberrant expression or activation, leading to oncogenesis. Many genes have been implicated as drivers of cancer (over 700 genes annotated by the 'cancer gene census') (Tate *et al.*, 2019), although only a few are enriched within cancers from the same tissue or cell of origin.

In the case of melanoma, UV light has been implicated as the main mutagenic source. Whilst UVA light usually causes a cytosine to thymine transition (C→T) (Hodis, Ian R Watson, *et al.*, 2012; Brash, 2015), it would therefore be expected that the most prevalent driver mutations should also be caused by a C→T substitution. However, this is not the unique molecular basis implicated in melanoma oncogenesis, as the mutations attributed to driving oncogenesis are not specifically encoded by C→T transitions (Hodis, Ian R Watson, *et al.*, 2012). Melanomas from chronically sun exposed regions do still tend to have the highest mutational burden (Krauthammer *et al.*, 2012), meaning that UV light is able to cause melanoma due to random mutations induced by ROS. These mutations cause melanoma when they occur in genes involved in a few commonly dysregulated signalling pathways driving oncogenic growth in melanocytes (David Polsky and Carlos Codon-Cardo, 2003; Hodis, Ian R Watson, *et al.*, 2012; Ticha *et al.*, 2019).

The two most common mutations driving melanoma both act as part of the RAS-RAF-MEK-ERK signalling pathway (Figure 1.1.3-1). *BRAF* and *NRAS* mutations are found in approximately 50% and 30% of all melanoma cases respectively (Ticher, I *et al.*, 2019) and are almost entirely mutually exclusive (Hodis, Ian R Watson, *et al.*, 2012). The

high prevalence of mutations in in the same pathway indicates its relevance for cell growth specifically in melanocytes. In addition, mutations can be found in other members of the same pathway such as *KRAS* and *MAP2K1*, although at a lower frequency (Ticher, I *et al.*, 2019). The prevailing role of this signalling pathway in many cancer types including melanoma deserves a more in-depth description that will follow in this chapter.

The *TP53* gene encoding for p53 is mutated in approximately 10-20% of melanoma cases (Hodis, Ian R. Watson, *et al.*, 2012; Xiao *et al.*, 2018; I *et al.*, 2019). Surprisingly though, the prevalence of *TP53* mutation is lower in malignant melanoma than in most other cancer types, where it can be mutated in up to 50% of cases(Olivier, Hollstein and Hainaut, 2010) as the most frequently mutated gene in human tumours (Mantovani, Collavin and Sal, 2019). Its resultant protein, p53 is activated in response to a diverse array of cellular stresses, such as oncogene expression, DNA damage, hypoxia, and metabolic dysfunction. The *ATM* gene was also found to be mutated in 8% of melanomas, which gives rise to the ATM protein, responsible for mediating the accumulation of p53 in response to DNA damage (Ticher, I *et al.*, 2019)(Figure 1.1.3-1).

Genes encoding for members of the PI3K-AKT/PTEN pathway are also frequently mutated in melanoma, with mutations in *PTEN* and *PI3KCA* reported to occur in 12% and 5% of melanomas respectively (Hodis, Ian R Watson, *et al.*, 2012). As part of the same signalling pathway, the activities of PTEN (Phosphatase and tensin homolog) and PI3K (Phosphoinositide 3-kinase) are opposed to each other, mediating signals from surface bound receptor tyrosine kinases (RTK). The activation of an RTK causes the autophosphorylation of residues in the cytoplasmic domain of the protein, to which proteins p85 and

p110 can dock. The docking of these proteins allows PI3K to subsequently bind to these proteins, and thus be localised to the membrane such that it has access to PIP2 (phosphatidylinositol bisphosphate), a phospholipid making up part of the membrane of a cell. When it is localised to PI3K, PIP2 can be phosphorylated to PIP3 (phosphatidylinositol triphosphate), a process that can be reversed by the phosphatase PTEN. Between PI3K and PTEN, levels of PIP3 are tightly regulated and normally reflect the presence of growth factors. A tight level of control over PIP3 levels is important as this phosphoinositide is bound by AKT (also known as protein kinase B or PKB), causing a conformational change to activate it. Subsequently to activation, AKT can phosphorylate and thus activate a range of further downstream transcription factors involved in growth, survival, and replication, making *PI3KCA* an oncogene and *PTEN* its opposing tumour suppressor (Figure 1.1.3-1). Aside from *PI3KCA* and *PTEN* mutation, a low level of *AKT1* mutation has also been detected in some melanomas (Ticher, I *et al.*, 2019) and *NRAS* activating mutations can also result in activation of this pathway (Liu and Sheikh, 2014) making it a key molecular pathway in melanoma tumorigenesis.

*CDK4* and *CDKN2A* mutations are somatic mutations (Ticher, I *et al.*, 2019) in melanoma but have also been associated with development of a familial form of melanoma (Liu and Sheikh, 2014). These genes control the cell cycle, initiating the progression from G1 to S phase in which the DNA is replicated (Liu and Sheikh, 2014). In the presence of Cyclin D1 which is synthesized during the G1 phase, CDK4 (Cyclin-dependent kinase 4) causes the phosphorylation of retinoblastoma protein (RB), which allows the release of E2F to modulate ribosome biogenesis and other transcription factors that

support cell cycle progression, nucleotide synthesis and DNA replication (Figure 1.1.3-1). Thus, CDK4 mediated RB1 phosphorylation is required for cell cycle progression (Sheppard and McArthur, 2013).

The development of targeted therapies in recent years has highlighted the potential of precision medicine (Chae *et al.*, 2017), which relies on the molecular characterisation of a given patient's tumour to select the best treatment for each patient (Liu and Sheikh, 2014). As for most cancer types, a combination of different mutations drives the growth of any given patient's melanoma, for which a targeted therapy may exist. Therefore, identifying the mutations driving a particular patient's tumour is important to offer the most effective therapy available.

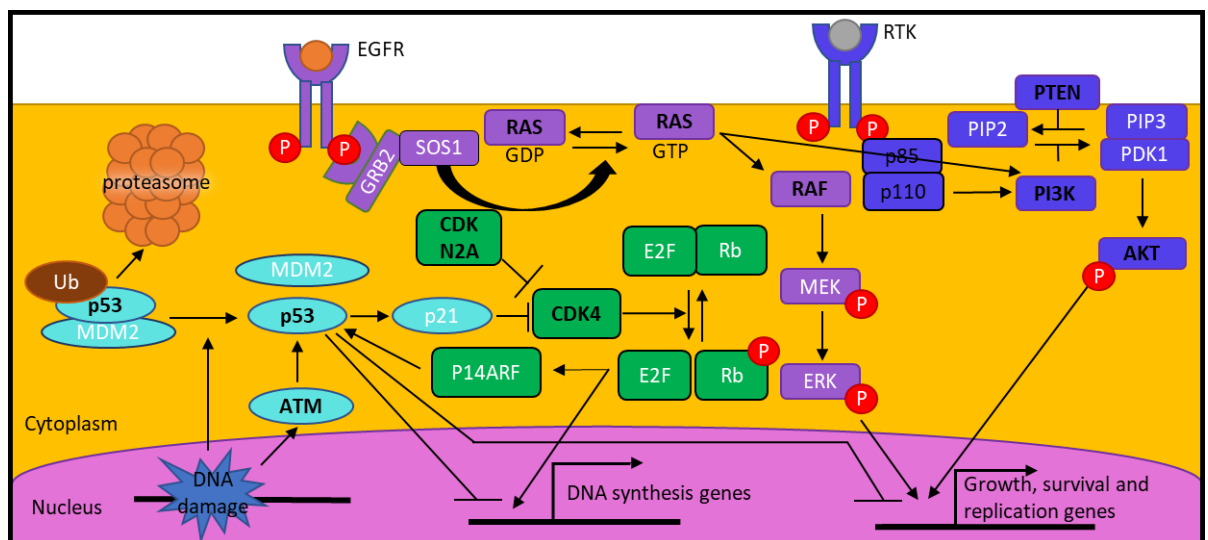


Figure 1.1.3-1: Diagram depicting the main molecular pathways driving the pathogenesis of melanoma. Commonly mutated genes are shown in black. The RAS-RAF-MEK-ERK signalling cascade is shown in purple, the PI3K-AKT/PTEN pathway in dark blue, the CDKN2A/CDK pathway is shown in green and p53 mechanism is shown in light blue.

#### 1.1.4 Diagnosis of Melanoma

Melanomas can develop from benign nevi, which are common lesions found on the skin. If a nevus grows deep enough or has developed mutations that allow it to spread to other parts of the body, it becomes known as malignant and is thus classified as a malignant melanoma. Regular examination of the size and shape of each lesion is important to determine if it is growing or changing, as diagnosis of a melanoma is usually carried out by a simple clinical assessment of a lesion. Clinicians characterise a lesion based on a set of defining characteristics pertaining to the visual appearance of the melanoma, known as the 'ABCDE' rule (asymmetry, irregular borders, colour variations, diameter, and elevated surface) (Liu and Sheikh, 2014). A lesion may then be resected based on clinical assessment both to prevent the growth and metastasis of the lesion, but also enable further classification based on depth of invasion. Multiple classification systems have been proposed for melanoma, however the most recent and commonly in use today is known as the TNM (tumour, nodes, metastasis) staging system (Table 1.1.4-1a-d). Based on the attributes of the primary tumour, the presence of the disease in localised lymph nodes and the existence of distant metastases, patients are assigned to a stage grouping that is strongly linked to survival (Davis, Shalin and Tackett, 2019). In general, tumours with a depth greater than 0.8mm or which have ulcerated will be surgically resected, along with the surrounding tissue. If lymph nodes have been infiltrated by the tumour, these will be identified either visually (infiltrated lymph nodes may be swollen) or by a sentinel lymph node biopsy (SNLB) (Swetter, 2021), in which radioactive tracers may be injected into the melanoma such that sentinel lymph nodes may be identified with a radioactive probe. The removal of

the primary tumour also provides biopsy material for more accurate molecular analysis with prognostic value.

| <b>T Category</b> | <b>Depth</b> | <b>Ulceration</b>          |
|-------------------|--------------|----------------------------|
| T1                | ≤1mm         | With or Without Ulceration |
| T1a               | <0.8mm       | Without Ulceration         |
| T1b               | <0.8mm       | With Ulceration            |
| T2a               | >1, ≤2mm     | Without Ulceration         |
| T2b               | >1, ≤2mm     | With Ulceration            |
| T3a               | >2, ≤4mm     | Without Ulceration         |
| T3b               | >2, ≤4mm     | With Ulceration            |
| T4a               | >4mm         | Without Ulceration         |
| T4b               | >4mm         | With Ulceration            |

Table 1.1.4-a

| <b>N Category</b> | <b>Number of tumour-involved regional lymph nodes and nodal metastatic burden</b>   |
|-------------------|---|
| N0                | No Regional Metastases  |
| N1                | 1 tumour involved node or in-transit (within the lymphatic vessels), satellite (macroscopically visible tumours within 2cm of the primary tumour), and/or microsatellite (microscopically visible tumours within 2cm of the primary tumour) metastases with no tumour involved nodes. |
| N2                | 2 or 3 tumour-involved nodes or in-transit, satellite, and/or microsatellite metastases with 1 tumour involved node   |

|    |  |
|----|--|
| N3 | ≥4 tumour involved nodes or in-transit, satellite, and/or microsatellite metastases with ≥2 tumour-involved nodes, or any number of matted (conjoined) nodes without or with in-transit, satellite, and/or microsatellite metastases |
|----|--|

Table 1.1.4-b

| M Category | Metastases   |
|------------|--|
| M0         | No Evidence of distant metastases                                      |
| M1         | evidence of distant metastases (usually in the liver, lung, and brain) |

Table 1.1.4.c

| Clinical stage | T Category | N Category | M Category |
|----------------|------------|------------|------------|
| IA             | T1a        | N0         | M0         |
| IB             | T1b        | N0         | M0         |
|                | T2a        | N0         | M0         |
| IIA            | T2b        | N0         | M0         |
|                | T3a        | N0         | M0         |
| IIB            | T3b        | N0         | M0         |
|                | T4a        | N0         | M0         |
| IIC            | T4b        | N0         | M0         |
| III            | Any T      | ≥N1        | M0         |
| IV             | Any T      | Any N      | M1         |

#### Table 1.1.4-d

Tables 1.1.4-1a-d: (a) Tumour category based on depth and ulceration of a tumour (b) Nodal metastases category based on number of regional lymph nodes infiltrated (c) Distant metastases category based on presence of metastases (d) Melanoma staging criteria based on tumour depth, lymph node metastases and distant metastases. (Adapted from the Eighth Edition American Joint Committee on Cancer (AJC) melanoma staging system (Keung, E Z and Gershenwald, J E, 2018)).

According to the patient's stage, a treatment plan will be prescribed, outlining whether a patient requires further surgical or adjuvant treatment. Usually, those in stage I or II (see Table 1.1.4–4 above) will be treated only with removal of the primary tumour and sentinel lymph nodes (which are the closest lymph nodes often connected to the tumour). For these patients, 5- and 10-year survival rates will largely be determined by the depth of the primary tumour but were reported as greater than 82% and 75% respectively (Keung, E Z and Gershenwald, J E, 2018). On the other hand, those in stage III or IV (with known clinically positive lymph node metastases) will usually be offered adjuvant therapy alongside removal of primary and resectable metastatic tumour (Swetter, 2021).

## 1.2 Melanoma Treatment and BRAF Inhibitor Resistance

### 1.2.1 The RAS-RAF-MEK-ERK Pathway and its Dysregulation

BRAF is the most frequently mutated gene in metastatic melanoma, occurring in about 50% of patients. 90% of *BRAF* mutations are found at codon 600 in which glutamic acid is exchanged for a valine (V600E). Alternative mutations occur at the same locus, including the V600K (substituting lysine for valine) in 5-6% of patients, and V600R (substituting arginine for valine) (Paolo A. Ascierto *et al.*, 2012). This codon on the activation loop of the serine/threonine kinase, causes an increase in the kinase activity of this protein (Bollag *et al.*, 2012). The mutation causes activation of the downstream MEK and ERK proteins, and therefore prevents negative feedback mechanisms that would normally inhibit the activation of the protein (Paolo A. Ascierto *et al.*, 2012). The constitutively active BRAF transduces the signal to downstream targets such as MEK and ERK proteins in the RAS-RAF -MEK-ERK signalling cascade.

The RAS-RAF-MEK-ERK signalling cascade is a major regulatory pathway controlling cell differentiation, survival, and replication. This pathway is disrupted in 90% of melanomas (Wellbrock and Arozarena, 2016), and has been intensely studied to identify if it can be therapeutically targeted. This pathway allows the transduction of signals from receptor tyrosine kinases on the plasma membrane. When bound to their ligand, receptor tyrosine kinases (for example the epidermal growth factor receptor which binds to its ligand, epidermal growth factor), trigger autophosphorylation in the inner membrane domain. This allows the docking of Grb-2 (Growth factor

receptor bound protein 2) and Sos (Son of Sevenless), which finally binds Ras (**RA**t Sarcoma virus). As a G protein, Ras is active when GTP is bound. Sos is a guanosine triphosphate exchange factor, which can exchange GDP for GTP and enable the activation of Ras. Once GTP bound, Ras can cause activation of Raf (Rapidly Accelerated Fibrosarcoma).

Raf is a serine-threonine kinase which undergoes a conformational change on binding to Ras. This change in conformation allows Raf to phosphorylate several proteins including MEK (**MAPK/ERK Kinase**, also known as *MAP2K*). This initiates a further signalling cascade, resulting in the eventual phosphorylation of ERK (**Extracellular signal-related kinase**, also known as *MAPK*). ERK then phosphorylates numerous downstream targets, such as nuclear transcription factors ([Figure 1.1.3-1](#)) (Jeremy M Berg, John L Tymoczko and Lubert Stryer, 2012). The downstream targets of ERK vary depending on cell type, but in the case of melanocytes and melanoma cells a key target of ERK is transcription of *MITF*. This gene encodes a transcription factor which controls the transcription of genes involved in differentiation (e.g. *TYR* gene), growth (e.g. the *CDH2* gene) and survival (e.g. *BCL2* gene) and thus can influence the biological processes causing tumour initiation and progression (Wellbrock and Arozarena, 2016).

### 1.2.2 Vemurafenib

Upon finding the high frequency of BRAF mutation in melanoma ([Figure 1.2.3-1](#)), a study was carried out to determine whether the activity of this protein as part of the RAS-RAF-MEK-ERK signalling cascade was driving melanoma initiation and growth. The treatment

of BRAF mutant cells with an inhibitor of the downstream protein - MEK, showed that BRAF mutation predicts whether growth inhibition can be elicited by MEK inhibitors, indicating that the BRAF mutation has an active role in driving cancerous growth through MEK (Solit *et al.*, 2006). This suggested that BRAF inhibition may prevent the growth of BRAF mutant melanomas, and thus a selective inhibitor of mutant BRAF was identified by screening a large library of compounds. PLX4720 was identified, which had an IC<sub>50</sub> of 13nM in a biochemical assay for BRAF V600E (Tsai *et al.*, 2008) (Figure 1.2.3-1). The IC<sub>50</sub> of PLX4720 was 160nM for BRAF itself, indicating that the inhibitor is more specific for mutant BRAF (Tsai *et al.*, 2008). It was found that this was because the compound caused its inhibition by binding the ATP binding site, which could be accessed more easily in the 'active' conformation occurring in the mutant BRAF V600E (Tsai *et al.*, 2008; Bollag *et al.*, 2012). Subsequently, PLX4032 (Vemurafenib) was designed as an analogue of PLX4720, with an IC<sub>50</sub> of 30nM against mutant BRAF (Yang *et al.*, 2010). Vemurafenib showed clinical efficacy in a Phase I clinical trial, with an 81% response rate. It was shown that only patients with BRAF mutation in their melanoma had any response to the drug, and thus patients without BRAF mutation were no longer included in subsequent trials (Bollag *et al.*, 2010). Subsequently, BRAF mutant patients were enrolled onto phase 3 randomized clinical trials in which Vemurafenib was compared to the current first line therapy for melanoma patients, which was Dacarbazine. This study found an 84% survival rate in the Vemurafenib treated group, compared to a 64% survival rate in the Dacarbazine group at 6 months (Chapman *et al.*, 2011).

### 1.2.3 Treatment of Melanoma

The primary treatment option for any melanoma is surgical resection. In the early stages, melanoma can be treated with surgery alone (Davis, Shalin and Tackett, 2019), with patients presenting with T1 lesions (primary melanoma of thickness  $\leq 1\text{mm}$ ) having a high survival rate. If melanoma cells have migrated to the sentinel lymph nodes, these may also be resected as well, possibly along with any metastatic tumours, although this is not usually curative (Davis, Shalin and Tackett, 2019). Patients with nodal or metastatic disease have historically had worse outcomes with a 10-year survival rate of 10% (Tyrell *et al.*, 2017).

Given the low survival rates for patients with stage 3 and 4 melanomas, an adjuvant therapy is commonly prescribed alongside resection of the primary tumour and accessible metastases. The first line regimens are an anti CTLA-4 therapy (Ipilimumab), anti PD-1 therapy (such as Nivolumab, Pembrolizumab) or a combination of a BRAF inhibitor (Vemurafenib, Dabrafenib or Encorafenib) and a MEK inhibitor (Cometinib, Trametinib and Binimetinib) (Swetter, 2021). These therapies will be prescribed based on the mutational status of each patient's tumour.

Immunotherapies have been shown to successfully treat patients with advanced melanoma, with 30% of patients responding to anti PD-1 therapy with long term disease control. Both CTLA-4 and PD-1 blockade can be used to treat melanoma because these receptors on the surface of effector T regulatory cells act as a checkpoint to suppress the immune response against the tumour cell. By inhibiting these suppressive checkpoints, the immune system can target melanoma cells. The monoclonal antibody treatment, Ipilimumab can

bind CTLA-4 in the place of its other substrates CD80 and CD86 expressed by melanoma cells, thus preventing them from triggering the immunosuppressive effects of CTLA4. Similarly, Nivolumab and Pembrolizumab can also bind the PD1 receptor on a T cell to prevent its binding to PD-L1 on the antigen presenting cell upon which it would usually inhibit its activation (Kuryk *et al.*, 2020).

Anti-CTLA4 and anti-PD1 therapy can be administered in combination, usually to patients with wildtype BRAF. In addition, they may be administered to patients with mutant BRAF if BRAF inhibitor treatment has failed (Kuryk *et al.*, 2020). Although immune checkpoint inhibitors may initially be effective, resistance to these therapies can be acquired by melanoma cells, which may be overcome by combination therapies (Pires da Silva *et al.*, 2021). One study tested the combination of Ipilimumab and Nivolumab showing a progression free survival rate of 11.5 months compared to 2.9 months and 6.9 months for those on Ipilimumab and Nivolumab alone, respectively (Larkin *et al.*, 2015). Whilst these treatments are effective, adverse effects were reported by 33% of patients in the combination group and 31% of the Ipilimumab only group, respectively. The adverse effects consisted predominantly of gastrointestinal problems (Pires da Silva *et al.*, 2021).

The alternative first-line therapy for BRAF mutant melanoma patients is a targeted therapy against MEK or BRAF. Dabrafenib, Vemurafenib and Encorafenib are all inhibitors of mutant BRAF V600E which have been shown to be effective in BRAF mutant melanoma patients. Initial studies showed that Vemurafenib and Dabrafenib could increase overall survival, progression free survival and overall response rate compared to Dacarbazine chemotherapy, the first-line therapy in use until 2011 (Tanda *et al.*, 2020). Further to this,

Encorafenib is another BRAF inhibitor developed more recently that was shown to give a greater overall survival, progression free survival and overall response rate than Vemurafenib alone (23.5 months median overall survival compared to 16.9 months overall survival respectively) (Tanda *et al.*, 2020).

Whilst initial studies demonstrated the efficacy of BRAF inhibitors on their own, MEK inhibition is now given in combination with a BRAF inhibitor. Whilst MEK itself is not mutated in melanoma, it acts downstream of the mutant RAF (Figure 1.1.3-1), thus mediates oncogenic signals from the oncoprotein. Therefore, MEK inhibitors Trametinib, Cobimetinib and Binimetinib were designed to inhibit MEK. Initial trials combining the BRAF inhibitor Dabrafenib with the MEK inhibitor Trametinib showed an increased median overall survival from 18.7 months to 25.1 compared to Dabrafenib alone, with more recent trials combining Encorafenib (BRAF inhibitor) and Binimetinib (MEK inhibitor) giving a median overall survival of 33.6 months (Tanda *et al.*, 2020). However, adverse effects following treatment with these two drugs combined were frequent, with 58% of patients receiving Encorafenib and Binimetinib reporting high grade adverse effects, consisting predominantly impaired liver function (Dummer *et al.*, 2018).

In recent years, the concept of combining immunotherapy and targeted therapy has been explored for patients with mutant BRAF (Swetter, 2021). The rationale for this approach is the fact that treatment with a BRAF inhibitor can impact on tumour immune response, increasing the infiltration of lymphocytes (Kakavand *et al.*, 2015) as well as melanoma antigen expression (Frederick *et al.*, 2013). For example, Atezolizumab (a PD-L1 inhibitor), Vemurafenib (a BRAF inhibitor) and Cobimetinib (a MEK inhibitor) were assessed in

a phase 3 clinical trial. It was found that by adding Atezolizumab to treatment after an initial treatment cycle (of 28 days) with Vemurafenib and Cobimetinib, progression free survival was significantly increased (Gutzmer *et al.*, 2020). Dabrafenib (BRAF inhibitor), Trametinib (MEK inhibitor) and Pembrolizumab (PD1 inhibitor) have also been assessed in a phase 3 clinical trial, with a greater progression free survival compared to the combination of Dabrafenib and Trametinib. Based on the rationale that BRAF inhibition causes increased immune infiltration, a sequential treatment of BRAF/MEK inhibition followed by PD1/PD-L1 as opposed to a concomitant triple therapy should maximise the therapeutic efficacy. Clinical trials are still ongoing to assess this hypothesis (Swetter, 2021).

For Patients progressing on both targeted and immune therapy or experiencing unacceptable adverse effects, cytotoxic therapies may be used. These may consist of treatments such as paclitaxel, carboplatin, cisplatin, and vinblastine in combination or as single agents (Swetter, 2021). These therapies act on processes common to proliferating cells, such as microtubule assembly and DNA repair.

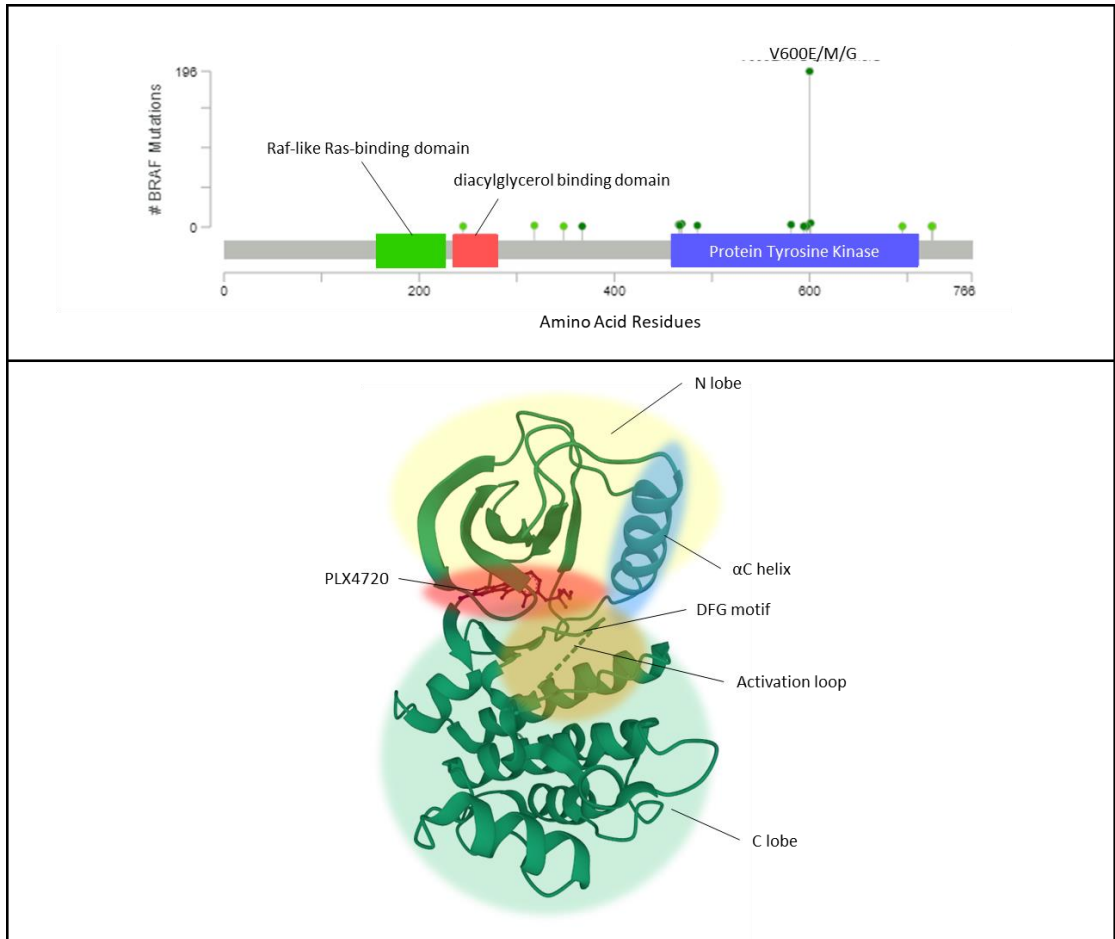


Figure 1.2.3-1: (above) Diagram depicting the location of BRAF mutation within the BRAF gene and the structure of BRAF kinase in complex with PLX4720. Figure adapted from Cbioportal.org (Cerami et al, 2014; Gao et al, 2012). The schematic shows regions of the gene in order of amino acid residues, with points marking mutations that were found within the ‘Skin Cutaneous Melanoma (TCGA, Firehose Legacy)’ dataset of 366 patients. The height of points corresponds to the number of patients found with the indicated mutation. Points marked in dark green are known to be missense driver mutations, whereas those shown in light green are missense mutations of unknown consequence. Most mutations are found in the protein tyrosine kinase region of the gene, with a hotspot mutation in the 600 position. (below) Diagram depicting the structure of the BRAF protein in complex with the BRAF inhibitor PLX4720. Figure adapted from the RCSB PDB structure 3C4C (Tsai *et al*, 2008). The diagram shows PLX4720 bound in the ATP binding site and the protein in it’s ‘DFG-in’ conformation, due to the activation loop to be locked away from the ATP binding site by a salt bridge between Glu 600 and Lys 507.

#### 1.2.4 Mechanisms of BRAF Inhibitor Resistance

Whilst BRAF inhibition increases patient survival, resistance to BRAF inhibitors is a frequent occurrence for patients treated with these therapies (Chapman, 2013). Several studies have attempted to understand the causes of BRAF inhibitor resistance. It has emerged that unlike other malignancies where development of secondary or “gatekeeper” mutations in the same target gene (i.e. in BRAF) are a common mechanism of resistance, no secondary mutations have been found to confer BRAF inhibitor resistance in melanoma (Villanueva, 2011). Instead, multiple mechanisms of resistance exist to overcome BRAF inhibitor treatment (Bollag *et al.*, 2012; Chapman, 2013), which involve either the reactivation of the RAS-RAF-MEK-ERK pathway, or activation of alternative oncogenic pathways.

The reactivation of the RAS-RAF-MEK-ERK pathway can be accomplished through mutation or changes in expression of any of the other proteins in this pathway. For example, other isoforms of Raf such as CRAF or ARAF, which are structurally similar and can also activate MEK (Desideri, Cavallo and Baccharini, 2015), can be expressed or overexpressed to reactivate the pathway in the place of the inhibited BRAF (Villanueva, 2011). Furthermore, clones harbouring mutant NRAS often do not respond to BRAF inhibition and may become enriched within a tumour by BRAF inhibitor treatment (Villanueva, 2011). Paradoxically, in cells with NRAS mutation, BRAF inhibitor treatment may even instigate more signalling through the RAS-RAF-MEK-ERK pathway, as it has been shown to induce hyperactivation of the RAS-RAF-MEK-ERK pathway. This is because mutant NRAS can hyperactivate CRAF, favouring BRAF/CRAF dimers which are stabilised by BRAF inhibitors (Kaplan *et al.*, 2011). Splice

variants of BRAF may also give rise to BRAF-CRAF heterodimers as well as BRAF homodimers, which BRAF inhibitors are unable to inhibit (Proietti *et al.*, 2020). A further mechanism of resistance was found to be by increased expression of BRAF in BRAF inhibitor resistant cells (das Thakur *et al.*, 2013).

Whilst resistance mechanisms can often involve direct reactivation of the RAS-RAF-MEK-ERK pathway, alternative pathways can contribute to reactivation this pathway, to cause BRAF inhibitor resistance. For example, activating mutations in receptor tyrosine kinases (RTKs) such as EGFR (epidermal growth factor receptor) and HGF (hepatocyte growth factor) constitutively activate the RAS-RAF-MEK-ERK signalling pathway (Proietti *et al.*, 2020). One study identified increased expression of IGF and PDGFR in several patient samples, which resulted in the activation of the PI3K/AKT pathway. Subsequently, AKT activation protected BRAF mutant cells from apoptosis in the presence of BRAF inhibition (Shao and Aplin, 2010). Furthermore, AKT activation can also occur through a PTEN loss of function mutation that may also confer resistance to BRAF inhibition (Paraiso *et al.*, 2011). Interestingly, lipid synthesis was shown to have a role in MEK inhibitor resistance via AKT activation, as it was demonstrated that inhibition of the mevalonate pathway could repress AKT activation following MEK inhibition. However it was not determined whether this mechanism occurs in human melanomas with BRAF inhibitor resistance (Iizuka-Ohashi *et al.*, 2018).

Aside from reactivation of the RAS-RAF-MEK-ERK signalling cascade, the cell cycle checkpoint consisting of cyclin D1, CDK4, E2F and RB can also influence BRAF inhibitor resistance (Figure 1.2.4-1). CDK4 expression and cyclin D1 amplification in a BRAF mutant cell line was found to confer BRAF inhibitor resistance (Smalley *et al.*, 2008).

Furthermore, it was later shown that the combination of the CDK4/6 inhibitor LY2835219 could delay tumour recurrence in melanoma xenografted tumours in combination with Vemurafenib (Yadav *et al.*, 2014). This alteration can release the cell cycle checkpoint by allowing the transcription of genes involved in DNA synthesis.

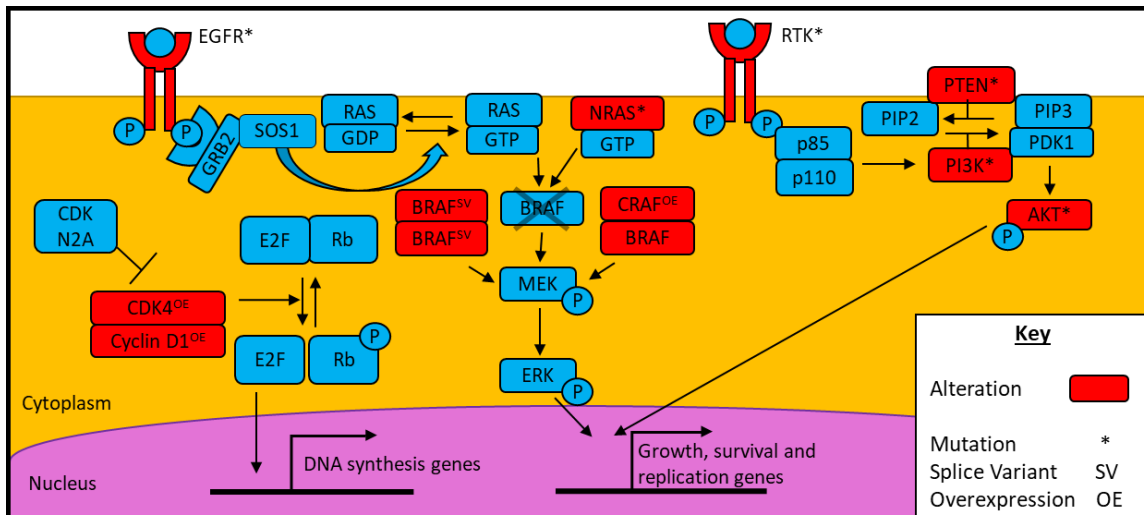


Figure 1.2.4-1: Schematic diagram showing resistance mechanisms of melanoma cells to BRAF inhibition. The key is shown in the lower right corner. Proteins shown in red indicate proteins in which alterations in expression or activity occur to cause BRAF inhibitor resistance. Proteins with “\*” following their name cause resistance by a mutant form. Proteins with “SV” following their name cause resistance by a splice variant. Proteins with “OE” following their name cause resistance by overexpression.

## 1.3 Metabolism in Cancer and Strategies to Target it

### 1.3.1 Metabolism in Cancer

A shift in the metabolism of cancer cells was first recognised by Otto Warburg, who described the phenomenon known as the “Warburg effect” (Warburg, 1956). This term describes the characteristic shift in metabolism of cancer cells from oxidative phosphorylation to glycolytic metabolism, regardless of the availability of oxygen (Frezza, 2019). More recently, reprogramming of metabolism has since been recognized as one of the hallmarks of cancer (Hanahan and Weinberg, 2011). Despite the advantage of this change not being fully elucidated, this phenomenon it is thought to be advantageous in rapidly dividing cells by redirecting glycolytic intermediates from being used in the TCA cycle and instead using anaerobic glycolysis. Therefore, by upregulating anaerobic glycolysis, energy is still supplied in the form of ATP (Heiden, Cantley and Thompson, 2009). According to this theory, if glycolytic ATP meets the energy demands of the cells, the switch to aerobic glycolysis ensures an adequate supply of nucleotides, amino acids, and lipids for anabolism (Heiden, Cantley and Thompson, 2009). Therefore, the Warburg effect which was originally thought to be a side effect of damaged or reduced numbers of mitochondria may in fact be selectively advantageous in terms of rapid proliferation (Fernandez-de-Cossio-Diaz and Vazquez, 2017).

Aside from the shift in means of energy production, several other changes in the metabolism of cancer cells have been discovered and are being investigated as actionable targets to prevent cancer progression. An example of the therapeutic potential of metabolic

targets is the drug Enasidenib (Mullard, 2017; Jinxiu Guo *et al.*, 2021), which was approved for clinical use in 2017 to treat those with IDH2 (isocitrate dehydrogenase 2) mutant AML (acute myeloid leukemia). The mechanism of this treatment relies on the high frequency of IDH2 mutations in AML which causes the generation of the oncometabolite 2-hydroxyglutarate, leading to epigenetic changes and differentiation of cancer cells (Jinxiu Guo *et al.*, 2021).

Another example of a potential cancer therapeutic, has been investigated for use to treat a variety of human cancers is ADI-PEG20, a pegylated arginine deaminase which can degrade the supply of dietary arginine (Tsai *et al.*, 2017; Tine *et al.*, 2021; Yao *et al.*, 2021). The effectiveness of this enzymatic drug relies on is the frequent loss of ASS1 (arginosuccinate synthase) expression in many human cancers, such that these cells which are unable to synthesize arginine from citrulline and aspartate and become auxotrophic for arginine (Yao *et al.*, 2021).

Epidemiological studies suggested that the anti-diabetic drug Metformin could have cancer preventative effects (Lord *et al.*, 2019). Biguanides have been investigated for their use as anticancer agents in cancer as well, including melanoma (Yuan *et al.*, 2013; Trousil *et al.*, 2017). Whilst the mechanism of action for Metformin is not fully understood, one prominent theory suggests that the use of on OXPHOS (oxidative phosphorylation) is impaired by biguanides (Zhao, Swanson and Zheng, 2021). OXPHOS is required to support the activity of the TCA cycle, by regenerating intermediates such as NAD<sup>+</sup> and FAD, thus it supports the pathways that enable production of nucleotides, amino acids and lipids. Therefore, a reduction in OXPHOS upon treatment with metformin may reduce the ability of cells to produce molecules growth and proliferation. More

specifically, Complex I of the ETC allowing OXPHOS was shown to be inhibited by Metformin. Complex I inhibition was shown to inhibit proliferation in the presence of glucose and cause cell death in its absence, thus demonstrating that Metformin also induces dependence on glycolysis. Mechanistically, the growth inhibition by metformin could be overcome by expression of the NADH dehydrogenase ND1, to replace the NAD<sup>+</sup> regenerating capacity of complex I (Wheaton *et al*, 2014). Therefore, inhibiting NADH regeneration in OXPHOS to enforce dependence on glycolysis is a second means through which Metformin targets the initiation and progression of cancer.

### 1.3.2 Metabolic Changes Induced by BRAF Mutation in Melanoma

Given the actionable potential of many metabolic enzymes as targets to prevent cancerous growth, several studies have been performed on models of BRAF mutant melanoma to identify novel metabolic targets. BRAF is part of the BRAF-MITF-PGC1 $\alpha$  axis, meaning that the constitutive activation of BRAF leads to the phosphorylation and suppression of MITF (microphthalmia associated transcription factor) and its downstream target PGC1 $\alpha$  (Haq, Shoag, Andreu-Perez, Yokoyama, Edelman, Glenn C. Rowe, *et al.*, 2013). PGC1 $\alpha$  is a master regulator of mitochondrial biogenesis, and BRAF mutation has been reported to reduce the activity of oxidative phosphorylation, as indicated by lower basal oxygen consumption rates in BRAF mutant cells compared to their wildtype counterparts (Ferretta *et al.*, 2016) (Figure 1.3.2-1).

Another observation linking BRAF mutation and melanoma metabolism identified that Hydroxy-methyl-glutaryl-Coa synthase 1 (HMGCS1) and Hydroxy-methyl-glutaryl-Coa lyase (HMGCL) as synthetic lethal partners of mutant BRAF (Zhao *et al.*, 2017). It was reported that mutant BRAF upregulates the transcription of HMGCL via the transcription factor Oct-1, allowing a positive feedback mechanism whereby the acetoacetate produced by HMGCL could selectively enhance the binding of mutant BRAF V600E to its downstream target, MEK (Kang *et al.*, 2015). HMGCL normally acts as part of the ketogenesis pathway, which allows the production of ketone bodies from fatty acids and results in the production of acetoacetate. HMGCS1, the enzyme immediately upstream of HMGCL in the ketogenesis pathways was shown to be a synthetic lethal partner of mutant BRAF V600E (Zhao *et al.*, 2017) as its silencing selectively reduced growth of melanoma cell lines harbouring a BRAF V600E mutation (Figure 1.3.2-1). It was found that giving mice a high fat diet which increased the serum levels of acetoacetate caused increased growth of xenografted tumours (Xia *et al.*, 2017), supporting the idea that the activity of the ketogenic pathway promoted BRAF mutant tumour progression.

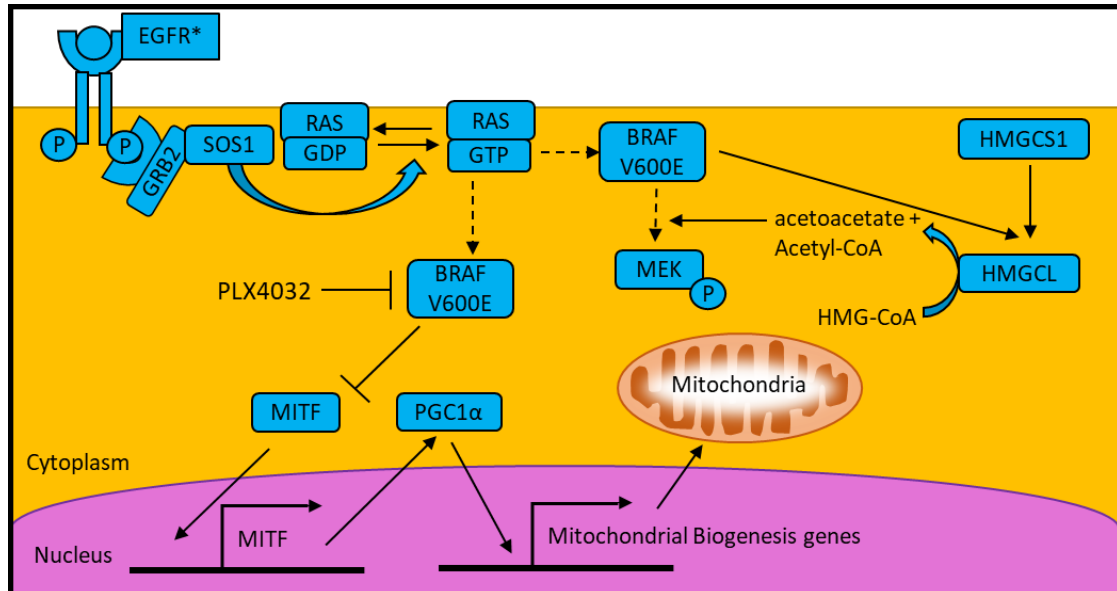


Figure 1.3.2-1: A schematic diagram showing changes in proteins associated with metabolism in association with BRAF mutation. Mutant BRAF V600E can inhibit the levels of MITF, which results in reduced transcription of the mitochondrial transcription factor PGC1 $\alpha$ . This subsequently results in reduced mitochondrial biosynthesis (Haq, Shoag, Andreu-Perez, Yokoyama, Edelman, Glenn C. Rowe, *et al.*, 2013). In addition, the ketogenesis enzymes HMGCL and HMGCS1 are synthetic lethal partners of BRAF V600E because HMGCL can produce acetoacetate, which can scaffold the interaction between BRAF V600E and its downstream phosphorylation target - MEK (Kang *et al.*, 2015). Knockdown of HMGCS1 can reduce acetoacetate production by HMGCL, and therefore it is also considered a synthetic lethal partner of BRAF V600E (Zhao *et al.*, 2017).

### 1.3.3 Metabolic Changes Induced by Mutant BRAF Inhibition and Resistance in Melanoma

Inhibition of mutant BRAF V600E in melanoma causes increased expression of transcription factors for mitochondrial biogenesis (Corazao-Rozas *et al.*, 2013; Baenke *et al.*, 2016). Specifically, inhibition of mutant BRAF was shown to induce an oxidative phosphorylation gene program as well as mitochondrial biogenesis and increased PGC1 $\alpha$  expression (Haq, Shoag, Andreu-Perez,

Yokoyama, Edelman, Glenn C. Rowe, *et al.*, 2013). On the other hand, mutant BRAF controls additional metabolic processes through regulation of AMPK as mutant BRAF activity leads to dissociation of LKB1 from AMPK (Zheng *et al.*, 2009), impairing sensitivity to the AMP:ATP ratio. Furthermore, the activity of AMPK is restored upon inhibition of BRAF (Zheng *et al.*, 2009), but not in BRAF inhibitor resistant cells where proteasomal degradation of AMPK is increased (Li *et al.*, 2017). AMPK is a master regulator of many metabolic processes, through its ability to phosphorylate a wide range of regulatory proteins such as mTORC1, ULK1, PGC1 $\alpha$  and enzymes responsible for the catabolism of Acetyl CoA - ACC1&2 and HMGCR (Mihaylova and Shaw, 2011). This demonstrates that through AMPK, BRAF has the potential for significant metabolic rewiring directly resulting from regulation by BRAF.

In fact, mutant BRAF A375 cells that had been treated with a BRAF inhibitor for 3 days *in vitro* show significant metabolic perturbation with respect to phospholipid synthesis, pyrimidine synthesis, one carbon metabolism and branched chain amino acid metabolism. Surprisingly, this study found that whilst levels of  $\alpha$ -ketoglutarate and succinate were decreased in response to BRAF inhibition, there was no significant change in the overall levels of TCA cycle intermediates (Karki *et al.*, 2021). This contradicted the increased expression of mitochondrial transcription factors that occurred in response to mutant BRAF inhibition (Corazao-Rozas *et al.*, 2013; Baenke *et al.*, 2016), however this may have been due to the relatively short exposure of BRAF mutant cells to a BRAF inhibitor (Karki *et al.*, 2021).

On the other hand, consistent with the change in expression and regulation of transcription factors associated with metabolism, an

increased dependence on the mitochondria and oxidative respiration was reported to occur in melanoma cells that are resistant to BRAF inhibition (Corazao-Rozas *et al.*, 2013; Baenke *et al.*, 2016). It has been reported that BRAF inhibitor resistant cells increase their anaplerotic supply of glutamine to the TCA cycle, replenishing its intermediates (Wang *et al.*, 2014; Baenke *et al.*, 2016; Ratnikov *et al.*, 2017). This is reportedly accompanied by increased expression of glutaminase (GLS), which is the rate limiting step for the anaplerotic flux of glutamine. This was also carried out in A375 cells, however for this study cells were treated with a BRAF inhibitor for 10 passages, which may indicate that acute BRAF inhibitor treatment has a different effect on the metabolism of cells than does long term treatment. Consistently with the increase in glutaminase expression, it has been reported that a compound inhibiting glutaminase, BPTES, was able to decrease the production of ATP and inhibit proliferation selectively in BRAF inhibitor resistant cells (Baenke *et al.*, 2016).

Increased reliance on OXPHOS was shown to occur in BRAF inhibitor resistant cells as demonstrated by the finding that the combination of a BRAF inhibitor and a complex I inhibitor, Phenformin, could synergistically reduce the growth of BRAF inhibitor resistant cells (Yuan *et al.*, 2013). In this study, it was suggested that BRAF inhibitor treatment could select for a sub-population of “slow-cycling” melanoma cells marked by JAIRD1B expression. These cells were shown to have increased use of OXPHOS, such that phenformin could prevent the emergence of BRAF inhibitor resistant cells (Roesch *et al.*, 2013).

Arginine deprivation is another example of metabolic dependency exacerbated by BRAF inhibitor resistance in melanoma. Pegylated arginine deaminase ADI-PEG20 is an enzymatic drug that works

extracellularly to convert arginine to citrulline. It was shown that Vemurafenib resistant cells enter an immediate apoptosis program on arginine deprivation, whereas sensitive cells are more capable of surviving the deprivation due to increased ability to elicit autophagy to generate free amino acids (Li *et al.*, 2016, 2017). Furthermore, it was demonstrated that BRAF inhibitor resistant cells had a decreased potential to elicit argininosuccinate synthase (ASS1) expression upon arginine deprivation. Mechanistically this ASS1 “silencing” seems to be caused by an apparent downregulation of the transcription factor, c-Myc, resulting in a reduced potential to generate arginine via the urea cycle (Li *et al.*, 2016).

ASS1 contributes to the production of arginine through the generation of Argininosuccinate from citrulline and aspartate, which is then converted to arginine and fumarate by argininosuccinate lyase (ASL). The suppression of ASS1 expression is known to occur in malignant melanoma among other cancer types, because of epigenetic silencing (Delage *et al.*, 2010) and is suspected to be advantageous for tumour growth by allowing the conservation of aspartate to support de novo nucleotide synthesis (Rabinovich *et al.*, 2015). Taken together, the epigenetic loss of ASS1 and sensitivity to ADI-PEG20 treatment suggests the potential for funnelling of aspartate into de novo pyrimidine synthesis in BRAF inhibitor resistance.

In addition to changes in amino acid metabolism, BRAF inhibition also alters lipid synthesis. It was shown that the regulator of lipogenesis, SREBP1, is downregulated in acute treatment with vemurafenib, and upregulated again upon acquisition of vemurafenib resistance. Inhibition of SREBP1 re-sensitizes resistant cells to vemurafenib, demonstrating that SREBP1 activity promotes BRAF inhibitor

resistance (Talebi *et al.*, 2018). The dependence on SREBP1 was explained by the protection against ROS damage provided by production of saturated lipids, which are less susceptible to peroxidation than unsaturated lipids. It was shown that mimicry of a polyunsaturated membrane by addition of linoleic acid and linolenic acid caused reduced cell proliferation in Vemurafenib treated cells, and that addition of the mono-unsaturated fatty acid oleic acid, could reverse this phenotype (Talebi *et al.*, 2018). An additional study supporting the importance of SREBP1 expression in BRAF inhibitor resistance found that activation of the mevalonate pathway, many of whose enzymes are transcriptionally regulated by SREBPs (Sakakura *et al.*, 2001), could confer resistance to MEK inhibitors by increasing the production of geranylgeranyl phosphate, an activator of the PI3K/AKT pathway (Iizuka-Ohashi *et al.*, 2018), which is known to support resistance to BRAF inhibitors in melanoma cells (Perna *et al.*, 2015).

Collectively, these findings indicate that several metabolic mechanisms exist through which BRAF mutant melanoma can survive and evade BRAF inhibition. These changes may allow the survival of cancer cells in response to treatment but can also expose new dependencies that could be targeted to prevent, delay or reverse BRAF inhibitor resistance.

#### 1.3.4 Glutamine Addiction in Cancer

Glutamine can be synthesized from glutamate by glutamine synthetase in cells which express this enzyme, and thus glutamine is considered a conditionally essential amino acid. Glutamine is the

most abundant amino acid found in the blood and kept at a roughly constant level due to de novo synthesis from the skeletal muscle, lung, and adipose tissue (Brian J. Altman, Zachary E. Stine and Chi V. Dang, 2016). Glutamine is also consumed, predominantly in the liver and kidney, which releases ammonia to maintain acid-basic homeostasis (Brian J. Altman, Zachary E. Stine and Chi V. Dang, 2016). In rapidly dividing cells such as lymphocytes and enterocytes, glutamine is used as an energy source, as well as a source of carbon and nitrogen to allow biomass generation (Brian J. Altman, Zachary E. Stine and Chi V. Dang, 2016). Some types of cancer cells also utilize glutamine as an energy source, and for these it becomes a nutrient essential to their survival. This phenomenon, known as 'glutamine addiction', has been reported to occur in non-small cell lung cancer, breast, brain, and pancreatic cancer as well as leukemia (Wise and Thompson, 2010; Choi and Park, 2018).

Glutamine can be consumed to produce energy as well as generate new biomass through a process called anaplerosis. In this process, glutamine is imported through several transporters on the membrane of the cell - most commonly the ASCT2 transporters encoded for by the SLC1A5 gene. The intracellular pools of glutamine can then be used either for biosynthesis and be metabolized in the anaplerotic pathway via glutaminase that converts glutamine to glutamate and ammonia.

Two forms of glutaminase enzyme are encoded for in humans - GLS (kidney type glutaminase) and GLS2 (liver type glutaminase)(Brian J. Altman, Zachary E. Stine and Chi V. Dang, 2016; Katt, Lukey and Cerione, 2017). The GLS gene gives rise to two splice variants with catalytic activity; a longer form known as kidney glutaminase (KGA); and a shorter form known as glutaminase C (GAC). The KGA form of

GLS has been extensively studied for its role in cancer progression, as it has been found to be highly expressed in leukemia, adrenocortical cancer, triple-negative breast cancer, colorectal cancer, kidney clear or papillary cell carcinoma, lung adenocarcinoma, melanoma, mesothelioma, pancreatic cancer, sarcoma, and thyroid cancer (Katt, Lukey and Cerione, 2017). KGA is localised to the mitochondria, where glutamine is imported by a splice variant of the SLC1A5 gene (Yoo *et al.*, 2020). This transporter is putatively a rate limiting step for glutamine anaplerosis (Yoo *et al.*, 2020), although the expression of this variant across different cancer types has not yet been well studied.

Subsequently to mitochondrial import and deamination to glutamate, the glutamine carbon backbone is released as  $\alpha$ -ketoglutarate by the mitochondrial enzyme glutamate dehydrogenase (GLUD1), which generates ammonia. Furthermore  $\alpha$ -ketoglutarate is then used as an intermediate of the TCA cycle (Brian J. Altman, Zachary E. Stine and Chi V. Dang, 2016), allowing the conversion of a further seven  $\text{NAD}^+$  to NADH and two FAD to FADH<sub>2</sub> (Figure 1.3.4-1). Whilst this reaction is crucial to enabling the anaplerotic flux of glutamine derived carbons into the TCA (tricarboxylic acid) cycle, it is not a rate limiting step of this process (Herranz, 2017). Alternative enzymes can also allow the synthesis of  $\alpha$ -ketoglutarate from glutamate, including the transaminase, GOT(1/2) which simultaneously converts oxaloacetate to aspartate instead of producing ammonia. This reaction itself may indeed be as crucial in glutamine addicted cells, as it has been shown that rapid cell proliferation can be prevented due to a lack of oxidative  $\text{NAD}^+$  regeneration from OXPHOS, which is needed to enable anaplerotic glutamine to be used for de novo aspartate synthesis (Figure 1.3.4-1) (Birsoy *et al.*, 2015; Sullivan *et al.*, 2015).

Furthermore, In support of the importance of aspartate synthesis in rapidly dividing cells, ASS1 is frequently silenced in cancer cells. As previously mentioned, this was reported to be an advantageous trait in cancer cells to conserve aspartate and prevent it's use in production of arginosuccinate (Rabinovich *et al.*, 2015).

Aspartate can be generated from the TCA cycle intermediate oxaloacetate through the activity of either the mitochondrial enzyme GOT2 or the cytosolic enzyme GOT1, although cytosolic aspartate availability is predominantly determined by mitochondrial aspartate production (Alkan *et al.*, 2018; Gorgoglione *et al.*, 2022)(Figure 1.3.4-1). Furthermore, glutamine derived nitrogen can also contribute the production of aspartate through the donation of an amine group from glutamate onto the newly formed aspartate via GOT(1/2) (Brian J. Altman, Zachary E. Stine and Chi V. Dang, 2016)(Figure 1.3.4-1).

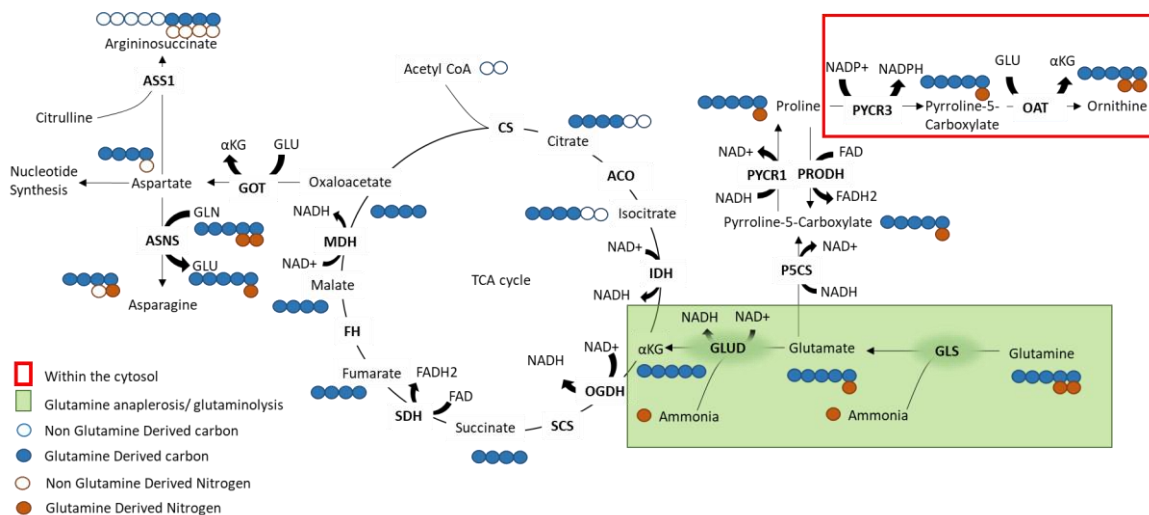


Figure 1.3.4-1: Schematic diagram showing the contribution of glutamine derived carbon and nitrogen to TCA cycle intermediates, aspartate, asparagine, argininosuccinate, proline and ornithine. Glutamine anaplerosis is highlighted in green. The steps of ornithine synthesis occurring only in the cytosol are surrounded in red. The carbon and nitrogen composition of each metabolite in the diagram is represented by a series of blue and brown circles, respectively. Filled blue and brown circles represent carbon and nitrogen derived directly from glutamine, whereas blank circles represent carbon and nitrogen derived from other sources (e.g. Glucose). GLS (glutaminase); GLUD (glutamate dehydrogenase); OGDH (2-oxoglutarate dehydrogenase); SCS (succinyl CoA synthase); SDH (succinate dehydrogenase); FH (fumarate hydratase); MDH (malate dehydrogenase); CS (citrate synthase); ACO (aconitase); IDH (isocitrate dehydrogenase); GOT (glutamic-oxaloacetic transaminase); ASNS (asparagine synthetase); ASS1 (argininosuccinate synthase); P5CS (pyrroline-5-carboxylate synthase); PYCR1/PYCR3 (pyrroline-5-carboxylate reductase); PRODH (proline dehydrogenase) and OAT (ornithine aminotransferase).

Aspartate is used in the malate-aspartate shuttle, that can allow the transport of electrons into the mitochondria (Figure 1.3.4-2). By extension, this implicates aspartate levels in energy generation via the electron transport chain (ETC). Aspartate itself is also a substrate to produce both purine and pyrimidines, providing nitrogen to GMP (guanosine monophosphate), AMP (adenosine monophosphate), UMP (uridine monophosphate) and CMP (cytidine monophosphate) (Sullivan *et al.*, 2015) (Figure 1.3.4-3&4), thus making it essential for the division of cells. This concept is supported by the evidence that aspartate supports cancerous growth (Patel *et al.*, 2016; Furkan Alkan *et al.*, 2018; Garcia-Bermudez *et al.*, 2018; Sullivan *et al.*, 2018) and that its depletion results in reduced levels of nucleotides (Sullivan *et al.*, 2015). In addition, it has been shown that aspartate is essential in cancer cells in which the demand for NAD<sup>+</sup> relative to

the demand for ATP was increased (i.e. cells that have low use of the TCA cycle because of low energetic demand cannot produce aspartate and thus are dependent on its extracellular availability for nucleotide synthesis and growth) (Luengo *et al.*, 2021).

Proline can be synthesized from GLS derived glutamate, by the two mitochondrial enzymes Pyrroline-5-carboxylate synthase (P5CS) and Pyrroline-5-carboxylate reductase (PYCR1) (Burke *et al.*, 2020).

PYCR1 is upregulated in melanoma, NSCLC, renal cell carcinoma, breast cancer, colorectal cancer, prostate cancer, and hepatocellular carcinoma, redirecting glutamine derived glutamate towards proline biosynthesis. This is in opposition to the enzyme reversing this reaction in the mitochondria, PRODH (Figure 1.3.4-1), which was reported to be a tumour suppressor because of its ability to trigger ROS-induced apoptosis in cancer (Burke *et al.*, 2020). As well as being directly linked to glutamine anaplerosis, proline is also connected with the urea cycle since it can be synthesized from ornithine via ornithine aminotransferase (OAT) and PYCR3 (Burke *et al.*, 2020) (Figure 1.3.4-1). However, the oxidation of NADP<sup>+</sup> to NADPH that drives this ornithine synthesis pathway in the cytosol can drive the pentose phosphate pathway (PPP), as NADP<sup>+</sup> is used by glucose-6-phosphate dehydrogenase and 6-phosphogluconate dehydrogenase, to produce phosphoribosyl pyrophosphate that can be used in nucleotide synthesis (Burke *et al.*, 2020). In addition, NADPH produced by PYCR3 can also be used in lipid synthesis, providing another means to support new biomass production. Furthermore, the NADPH produced can enable regulation of ROS through its use by glutathione reductase to regenerate reduced glutathione (GSH), thus allowing cells to withstand any ROS produced in energy generation. Overall, the synthesis of ornithine and proline from glutamine

derived carbon and nitrogen can support cancerous growth, offering a further explanation for glutamine addiction in cancer.

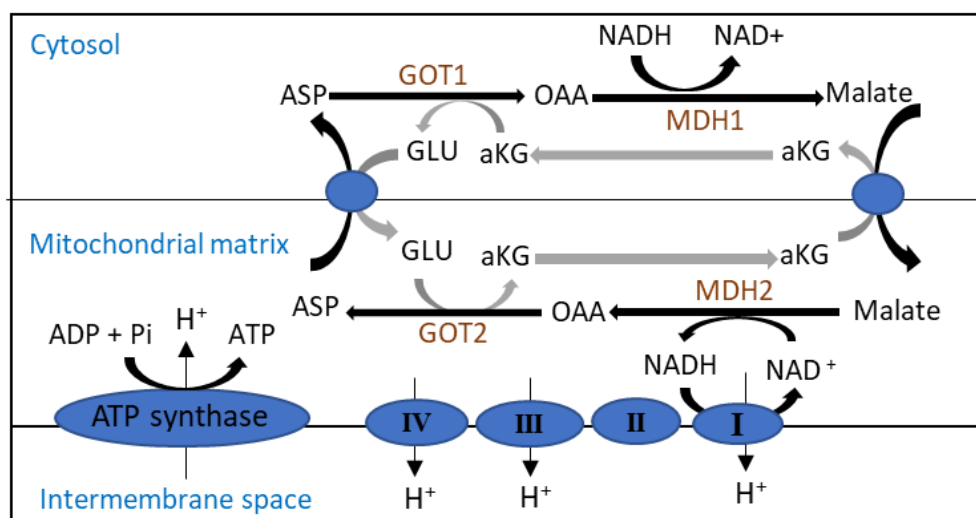


Figure 1.3.4-2: Schematic diagram depicting the Malate-Aspartate shuttle allowing the transfer of electrons into the mitochondria to be used by the electron transport chain to make ATP. The enzymes involved in this cycle GOT1/2 (glutamic-oxaloacetic transaminase) and MDH1/2 (Malate dehydrogenase) are labelled in brown. The two mitochondrial membranes are represented by black lines. Arrows represent the equilibrium of each reaction. The malate- $\alpha$ -ketoglutarate antiporter and glutamate-aspartate antiporter are represented by blue circles on the outer mitochondrial membrane. The proteins making up the electron transport chain are represented by blue circles on the inner mitochondrial membrane. The Malate-Aspartate shuttle intermediates ASP (aspartate), GLU (glutamate), OAA (oxaloacetate),  $\alpha$ KG ( $\alpha$ -ketoglutarate) and malate are labelled in black, along with cofactors NAD<sup>+</sup>/NADH, ATP/ADP and Pi (Phosphate).

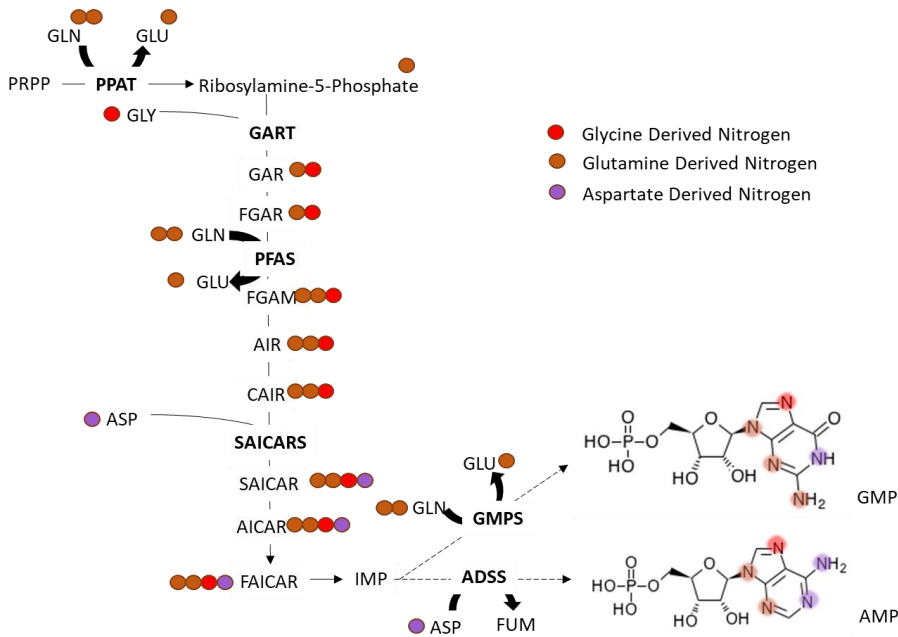


Figure 1.3.4-3: A schematic diagram depicting the use of glutamine, glycine and aspartate derived nitrogen in purine synthesis. Circles filled with brown represent nitrogen derived from glutamine, whereas circles filled with red represent nitrogen derived from glycine and purple from aspartate. Brown circles are a representation of all nitrogen but do not represent chemical structures. At the end of the pathway, chemical structures of AMP and GMP are shown, with nitrogen contributed directly from glutamine highlighted in brown, glycine in red and aspartate in purple. Enzymes responsible for incorporating nitrogen are shown in bold. Solid lines represent a direct reaction, whereas broken lines represent more than one reaction of which only reactions which contribute nitrogen is shown for simplicity.

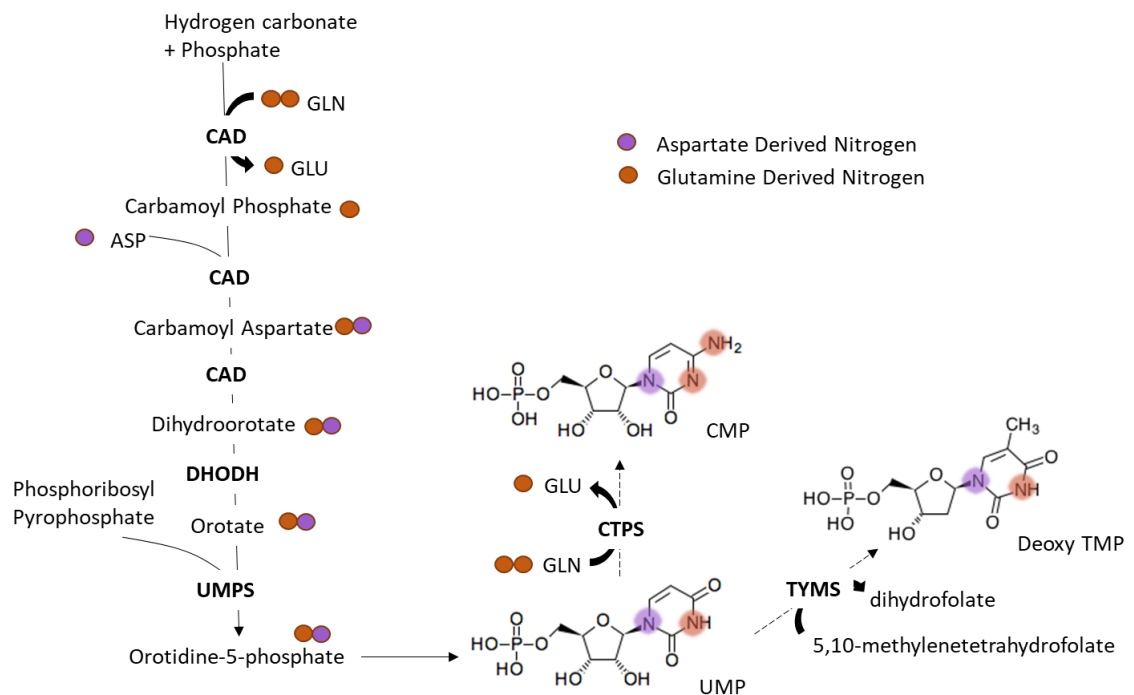


Figure 1.3.4-4: A schematic diagram depicting the use of glutamine and aspartate derived nitrogen in purine synthesis. Brown circles are a representation of all nitrogen but do not represent chemical structures. Circles filled with brown represent nitrogen derived from glutamine, whereas purple circles represent nitrogen derived from aspartate. At the end of the pathway, chemical structures of UMP, CMP and deoxy TMP are shown, with nitrogen contributed directly from glutamine highlighted in brown. Enzymes responsible for incorporating both glutamine derived, and non-glutamine derived nitrogen are shown in bold. Solid lines represent a direct reaction, whereas broken lines represent more than one reaction of which only that which contributes nitrogen is shown for simplicity.

Aside from these key pathways consuming glutamine in cancer cells, glutamine has been shown to have an essential role in buffering reactive oxygen species (ROS) in cancer (Perillo *et al.*, 2020). Glutamine plays a key part in this antioxidant system for two reasons. Firstly, glutamine derived glutamate is required to synthesize the tripeptide, glutathione (GSH) which reacts with ROS molecules such as hydrogen peroxide and prevents their damage to

other important cellular components such as DNA (Figure 1.3.4-5). Secondly, glutamine derived glutamate is required for the import of cystine, which is reduced to cysteine, the redox active moiety of the glutathione tripeptide (Figure 1.3.4-5). It has been shown that activity of the xCT transporter, which exchanges glutamate for cystine on the cell surface, can influence the levels of glutamine anaplerosis as well as drive the phenotype of glutamine addiction. Reduced expression of the xCT transporter improved the survival of breast cancer cells in glucose deprived conditions, indicating that glutamine addiction caused by the xCT transporter can be a metabolic vulnerability (Shin *et al.*, 2017). Furthermore, A549 lung carcinoma cells cultured in adult bovine serum containing less cystine than non-physiological media showed reduced levels of glutaminase activity, and reduced growth inhibition by the GLS inhibitor CB839. Glutaminase activity could be increased by the addition of cystine to adult bovine serum, which also increased the sensitivity to CB839 (Muir *et al.*, 2017).

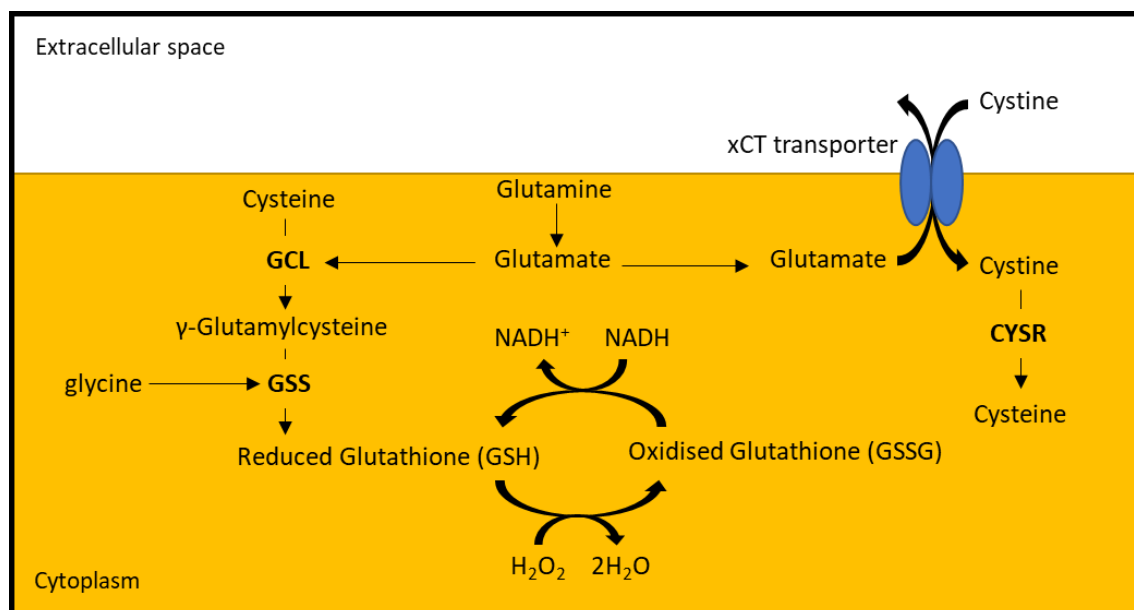


Figure 1.3.4-5: A schematic depicting the use of glutamine derived glutamate in the ROS buffering system. The xCT transporter on the cell membrane is shown in blue, which exchanges the glutamate for cystine. Enzymes involved in the production of GSH; **CYSR** (cystine reductase); **GCL** (glutamate-cysteine ligase) and **GSS** (glutathione synthase) are shown in bold. The cytoplasm of the cell is shown in yellow with the extracellular space shown in white.

## 1.4 Methods to Study Cancer Metabolism

### 1.4.1 Cell Culture and Media

Two-dimensional cell culture has been used since the early 1900's, to study tissue growth, virus biology and vaccine development as well as the role of genes in disease and health (Segeritz and Vallier, 2017; Jensen and Teng, 2020). Whilst initially, murine cancer cell lines were able to be grown for many years by Warren Lewis in the 1930's, a continuous culture of human cancer cells remained elusive until the 1950's when the HeLa cell line, derived from cervical cancer cells, was isolated and grown (Masters, 2002). Since then, many cell lines have been derived from human cancers, which allow researchers to model this complex human pathology. Although these cell lines are advantageous in that they provide a reductionist isolated system to study basic cell biology (Segeritz and Vallier, 2017), they have limitations in replicating the *in vivo* metabolic, structural, immunological, and endocrine environments of the human body.

To improve the modelling of the physiological metabolic environment, media have been formulated that attempt to replicate the nutrient composition of human plasma. Human Plasma Like Medium (HPLM) is formulated with concentrations of amino acids and vitamins like that of human plasma (Cantor *et al.*, 2017). It was shown that cells cultured in HPLM had extensive alterations in their metabolism, compared to cells cultured in non-physiological media (Cantor *et al.*, 2017). Similarly, another media called Plasmax<sup>TM</sup> was formulated with amino acids, vitamins, salts, and other key nutrients at the concentrations found in human plasma (Voorde *et al.*,

2019)(Table 1.4.1-1). It was shown by comparison with the commercial media DMEM-F12, that Plasmax enabled cells to survive at low density due to the presence of sodium selenite, and that a supraphysiological concentration of arginine in DMEM-F12 media artificially reversed the catalytic activity of argininosuccinate lyase enzyme (Voorde *et al.*, 2019).

|                 | human plasma<br>( $\mu\text{M}$ ) | Plasmax<br>( $\mu\text{M}$ ) | DMEM<br>high<br>glucose<br>( $\mu\text{M}$ ) |
|-----------------|-----------------------------------|------------------------------|--|
| L-Alanine       | 230 -510                          | 510                          | NA   |
| L-Arginine      | 13 - 64                           | 64                           | 398  |
| L-Asparagine    | 45 -130                           | 41                           | NA   |
| L-Aspartic acid | 0 - 6                             | 6                            | NA   |
| L-Cysteine      | 23.2 - 43.8                       | 33                           | NA   |
| L-Glutamate     | 32 -140                           | 98                           | NA   |
| L-Glutamine     | 420 -720                          | 650                          | 4000   |
| Glycine         | 170 - 330                         | 330                          | 400  |
| L-Histidine     | 26 - 120                          | 120                          | 200  |
| L-Isoleucine    | 42 - 100                          | 140                          | 802  |
| L-Leucine       | 66 - 170                          | 170                          | 802  |
| L-Lysine        | 150 - 220                         | 220                          | 798  |
| L-Methionine    | 16 - 30                           | 30                           | 201  |
| L-Phenylalanine | 41 - 68                           | 68                           | 400  |
| L-Proline       | 110 -360                          | 360                          | NA   |
| L-Serine        | 56 - 140                          | 140                          | 400  |
| L-Threonine     | 92 - 240                          | 240                          | 798  |
| L-Tryptophan    | 44.8 - 64.2                       | 78                           | 78   |
| L-Tyrosine      | 45 - 74                           | 74                           | 399  |
| L-Valine        | 150 -310                          | 230                          | 803  |

Table 1.4.1-1: Chart depicting the concentrations of 20 proteogenic amino acids in Plasmax™ and DMEM with high glucose and the normal concentration range for human serum (adapted from “Cell Culture Medium Formulation and Its Implications in Cancer Metabolism” (Ackermann and Tardito, 2019)). Cells in the DMEM column are coloured in red with an intensity proportional to increased concentration of each component relative to Plasmax™, or in grey if they are absent.

Whilst the usual formulation of these two plasma-like media can improve the model system in which cultured cells can be studied, they are also limited in their ability to replicate human plasma. Cells cultured with physiological concentrations of nutrients can exhaust the most avidly consumed ones, and waste metabolites can build up over time. More frequent replacement of medium can mitigate these limitations. However, cell culture systems are inherently limited in their ability to inform about the effects of pharmacological intervention on the systemic metabolism. Thus, *in vivo* models can be used in conjunction with *in vitro* models to overcome these limitations.

#### 1.4.2 Mouse Models of Mutant BRAF Melanoma

Mouse models of melanoma consist primarily in two categories: Genetically engineered mouse models (GEMM) and xenograft models (Rebecca, Somasundaram and Herlyn, 2020). Early GEMM models of melanoma were designed on the knowledge of genes involved in melanocyte development, as well as genes found to be frequently mutated in melanoma such as *BRAF*, *CDKN2A*, *CDK4* and *NRAS* (Rebecca, Somasundaram and Herlyn, 2020). This led to the

development of a commonly used GEMM replicating BRAF mutation in melanoma, which carries the  $BRAF^{V600E}$  and  $PTEN^{lox/lox}$  alleles. This model relies on the activation of the Cre recombinase using 4-hydroxytamoxifen (4-OHT), which is applied topically to the skin (Meeth *et al.*, 2016). Upon its application, 4-OHT activates the Cre recombinase protein via a tamoxifen responsive element, which can be expressed under the control of a cell specific promoter - in the case of melanoma a tyrosinase (TYR) gene promoter. Upon its expression, Cre recombinase can excise the wild-type copy of  $BRAF$  as well as both copies of  $PTEN$ , leaving only a mutant  $BRAF$  copy to be expressed and preventing the expression of the tumour suppressor (Dankort *et al.*, 2009) (Figure 1.4.2-1).

The  $BRAF^{V600E} PTEN^{lox/lox}$  mouse model recapitulates the immune, metabolic and microenvironmental landscape of melanoma. However, there has been limited success in replicating BRAF inhibitor resistance in this model. When C57BL/6 mice bearing  $BRAF^{V600E} PTEN^{lox/lox}$  tumours were treated with a chow diet containing PLX4720, a reduction in growth rate could be seen, but no tumour regression was observed (Hooijkaas *et al.*, 2012). It is theorised that this is because PTEN loss prevents cell death by BRAF inhibitor treatment (Paraiso *et al.*, 2011). During the early development of  $BRAF^{V600E}$  murine models of melanoma it was found that induction of BRAF mutation alone resulted in induction of benign hyperplasia, which did not progress to melanoma (Dankort *et al.*, 2009).

To overcome this problem, an allograft model was created using cells generated from a  $BRAF^{V600E} PTEN^{-/-} Cdkn2^{-/-}$  GEMM to generate tumours. These cells were injected into immunocompetent C57BL/6 mice without immune rejection due to the inbred nature of the strain (Figure 1.4.3-1). Injection of these (YUMM1.7) cells could mimic

the clinical response of patients to a BRAF inhibitor. Upon treatment with PLX4720 one week after implantation of cells, tumour growth was inhibited for 50 days, after which the tumour grew rapidly (Meeth *et al.*, 2016). The allograft model thus enables exploration of BRAF inhibitor resistance that was generated in an *in vivo* setting.

Xenograft models of human melanoma cells exist as an alternative to GEMM models that allow the study of human cancer in an *in vivo* environment. This model is generated by the implantation of cells (established cell lines cultured on plastic or primary tumour explants) into immunocompromised mice (Figure 1.4.3-1). Engrafted cells are then able to develop physical and secretory interactions with murine stroma, including vascularisation. Two immunocompromised mouse models that are commonly used are the NSG and nude mouse models. The NSG mouse model (NOD/*Prkdc*<sup>scid</sup>/*IL2rg*<sup>tm1Wjl</sup>), so named for the use of an inbred NOD mouse strain, with mutation of the *Prkdc* gene (Protein Kinase, DNA-Activated, Catalytic Subunit) as well as of the *Il2ry* gene (interleukin 2 receptor subunit gamma), is the most immunocompromised strain of the two. The mutant *Prkdc*<sup>scid</sup> gene results in the phenotype of severe combined immunodeficiency (scid) because of a lack of development of T and B lymphocytes, meaning that the adaptive immune response is not functional (Blunt *et al.*, 1995). When combined with the disruption of the *Il2ry* gene, which prevents the activation of natural killer cells, the resulting NSG mouse lacks both the adaptive and innate immune response, thus preventing rejection of engrafted cells (Yang *et al.*, 2018). The nude mouse model on the other hand is less severely immunocompromised, with only mutation of the *Foxn1* gene, which prevents thymic development and therefore the adaptive immunity, whilst retaining their innate

immunity (Rossa and D'silva, 2019). Given the success of the immunotherapy drug, Ipilimumab, and the importance of T cell activation in melanoma progression (Wolchok *et al.*, 2013), the use of immunocompromised mouse models has significant limitation when studying melanoma response to treatment. However, xenograft models enable the study of tumour biology in a structural and metabolic environment that recapitulate a human tumour better than *in vitro* cell culture (Figure 1.4.2-1).

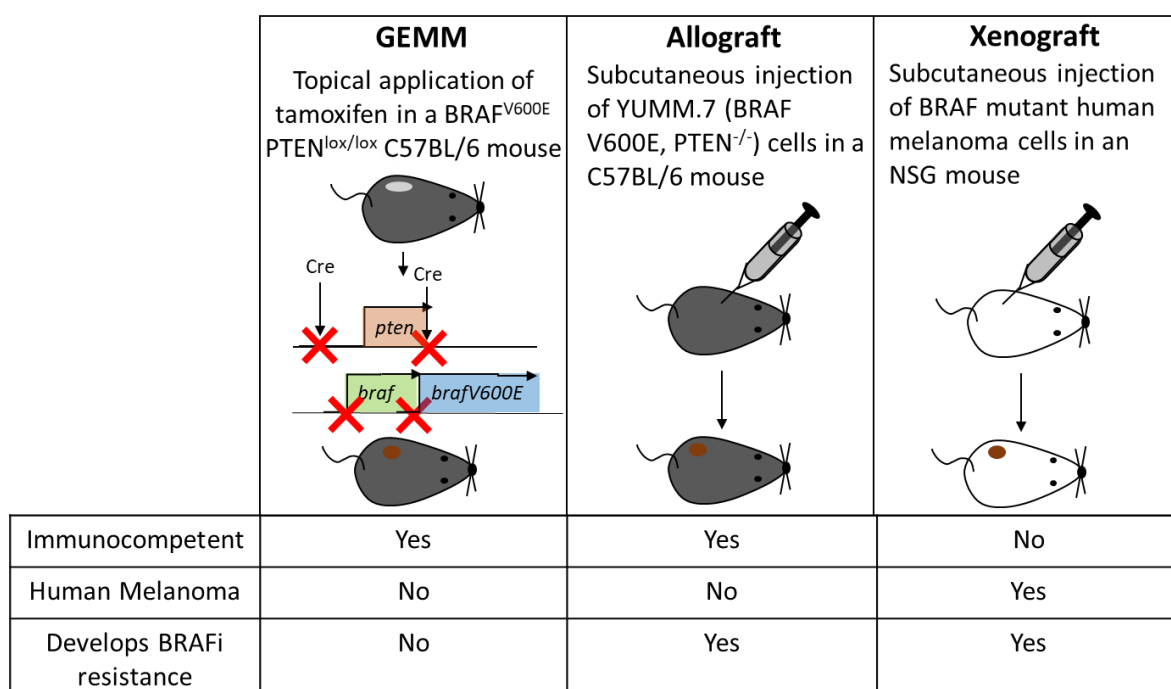


Figure 1.4.2-1: A schematic diagram depicting three different types of mouse models available to study BRAF mutant melanoma and their advantages and limitations.

### 1.4.3 Studying Cancer Metabolism with Metabolomics

A wealth of information has been published in the field of metabolomics in the last two decades, with numbers of papers in the

PubMed repository using the phrase “metabolomics” increasing from just 2 in the year 2000 to over 10,000 in 2021. Metabolomics is the study of all small molecules, often referred to as metabolites, within a biological system. These metabolites are the substrates, intermediates and end products of metabolic pathways mediated by enzymes. As a form of high throughput or ‘omics’ analysis, metabolomics can provide a readout of all detectable metabolites. Metabolism is more responsive to phenotypic changes than gene expression. This means that compared to other ‘omics’ technologies such as transcriptomics or proteomics, metabolomics gives more readouts that are indicative of a phenotypic change. In addition, metabolism is responsive to intrinsic factors as well as extrinsic factors such as the nutrient availability. Metabolomics can be performed using several techniques, although the most predominantly used are nuclear magnetic resonance (NMR) spectroscopy and mass spectroscopy (MS) which is often coupled with chromatography to become liquid chromatography-mass spectrometry (LC-MS) or gas chromatography-mass spectrometry (GC-MS) (Aderemi *et al.*, 2021).

For NMR spectroscopy, a strong magnetic field aligns protons in the atoms of a sample, which is opposed by a field of radio frequency waves giving rise to resonance. The change in energy when protons go back to their original position is detected and visualized as peaks, which are characteristic to the abundance and environment of the atomic nuclei (Jayesh, 2015). An advantage of NMR spectroscopy is the level of information it can provide about the structure of compounds for elucidation of their identity. Whilst NMR also requires little sample preparation for biofluids and is inherently quantitative

with high reproducibility, it is limited in the sensitivity and variety of metabolites it can analyse (Aderemi *et al.*, 2021).

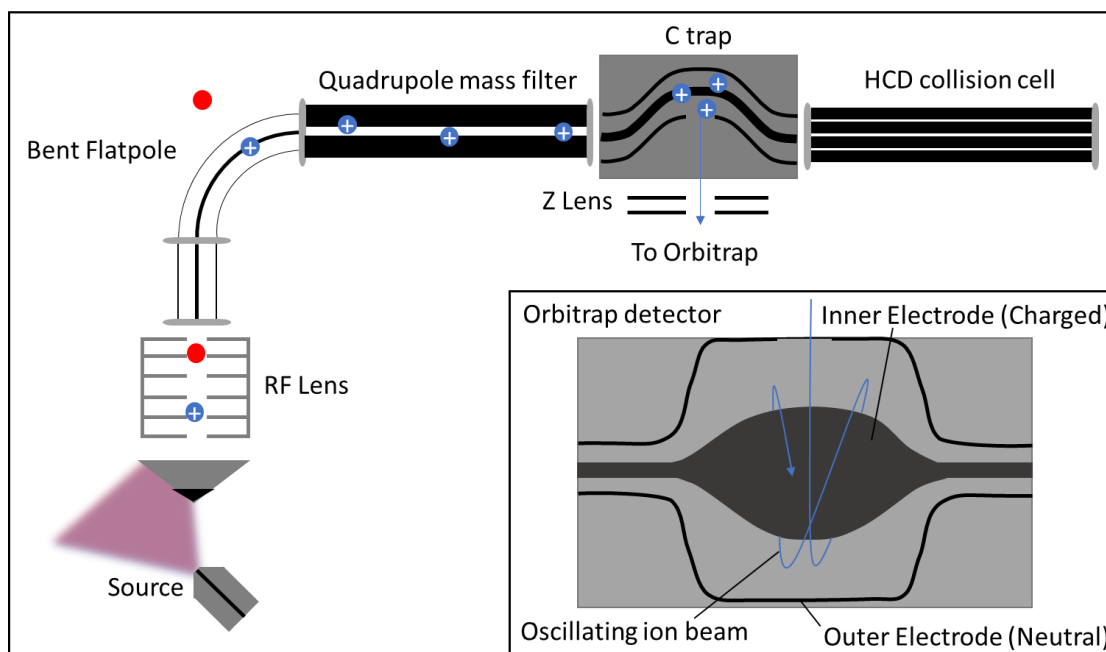


Figure 1.4.3-1: A diagram depicting a cross sectional diagram of the basic components of an orbitrap mass spectrometer (adapted from Thermo Fisher Scientific™ “Mass Analyzer Technology Overview” (‘Mass Spectrometry Learning Center - UK’, 2022)). Positive ions are represented by blue circles. Ions are ionised at the source, and those that reach the entrance of the machine are focused as an ion beam through the RF (radio frequency) lens. Neutral droplets (represented by red circles) are filtered out by a bent flat pole. A quadrupole mass filter can subsequently be used to filter out ions of a certain  $m/z$  (mass to charge ratio) range. Ions can be sent over to an HCD collision cell for fragmentation or can be passed directly to a C trap to cool ions and inject them into the orbitrap. On injection to the orbitrap detector, ions rapidly oscillate around the central spindle shaped electrode at a rate based on their mass to charge ratio ( $m/z$ ). The image current of ions is detected in the outer electrodes, to which a Fourier transformation is applied to produce a mass spectrum of all ions detected.

Mass spectrometry is typically hyphenated with liquid or gas chromatography. HILIC chromatography is frequently used for metabolomics due to its ability to separate polar metabolites. The SeQuant® ZIC-pHILIC® column is a frequently used example, which is packed with zwitterionic sulfobetaine groups attached to porous polymer beads. Analytes interact with sulfobetaine groups through weak electrostatic interactions when delivered in an organic solvent such as acetonitrile at the start of a gradient separation, resulting in their retention in the column. When an increasing proportion of an aqueous buffer such as 20mM ammonium carbonate is delivered to the column, polar molecules are eluted in order of their hydrophobicity (Figure 1.4.3-1). As samples in the column undergo partitioning, this results in their entry to the mass spectrometer at different time points, known as a retention time (RT). Throughout the separation, repeated measurements can be made at regular intervals by the mass spectrometer to detect chromatographic peaks (Mackay *et al.*, 2015).

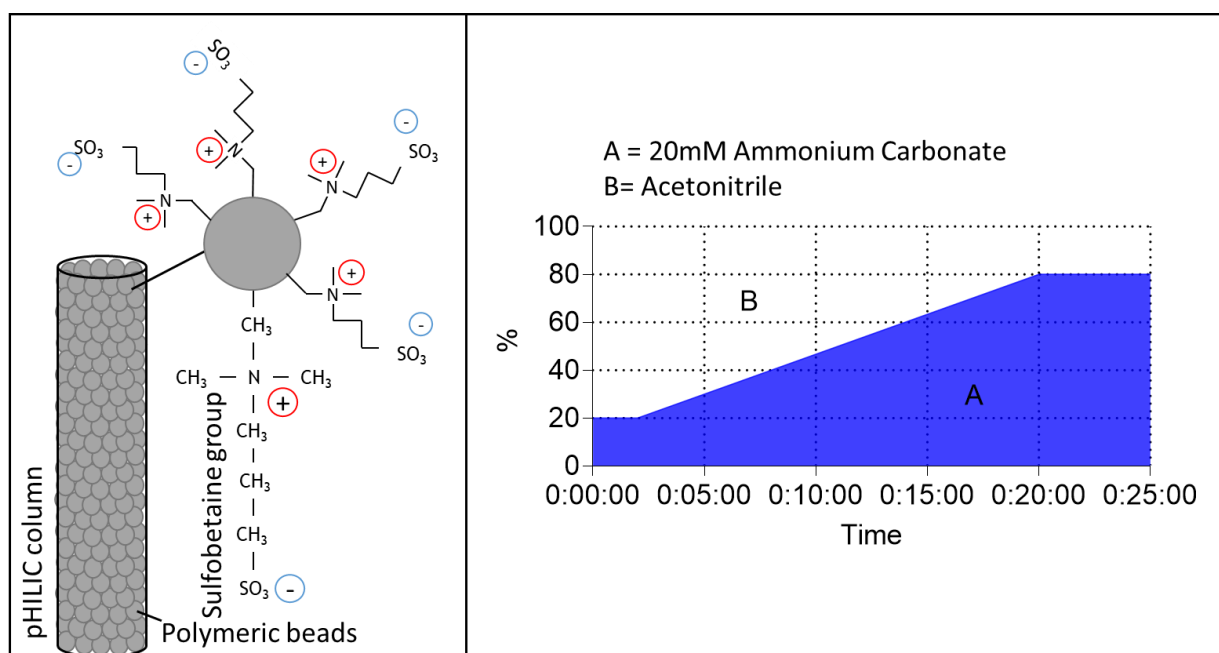


Figure 1.4.3-2: A diagram depicting the main concepts of pHILIC chromatography (adapted from SeQuant® ZIC-pHILIC® brochure by Merck Millipore (Merck, 2022)).

For this to occur, the chromatographic eluant must be converted from liquid to ions in the gas phase. This is achieved through a process known as electrospray ionization (ESI) which occurs in the source of the mass spectrometer by application of a high voltage to the liquid promoting the formation of ions in solution. As it is pumped through a capillary, the narrow tip causes the sample to be nebulised. The resulting spray of ions is directed at an orthogonal angle to the entrance of the mass spectrometer to avoid contamination (Pitt, 2009). The RF lens immediately behind the entrance of the Q Exactive Plus mass spectrometer focuses the beam of ions to increase sensitivity, and subsequently the bent flat pole reduces noise by removing neutral droplets from the beam (*Thermo Fisher Scientific - UK, 2022*). A quadrupole mass filter can then select ions within a chosen mass range for more accurate detection of low abundance ions. This can be used to improve the measurement of low abundance ions in an approach called selective ion monitoring (SIM), or to isolate ions for fragmentation in an MS2 experiment, which is often used to assist identification of ions. During an MS2 scan, ions are collided at high velocity with inert gas (which is often nitrogen) to induce fragmentation in the collision cell, prior to being detected in the orbitrap (Figure 1.4.3-1).

#### 1.4.4 Processing of LC-MS Data for Metabolomics

Raw LC-MS data represents the relative levels of all detectable polar metabolites but must be processed to determine the relative abundance of each metabolite. This can be done by integrating the area under a peak generated from successive measurements of the relative abundance of a single  $m/z$  centred around the retention time of that metabolite. The total area of the XIC (extracted ion chromatogram) within a sample relates to the relative abundance of that ion in that sample and is referred to as the peak area (Figure 1.4.4).

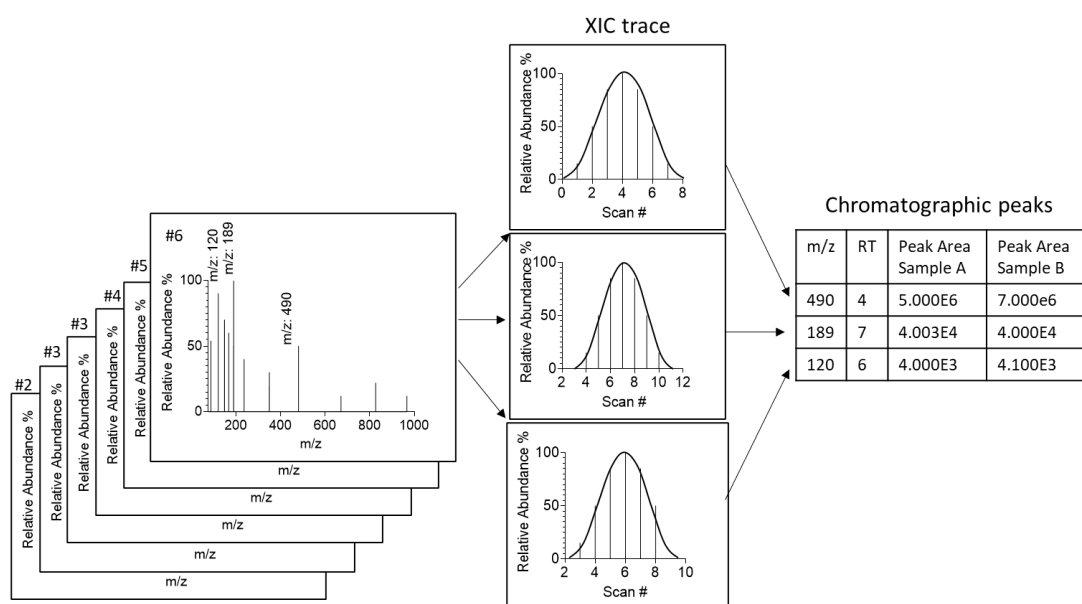


Figure 1.4.4-1: Diagram depicting the generation of an XIC trace from successive MS scans.

The analysis of LC-MS data can be broadly separated into two approaches: targeted and untargeted analysis. A targeted analysis is a supervised approach in which chemical standards for a chosen list of metabolites are used to determine the retention time and  $m/z$  for the most abundant adduct of each metabolite. The XIC for each of these metabolites can then be generated from this information in

any raw LC-MS dataset generated using the same LC-MS method. This guarantees correct metabolite identification.

A common targeted experiment is a metabolite tracing experiment, which can determine the metabolic pathways in which a labelled metabolite is used. This can be carried out by feeding nutrients incorporating the stable isotopes such as  $^{13}\text{C}$  or  $^{15}\text{N}$  to a biological system (Figure 1.4.4-2). The incorporation of these labelled atoms can be detected in the pool of downstream metabolites as an ion at the same retention time with an  $m/z$  ratio increased (by approximately 1 Da for each labelled atom) compared to the unlabelled metabolite (isotopologues) (MacKay *et al.*, 2015). By measuring the fractional enrichment of each isotopologue to the total pool of a given metabolite, the contribution of the tracer to a specific metabolic pathway can be inferred.

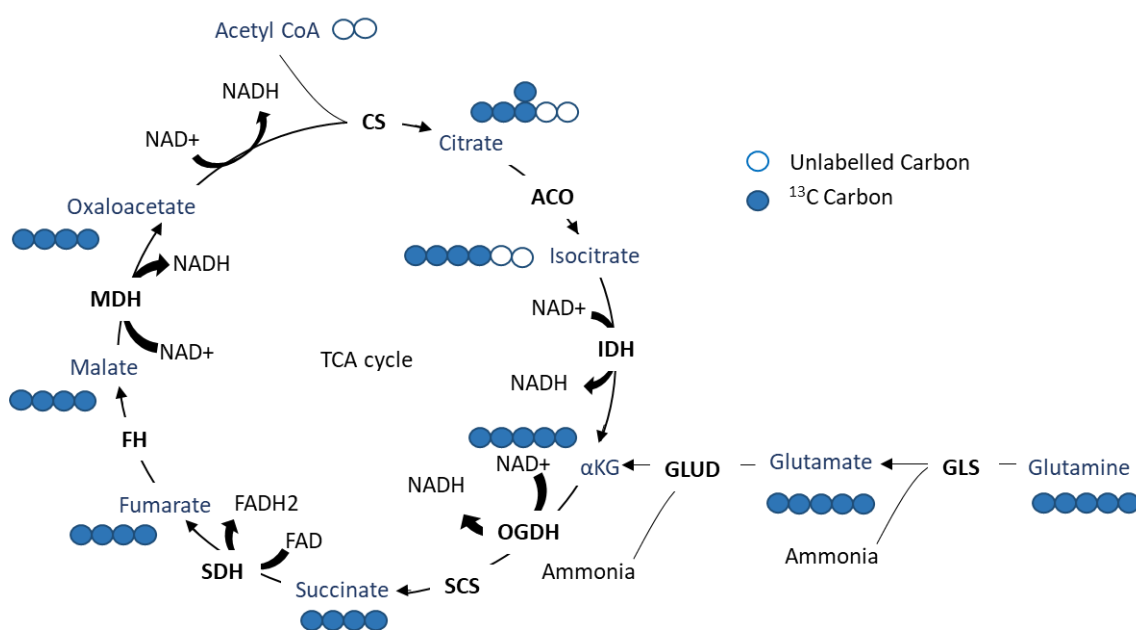


Figure 1.4.4-2: Schematic diagram representing the use of  $^{13}\text{C}$  labelled glutamine in glutamine anaplerosis and the TCA cycle.

Targeted analysis allows the measurement of levels of a pre-defined set of metabolites, and as such this approach limits the coverage of the metabolome and consequently the discovery potential of metabolomics. To overcome this, an untargeted approach uses specialised software to perform unsupervised integration of all detectable chromatographic peaks from the raw LC-MS data (Gertsman and Barshop, 2018). Whilst this allows measurement of a much broader set of metabolites, this analysis method is limited by the quality of peak integration as well as the identification of metabolic features.

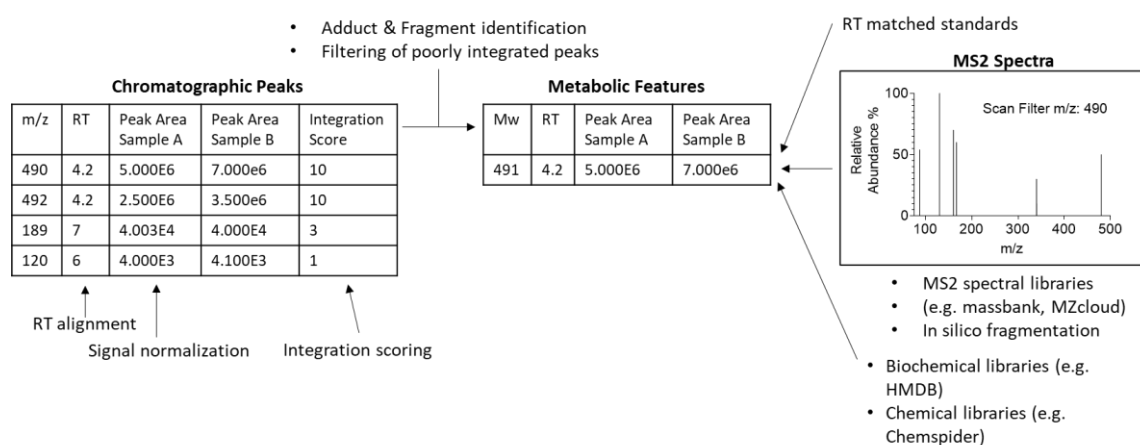


Figure 1.4.4-3: A diagram showing pre and post processing steps of an untargeted metabolomic analysis from a list of chromatographic peaks produced from raw LC-MS data. The central metabolic features table show the retention time (RT) molecular weight (Mw) of the metabolic features detected by the analysis.

To increase the quality of peak integration, pre and post processing steps can be used (Figure 1.4.4-3). Peak alignment is performed to reduce inaccurate peak selection when analytes have small deviations in elution time. In addition, signal normalisation can be carried out to reduce the time dependent shift in signal intensity

often observed with LC-MS instruments (Gertsman and Barshop, 2018; Karpievitch *et al.*, 2014). This can be done by using a pooled sample run at regular intervals throughout a batch of samples and applying linear integration to extrapolate the shift in signal intensity for all samples in the batch. More recently, peak integration software has also included the use of integration scoring, which allows filtering of poorly integrated peaks. Unsupervised integration can result in the selection of low abundance contaminants and artefacts as chromatographic peaks, so manual curation of integrated peaks is still a necessary final step in the analysis.

Identification of the detected ions is often the most challenging part of the analysis. Because metabolites ionise during ESI (Gao, Zhang and Karnes, 2005), they can give rise to a range of adducts with different masses. In addition, electrospray ionization can cause fragmentation of ions, resulting in ‘fragment ions’ (Jian Guo *et al.*, 2021). As a result, multiple chromatographic peaks may be created by a single parent ion which share a retention time and peak shape and correlate strongly in their abundance across all samples.

Therefore, identifying groups of peaks corresponding to the same metabolite can remove redundancies from the list of metabolic features. This can be done by grouping all peaks based on RT, peak shape similarity and abundance correlation across samples followed by annotation using known lists of frequently occurring adducts (Li *et al.*, 2013). More recent development of processing tools for metabolite identification have combined the annotation of peaks based on ‘abiotic connections’ such as adducts or fragments with annotation based on ‘biotic connections’ such as association with the same biochemical pathway. This form of optimisation during annotation was used in a new annotation tool known as NetID (Chen

*et al.*, 2021), which aimed to increase annotation coverage both from a chemical and a biochemical perspective.

Typically, the processed data consists of an  $m/z$  ratio, retention time and peak area for each metabolic feature (Figure 1.4.4-3). This leaves the challenge of peak identification. To improve metabolite identification, MS2 data can be collected along with LC-MS data from a pooled sample containing an equal mix of all samples. The highest abundance ions can be fragmented in a collision cell as described earlier (Figure 1.4.3-1), giving an indication of the structural arrangement of atoms. Metabolite identification is then performed using spectral libraries, matching accurate mass (MS1), or fragment ions (MS2) to compounds (Bingol and Brüscheweiler, 2015). These libraries can be produced by experimental data or by *in silico* techniques, which extrapolate from experimental data to generate spectra. In house retention time databases can also be used as an independent identifier, if available. Once a metabolic feature has been identified with a reasonable degree of confidence, a chemical standard can then be used to confirm its identity by ensuring that the metabolic feature matches the RT and MS2 fragmentation on the same instrument method.

Several libraries have been developed for the annotation of metabolic features, consisting of molecular structure databases and MS2 spectral databases. For example, the HMDB metabolite library is a structure database containing records of 217,920 metabolites as well as a record of the concentration in human tissues and biofluids if this is known (Wishart *et al.*, 2022). This library also includes experimentally observed MS2 spectra for some entries, and a predicted MS2 spectra for all its entries (although these are produced *in silico* which limits their reliability). On the other hand, several

MS2 spectral libraries have been created using MS2 data produced experimentally, which are more accurate for confirmation of molecular structures, although typically contain fewer entries. These include open-source databases such as MassBank, which are deposited from users into the repository (Horai *et al.*, 2010). Closed-source versions such as mzCloud (*Thermo Fisher Scientific*, 2022) are available, which can be advantageous due to their dedicated collection of data produced on a selected instrument type. This allows users to replicate experimental conditions for that database in their initial data capture, improving MS2 spectral matching for compounds in the database.

Statistical tests are often used to determine which features are significantly altered compared to a background or control samples. Many data analysis and statistical tools are available to determine which metabolic features are of most relevance to an experimental hypothesis. Principal component analysis (PCA) and partial least squares analysis (PLS-DA) collapse the number of dimensions of a given dataset (Sugimoto *et al.*, 2012). This can be useful to visualise data quality and biological changes.

Similarly, a differential analysis often using t-tests can be performed on each metabolic feature to identify features significantly changed between biological groups. This outputs a series of p values, that indicate statistical significance (which is a measure of the confidence in the null hypothesis that there is no significant difference between two groups of the differential analysis). For large datasets involving many comparisons, such as those produced by an untargeted metabolomics study, a false discovery rate should be applied to control the probability of introducing type 1 error (Benjamini and Hochberg, 1995) (rejecting the null hypothesis when it is true).

### 1.5.1 Study Aims

In this study, we first aimed to confirm whether the use of a glutaminase inhibitor can be used to reduce the growth BRAF inhibitor resistant melanoma. We aimed to do this using the clinically relevant glutaminase inhibitor, CB839, using both *in vitro* and *in vivo* models. Subsequently to this, we aimed to determine the metabolic effects of glutaminase inhibition in *in vitro* and *in vivo* models of BRAF inhibitor resistant melanoma. By determining metabolic changes accompanying growth changes caused by CB839, we aimed to reveal the metabolic causes of reduced growth in BRAF inhibitor resistant melanoma caused by glutaminase inhibition.

## Chapter 2: Methods

### 2.1 Cell culture and Treatment

Human Cell lines A375, A375R, COLO829 and COLO829R were kindly given by Franziska Baenke of the Cancer Research UK Manchester institute (Baenke *et al.*, 2016). Cells were cultured in MEM supplemented with 0.65mM L-glutamine (Gibco, 25030-032), 1X non-essential amino acids (Gibco, 11140-035), 10% FBS (Gibco, 10270-106) and 0.1mM sodium pyruvate (Sigma-Aldrich, 58636). Cells were incubated at 37°C with 5% CO<sub>2</sub>.

For all culture of A375R and COLO829R cells, media are dosed with 1µM PLX4720 unless otherwise specified. For 10µM PLX4720 treatment, media was dosed by adding 10mM PLX4720 (Selleckchem, S1152) dissolved in DMSO (Fisher Chemical, D/4125/PB08) at a dilution of 1:1000. For all lower doses, including for the dose response experiment, concentration was adjusted by carrying out serial dilutions in DMSO and dosing media with the appropriate concentration from a 1:1000 dilution.

### 2.2 *In vitro* Assays

#### 2.2.1 Experimental Media

For all cell culture experiments, cells were seeded MEM (Table 2.2.1-1) before having their media changed to Plasmax™ (formulated as specified previously (Voorde *et al.*, 2019)) or DMEM (Gibco, 21969-035) with 5mM glutamine, both supplemented with 10% dialyzed FBS.

FBS was dialyzed in house with snakeskin™ dialysis tubing, MWCO 3.5kDa (Thermo Scientific, 88244) for 24 hours in 0.9% NaCl.

|         | Volume of MEM | Volume of DMEM/ Plasmamax™ |
|---------|---------------|----------------------------|
| 6 well  | 2mL           | 8mL                        |
| 24 well | 0.5mL         | 2mL                        |
| 96 well | 0.1mL         | 0.2mL                      |

Table 2.2.1-1: Table showing the volumes of MEM media in which cells were seeded in for 24 hours.

## 2.2.2 Supplementation of Metabolites & Glutaminase Inhibition

Where doses of 1µM CB839 are indicated, media was dosed by adding 1mM CB839 (acquired by MTA with Calithera Biosciences) dissolved in DMSO at a dilution of 1:1000. For all lower doses of both drugs, concentration was adjusted by carrying out serial dilutions in DMSO and dosing media with the appropriate concentration from a 1:1000 dilution.

Supplementation of aspartic acid sodium salt monohydrate (Sigma-Aldrich, A6683), dimethyl- $\alpha$ -Ketoglutarate (Sigma-Aldrich, 349631), oxaloacetate (Sigma-Aldrich, O7753), dihydroorotate (Sigma-Aldrich, D7003), adenosine (Sigma-Aldrich, A4036), guanosine (Sigma-Aldrich, G6264), cytosine (Sigma-Aldrich, C3506), thymidine (Sigma-Aldrich, T1895), uridine (Sigma-Aldrich, U3003), inosine (Sigma-Aldrich, I4125), sodium lactate (Sigma-Aldrich, L7022), carbamoyl aspartate (Alfa Aesar, A17166), ornithine (Sigma-Aldrich, O2375), asparagine (Sigma-Aldrich, A0884), glutamate (Sigma-Aldrich, G1251), proline (Sigma-Aldrich, P0380), alanine (Sigma-Aldrich,

05129) and  $^{13}\text{C}$  glutamine (Cambridge Isotope Laboratories Inc, CLM-1822-H-PK) was done by weighing and dissolving in the appropriate concentration in the media specified. Where necessary, pH was adjusted with either concentrated HCl or NaOH, and media was then filtered using a 0.2 $\mu\text{M}$  sterile membrane filter (Pall).

Supplementation of 1mM Pyruvate was done using a solution of sodium pyruvate (Sigma-Aldrich, 58636).

### 2.2.1 Growth Response Experiment by Lowry Assay

For cell growth assays by Lowry assay, cells were seeded in 96 well plates, 4000 cells/well for all cell lines or in 24 well plates, 10,000 cells/well. Cells were allowed to grow for 72 hours, before having their media removed, washed with phosphate buffered saline (PBS) and the amount of protein quantified by Lowry protein (Lowry *et al.*, 1951) assay to quantify absolute amount of protein in each well.

### 2.2.2 Growth Assays by Cell Counting

To determine cell growth, cells were seeded in 24 well plates, 10,000 cells/well for A375 and A375R cells, and 15,000 cells/well for COLO829 and COLO829R cells. Cells were grown for 72 hours, before having their media removed, washed with PBS, and dissociated from the plate using 1X Trypsin (gibco, 15090-046). 0.4mL of the dissociated cells were suspended in 19.4mL of PBS and immediately counted using a CASY cell counter (Cambridge Bioscience).

### 2.2.3 SDS-PAGE Western Blot

Cells were seeded in a 6 well plate (250,000 cells/well for A375 and A375R cells, 300,000 cells/well for COLO829R cells and 400,000 cells/well for COLO829 cells). After 48 hours incubation media was removed, and cells were washed with ice cold PBS followed by lysis with 10X RIPA Lysis Buffer (Merk Millipore, 20-188) diluted 1:10 with distilled water and supplemented with a Pierce<sup>TM</sup> Protease and Phosphatase Inhibitor Mini Tablet (Thermo Scientific, A32961). Lysates were centrifuged at 16000g for 10 minutes at 4 °C and supernatant was removed for analysis. Samples were treated with Laemmli sample buffer (Bio-Rad, 1610747) supplemented with 2-mercaptoethanol, before being heated at 95 °C for 5 minutes and loaded on a 10% SDS-poly acrylamide gel (Bio-Rad, 456-1033) along with a protein ladder (Thermo Scientific, Page Ruler, 26620). After electrophoresis, proteins were blotted onto 0.2 µm nitrocellulose membranes (Amersham, 10600001), and stained with Ponceau red stain (Sigma-Aldrich, 141194). Light field images were taken of the membrane using a myECL imager (Thermo Scientific) before being rinsed with distilled water and blocked for an hour at room temperature in 5% non-fat dry milk in tris buffered saline and Tween (NFDN/TBST). It was then washed and incubated overnight at 4 °C with the following primary antibodies: anti glutaminase (kidney isoform) 1:5000 (abcam, ab60709). Membranes were washed and incubated for one hour at room temperature with near-infrared fluorescent secondary antibodies (1:5000; LI-COR, NE, USA). Proteins were detected with the LI-COR Odyssey CLx Imaging System. Proteins were quantified using the Gel Analyzer function on

ImageJ(Davarinejad, 2022; Schneider, Rasband and Eliceiri, 2012) which output a plot of the mean grey value across the width of an 8 bit, grayscale image of adjacent protein bands. Each band was represented by a peak, for which the area was calculated and used as a measure of relative band intensity. Relative band intensity for GLS protein levels were normalized to the relative band intensity of Ponceau stain between 120-25kDa.

#### 2.2.4 Glutamine and Glutamate Uptake/Secretion by Bioanalyser

25,000 cells were seeded in each well of a 24 well plate. Media was changed to Plasmax™ or DMEM after 24 hours and CB839 treatment was added, at which point blank wells were also filled with Plasmax™ or DMEM to be incubated alongside cells. After a 24 hour incubation, media was removed and centrifuged for 10 minutes at 16,000g. The amount of protein left by the remaining layer of cells was quantified by Lowry assay (Porter J *et al*, 2022) for normalization. The supernatant was then analyzed with a glutamate membrane kit (YSI 2754) on a YSI bioanalyzer, along with samples from blank wells to determine the concentration of metabolites in the media. All samples were then transferred to a 96 well plate for quantification by the bioanalyzer. Consumption or secretion rates were then calculated as  $\left(\frac{\Delta \text{ nmoles glutamate}}{\mu\text{g of protein in well}}\right)$  where  $\Delta$ nmoles of glutamate was calculated as  $\frac{[\text{GLU}]_{\text{spent media}} - [\text{GLU}]_{\text{blank media}}}{2000}$  for 0.5mL samples where where [GLU] was in nM.

### 2.2.5 Extraction of Intracellular Metabolites

Cells were seeded in 6 well plates (250,000 cells/well for A375 and A375R cells, 300,000 cells/well for COLO829R cells and 400,000 cells/well for COLO829 cells). After 24 hours, cells were washed with PBS and media was replaced with Plasmax™ or DMEM with the indicated treatment. Treatment with CB839 or otherwise specified nutrient supplements were then added to media. Cells were then incubated in for 24 hours. For  $^{13}\text{C}_5$  glutamine tracing, Plasmax™ containing 0.65mM  $^{13}\text{C}_5$  glutamine was used, and cells were incubated for 48 hours.

For metabolite extraction, cells were rinsed with ice cold PBS. Intracellular metabolites were extracted using a solution of acetonitrile, methanol, and water in the ratio 3:5:2 respectively (extraction solution). 400 $\mu\text{l}$  for the extraction solution was added to wells, and plates were agitated for 10 minutes at 4°C. The solution was transferred to Eppendorf tubes and centrifuged at 16,000g for 10 minutes. The supernatant was stored at -70°C until its use for LC-MS analysis.

The extracted cell monolayers were air dried, and the amount of cellular protein was quantified by Lowry assay (Porter *J et al*, 2022) for normalization so that the protein content was measured directly from the well from which the metabolites were extracted.

Normalization was performed by the equation:  $\frac{\text{peak area}}{\text{ug protein for individual sample}}$ .

## 2.3 *In vivo* Models of Melanoma

### 2.3.1 Transplantation of Cells

For xenograft tumor models of A375 or COLO829 derived tumors in NSG mice, cells were cultured in MEM as described above in a dish 20cm in diameter with 30mL of media for 2 days, until cells were grown to ~100% confluence. Cells were then detached with trypsin, centrifuged at 180 rcf for 5 minutes and resuspended in PBS at a concentration of 10 million cells/mL. 1 million cells were injected subcutaneously into the right flank of NSG mice.

For allograft models of YUMM1.7 cells in C57BL/6 mice, cells were obtained from ATCC (CRL-3362) and thawed in DMEM: F12 (Gibco, 21331-020) media with 0.65mM Glutamine and 10% FBS. After one passage, cells were cultured in MEM as describe above for all passages. For transplantation, cells were passaged and suspended in PBS as described above for A375 and COLO829 cells and 250,000 cells were injected into the right flank of C57BL/6 mice unless otherwise stated.

Subsequently to transplantation of cells, all mice were weighed and had their tumors measured three times each week. The endpoint for tumor growth was pre-defined as a maximal dimension of 15mm. All *in vivo* experiments were carried out in a dedicated barriered facility under the Animal (Scientific Procedures) Act 1989.

### 2.3.2 Analysis of Tumour volume

Tumour volume was calculated using the following formula:  $L \times W^2$

Where L=tumour length (longest dimension) and W=tumour width (longest dimension at a perpendicular angle to tumour width).

Relative tumour volume is calculated based on the tumour volume, using the following formula:  $\frac{V_{Dn}}{V_{D0}}$  Where  $V_{Dn}$  is the tumour volume on day n and  $V_{D0}$  is the tumour volume on day 0.

### 2.3.3 Treatment regimes

For treatment of NSG and C57BL/6 mice, CB-839 was given twice daily dose of 200mg/kg (10uL/g) via oral gavage, in a vehicle of 25% (w/v) hydroxypropyl- $\beta$ -cyclodextrin in 10 mmol/L citrate (pH 2).

For NSG mice, PLX4032 (Adooq Bioscience) was given once daily via an intraperitoneal injection of 10mg/kg (4uL/g) in a vehicle of 4% DMSO, 4% TWEEN80 and 92% PBS. For C57BL/6 mice, PLX4032 was given once daily via an intraperitoneal injection of 20mg/kg (8uL/g) in a vehicle of 4% DMSO, 4% TWEEN 80 and 92% PBS.

### 2.3.4 Dissection

Once mice approached endpoint, they were humanely culled by CO<sub>2</sub> asphyxiation. Blood was sampled postmortem by cardiac puncture and serum was obtained by leaving the blood samples to coagulate at room temperature for 5 minutes and then centrifuged at 2800 rcf for

5 minutes. The supernatant (serum) was collected and stored at -70°C. Tumours were immediately removed and cut in half lengthwise. One half was preserved in buffered formalin for 24 hours, and then transferred to 70% ethanol to be used for immunohistochemistry (IHC). The remaining half was dissected into ~1mm<sup>3</sup> fragments, from which 3 were frozen at -70°C to be used for metabolomic analysis, 3 were preserved in RNA later and frozen at -70°C after 30 minutes.

### 2.3.5 Preparation of Tissue Samples for Metabolomic Analysis

Tumour fragments were weighed and put in homogenization tubes containing large ceramic beads (Bertin Corp, P000911-LYSKO-A), with extraction solution at 20µg tissue /mL. Samples were then homogenized using a Precellys evolution homogenizer (Bertin instruments) and centrifuged at 16,100g for 10 minutes. The supernatant was then removed and stored at -70°C until being used for LC-MS analysis.

### 2.3.5 Preparation of Serum for Metabolomic Analysis

20uL of serum was diluted into 980uL of extraction solution, before being agitated at 4°C for 10 minutes. Samples were then centrifuged at 16,100g for 10 minutes. The supernatant was then removed and stored at -70°C until being used for LC-MS analysis.

### 2.3.6 Quantification of Serum Ammonia

Serum was thawed immediately prior to ammonia quantification and diluted 1:4 with distilled water. 20 $\mu$ L of the diluted serum was pipetted onto a reagent strip and a blood ammonia meter (PocketChem BA PA-4140, Arkray) was used to measure the level of ammonia in the sample. The concentration was multiplied by four to calculate the original concentration.

### 2.3.6 Immunohistochemistry

All Immunohistochemistry (IHC) staining were performed by the CRUK Beatson Institute histology facility. 4 $\mu$ m formalin fixed paraffin embedded sections (FFPE) were used, which had previously been heated at 60°C for 2 hours.

FFPE sections for ASS1 (70720, Cell Signaling) were stained on a Leica Bond Rx autostainer undergoing on-board dewaxing (AR9222, Leica) and antigen retrieval using ER2 solution (AR9640, Leica) for 20 minutes at 95°C. Sections were rinsed with Leica wash buffer (AR9590, Leica) before peroxidase block was performed using an Intense R kit (DS9263, Leica). FFPE sections were rinsed with wash buffer and ASS1 applied at 1/1500 optimised dilution for 30 minutes. The sections were rinsed with wash buffer and rabbit envision secondary antibody applied for 30 minutes. The sections were rinsed with wash buffer, visualised using DAB and then counterstained with Haematoxylin in the Intense R kit.

To complete the IHC staining, sections were rinsed in tap water, dehydrated through graded ethanols, and placed in xylene. The

stained sections were cover slipped in xylene using DPX mountant (CellPath, UK).

Slides were then scanned on the Aperio AT2 at 20X magnification. Areas of necrosis were identified by from the H&E stained slides, using a Random Forest Algorithm on HALO v3.4. software. H&E stained sections were taken immediately adjacent to sections that were stained with pAMPK, such that the corresponding regions of necrosis seen with H&E staining could be superimposed onto the images of pAMPK staining. pAMPK stained images were then analysed using the Indica Labs - area quantification v2.2.4 algorithm settings, excluding regions of necrosis. The % area of positive staining was then calculated using the following equation:

$$\% \text{ positive area} = \left( \frac{a_{\text{positive}}}{a_{\text{negative}}} \right) \times 100$$

Where  $a_{\text{positive}}$  is the total area of positive staining and  $a_{\text{negative}}$  is the area of negative staining.

### 2.3.7 RNAseq Preparation

Tumour samples were thawed immediately before RNA extraction. Fragments were weighed and a mass of 200-300mg tissue was used per sample. RNA extraction was performed using an RNeasy mini kit (Qiagen, 74106) with a RNase-Free DNase Set (Qiagen, 79254) and QIAshredder columns (Qiagen, 79656).

RNAseq was performed by the CRUK Beatson Institute Molecular Technology Facility. Quality control of all RNA samples was performed using High Sensitivity RNA screen tape (Agilent, 5067-

5579) on an Agilent Tapestation 2200. All samples had an RNA integrity number (RIN) value >8 and so were processed. RNA concentrations were determined by Qubit Fluorometer using the Qubit RNA Broad Range assay (both Thermo Fisher). 1ug of total RNA was used as input.

Libraries were prepared using Illumina Stranded mRNA(Illumina, 2021) with IDT for Illumina RNA UD Indexes (Illumina, 20027213) used to index libraries. Post library QC was then performed using High Sensitivity D1000 screentape (Agilent, 5067-5584) for library sizing and profiling and quantified using Qubit High Sensitivity DNA assay. Libraries were then pooled equimolar, to a final concentration of 4nM prior to sequencing. The library pool was then sequenced on an Illumina NextSeq 500 instrument, on a High-Output 75 cycle run with paired-end 34bp read length.

### 2.3.8 RNAseq Analysis

Quality checks and trimming on the raw fastq RNA-Seq data files were done using FastQC version 0.11.9 (*Babraham Bioinformatics - FastQC A Quality Control tool for High Throughput Sequence Data*, 2022), FastP version 0.20.1 (Shifu Chen *et al.*, 2021) and FastQ Screen version 0.14 (Wingett SW and Andrews S, 2018). RNA-Seq paired-end reads were aligned to the GRCm38.104 version of the mouse genome and annotation (Newman *et al.*, 2018), using HiSat2 version 2.2.1 (Kim D *et al.*, 2019) and sorted using Samtools version 1.7 (Li H *et al.*, 2009). Aligned genes were identified using Feature Counts from the SubRead package version 2.0.1 (Liao, Smyth and Shi, 2014).

Expression levels were determined and statistically analysed using the R environment version 4.2 (*R: a language and environment for statistical computing*, 2022) and utilizing packages from the Bioconductor data analysis suite (Huber *et al.*, 2015). Differential gene expression was analysed based on the negative binomial distribution using the DESeq2 package version 1.36 (Love, Huber and Anders, 2014) and adaptive shrinkage using Apeglm (Zhu, Ibrahim and Love, 2019). A PCA of normalised gene expression data performed using ggplot2 and tidyverse (Wickham *et al.*, 2019).

Enrichment analysis was performed using MetaCore from Clarivate Analytics (<https://portal.genego.com/>).

Computational analysis was documented at each stage using MultiQC (Ewels *et al.*, 2016), Jupyter Notebooks (Kluyver *et al.*, 2016) and R Notebooks (Allaire, 2022).

## 2.4 Metabolomic Analysis

### 2.4.1 pHILIC Chromatography

Liquid chromatography-mass spectrometry was performed using a Thermo Fisher Scientific Ultimate 3000 high-performance liquid chromatography HPLC system or otherwise a Thermo Fisher Scientific Vanquish MD HPLC system. A SeQuant® ZIC-pHILIC column of 150 mm by 2.1 mm (Merck Millipore, 150460) with beads of 5 µm diameter was used, with a SeQuant® ZIC-pHILIC guard column of 20 mm by 2.1 mm (Merck Millipore, 150437). 5µL of the metabolite extraction was injected and separated using 24.5 minute run including a 16 minute linear gradient with an aqueous mobile phase of (A) 20mM

ammonium carbonate with 0.1% ammonium hydroxide (pH 9.2) and (B) acetonitrile. The gradient switched from 80% (B) and 20% (A) to 20% (B) and 80% (A) As depicted in (Figure 1.4.3-1). The flow rate was kept at 200 $\mu$ L/min and temperature kept at 45 $^{\circ}$ C.

## 2.4.2 QE and QE+ Acquisition

For targeted and untargeted analysis, samples were analyzed with Q Exactive Plus or Q Exactive orbitrap mass spectrometer (Thermo Fisher Scientific). Scans were performed with a resolution of 75,000 at 200 mass/charge ratio (m/z), a mass range of 75 to 1,000 m/z, and automatic gain control (AGC) target of 1E6 but a maximum scan time of 250ms. Electrospray ionization and was used with polarity switching for the detection of ions in both positive and negative mode. This was done by switching the voltage of the electrospray from positive to negative between each scan to obtain alternately positive and negative scans throughout the run.

Where a SIM was used, the method was created with scan filters at specific time points throughout the run (Table 2.4.2). Scans were performed with an AGC target of 2E5 and the maximum scan time of 240ms. Electrospray ionization was used. Data were acquired with Thermo Xcalibur 4.1 software.

| Scan Filter Mass (m/z) | Polarity | Start (min) | End (min) | Metabolite |
|------------------------|----------|-------------|-----------|------------|
|                        |          |             |           |            |

|           |          |      |       |            |
|-----------|----------|------|-------|------------|
| 367.01840 | Negative | 7.00 | 15.00 | OMP        |
| 323.02810 | Negative | 7.00 | 10.50 | UMP        |
| 157.02500 | Negative | 2.00 | 7.00  | DH orotate |
| 155.00930 | Negative | 2.00 | 7.00  | Orotate    |

Table 2.4.2: Scan filters and their timing windows used in a SIM to detect intermediates of nucleotide synthesis.

Where an untargeted analysis was performed, a pooled sample was used to generate MS2 spectra of the most abundant ions in each scan using a data dependent acquisition (DDA) method. Full scans were performed with a resolution of 35,000 at 200 mass/charge ratio (m/z), a mass range of 75 to 1,000 m/z, automatic gain control (AGC) target of 1E6 and a maximum scan time of 100ms. DDA MS2 was performed with a loop count of 10, resolution of 17,500 at 200 mass/charge ratio (m/z), a mass range of 75 to 1,000 m/z, automatic gain control (AGC) target of 1E5 and a maximum scan time of 100ms. Electrospray ionization was used, and separate runs were used for negative and positive. Data were acquired with Thermo Xcalibur software.

### 2.4.3 Targeted Analysis

Thermo Tracefinder 4.1 was used for targeted analysis. Metabolites were identified by the exact mass of their singly charged ion (5 ppm window) and by their retention time, which was predetermined using a library of chemical standards. For glutamine tracing experiments, the <sup>13</sup>C labelling patterns were determined by measuring peak areas for the accurate mass of each isotopologue of metabolites.

Intracellular metabolites were normalized to amount of protein, which was obtained by Lowry assay.

For volcano plots, the  $\log_2$  fold change between the peak areas of all metabolites in two groups was calculated for each metabolite. The  $-\log_{10}$  p value was calculated using a p value generated from a two tailed, unpaired, two-sample equal variance t test on independent experiments (e.g.  $n_{\text{tumours}}$  or  $n_{\text{expts}}$ ).

#### 2.4.5 Untargeted Analysis

Thermo Compound discoverer 3.3 was used for untargeted analysis. Retention times (RT) were aligned for all files (max shift 2 mins, mass tolerance 5 ppm). Compound detection and grouping were carried out across samples, with a minimum peak intensity of  $5 \times 10^5$  for detection and RT tolerance of 0.7 minutes for grouping and a mass tolerance of 5PPM for both, considering  $[M+Cl]-1$ ,  $[M+H]+1$ ,  $[M+H-H_2O]+1$ ,  $[M+K]+1$ ,  $[M+Na]+1$ ,  $[M+NH_4]+1$ ,  $[M-H]-1$ ,  $[M-H+H_2O]-1$  ions. The fill gaps feature was used to identify low abundance ions with a mass tolerance of 5ppm and signal/noise threshold of 1.5.

Background compounds were filtered out from the analysis.

Perseus 1.6.2.2 (Tyanova *et al*, 2016)

(<http://www.coxdocs.org/doku.php?id=perseus:start>) was used perform a  $\log_2$  transformation of the data and subsequently to calculate the p values from comparisons in the levels of metabolic features between tumors obtained from different treatment groups. Adjusted p values are calculated in Perseus

using a permutation-based FDR (false discovery rate) with a threshold of 0.05 with 250 permutations. This FDR is calculated by performing the specified number of permutations on the data and using the cutoff value to calculate the empirical distribution of values under the null hypothesis. P values are then adjusted to the new FDR.

## Chapter 3: Results

### 3.1 BRAF Inhibition Results in Greater Growth Inhibition, and Depletion of Glutamate and Aspartate in Response to Glutaminase Inhibition.

#### 3.1.1 Greater Growth Inhibition in Response to Glutaminase Inhibition Occurs Under BRAF Inhibition

In this study, two BRAF mutant melanoma cell lines - A375 and COLO829 were used, as well as a BRAF inhibitor resistant subclone of each of these - A375R and COLO829R. These cells were generated and kindly donated by Prof. Marais' group at the CRUK Manchester Institute (see chapter 2.1). These cells had previously been cultured and selected for BRAF inhibitor resistance in the commercial medium DMEM. A dose: response experiment was carried out by determining the growth of each cell line in response to different concentrations of the BRAF inhibitor, PLX4720.

The  $IC_{50}$  for each of the cell lines was  $0.093\mu\text{M}$  and  $0.114\mu\text{M}$  for the A375 and COLO829 cells respectively and  $0.197\mu\text{M}$  and  $3.255\mu\text{M}$  for A375R and COLO829R cells respectively (Figure 3.1.1-1). This experiment therefore demonstrated that in Plasmax, the BRAF inhibitor resistant subclones (A375R and COLO829R) have an increased  $IC_{50}$  and are indeed more resistant to PLX4720 compared to the parental cells (A375 and COLO829).

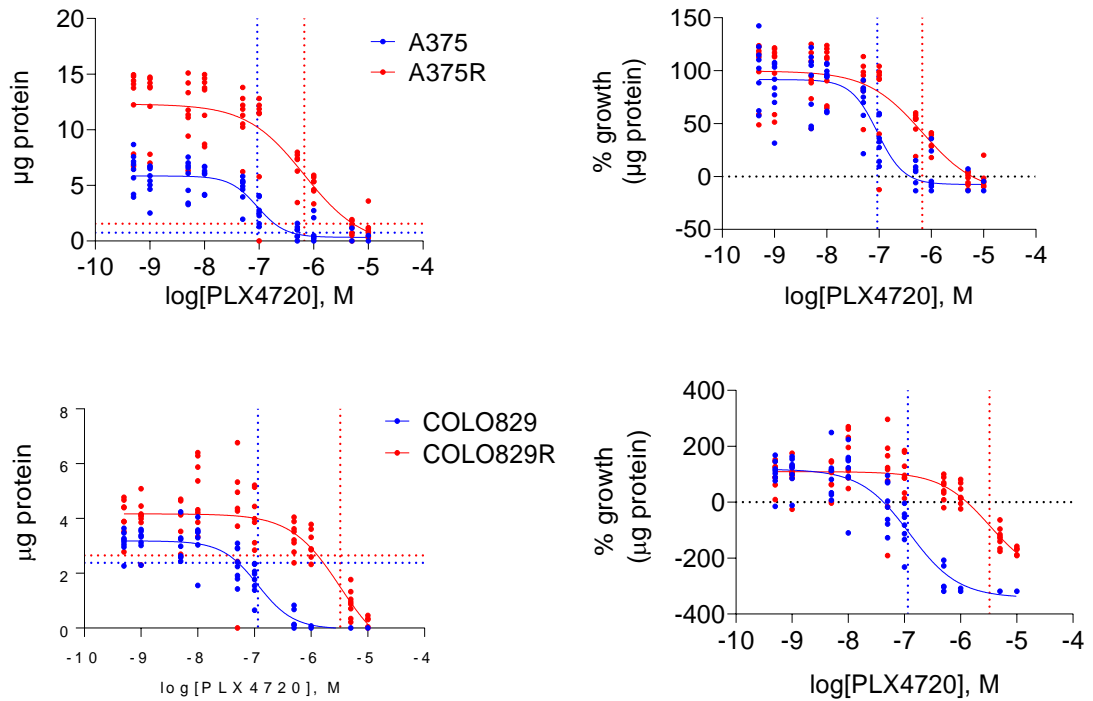


Figure 3.1.1-1: dose-response of melanoma cell lines A375 (above) and COLO829 (below), as well as their BRAF inhibitor resistant sub-clones A375R and COLO829R to the BRAF inhibitor PLX4720. Cell growth is quantified as the amount of protein per well at the end of a 72-hour experiment (left). The amount of protein is represented as the % growth which was calculated relative to the amount of protein at  $t_0$  (0%) and the amount of protein in untreated controls (100%) (right). Horizontal dotted lines represent the  $t_0$  amount of protein - the amount of protein in a plate seeded simultaneously, recorded at the time at which PLX4720 was added to the experimental plate. Individual dots represent each technical replicate ( $n_{\text{wells}}=8$ ,  $n_{\text{exp}}=1$ ). Solid lines represent the dose: response curve used to calculate the  $IC_{50}$  using GraphPad Prism 9.3.0 (sigmoidal, log dose vs response). Vertical dotted lines represent the  $\text{Log } IC_{50}$ , which are colour coded according to the cell line they correspond to.

It was previously reported that the level of glutaminase is increased in BRAF inhibitor resistant subclones (Baenke *et al.*, 2016). To test if this phenotype was maintained in more physiological conditions, cells were cultured in Plasmax™ for 48 hours and an SDS-PAGE/Western blot was carried out to determine the levels of glutaminase. This

demonstrated that the BRAF inhibitor resistant subclones had increased expression of glutaminase both in DMEM, where glutamine is exceeds the physiological levels (4mM) as well as in Plasmax™ where glutamine is present at the levels found in human plasma (0.65mM) (Figure 3.1.1-2).

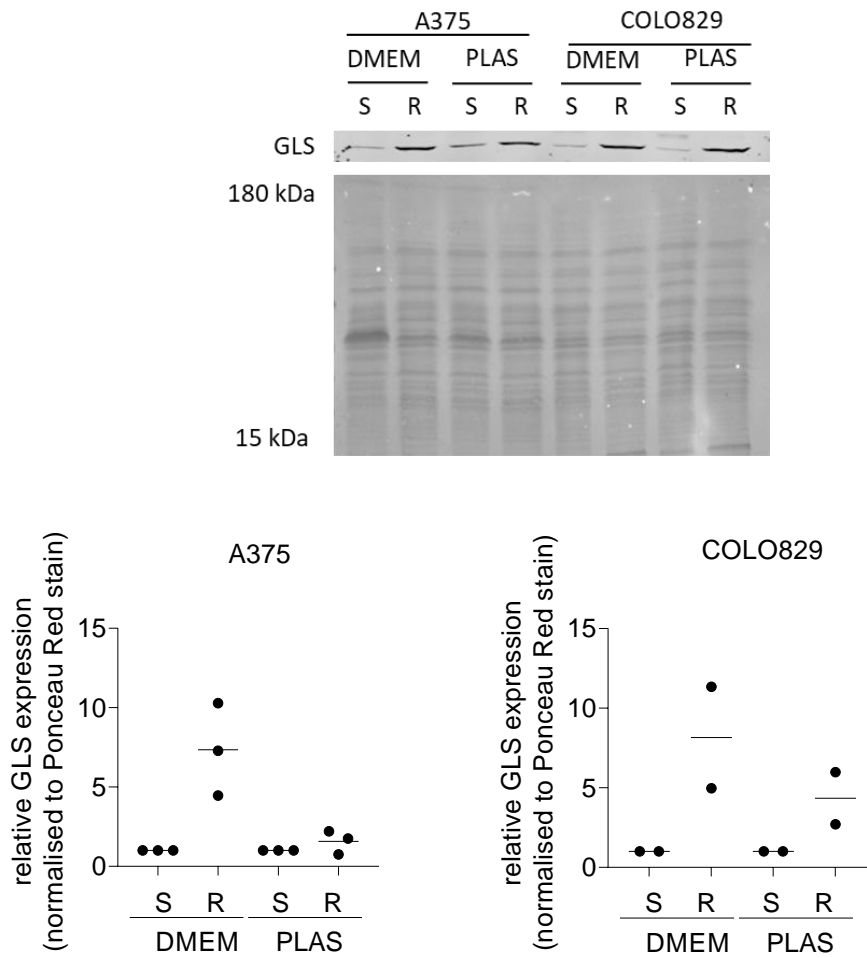


Figure 3.1.1-2: A representative western blot of glutaminase in BRAF inhibitor resistant (R) and sensitive (S) melanoma cell lines A375 (S), A375R (R), COLO829 (S) and COLO829R (R) (above). Cells were incubated in Plasmix™ (PLAS) or DMEM as indicated for 48 hours prior to protein extraction with RIPA buffer. The intensity of each band was measured and normalised to total ponceau red stain, which was detected on the same membrane. Relative levels of glutaminase were then calculated for each independent experiment (graphs below) (A375  $n_{exp}=3$ , COLO829  $n_{exp}=2$ ). Lines above each graph indicate comparisons made by an unpaired t test performed on the independent experiments. Each dot on the graph represents one experimental replicate, so that all points in the same colour are from the same experimental replicate across both graphs.

Next, the response of the four cell lines to the glutaminase inhibitor, CB839 was assessed. CB839 is a second-generation glutaminase inhibitor, with an  $IC_{50}$  of less than 100nM against recombinant human glutaminase (Gross *et al.*, 2014). We tested whether the nutrient availability offered by the media might affect responsiveness to glutaminase inhibition by incubating the cells with CB839 in DMEM and Plasmix™.

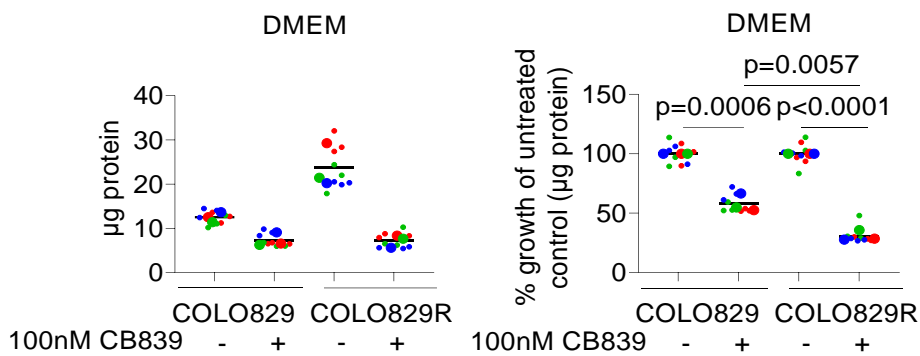
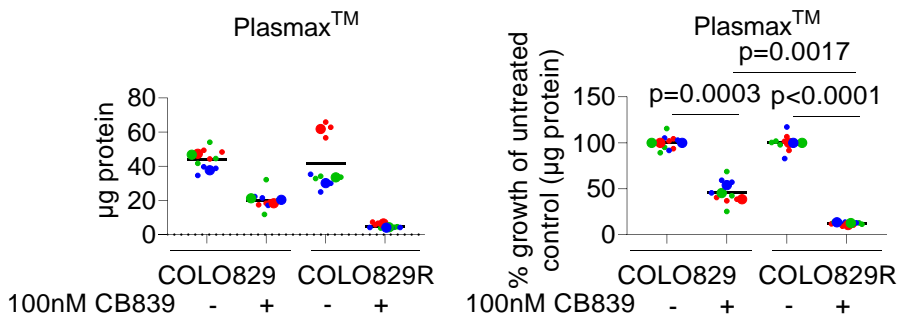
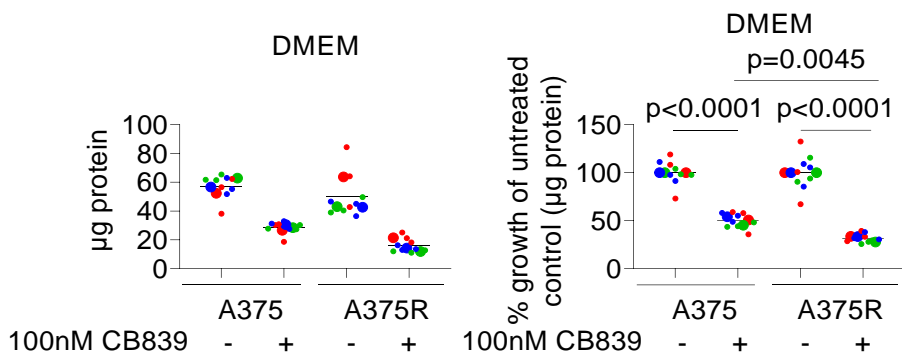
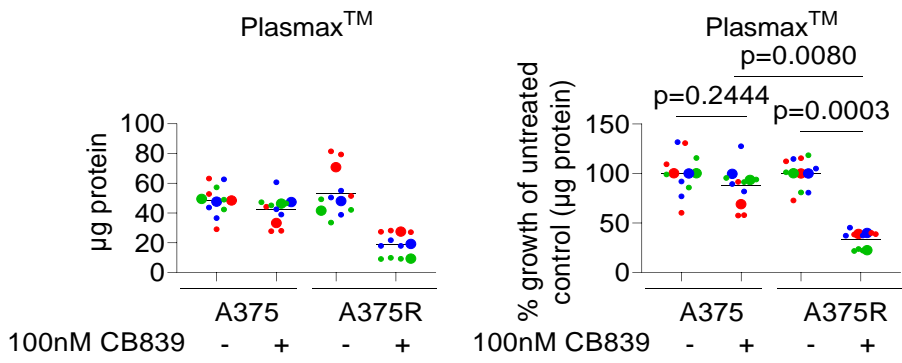


Figure 3.1.1-3: Graphs showing the growth response of A375, A375R, COLO829 and COLO829R cells to 100nM CB839 treatment relative to untreated cells. Cells were incubated in the indicated media, with the indicated dose of CB839 for 72 hours, after which the amount of protein was quantified by Lowry assay (left). The protein amounts are represented as the % growth which calculated relative to the amount of protein at  $t_0$  (0%) and the amount of protein in untreated controls (100%) (right). Each large point represents one independent experiment, which is the average of three wells, which are shown as a smaller point in the same colour ( $n_{\text{expt}}=3$ ,  $n_{\text{wells}}=3$ ). Lines above each graph indicate comparisons made by an unpaired t test performed on three independent experiments.

In Plasmax™, CB839 caused a significant decrease in the growth of A375R, COLO829 and COLO829R cells. Growth of A375 and COLO829 cells was decreased to 87% and 46% of untreated, respectively, whereas in A375R and COLO829R cells growth was decreased to 33% and 12% of untreated, respectively. This revealed that the BRAF inhibitor resistant subclones have increased sensitivity to glutaminase inhibition by CB839 in Plasmax™ compared to their parental counterparts (Figure 3.1.1-3). In addition, the growth of A375 cells was further reduced by CB839 in DMEM compared to Plasmax™ (from 87% to 50, respectively) (Figure 3.1.1-3). This suggested that for A375 cells, the difference in the two media exacerbated the difference in growth inhibition between parental and BRAF inhibitor resistant cells.

BRAF inhibitor resistant subclones therefore have increased sensitivity to glutaminase inhibition by CB839 in Plasmax™, however the experiment in which this was demonstrated involved cells that were still in the presence of BRAF inhibition. Therefore we sought to determine whether the presence of the BRAF inhibitor itself affects the responsiveness of BRAF inhibitor resistant cells to glutaminase

inhibition. Both BRAF inhibitor resistant subclones were treated with CB839 in the absence of PLX4720.

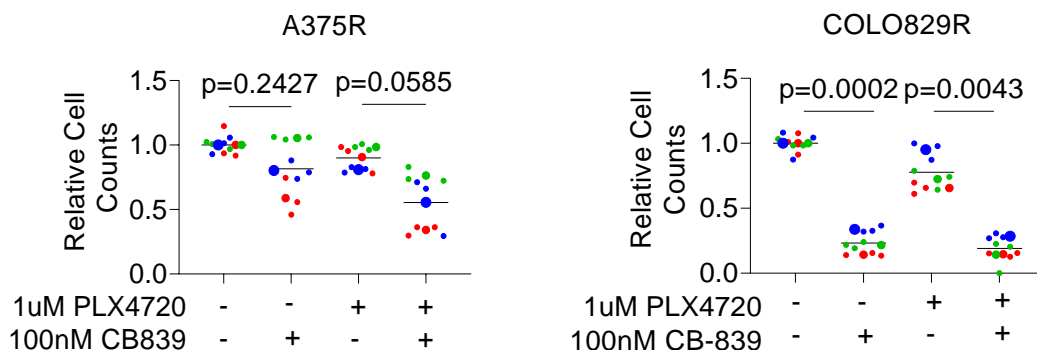


Figure 3.1.1-4: Graphs showing the growth response of A375R and COLO829R cells to 100nM CB839 and 1 $\mu$ M PLX4720 treatment as indicated, relative to untreated cells. Cells were incubated in Plasmax<sup>TM</sup>, with the indicated doses of PLX4032 and CB839 for 72 hours, after which cells were counted. Relative cell counts were calculated as a proportion of cell numbers in the untreated control. Each large point represents one biological replicate which is the average of 3 technical replicates shown as a smaller point in the same colour ( $n_{\text{expt}}=3$ ,  $n_{\text{wells}}=3$ ). Lines above each graph indicate comparisons made by an unpaired t test performed on three independent experiments.

These experiments demonstrated that glutaminase inhibition caused significant growth inhibition of COLO829R cells both with and without BRAF inhibition (Figure 3.1.1-4). However, CB839 inhibited the growth of A375R to a greater extent in the absence of BRAF inhibition than in the presence, showing that PLX4720 may sensitize A375R cells to glutaminase inhibition.

Overall, these experiments demonstrate that A375R and COLO829R cells are more resistant to PLX4720 than A375 and COLO829 cells and have increased expression of glutaminase, as well as reduced growth in response to glutaminase inhibition. This suggests that BRAF

inhibitor resistant cells have higher glutaminase expression and thus increased sensitivity to glutaminase inhibition. Indeed, in COLO829R cells, the absence of a BRAF inhibitor does not diminish the response to glutaminase inhibition. However, in A375R cells the presence of a BRAF inhibitor increases sensitivity to glutaminase inhibition, demonstrating that in some melanoma cells, BRAF inhibition itself rather than the acquired resistance makes cells more vulnerable to glutaminase inhibition.

### 3.1.2 Plasmax™ Reduces Glutamine Consumption and Glutamate Secretion Compared to DMEM.

Having shown that A375 cells have a reduced response to CB839 in DMEM (Figure 3.1.1-3), we sought to determine if the media affected the consumption and secretion of glutamine and glutamate. The levels of glutamine and glutamate flux in the four cell lines was measured using a YSI biochemistry analyser, which measured absolute levels of glutamine and glutamate in spent media after 48 hours culture with each of the four cell lines.

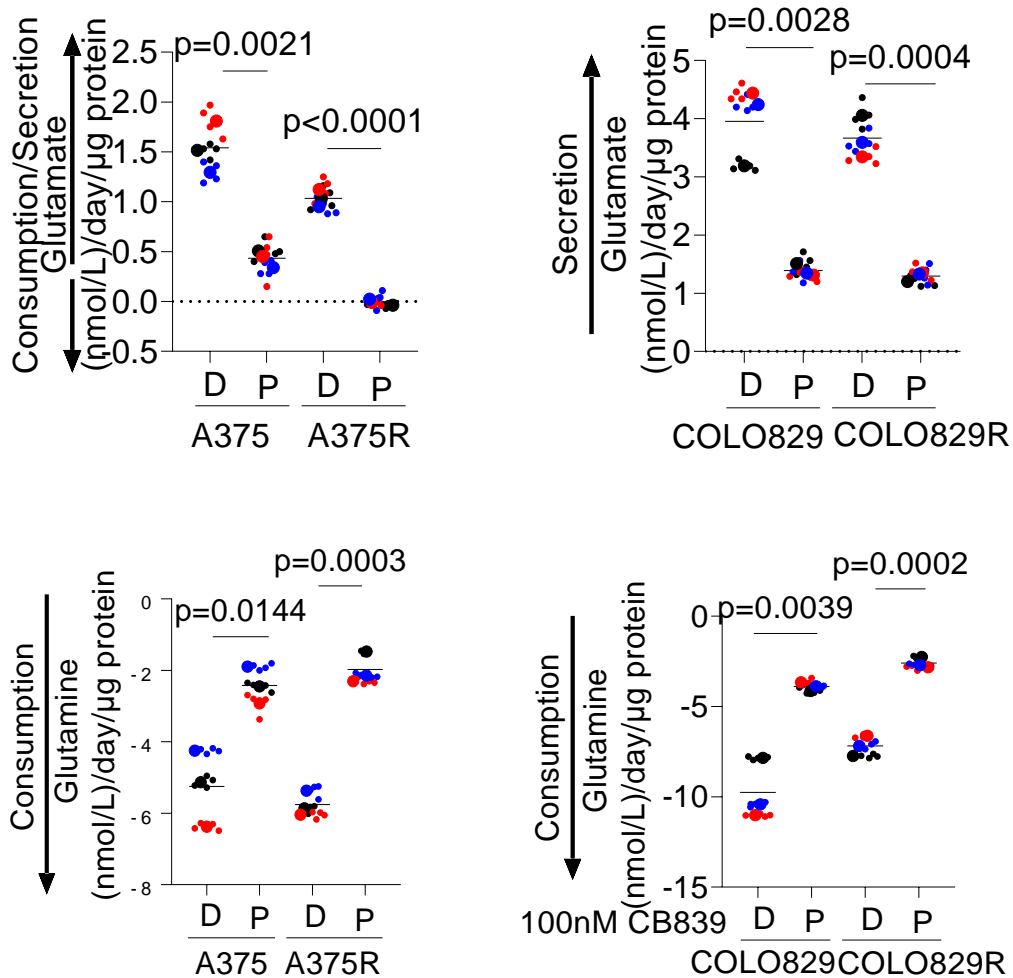
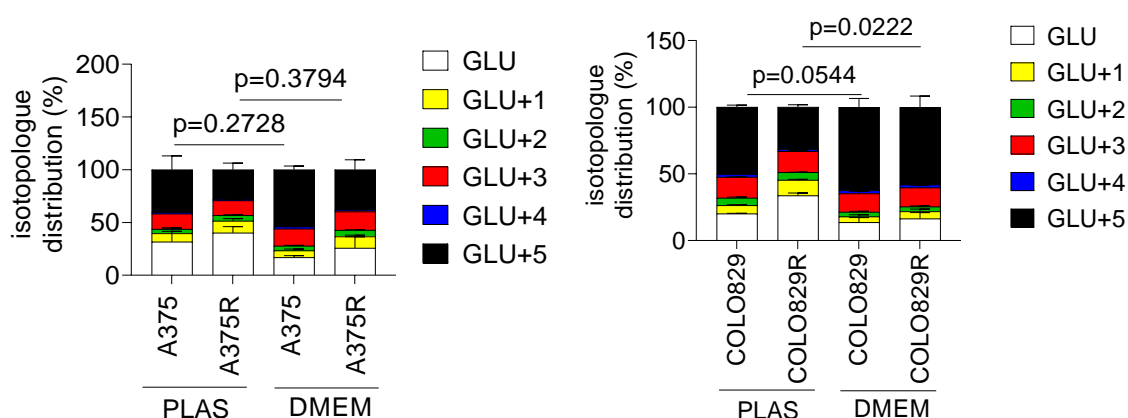


Figure 3.1.2-1: Graphs depicting the glutamine and glutamate consumption and secretion rates of melanoma cell lines A375, A375R, COLO829 and COLO829R in Plasmax (P) and DMEM (D) media with or without 100nM CB839, over a 48-hour incubation. Each large point represents one biological replicate which is the average of 4 technical replicates shown as a smaller point in the same colour ( $n_{\text{expt}}=3$ ,  $n_{\text{wells}}=4$ ). Lines above each graph indicate comparisons made by an unpaired t test performed on three independent experiments.

All cell lines had a net consumption of glutamine and secretion of glutamate in DMEM, and Plasmax™ reduced the consumption of glutamine and secretion of glutamate in all cell lines compared to DMEM (Figure 3.1.2-1). There was reduced consumption of glutamine and secretion of glutamate in Plasmax™ compared to DMEM demonstrates that Plasmax™ perturbs the normal flux of glutamine anaplerosis intermediates in all cell lines. In addition, both BRAF inhibitor resistant subclones had a slight reduction in glutamate secretion and glutamine uptake compared to their parental counterparts.



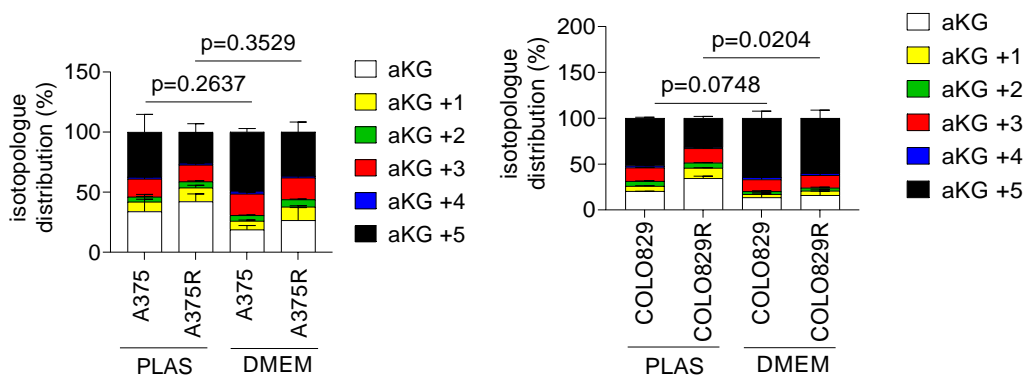
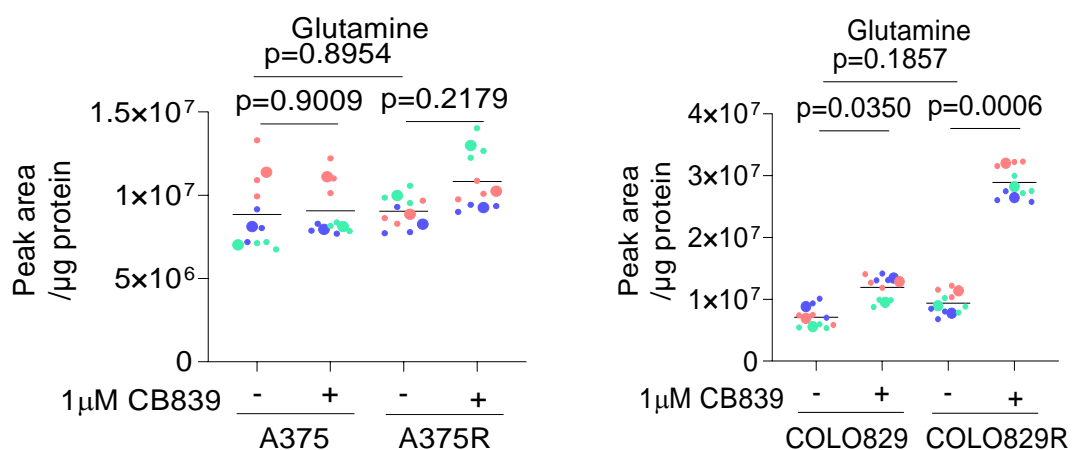


Figure 3.1.2-2: Graphs depicting the isotopologue distribution of glutamate and  $\alpha$ -ketoglutarate in A375, A375R (left) COLO829 and COLO829R (right) cells after a 48-hour incubation in 8mL 0.65mM  $^{13}\text{C}_5$  glutamine in Plasmax<sup>TM</sup> or in 8mL 5mM  $^{13}\text{C}_5$  glutamine in DMEM. Values are stacked, such that the total distribution is 100%. Error bars represent standard deviation for each isotopologue. Bars represent the mean values for 3 independent experiments ( $n_{\text{expt}}=3$ ,  $n_{\text{wells}}=3$ ). Lines above each graph indicate comparisons made on GLU+5 by a ratio paired t test performed on three independent experiments.

Having shown that DMEM increased the consumption of glutamine and decreased the secretion of glutamate, this suggested that use of glutaminase was increased in DMEM. We therefore performed  $^{13}\text{C}_5$  glutamine tracing to determine if this was the case. We found a trend towards an increased the level of M+5 glutamate in DMEM media compared to Plasmax, for A375, A375R and COLO829 cells and this difference was significant for COLO829R cells. This indicated that culture in DMEM could increase the proportion of directly glutamine derived glutamate (Figure 3.1.2-2). The potential for media to change glutamine uptake and glutaminase use suggests a possible explanation for the difference in sensitivity of A375 cells to CB839 based on media. Taken together the results suggest that increased levels of glutamine in DMEM may cause increased glutaminase use in A375 cells and therefore increased sensitivity to CB839.

### 3.1.3 TCA cycle activity is More Dependent on Glutaminase Activity in BRAF Inhibitor Resistant Cells

To determine if the BRAF inhibitor resistant subclones had differences in their glutaminase activity, the levels of glutamine, glutamate and  $\alpha$ -ketoglutarate were measured using LC-MS. The results of this showed that there was no significant difference in the basal levels of glutamine, glutamate, and  $\alpha$ -ketoglutarate between the A375 and COLO829 cells, compared to A375R and COLO829R cells respectively (Figure 3.1.3-1). CB839 significantly decreased intracellular  $\alpha$ -ketoglutarate and glutamate in A375R and COLO829R cells to a greater extent than in A375 and COLO829 cells (Figure 3.1.3-1). Taken together, this demonstrated that CB839 disrupts the equilibrium of each of the intermediates of glutamine anaplerosis to a greater extent in BRAF inhibitor resistant cells than in sensitive cells. This suggests that BRAF inhibitor resistant cells have increased use of glutaminase.



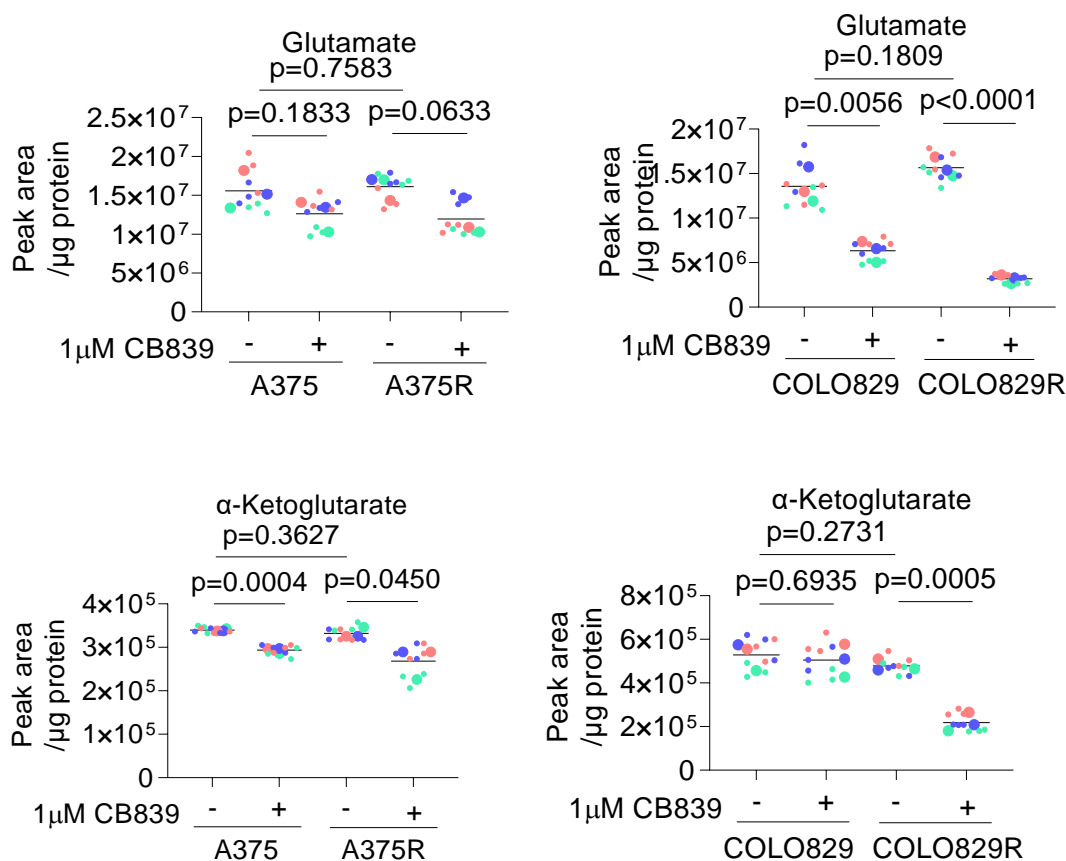


Figure 3.1.3-1: Graphs depicting the intracellular levels of glutamine, glutamate and  $\alpha$ -ketoglutarate in A375, A375R, COLO829 and COLO829R cells in Plasmix™, in response to a 24 hour treatment with 1 $\mu$ M of CB839. Each large point represents one biological replicate which is the average of three technical replicates shown as a smaller point in the same colour ( $n_{\text{expt}}=3$ ,  $n_{\text{wells}}=3$ ). Lines above each graph indicate comparisons made by an unpaired t test performed on three independent experiments.

To examine the hypothesis that BRAF inhibitor resistant cells have increased use of glutaminase, the level of glutamine derived carbons converted to glutamate were determined by performing <sup>13</sup>C<sub>5</sub> glutamine tracing in each of the four cell lines and in response to glutaminase inhibition by CB839. BRAF inhibitor resistant subclones had a smaller proportion of M+5 glutamate and a greater proportion of M+0 glutamate than their parental counterparts (Figure 3.1.3-2). This was repeated in the distribution for  $\alpha$ -ketoglutarate+5 and  $\alpha$ -

ketoglutarate+0 (Figure 3.1.3-3), demonstrating that the BRAF inhibitor resistant subclones have lower levels of directly glutamine derived glutamate than parental cells.

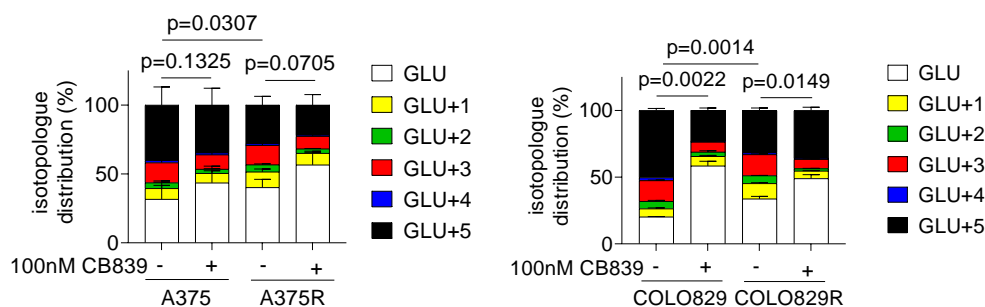


Figure 3.1.3-2: Graphs depicting the isotopologue distribution of glutamate in A375, A375R (left) COLO829 and COLO829R (right) cells after a 48-hour incubation in 8mL 0.65mM  $^{13}\text{C}_5$  glutamine in Plasmax<sup>TM</sup>. Values are stacked, such that the total distribution is 100%. Error bars represent standard deviation for each isotopologue. Bars represent the mean values for 3 independent experiments ( $n_{\text{expt}}=3$ ,  $n_{\text{wells}}=3$ ). Lines above each graph indicate comparisons made on GLU+5 by a ratio paired t test performed on three independent experiments.

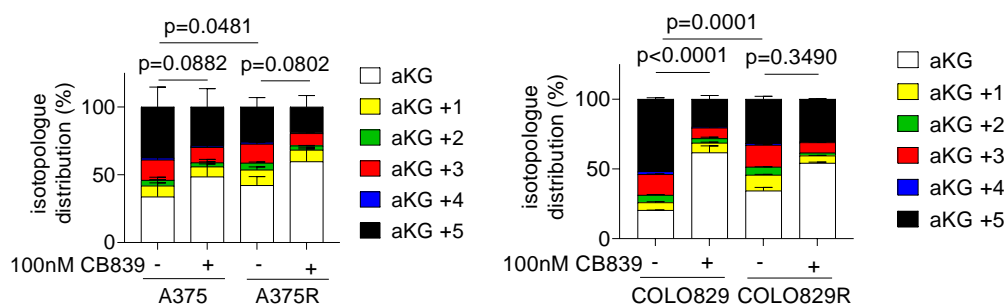


Figure 3.1.3-3: Graphs depicting the isotopologue distribution of  $\alpha$ -ketoglutarate ( $\alpha$ -KG) in A375, A375R (left) COLO829 and COLO829R (right) cells after a 48 hour incubation in 8mL 0.65mM  $^{13}\text{C}_5$  Glutamine in Plasmamax<sup>TM</sup>. Values are stacked, such that the total distribution is 100%. Error bars represent standard deviation for each isotopologue. Bars represent the mean values for 3 independent experiments ( $n_{\text{expt}}=3$ ,  $n_{\text{wells}}=3$ ). Lines above each graph indicate comparisons made on  $\alpha$ -ketoglutarate +5 by a ratio paired t test performed on three independent experiments.

Glutaminase inhibition decreased the proportion of M+5 glutamate and  $\alpha$ -ketoglutarate significantly in COLO829 cells and caused a trend toward decreasing in A375 and A375R cells. Glutaminase inhibition also reduced the proportion of M+3 glutamate and  $\alpha$ -ketoglutarate in A375R, COLO829 and COLO829R cells but not A375 cells (Figure 3.1.3-2&3). M+3 glutamate can be produced by the oxidation of M+5  $\alpha$ -ketoglutarate to M+4 malate, oxaloacetate and citrate, and subsequent oxidation of M+3  $\alpha$ -ketoglutarate and M+3 glutamate (Zhang *et al.*, 2014). Therefore glutaminase inhibition causes depletion of glutamate produced directly from glutamine as well as from other carbon sources via the TCA cycle.

Overall, these results show that the greater growth inhibition in response to glutaminase inhibition in BRAF inhibitor resistant cells is accompanied by greater depletion of glutamate in response to glutaminase inhibition. However, by performing glutamine tracing, it was found that BRAF inhibitor resistant have decreased production of directly glutamine derived glutamate. Glutaminase inhibition caused a decrease in the proportion of glutamate produced from directly from glutamine and indirectly through the TCA cycle in A375R cells.

### 3.1.4 Glutaminase Inhibition Results in Depletion of Aspartate and Nucleotide Synthesis in BRAF Inhibitor Resistant Cells

Having shown that glutaminase inhibition reduced the growth of BRAF inhibitor resistant cells, the metabolic effects caused by glutaminase inhibition were determined next. A targeted metabolomic analysis was used to determine the response to CB839 in A375R and COLO829R cells. This analysis showed that aspartate was the most significantly depleted metabolite in response to glutaminase inhibition in both BRAF inhibitor resistant cell lines. Carnitine was also significantly depleted in both BRAF inhibitor resistant cell lines, which was accompanied by a significant increase in acetyl-carnitine in response to glutaminase inhibition (Figure 3.1.4-1). Lactate, Acetyl CoA, glyceraldehyde-3-phosphate, and fructose-1,6-bisphosphate were all increased in response to glutaminase inhibition, collectively suggesting an increase in glycolytic metabolism.

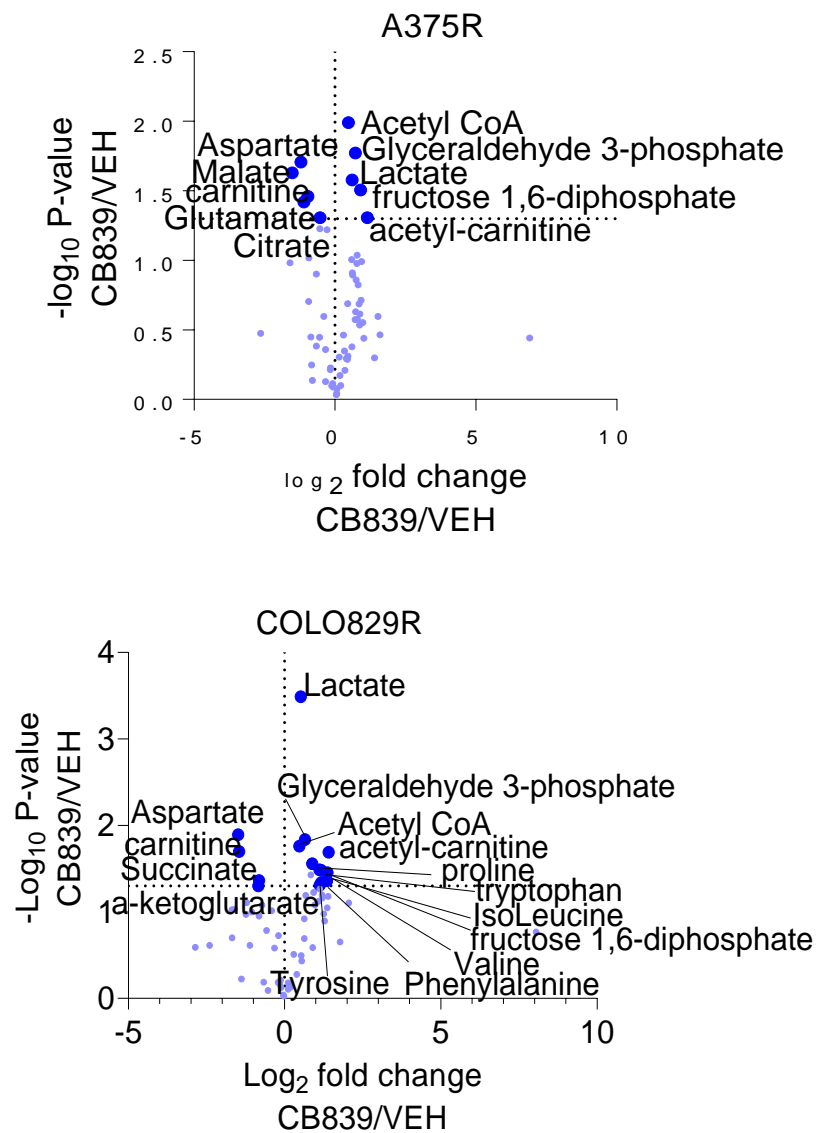


Figure 3.1.4-1: Volcano plots showing the  $\log_2$  fold change and  $-\log_{10}$  p value for an unpaired t test comparing the intracellular levels of 66 metabolites between vehicle and CB839 treated A375R (left) and COLO829R (right) cells in vitro. Each point represents the calculated  $\log_2$  fold change and  $-\log_{10}$  p value for three biological replicates, ( $n_{\text{expt}}=3$ ,  $n_{\text{wells}}=3$ ). Larger and darker blue points represent metabolites with statistical significance ( $p < 0.05$ ) in the t test between CB839 and vehicle treated cells and are labelled with the name of the metabolite which they represent.

Aspartate was significantly depleted in response to CB839 in both BRAF inhibitor resistant cell lines but not in A375 cells and to a lesser extent in COLO829 cells (Figure 3.1.4-2). Interestingly, not only was

aspartate the most significantly depleted metabolite in the targeted list of 66 standards (including all 20 proteogenic amino acids), but its levels also followed the pattern of glutamate levels and cell growth in response to CB839 (Figure 3.1.1-3). Aspartate levels were also not significantly different in BRAF inhibitor resistant cell lines compared to their parental cell lines, demonstrating that BRAF inhibitor resistance did not perturb the basal equilibrium of aspartate.

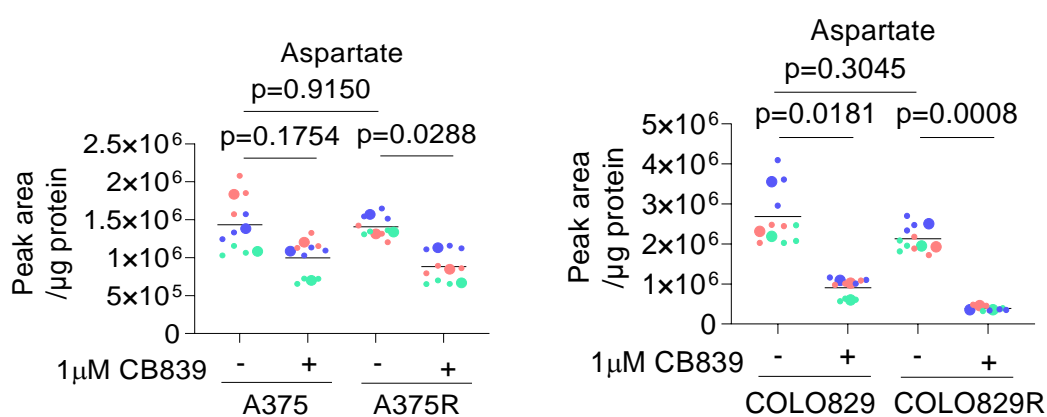
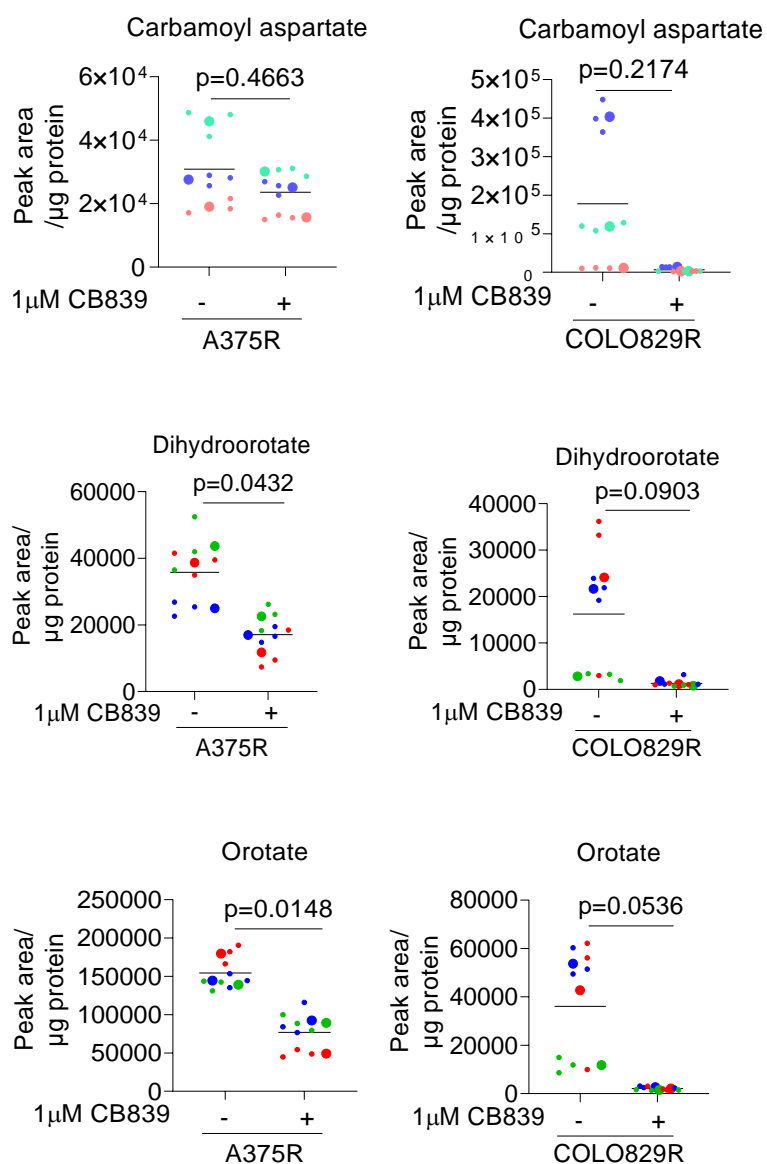


Figure 3.1.4-2: Graphs depicting the intracellular levels of aspartate in A375R (left) and COLO829R (right) cells in Plasmax™, in response to a 24-hour treatment with 1μM of CB839. Each large point represents one biological replicate which is the average of 3 technical replicates shown as a smaller point in the same colour ( $n_{\text{expt}}=3$ ,  $n_{\text{wells}}=3$ ). Lines above each graph indicate comparisons made by an unpaired t test performed on three independent experiments.

Aspartate availability has been previously reported to determine cell survival when glutamine is limiting (Alkan *et al.*, 2018), and has been shown to influence cancerous growth via contribution of carbon and nitrogen to nucleotide synthesis. Aspartate contributes both carbon and nitrogen to the production of carbamoyl aspartate in pyrimidine synthesis (Kodama *et al.*, 2020). Therefore, we measured levels of

pyrimidine synthesis intermediates to determine whether the depletion of aspartate caused by glutaminase inhibition affected the levels of each of the intermediates in nucleotide synthesis. Due to the low abundance of the intermediates (except for carbamoyl aspartate) we used selective ion monitoring (SIM) on an orbitrap Q Exactive plus mass spectrometer to boost the sensitivity of the LC-MS method. This improved the detection and relative quantification of these intermediates (Figure 3.1.4-3).



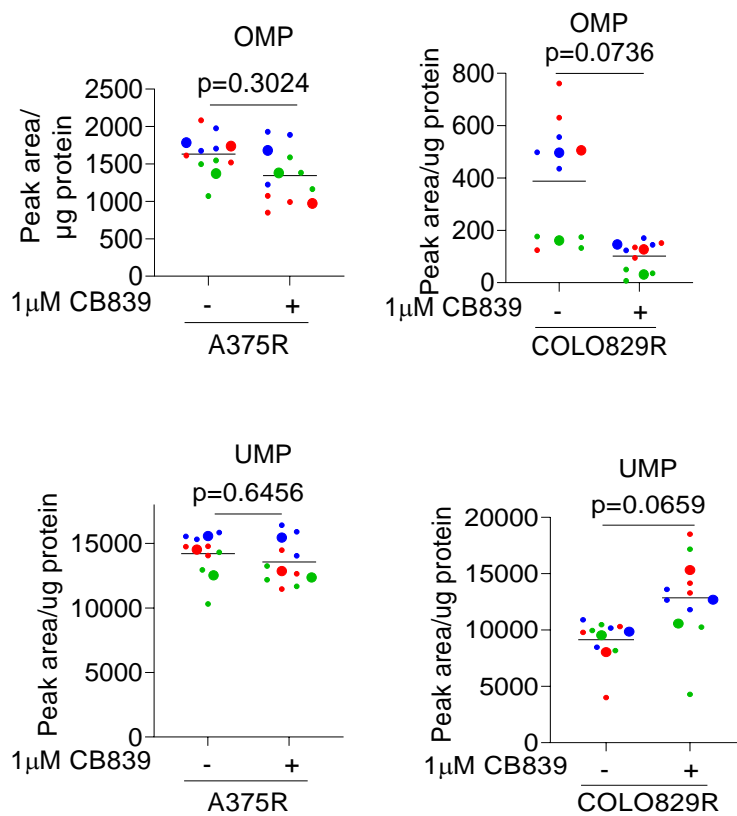


Figure 3.1.4-3: Graphs depicting the intracellular levels of pyrimidine synthesis intermediates (in order; carbamoyl aspartate, dihydroorotate, orotate and orotidine monophosphate and UMP) in A375R (left) and COLO829R (right) cells in Plasmax™, in response to a 24-hour treatment with 1 μM of CB839. Each large point represents one biological replicate which is the average of three technical replicates shown as a smaller point in the same colour ( $n_{\text{expt}}=3$ ,  $n_{\text{wells}}=3$ ). Lines above each graph indicate comparisons made by an unpaired t test performed on three independent experiments.

This demonstrated a decrease in carbamoyl aspartate, resulting in a decrease in each of the intermediates of purine synthesis in response to glutaminase inhibition by CB839. The levels of the final product, uridine monophosphate (UMP), can be influenced by many factors, including the rate of cell division, and it was not significantly affected by glutaminase inhibition (Figure 3.1.4-3).

Overall, this revealed a slight decrease in the level of each of the intermediates of pyrimidine synthesis in response to glutaminase inhibition. Given that glutaminase inhibition resulted in reduced growth of BRAF inhibitor resistant cells and that nucleotide synthesis is essential for proliferating cells (Sullivan *et al.*, 2015), glutaminase inhibition may reduce growth in melanoma cells by reducing levels of nucleotide synthesis. To test this hypothesis, cells were counted after being grown in Plasmix™ supplemented with dihydroorotate, carbamoyl aspartate and a mixture of purine and pyrimidine nucleosides in the presence of CB839. This experiment demonstrated that supplementation of pyrimidine synthesis intermediates does not rescue the growth defect caused by glutaminase inhibition (Figure 3.1.4-5).

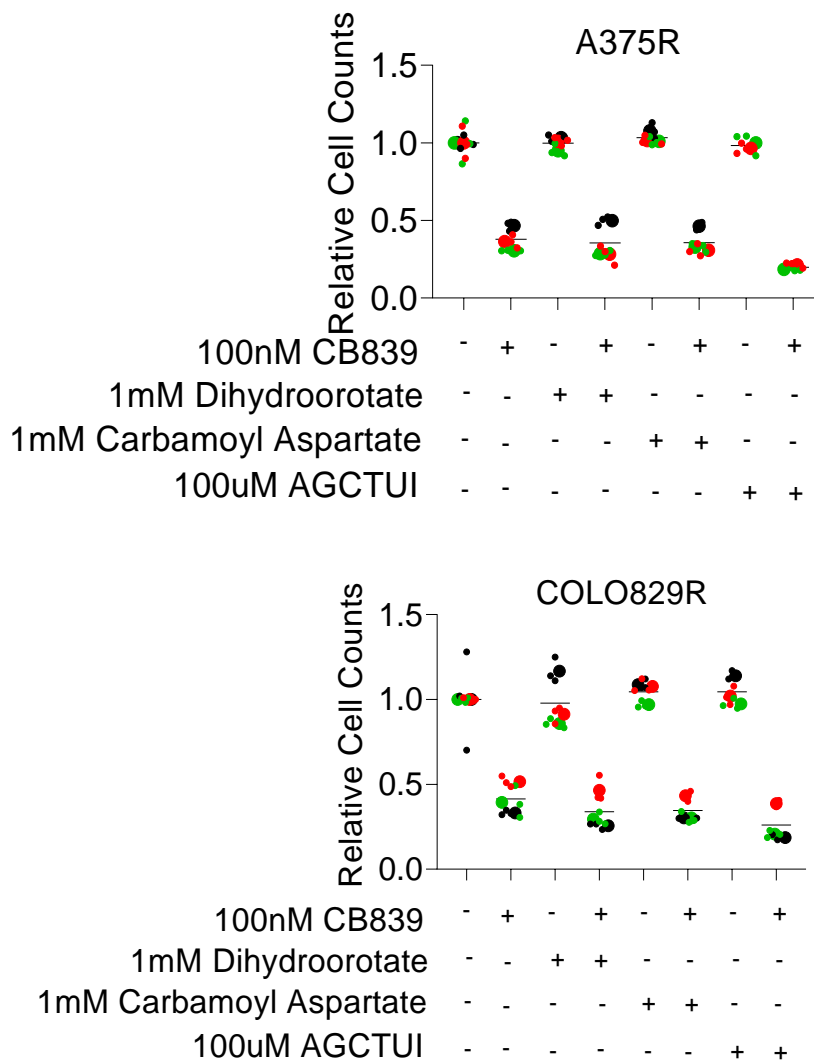


Figure 3.1.4-5: Graphs depicting the number of A375R (above) and COLO829R (below) cells after supplementation of 1mM dihydroorotate, 1mM carbamoyl aspartate or a mixture of 100µM each of adenosine, guanosine, cytosine, thymidine, uridine, and inosine (AGCTUI) and treatment with 100nM CB839, relative to cells grown in Plasmax™. Each large point represents one biological replicate which is the average of three technical replicates shown as a smaller point in the same colour ( $n_{\text{expt}}=3$ ,  $n_{\text{wells}}=3$ ). Lines above each graph indicate comparisons made by an unpaired t test performed on three independent experiments.

### 3.1.5 Growth Inhibition by Glutaminase Inhibition Can be Reduced by Supplementing Aspartate or NAD<sup>+</sup> Regenerating Metabolites

The fact that aspartate was significantly depleted in BRAF inhibitor resistant cells in response to glutaminase inhibition suggested that glutamine derived carbons contributed to aspartate synthesis. To determine if this was the case, the contribution of glutamine derived carbons to aspartate in the presence of glutaminase inhibition by CB839 and in each of the cell lines, was determined.

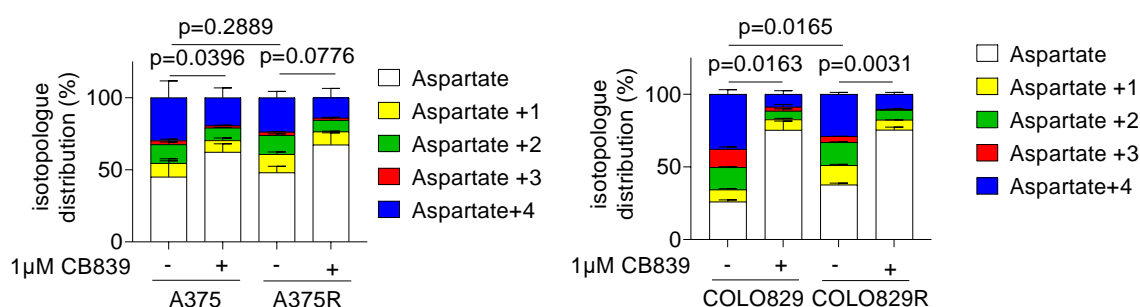


Figure 3.1.5-1: Graphs depicting the isotopologue distribution of aspartate in A375, A375R (left) COLO829 and COLO829R (right) cells after a 48 hour incubation in 8mL 0.65mM <sup>13</sup>C<sub>5</sub> Glutamine in Plasmax<sup>TM</sup>. Values are stacked, such that the total distribution is 100%. Error bars represent standard deviation for each isotopologue. Bars represent the mean values for three independent experiments (n<sub>expt</sub>=3, n<sub>wells</sub>=3). Lines above each graph indicate comparisons made on aspartate + 4 by a ratio paired t test performed on three independent experiments.

A significant decrease in M+4 aspartate was recorded in COLO829R cells in response to glutaminase inhibition. In addition, a significant decrease in the proportion of M+1, M+2 and M+3 aspartate and

increase in M+0 aspartate was recorded in both BRAF inhibitor resistant cell lines in response to glutaminase inhibition (Figure 3.1.5-1). This demonstrated that the decrease in aspartate levels in response to glutaminase inhibition was at least partially due to a lack of glutamine derived carbons.

Having shown that glutamine derived aspartate synthesis was significantly reduced by glutaminase inhibition in BRAF inhibitor resistant cells, but that the use of aspartate in nucleotide synthesis was not detrimental to cell growth, it was next tested whether aspartate itself was sufficient to rescue the growth of BRAF inhibitor resistant cells upon glutaminase inhibition. 10mM aspartate was supplemented to BRAF inhibitor resistant cells to determine if this could rescue growth upon glutaminase inhibition.

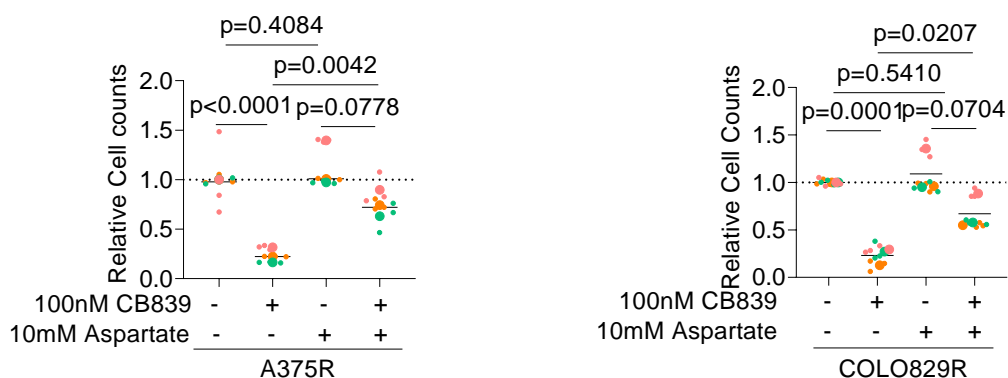


Figure 3.1.5-2: Graphs depicting the number of A375R (left) and COLO829R (right) cells after supplementation of 10mM aspartate and treatment with 100nM CB839, relative to cells grown in Plasmax™. Each large point represents one biological replicate which is the average of three technical replicates shown as a smaller point in the same colour ( $n_{\text{expt}}=3$ ,  $n_{\text{wells}}=3$ ). Lines above each graph indicate comparisons made by an unpaired t test performed on three independent experiments.

These results demonstrated that supplementation of aspartate was sufficient to rescue growth inhibition by glutaminase inhibition (Figure 3.1.5-2). Thus, glutaminase-dependent aspartate production is necessary for the growth of BRAF inhibitor resistant cells. Next, we sought to determine the use of aspartate in BRAF inhibitor resistant cell growth.

One report demonstrated that oxidative reactions of the activity of allowed synthesis of aspartate and subsequently of biosynthetic precursors such as nucleotides, and that a lack of  $\text{NAD}^+$  generation reduced the reactions in which  $\text{NAD}^+$  is used which is detrimental to cell growth (Luengo *et al.*, 2021). In addition, as part of the malate-aspartate shuttle, aspartate also allows the transfer of electrons into the mitochondria by regenerating mitochondrial NADH (Birsoy *et al.*, 2015) and the production of aspartate by the malate-aspartate shuttle enzymes GOT1 or GOT2 is essential in rapidly proliferating cells (Sullivan *et al.*, 2015). Thus, aspartate levels are closely associated with the  $\text{NAD}^+/\text{NADH}$  ratio, so we measured the  $\text{NAD}^+/\text{NADH}$  ratio in BRAF inhibitor resistant cells under glutaminase inhibition by CB839. This showed that glutaminase inhibition may affect the processes responsible for regenerating  $\text{NAD}^+$  from NADH in all four cell lines. Interestingly, BRAF inhibitor resistant cells had a higher ratio of  $\text{NAD}^+/\text{NADH}$  (Figure 3.1.5-3).

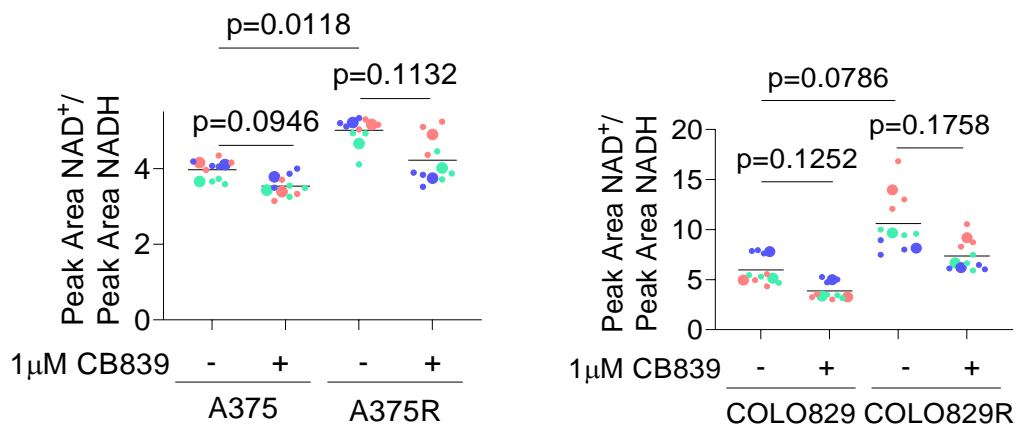


Figure 3.1.5-3: Graphs depicting the ratio of NAD<sup>+</sup> to NADH in A375R (left) and COLO829R (right) cells in Plasmax<sup>TM</sup>, in response to a 24-hour treatment with 1µM of CB839. Each large point represents one biological replicate which is the average of three technical replicates shown as a smaller point in the same colour ( $n_{\text{expt}}=3$ ,  $n_{\text{wells}}=3$ ). Lines above each graph indicate comparisons made by an unpaired t test performed on three independent experiments.

We hypothesized that glutaminase inhibition could reduce cell growth by disrupting the equilibrium of the malate-aspartate shuttle, so we tested whether restoring levels of components of the malate-aspartate shuttle could partially rescue cell growth in the presence of glutaminase inhibition. Cell growth was measured in response to CB839 after supplementation of oxaloacetate and dimethyl-s-malate.

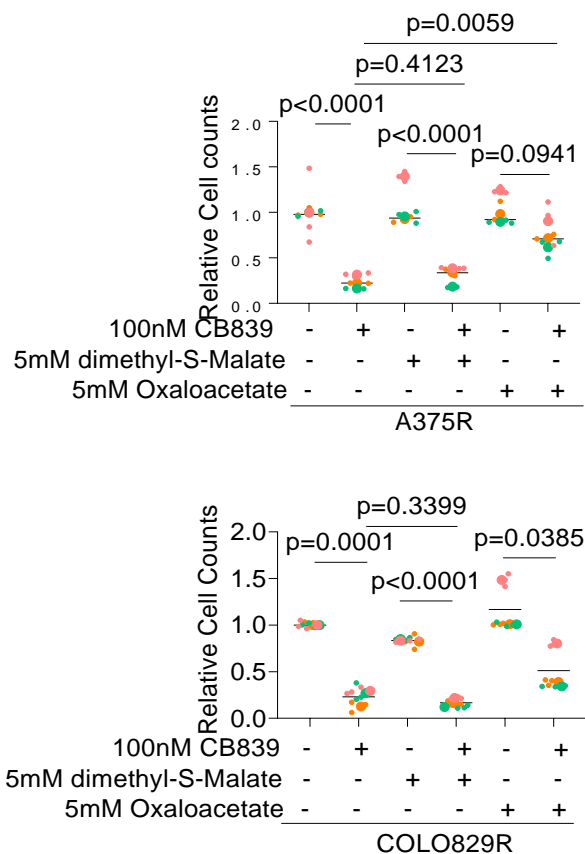


Figure 3.1.5-4: Graphs depicting the number of A375R (left) and COLO829R (right) cells after supplementation of 5mM dimethyl-s-malate, 5mM oxaloacetate and treatment with 100nM CB839, relative to cells grown in Plasmix™. Each large point represents one biological replicate which is the average of three technical replicates shown as a smaller point in the same colour ( $n_{\text{expt}}=3$ ,  $n_{\text{wells}}=3$ ). Lines above each graph indicate comparisons made by an unpaired t test performed on three independent experiments.

The results showed that while dimethyl-s-malate was unable to prevent the growth inhibition caused by glutaminase inhibition, while the addition of oxaloacetate was able to partially rescue the growth of A375R and COLO829R cells (Figure 3.1.5-4). Malate requires the conversion of  $\text{NAD}^+$  to NADH in order be incorporated into the malate-aspartate shuttle, which would cause a further reduction in the  $\text{NAD}^+/\text{NADH}$  ratio.

In the cytosol, oxaloacetate can be reduced to malate, oxidizing NADH to NAD<sup>+</sup> in the process. However, it has been reported that oxaloacetate can also spontaneously decarboxylate to pyruvate (Tsai, 1967), which can increase the NAD<sup>+</sup>/NADH ratio if converted to lactate by lactate dehydrogenase (LDH). Therefore the rescuing effects of oxaloacetate may be caused by either of these effects. We tested if pyruvate itself could rescue growth from glutaminase inhibition. In addition, lactate, the reduced form of pyruvate may prevent the rescuing effect of pyruvate, by shifting the equilibrium of LDH toward oxidation and NADH generation, as had previously been shown to prevent to occur in 143B cells (Luengo *et al.*, 2021). Therefore, growth response to lactate supplementation was also determined.

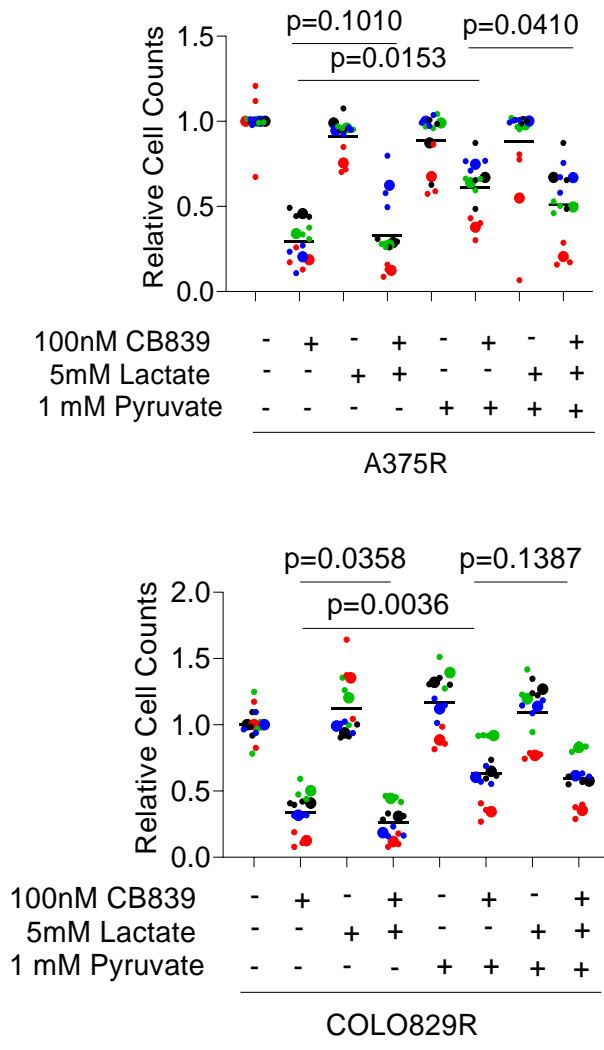


Figure 3.1.5-5: Graphs depicting the number of A375R (left) and COLO829R (right) cells after supplementation of 5mM lactate and 1mM Pyruvate and treatment with 100nM CB839, relative to cells grown in Plasmag<sup>TM</sup>. Each large point represents one biological replicate which is the average of three technical replicates shown as a smaller point in the same colour ( $n_{\text{expt}}=3$ ,  $n_{\text{wells}}=3$ ). Lines above each graph indicate comparisons made by an unpaired t test performed on three independent experiments.

Addition of 1mM pyruvate partially rescued the growth of both A375R and COLO829R cells from glutaminase inhibition. This supports the theory that oxaloacetate can rescue from growth inhibition by CB839 by spontaneously decarboxylating to pyruvate. Oxaloacetate supplementation could therefore be interpreted as oxaloacetate and

pyruvate supplementation. On the other hand, 5mM lactate caused a slightly greater decrease in growth in response to glutaminase inhibition in COLO829R cells, while 5mM lactate in the presence of 1mM pyruvate caused a slightly greater decrease in growth in response to glutaminase inhibition in A375R cells (Figure 3.1.5-5). This suggests that shifting the equilibrium toward the conversion of NAD<sup>+</sup> to NADH by LDH can exacerbate growth inhibition by glutaminase inhibition in some conditions.

The fact that aspartate, oxaloacetate/pyruvate supplementation but not dimethyl-s-malate supplementation were able to rescue the growth of BRAF inhibitor resistant cells from glutaminase inhibition, supported the idea that metabolites increasing the NAD<sup>+</sup>/NADH ratio, or supplying intermediates of the malate-aspartate shuttle were responsible for the rescuing effect. The use of  $\alpha$ -ketoglutarate in the transamination reactions of the malate-aspartate shuttle was also investigated for its ability to rescue growth from glutaminase inhibition. By supplementing a cell permeable form of  $\alpha$ -ketoglutarate - dimethyl- $\alpha$ -ketoglutarate, we obtained inconsistent results between cell lines. Dimethyl- $\alpha$ -ketoglutarate completely rescued the growth of COLO829R cells from glutaminase inhibition but reduced the growth of A375R cells in the absence of glutaminase inhibition (Figure 3.1.5-6).

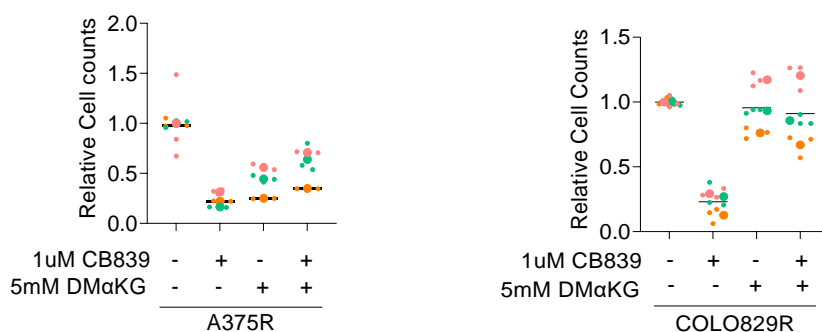
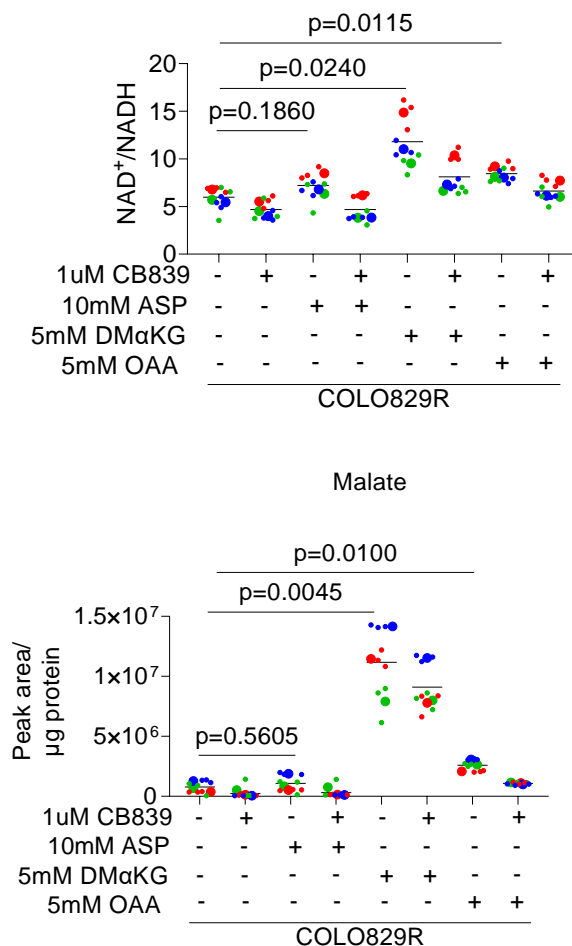


Figure 3.1.5-6: Graphs depicting the number of A375R (left) and COLO829R (right) cells after supplementation of 5mM dimethyl- $\alpha$ -ketoglutarate (DM $\alpha$ KG) and treatment with 100nM CB839, relative to cells grown in Plasmax™. Each large point represents one biological replicate which is the average of three technical replicates shown as a smaller point in the same colour ( $n_{\text{expt}}=3$ ,  $n_{\text{wells}}=3$ ).

Having demonstrated that aspartate, oxaloacetate, and dimethyl- $\alpha$ -ketoglutarate were able to rescue the growth of COLO829R cells from glutaminase inhibition, we measured the NAD<sup>+</sup>/NADH ratio in COLO829R cells after supplementation with aspartate, oxaloacetate and dimethyl- $\alpha$ -ketoglutarate.



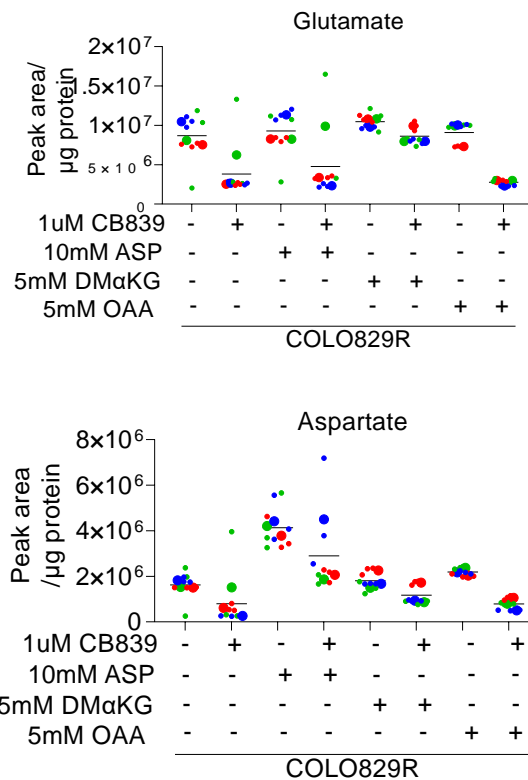


Figure 3.1.5-7: Graphs depicting the ratio of  $\text{NAD}^+$  to  $\text{NADH}$ , as well as the level of malate, aspartate and glutamate in COLO829R cells in Plasmax™, in response to a 24-hour treatment with  $1\mu\text{M}$  of CB839. Each large point represents one biological replicate which is the average of three technical replicates shown as a smaller point in the same colour ( $n_{\text{expt}}=3$ ,  $n_{\text{wells}}=3$ ). Lines above each graph indicate comparisons made by an unpaired t test performed on three independent experiments.

This showed that oxaloacetate/pyruvate, and dimethyl- $\alpha$ -ketoglutarate supplementation significantly increased the  $\text{NAD}^+/\text{NADH}$  ratio and the levels of malate in COLO829R cells. However, aspartate did not change the  $\text{NAD}^+/\text{NADH}$  ratio or the levels of malate. Furthermore, aspartate supplementation increased levels of aspartate, but oxaloacetate/pyruvate and dimethyl- $\alpha$ -ketoglutarate did not (Figure 3.1.5-7). Therefore, glutaminase dependent aspartate synthesis or an increased  $\text{NAD}^+/\text{NADH}$  ratio is required for the growth of BRAF inhibitor resistant cells, but one is

not dependent on the other. Having demonstrated this, we measured the levels of glutamate in response to each of these three supplements, which showed that only dimethyl- $\alpha$ -ketoglutarate increased the levels of glutamate, and thus maintaining glutamate production is also not the point of convergence of aspartate, oxaloacetate/pyruvate and dimethyl- $\alpha$ -ketoglutarate (Figure 3.1.5-7).

Overall, we showed that the demand for glutamine derived glutamate can be quenched by increasing aspartate, which is involved in several transamination reactions and may therefore replace the role of glutamine in these reactions. Otherwise, demand for glutamine derived glutamate may be reduced by adding supplements that maintain a  $\text{NAD}^+/\text{NADH}$  ratio, which is required for optimal growth.

## 3.2 Generating *in vivo* models of BRAF Inhibitor Resistant Melanoma *in vivo* to Determine CB839 Therapeutic Efficacy

### 3.2.1 Treatment with CB839 causes changes in serum metabolites

To investigate the effects of glutaminase inhibition in healthy NSG mice, a treatment regime of 200mg/kg CB839 dosed by oral gavage was given to tumour free NSG mice for 2 weeks. This treatment regime did not cause any significant difference in body weight (Figure 3.2.1-1).

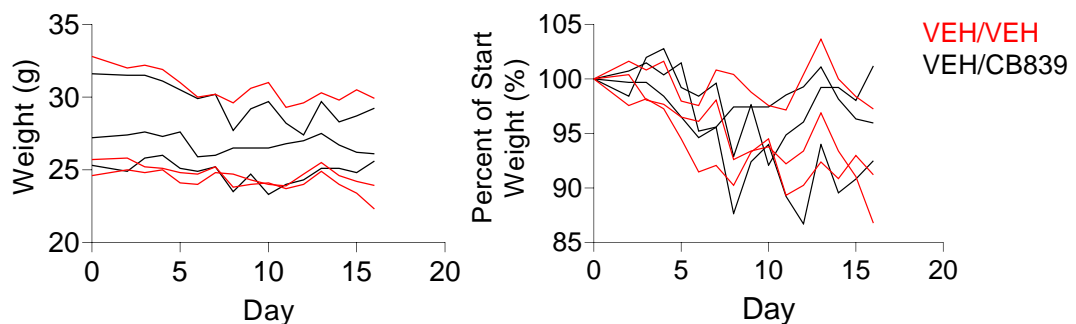


Figure 3.2.1-1: Graph depicting the weight of NSG mice (left) and percent of start weight (right) in response to 200mg/kg CB839 and a vehicle for PLX4032 treatment over 2 weeks of treatment. Each line represents one mouse, with the colour of each line representing the treatment administered.

GLS1 is expressed in the kidney of healthy mice, and the effects of its systemic inhibition have not been fully elucidated. Thus, a targeted metabolic analysis was performed on the serum of tumour free mice treated with CB839 (Figure 3.2.1-2).

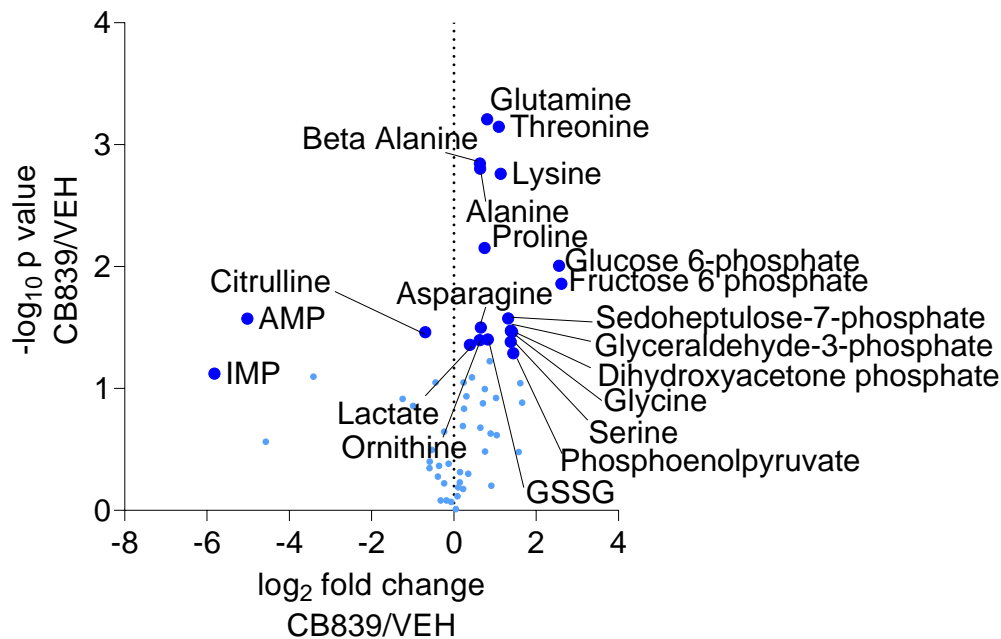


Figure 3.2.1-2: Volcano plots showing the  $\log_2$  fold change and  $-\log_{10}$  p value for an unpaired t test comparing the serum levels of 66 metabolites between vehicle and CB839 treated NSG mice. Each point represents the calculated  $\log_2$  fold change and  $-\log_{10}$  p value for two treatment groups ( $n_{\text{mice}}=6$ ). Larger and darker blue points represent metabolites with statistical significance ( $p < 0.05$ ) in the t test between CB839 and vehicle treated mice and are labelled with the name of the metabolite which they represent, including Inosine monophosphate (IMP), adenosine monophosphate (AMP) and glutathione disulphide (GSSG).

19 metabolites were found to be significantly increased in response to CB839 and 3 were significantly decreased. In accordance with the effect of CB839 on cells *in vitro*, lactate, glyceraldehyde-3-phosphate, fructose-6-phosphate, asparagine, and glutamine were increased (Figure 3.2.1-2). Therefore, *in vivo* CB839 affects the systemic availability of metabolites, which may play a part in explaining the effects of CB839 on tumour cells *in vivo*. Systemic aspartate levels were not significantly decreased, which differed from the results obtained in A375R and COLO829R cells *in vitro*, and

in fact were slightly increased in the serum of CB839 treated mice (Figure 3.2.1-3). Interestingly, the levels of systemic ornithine were increased which were accompanied by a decrease in citrulline (Figure 3.2.1-3). This could be explained by reduced ammonia production by glutaminase, and thus reduced activity of ornithine carbamyltransferase, the entry point for ammonia in the urea cycle

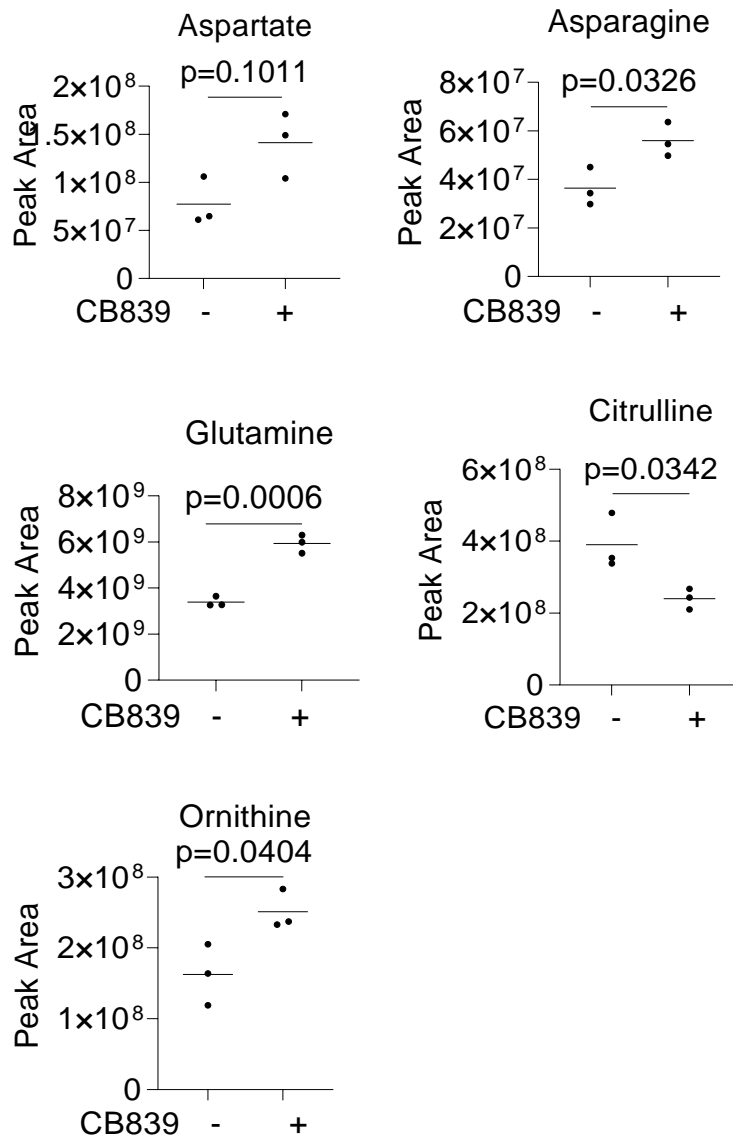


Figure 3.2.1-3: Graphs depicting the level of aspartate, asparagine glutamine, citrulline and ornithine in the serum of vehicle and CB839 treated NSG mice. Each point represents one mouse ( $n_{\text{mice}}=6$ ). Lines above each graph indicate comparisons made by an unpaired t test performed on the two treatment groups, with the p value from each comparison shown above. Lines above each graph indicate comparisons made by an unpaired t test performed on three serum samples.

### 3.2.2 Intraperitoneal PLX4032 Treatment Decreases the Growth of Naïve Melanoma Xenografts

To investigate the effects of combined BRAF and glutaminase inhibition *in vivo*, a treatment regime allowing the administration of PLX4032 and CB839 was designed. CB839 was given twice daily via oral gavage (as recommended by the supplier, Calithera Biosciences) which prevented the administration of any further doses by oral gavage under the Workman guidelines (Workman *et al.*, 2010). This meant that PLX4032 could not be administered orally as it is in patients. Therefore, intraperitoneal injection was chosen as the administration route for PLX4032, that was given daily at 10mg/kg PLX4032. This regime did not cause body weight loss or signs of adverse effects (Figure 3.2.2-1). In addition, this could be administered in combination with 200mg/kg CB839 without body weight loss or adverse effects (Figure 3.2.2-2). The PLX4032 regime was used in NSG mice bearing xenografted tumours derived from A375 or COLO829 cells and in C57/BL/6 mice bearing allografted tumours derived from YUMM1.7 cells. The intraperitoneal dose of 10mg/kg PLX4032 reduced the growth rate of tumours derived from all cell types (Figure 3.2.2-3).

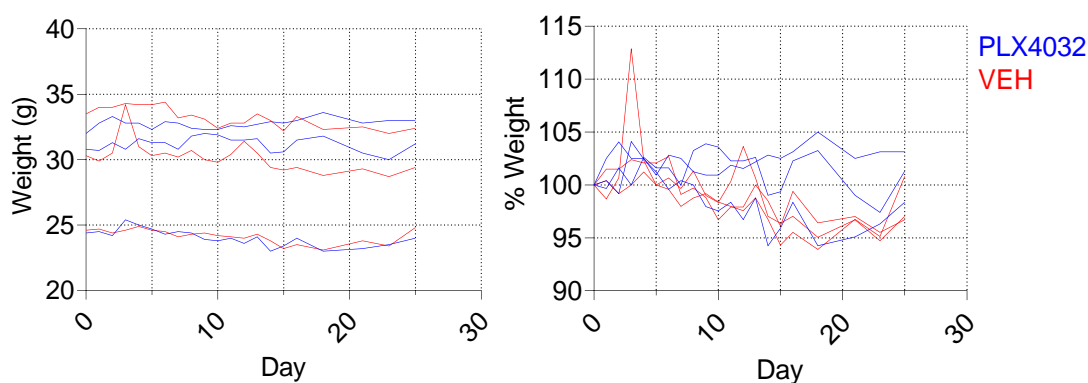


Figure 3.2.2-1: Graph depicting the weight of each mouse since start of treatment with 10mg/kg PLX4032 or a vehicle (left) and the % change in the weight of each mouse since treatment start (right). Each line represents one mouse ( $n_{\text{mice}}=6$ ), with the colour of each line corresponding to the treatment administered.

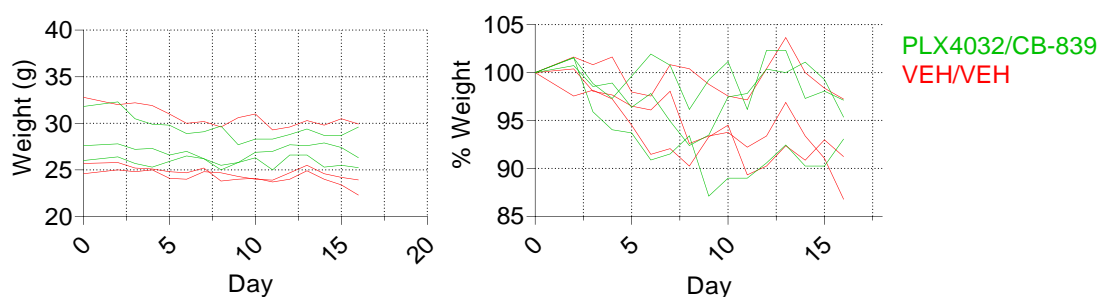


Figure 3.2.2-2: Graph depicting the weight of each mouse since start of treatment with 10mg/kg PLX4032 and 200mg/kg CB839 or a vehicle (left) and the % change in the weight of each mouse since treatment start (right). Each line represents one mouse ( $n_{\text{mice}}=6$ ), with the colour of each line corresponding to the treatment administered.

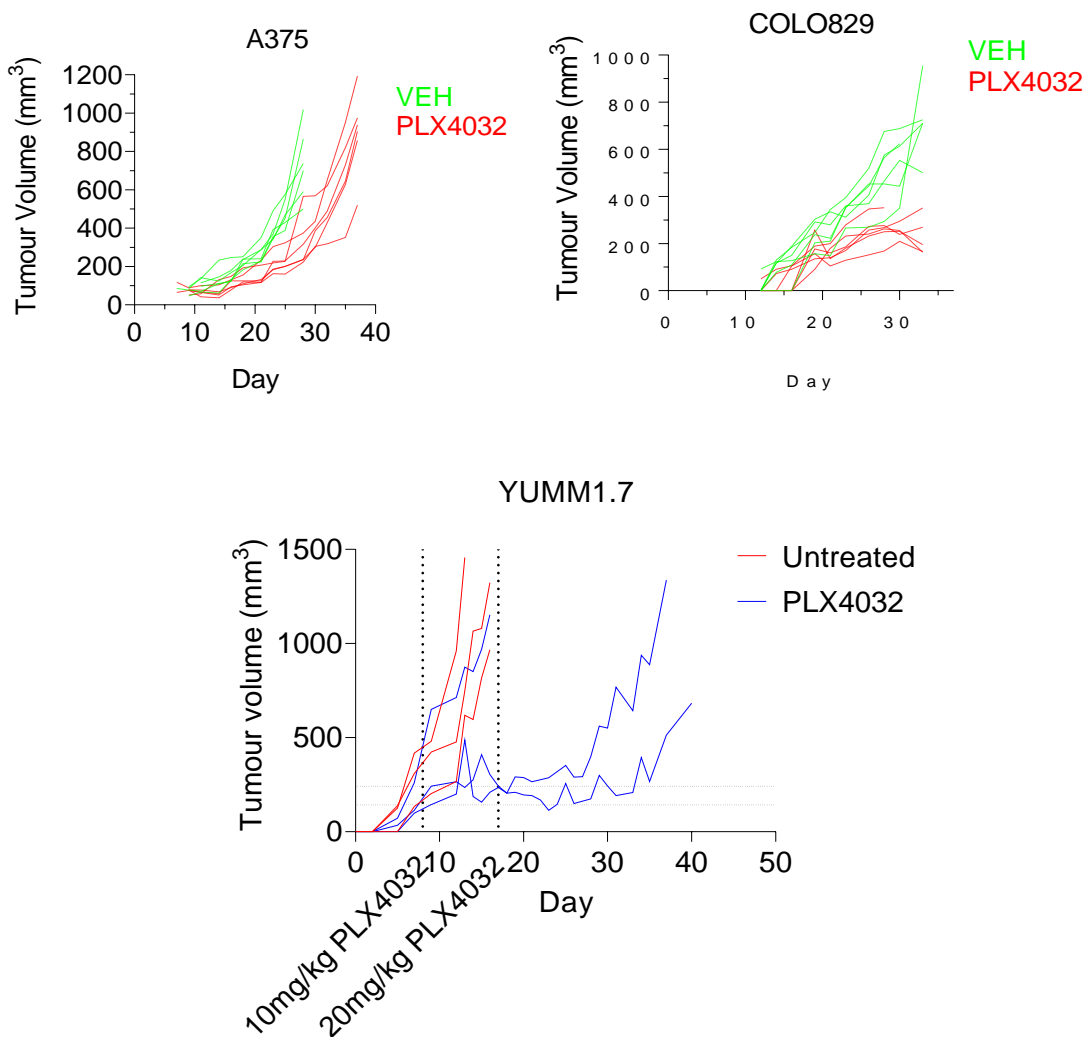


Figure 3.2.2-3: Figure depicting the growth of each tumour since the subcutaneous injection of 1 million A375 (left), COLO829 (right) or YUMM1.7 (below) cells into the flank of mice. NSG mice are used for COLO829 and A375 cells and C57BL/6 mice are used for YUMM1.7 cells. Each line represents the measurements of one tumour from one mouse (for A375 and COLO829, n<sub>tumours</sub>=6) (for YUMM1.7 cells, n<sub>tumours</sub>=3). For NSG mice, 10mg/kg PLX4032 was used, and for C57BL/6 mice, the dose was changed throughout treatment and is indicated on the graph.

A targeted metabolic analysis was performed on the serum of non-tumour-bearing mice to determine the effects of PLX4032 on the systemic metabolism of NSG mice. PLX4032 caused a small increase in carnitine, citrate, glyceraldehyde-3-phosphate, uracil, and N-

acetyl aspartate in the serum (Figure 3.2.2-4). The systemic levels of amino acids such as aspartate and glutamine were not significantly altered by PLX4032 (Figure 3.2.2-4).

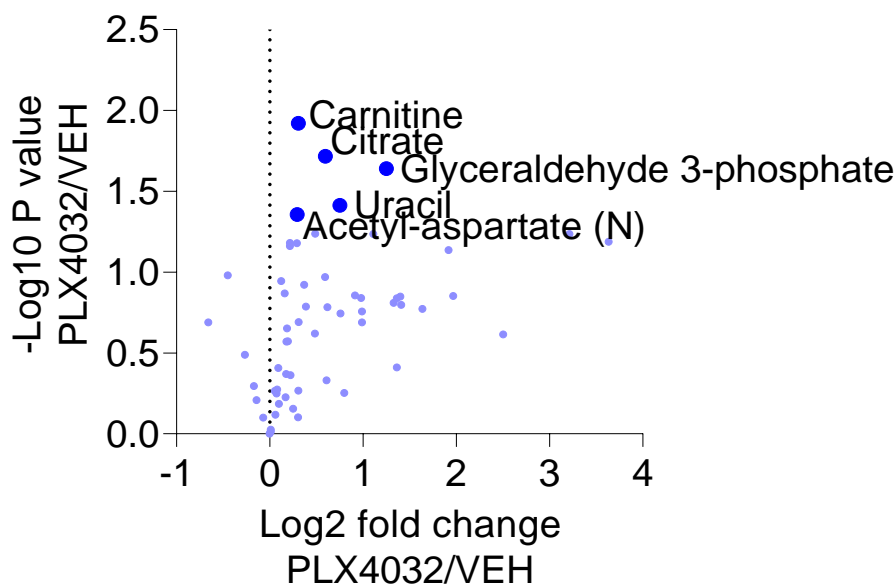


Figure 3.2.2-4: Volcano plots showing the log<sub>2</sub> fold change and -log<sub>10</sub> p value for an unpaired t test comparing the serum levels of 66 metabolites between vehicle and PLX4032 treated NSG mice. Each point represents the calculated log<sub>2</sub> fold change and -log<sub>10</sub> p value for two treatment groups (nmice=6). Larger and darker blue points represent metabolites with statistical significance (p<0.05) in the t test between PLX4032 and vehicle treated mice and are labelled with the name of the metabolite which they represent.

## 3.3 Glutaminase Inhibition Reduces the Growth of BRAF Mutant Melanoma when Given in Combination with BRAF Inhibitors

### 3.3.1 Combined Glutaminase Inhibition and BRAF Inhibition Causes Significantly Reduced Growth of Xenograft Tumours from BRAF Mutant Cell Lines

Having shown that BRAF mutant cells treated with PLX4720 *in vitro* have increased sensitivity to glutaminase inhibition by CB839, we next asked if these results could be recapitulated *in vivo*. To test if CB839 could improve the therapeutic response of human BRAF mutant cell line derived tumours to BRAF inhibitor treatment, A375 or COLO829 cells were injected into NSG mice and treated with CB839, PLX4032, or a combination of the two using the treatment regimes described above. The growth curves for each treatment group were compared (using a CGGC permutation test (Elsó *et al.*, 2004)).

For A375 derived tumours, CB839 did not cause a significant difference in the tumour volume compared to control tumours in mice treated with vehicle. This is consistent with the observation that in Plasmax, A375 cells do not respond to CB839 treatment with an appreciable growth reduction (Figure 3.1.1-3). However, tumours treated with the combination of PLX4032 and CB839 had a significant reduction in their growth rate compared to those treated with PLX4032 alone (Figure 3.3.1-1). This demonstrates that whilst CB839 on its own did not significantly reduce the growth rate of BRAF mutant xenograft tumours, CB839 confers an additional therapeutic benefit

when given in combination with PLX4032. This recapitulates the findings *in vitro*, showing that glutaminase inhibition only caused significant growth inhibition for A375R cells in the presence of a BRAF inhibitor (Figure 3.1.1-4).

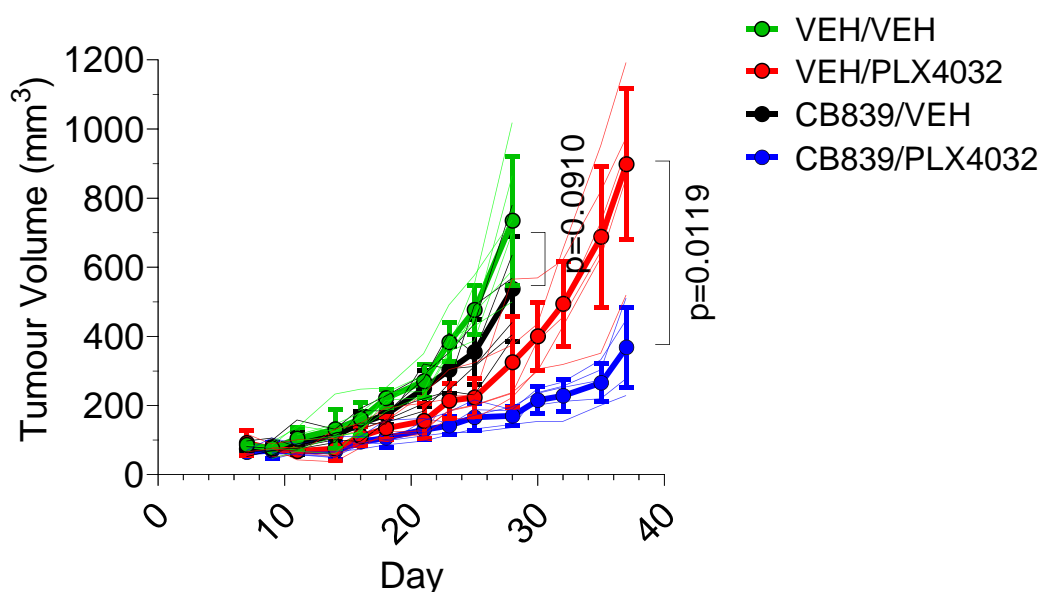


Figure 3.3.1-1: Growth of tumours derived from A375 cells injected subcutaneously into the flank of an NSG mouse treated with 200mg/kg CB839 and/or 10mg/kg PLX4032 as indicated. Cells were injected on day 0, and treatment was started on day 9. Large points joined by thick lines show the average tumour volume for each tumour group (n<sub>mice</sub>=6), whereas thin lines show the tumour volume of each individual tumour, where the colour of each line corresponds to the treatment group. Lines at the end of each graph indicate comparisons made between growth curves, with the p value from each comparison stated.

Whilst A375 derived tumours were not significantly responsive to CB839, COLO829 tumours showed a small but significant decrease in growth when treated with CB839. In this model, the treatment with

CB839 did not enhance the therapeutic effects of PLX4032 treatment (Figure 3.3.1-2).

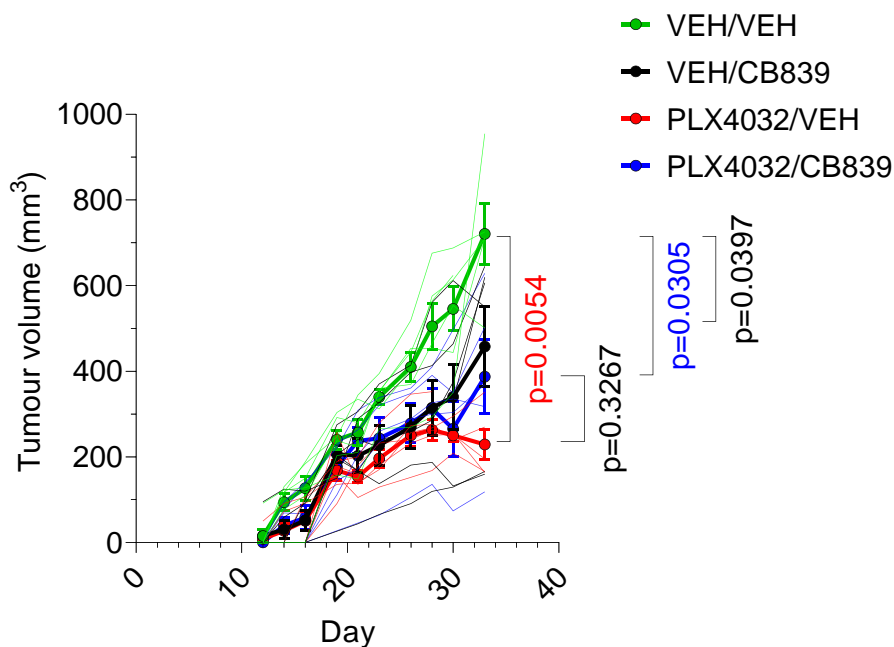


Figure 3.3.1-2: Growth of tumours derived from COLO829 cells injected subcutaneously into the flank of an NSG mouse treated with 200mg/kg CB839 and/or 10mg/kg PLX4032 as indicated. Cells were injected on day 0, and treatment was started on day 9. Large points joined by thick lines show the average tumour volume for each tumour group ( $n_{\text{mice}}=6$ ), whereas thin lines show the tumour volume of each individual tumour, where the colour of each line corresponds to the treatment group. Lines at the end of each graph indicate comparisons made between growth curves, with the p value from each comparison stated.

These results demonstrated that combined CB839 and PLX4032 treatment reduced the growth of A375 derived tumours in severely immunocompromised mice. Interestingly, glutaminase knockdown in T cells *in vivo* diminished Th-17 cell numbers in inflammatory disease and led to initially elevated function of Th-1 cells against leukemia

but led to their exhaustion over time(Johnson *et al.*, 2018). NSG mice are deficient in T cells, therefore we decided to test the effects of combined CB839 and PLX4032 treatment in an immunocompetent model of BRAF mutant melanoma. C57BL/6 mice were injected with YUMM1.7 cells, after which PLX4032 or combined PLX4032 and CB839 treatment was given. A pilot experiment had shown that C57BL/6 mice could tolerate a dose of 20mg/kg of PLX4032 and that it caused a delay in growth of YUMM1.7 derived tumours (Figure 3.2.3-3). The addition of CB839 treatment to PLX4032 treatment resulted in a significant decrease in tumour growth compared to PLX4032 alone (Figure 3.3.1-3). These results demonstrated that the therapeutic benefit of adding CB839 treatment to PLX4032 was conserved across cell models and in the presence of a functional immune system.

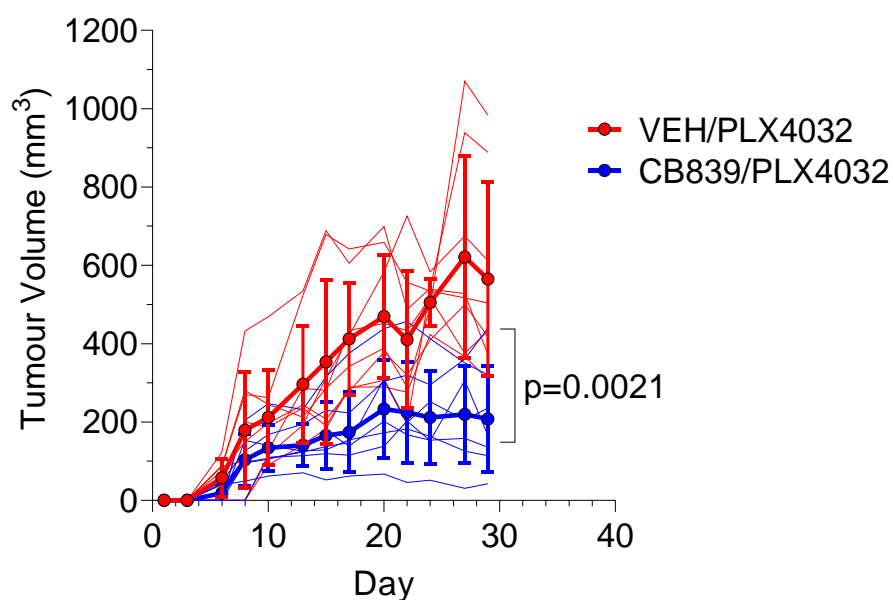


Figure 3.3.1-3: Growth of tumours derived from YUMM1.7 cells injected subcutaneously into the flank of an C57BL/6 mouse treated with 200mg/kg CB839 and/or 20mg/kg PLX4032 as indicated. Cells were injected on day 0, and treatment was started on day 8. Large points joined by thick lines show the average tumour volume for each tumour group ( $n_{\text{mice}}=8$ ), whereas thin lines show the tumour volume of each individual tumour, where the colour of each line corresponds to the treatment group.

### 3.3.2 The Acquisition of BRAF Inhibitor Resistance *in vivo* does not Increase Sensitivity to Glutaminase Inhibition

Having shown that the addition of CB839 to PLX4032 treatment confers a therapeutic advantage to prevent the growth of A375 derived tumours but that CB839 alone does not (Figure 3.1.1-1), we sought to determine whether the acquisition of resistance to a BRAF inhibitor *in vivo* could sensitize melanoma cells to CB839. To test this hypothesis, the daily treatment with PLX4032 was started immediately after injection of A375 cells into the flank of NSG mice, until tumours reached a volume greater than 200mm<sup>3</sup>. Mice were subsequently switched to the three treatment arms of; CB839 and a vehicle for PLX4032; CB839 and PLX4032; or PLX4032 treatment with a vehicle for CB839.

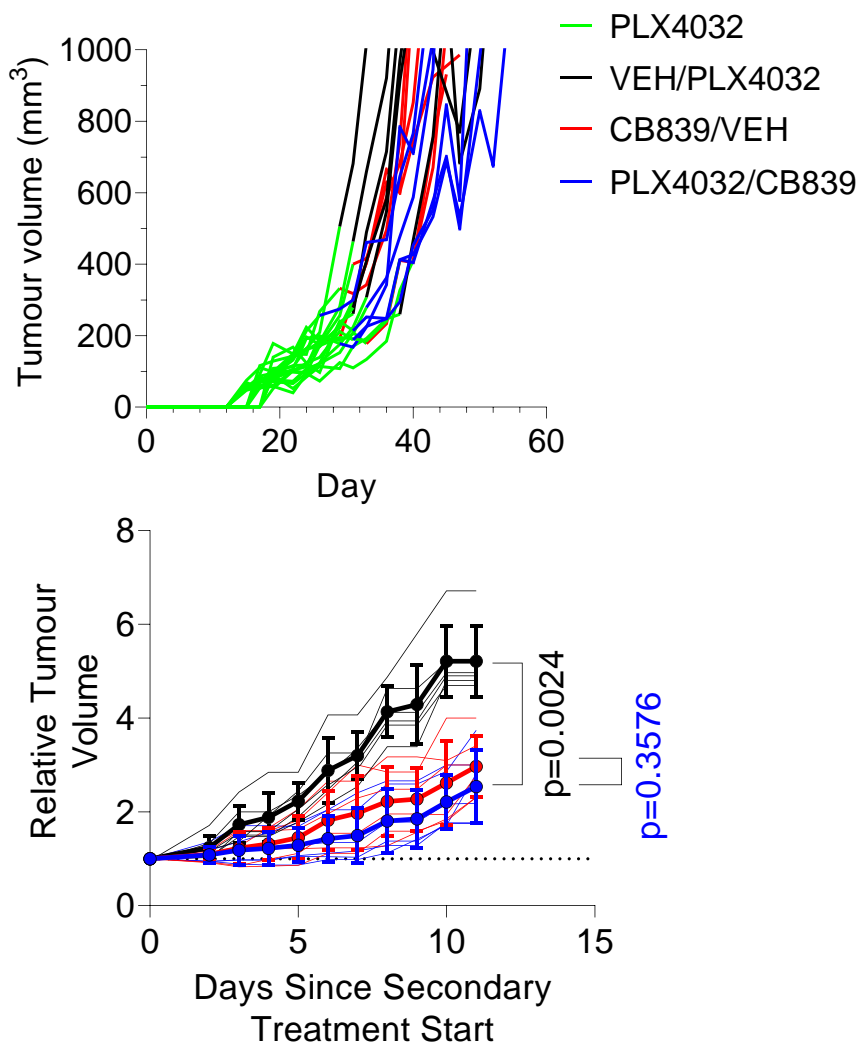


Figure 3.3.2-1: (above) Volume of tumours derived from A375 cells injected subcutaneously into the flank of an NSG mouse treated with 10mg/kg PLX4032 until tumours reached >200mm<sup>3</sup>, before being switched to 200mg/kg CB839 and/or 10mg/kg PLX4032 as indicated. Cells were injected on day 0, and treatment was started on day 0. Each line shows the tumour volume of each individual tumour, where the colour of each line corresponds to the treatment at the time the volume was recorded. (below) 4 day rolling average of relative volume for each tumour. Large points joined by thick lines show the average tumour volume for each tumour group ( $n_{mice}=6$ ), whereas thin lines show the tumour volume of each individual tumour, where the colour of each line corresponds to the treatment group.

Whilst A375 derived tumours in untreated NSG mice took 14-21 days to reach  $>200\text{mm}^3$  (Figure 3.3.1-1) tumours in PLX4032 treated NSG mice took between 24-40 days to reach a comparable size (Figure 3.3.2-1) demonstrating that A375 derived tumours overcame growth inhibition by PLX4032. Since not all tumours were exactly  $200\text{mm}^3$  when switched to secondary treatment, a relative tumour volume was calculated by normalizing each tumour measurement to its respective volume at the start of secondary treatment. A 4-day rolling average was then calculated for each tumour on each day using the relative tumour volume. Tumours grew for a minimum of 11 days subsequently to secondary treatment. After prolonged treatment with PLX4032, the addition of CB839 treatment caused no significant difference in relative tumour growth compared to continued PLX4032 treatment alone. In addition, switching from PLX4032 to CB839 treatment significantly increased tumour growth compared to remaining on PLX4032 treatment (Figure 3.3.2-1).

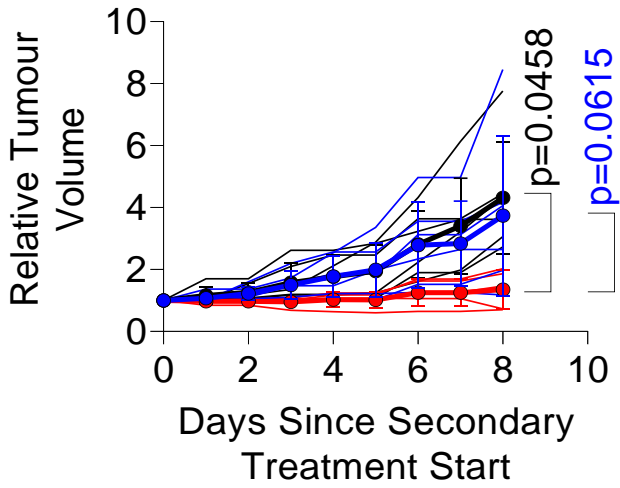
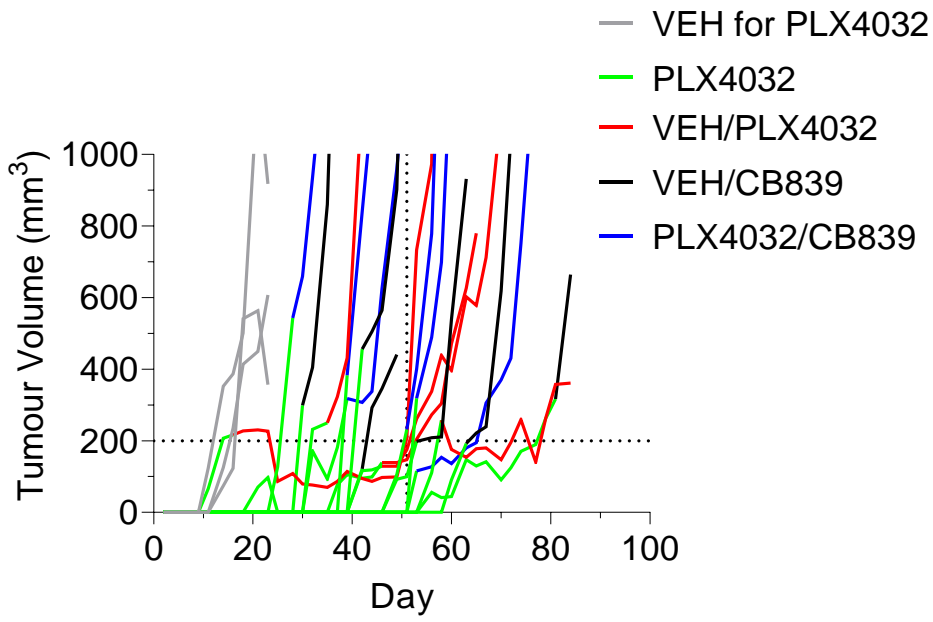


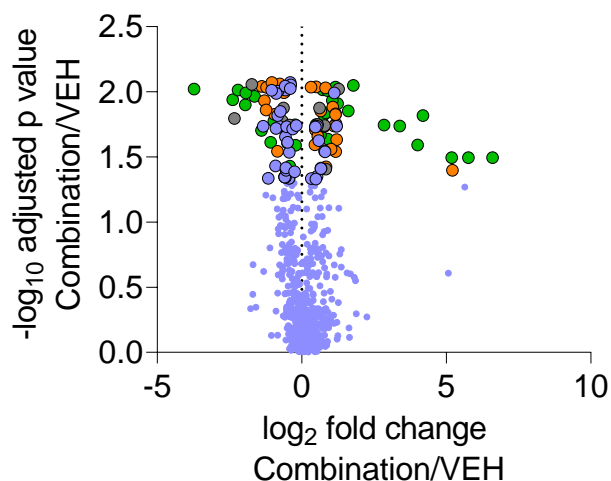
Figure 3.3.2-2: (above) growth of tumours derived from YUMM1.7 cells injected subcutaneously into the flank of a C57BL/6 mouse treated with 20mg/kg PLX4032 until tumours reached  $>200\text{mm}^3$ , before being switched to 200mg/kg CB839 and/or 20mg/kg PLX4032 as indicated. Cells were injected on day 0, and treatment was started on day 0. Each line shows the tumour volume of each individual tumour, where the colour of each line corresponds to the treatment at the time the volume was recorded. (below) 4 day rolling average of relative volume for each tumour. Large points joined by thick lines show the average tumour volume for each tumour group ( $n_{\text{mice}}=6$ ), whereas thin lines show the tumour volume of each individual tumour, where the colour of each line corresponds to the treatment group.

We used a similar approach in the immunocompetent C57BL/6 model grafted with YUMM1.7 cells. These mice, treated with PLX4032 from the day of cell injection, developed tumours  $>200\text{mm}^3$  between 14-65 days after transplantation. Thus, cells were exposed to a BRAF inhibitor for even longer than A375 derived tumours in NSG mice. Despite this, switching from PLX4032 treatment to CB839 treatment was not therapeutically beneficial compared to remaining on PLX4032 treatment. Addition of CB839 treatment to PLX4032 treatment caused a wide range in tumour growth rates but had no significant effect on tumour growth compared to PLX4032 alone, and therefore did not confer a therapeutic advantage over PLX4032 (Figure 3.3.2-2).

## 3.4 PLX4032 and CB839 Rewire the Metabolism of A375 Derived Tumours and Change Glutamine and Citrulline Levels

### 3.4.1 Several Metabolic Features are Altered in Response to PLX4032 and CB839

Having shown that combined CB839 and PLX4032 treatment resulted in a significant clinical benefit for mice bearing A375 derived tumours, we sought to identify metabolites that were altered by the combination treatment. An untargeted metabolomic analysis was carried out on the tumours which detected 1013 metabolic features across all tumour samples. The levels of 120 of these were significantly changed ( $p < 0.05$ , students t test, permutation-based FDR) between combined PLX4032 and CB839 (combination) treatment compared to the vehicle treated tumours (Figure 3.4.1-1). None of these 120 features were significantly changed by PLX4032 or CB839 treatment compared to combination treatment (Figure 3.4.1-2). Indeed, 6 of the 120 features were significantly changed in a comparison of combination treatment compared to PLX4032 treatment (Figure 3.4.1-2) in accordance with the changes in tumour growth (Figure 3.3.1-1), however all of these were identified as various adducts and fragments of CB839.



- adjusted  $p < 0.05$  (Combination/VEH & PLX4032/VEH & CB839/VEH)
- adjusted  $p < 0.05$  (Combination/VEH & PLX4032/VEH)
- adjusted  $p < 0.05$  (Combination/VEH & CB839/VEH)
- Adjusted  $p < 0.05$  (Combination/VEH)  
& Adjusted  $p > 0.05$  (PLX4032/VEH & CB839/VEH)

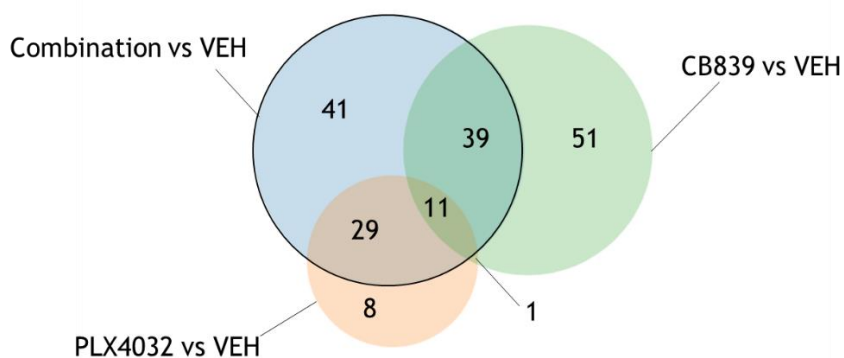


Figure 3.4.1-1: (above) Volcano plot showing the  $-\log_{10}$  adjusted p value and  $\log_2$  fold change in a comparison between combination treatment and vehicle treatment. 1013 metabolic features were reported by Compound Discoverer 3.3.1. Hits with  $p \text{ value} < 0.05$  ( $n=120$ ) (students t test, permutation-based FDR) for the comparison of combination vs vehicle treatment are enlarged and circled in black. Hits are coloured based on their significance in the comparison of PLX4032 vs vehicle and CB839 vs vehicle treatment. (below) Venn diagram showing the number of hits found in each of the three comparisons highlighted in the volcano plot. Diagram produced using <https://www.meta-chart.com/venn#/display>.

Despite this, 41 of the 120 features were found not to be significantly changed by PLX4032 or by CB839 alone compared to the vehicle treatment (Figure 3.4.1-2). This aligned with the fact that combined CB839 and PLX4032 treatment decreased the growth of the tumours in response to combination treatment more than either treatment alone (Figure 3.3.1-1). These features were annotated using a combination of in-house retention time (RT) matched standards and MS2 spectra, as well as MS2 spectra from online spectral libraries such as Thermo's mzcloud and the accurate mass library - chemspider. This resulted in a list of features with varying degrees of confidence in their annotation. Those identified at the highest confidence level are shown in a heatmap and table of identities (Table 3.4.1-1) (Figure 3.4.1-3).

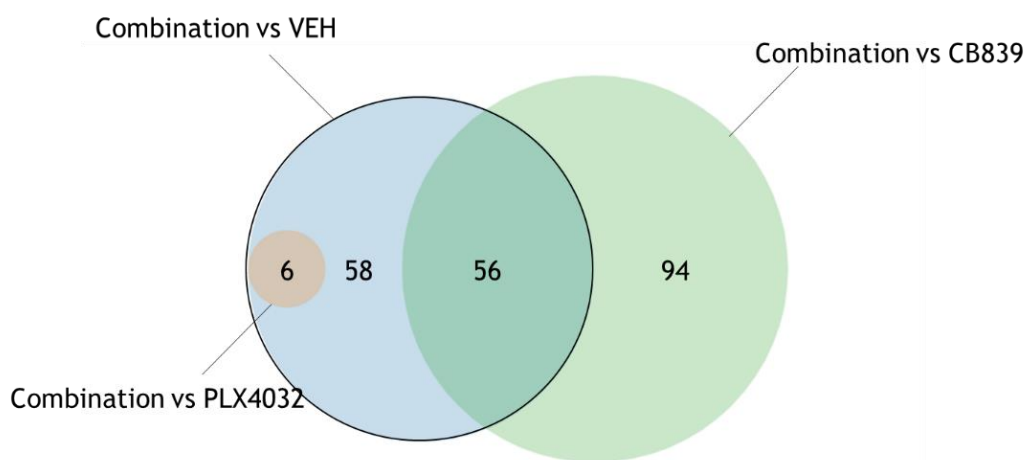


Figure 3.4.1-2: Venn diagram showing the number of hits that were significant ( $p < 0.05$ , students t test, permutation-based FDR) between combination treatment against vehicle treatment, combination against CB839 treatment and combination against PLX4032 treatment. Diagram produced using <https://www.meta-chart.com/venn#/display>.

| RT    | m/z      | Identity                                   | Confidence | log <sub>10</sub><br>adjusted p<br>value | -log <sub>2</sub> fold change<br>(combination vs vehicle) |
|-------|----------|--|------------|--|---|
| 7.109 | 173.0927 | N-acetylnornithine                         | 1a         | 2.013                                    | -1.042  |
| 9.845 | 223.0746 | Cystathionine                              | 1a         | 1.817                                    | -0.830  |
| 9.491 | 179.0557 | Myo Inositol                               | 1a         | 2.013                                    | -0.568  |
| 10.51 | 305.0977 | N-acetyl-aspartyl-glutamate                | 1a         | 1.732                                    | -0.526  |
| 9.884 | 168.9908 | Dihydroxyacetone Phosphate                 | 1a         | 1.609                                    | -0.499  |
| 8.7   | 174.0403 | N-acetyl-aspartate                         | 1a         | 2.052                                    | -0.378  |
| 6.578 | 189.1233 | N-acetyl-lysine                            | 1a         | 1.387                                    | -0.248  |
| 8.717 | 106.0499 | Serine                                     | 1a         | 1.731                                    | 0.473   |
| 8.388 | 131.0462 | Asparagine                                 | 1a         | 1.736                                    | 0.528   |
| 9.376 | 243.0275 | 2-deoxyglucose-6-phosphate                 | 1b         | 1.736                                    | -1.337  |
| 8.276 | 218.0668 | O-succinyl-homoserine                      | 1b         | 1.735                                    | -0.784  |
| 1.589 | 115.0765 | Hexanoate                                  | 1b         | 1.417                                    | -0.547  |
| 8.7   | 130.0509 | 4-hydroxyproline                           | 1b         | 2.071                                    | -0.393  |
| 13.31 | 137.071  | 1-Methylnicotinamide/ 6-Methylnicotinamide | 1b / 2     | 1.735                                    | 1.207   |

Table 3.4.1-1: Table depicting 41 metabolic features significantly different (students t test, permutation based FDR adjusted p value <0.05) (see section 1.4.4) between vehicle and combination treated tumours and not between vehicle and PLX4032 or to CB839 treated tumours. Metabolic features are ranked by evidence level for metabolite identification where the grading is as follows: 1a - Confirmed by standard (MS2 and RT); 1b - Confirmed by standard (mass and RT); 2 Tentative Candidate (Present in MS2 spectra)

This analysis selected features whose levels were significantly changed from vehicle treatment by combination treatment and not by PLX4032 or by CB839. On a closer inspection of the data, it was evident that 27 of these features also had a greater difference in fold change in response to combination treatment than PLX4032 or CB839. The features identified as 2-deoxyglucose-6-phosphate, n-acetylornithine, succinyl homoserine, myo inositol and hexanoate were decreased by combination treatment, and Serine, Asparagine and (1 or 6) methyl nicotinamide were increased (Figure 3.4.1-4). A more in-depth analysis is required to see how these changes relate to other metabolites upstream and downstream in their respective metabolic pathways as well as to changes in the systemic metabolism. However, given that their levels are significantly changed by combination treatment, and not in CB839 or PLX4032 treatment it is plausible that their levels may relate to the observed greater growth inhibition under combination treatment (Figure 3.3.1-1).

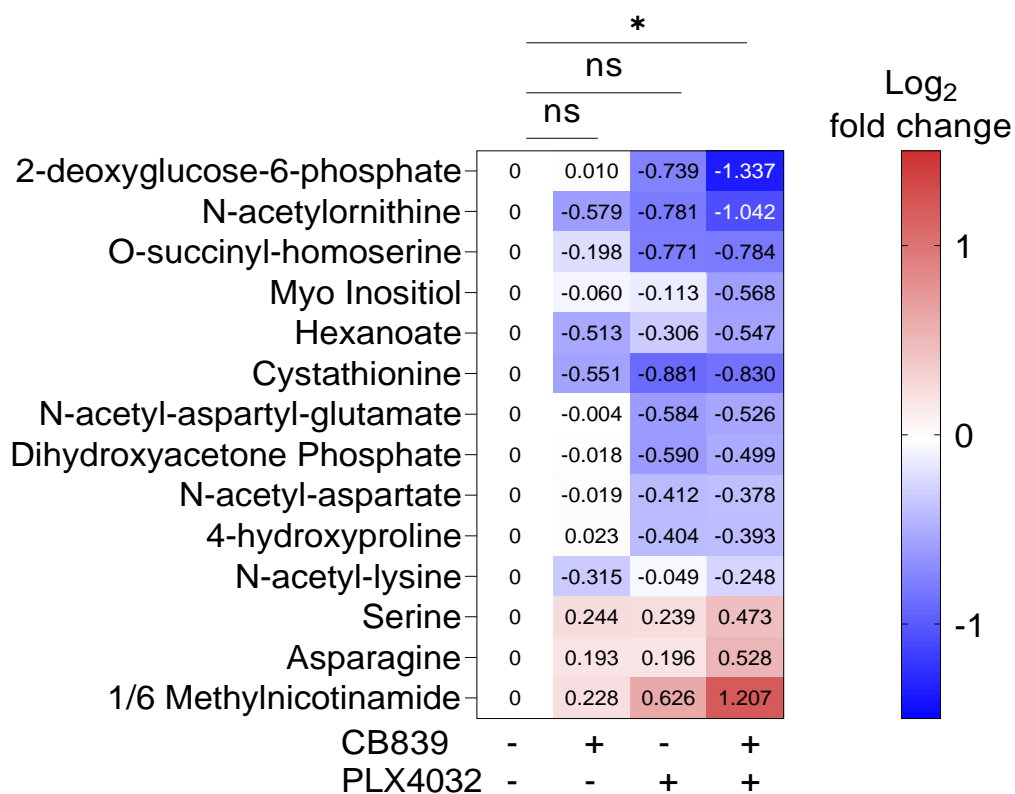


Figure 3.4.1-3: Heatmap showing the Log<sub>2</sub> fold change of 8 features changing significantly (students t test, permutation-based FDR adjusted p value <0.05) between vehicle and combination treated tumours and not between vehicle and PLX4032 or to CB839 treated tumours. All features are identified with an RT and MS2 match to a standard.

### 3.4.2 PLX4032 Causes Metabolic Rewiring, Resulting in Changes in Aspartate, Glutamine and Citrulline.

Following the observation that glutaminase inhibition in BRAF inhibitor resistant cells *in vitro* depletes aspartate, the levels of aspartate in A375 derived tumours treated with PLX4032 and CB839 were measured (Figure 3.4.2-1). Glutaminase inhibition significantly decreased, and BRAF inhibition inversely increased levels of aspartate in the tumour. An increase in aspartate was observed in

the tumours treated with the drug combination, compared to vehicle treated tumours (Figure 3.4.2-1). This contrasted to the *in vitro* results, where, under glutaminase inhibition, BRAF inhibitor resistant cells grown in the presence of BRAF inhibition had decreased levels of aspartate compared to parental cells (Figure 3.1.3-2). As shown previously in tumour-free mice, serum aspartate levels were not increased by PLX4032 treatment (Figure 3.4.2-1). Therefore, the increase in tumour aspartate cannot be attributed to systemic effects of PLX4032 and demonstrates that BRAF inhibition alone can cause metabolic rewiring.

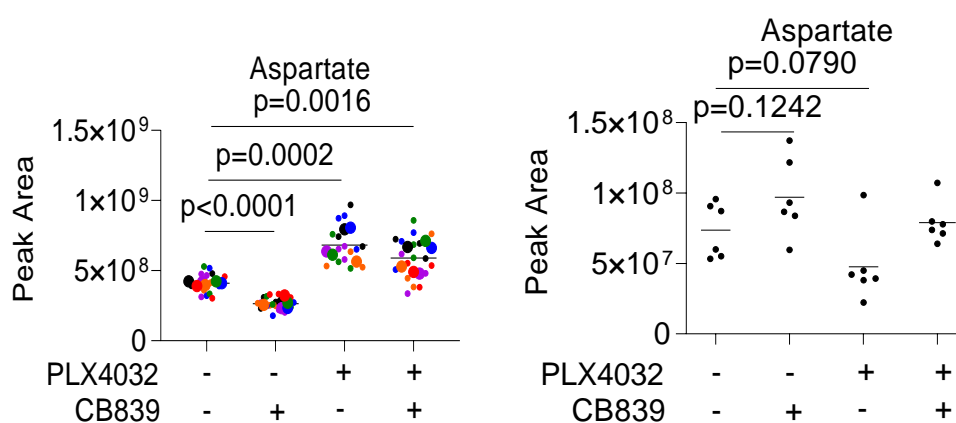


Figure 3.4.2-1: Aspartate levels measured from tumour tissue (left) or serum (right) taken from NSG mice that were subcutaneously injected with A375 cells and treated with PLX4032, CB839 or a combination of the two. Samples were taken at endpoint and metabolite levels were measured using LC-MS. For tumour samples, large points represent one tumour, which was generated from an average of three tumour fragments in the same colour, represented by small points ( $n_{\text{tumours}}=6$ ,  $n_{\text{fragments}}=3$ ). For serum, points represent serum from one mouse, ( $n_{\text{mice}}=6$ ). Lines above groups represent the p value from an unpaired t test performed between each tumour or serum sample.

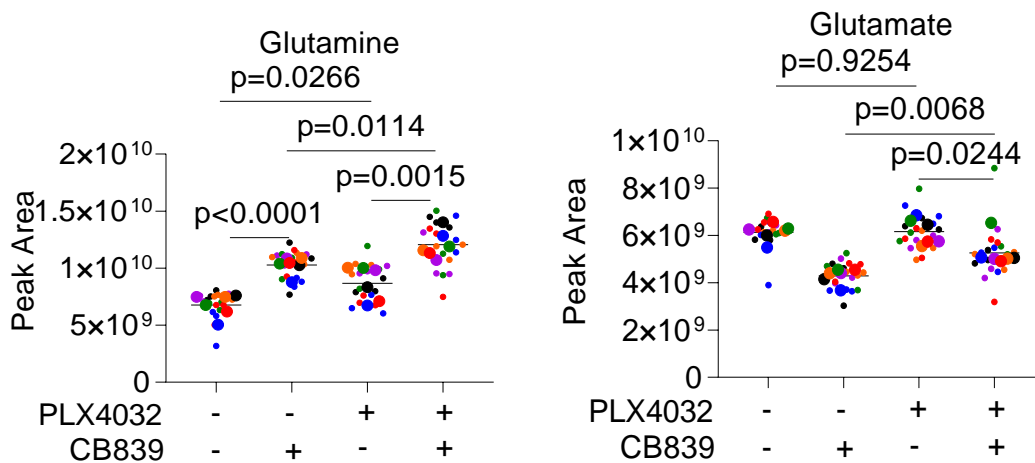


Figure 3.4.2-2: Glutamine (left) and glutamate (right) levels measured from tumour tissue taken from NSG mice that were subcutaneously injected with A375 cells and treated with PLX4032, CB839 or a combination of the two. Samples were taken at endpoint and metabolite levels were measured using LC-MS. Large points represent one tumour, which was generated from an average of 3 tumour fragments in the same colour, represented by small points ( $n_{\text{tumours}}=6$ ,  $n_{\text{fragments}}=3$ ). Lines above groups represent the p value from an unpaired t test performed between each tumour.

Having found that aspartate levels did not follow the same response pattern as the *in vitro* results, we measured the levels of glutamine and glutamate to see how these key glutaminolysis intermediates responded to PLX4032 and CB839 treatment in the tumours. This showed that glutamine levels were increased, and glutamate levels were decreased in response to CB839 compared to vehicle treatment (Figure 3.4.2-2). In addition, glutamine levels were increased in response to PLX4032 treatment compared to vehicle treatment, and glutamate levels were increased in combination treated tumours compared to CB839 treated tumours. This result contrasted to the *in vitro* results, which showed that BRAF inhibitor resistant cells grown in the presence of PLX4720 had no difference in their levels of

glutamine compared to parental cells (Figure 3.1.3-1). This also suggested that PLX4032 affected use of glutaminase.

To determine if levels of glutamine or glutamate had been changed by systemic levels of these metabolites, the levels of glutamine and glutamate were measured in the serum in response to PLX4032 and CB839. This showed that CB839 increased the levels of glutamine in the serum but did not decrease levels of glutamate. In addition, PLX4032 did not significantly change the levels of glutamine in the serum as had been the case in non-tumour bearing mice (Figure 3.2.2-3). However, PLX4032 decreased serum glutamate so that glutamate levels in the serum of mice treated with the combination were significantly lower than in mice treated with CB839 only (Figure 3.4.2-3). Together these results demonstrate that PLX4032 causes metabolic rewiring that results in an increase in tumour glutamine and a decrease in systemic glutamate. It is not clear whether the changes in these two metabolites are related, however these results could be indicative of PLX4032 reducing the use of glutaminase, such that the tumour reduces its secretion of glutamate.

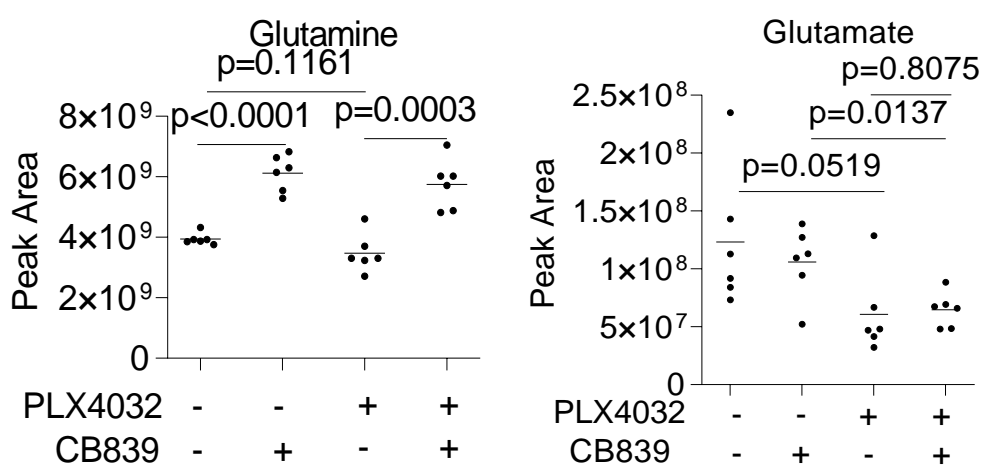


Figure 3.4.2-3: Glutamine (left) and citrulline (right) levels measured from serum taken from NSG that were subcutaneously injected with A375 cells and treated with PLX4032, CB839 or a combination of the two. Samples were taken at endpoint and aspartate levels were measured using LC-MS. Each point represents serum from one mouse, ( $n_{\text{mice}}=6$ ). Lines above groups represent the p value from an unpaired t test.

Having shown that metabolic rewiring occurs in response to PLX4032 and causes changes in the levels of glutamine and aspartate we used our list of in-house standards to determine other metabolites whose levels were changed in response to PLX4032 treatment. We found several metabolites, whose levels were changed in response to PLX4032 treatment (Figure 3.4.1-4). This included a reduction in citrulline, whose levels were also decreased by CB839 (Figure 3.4.2-5).

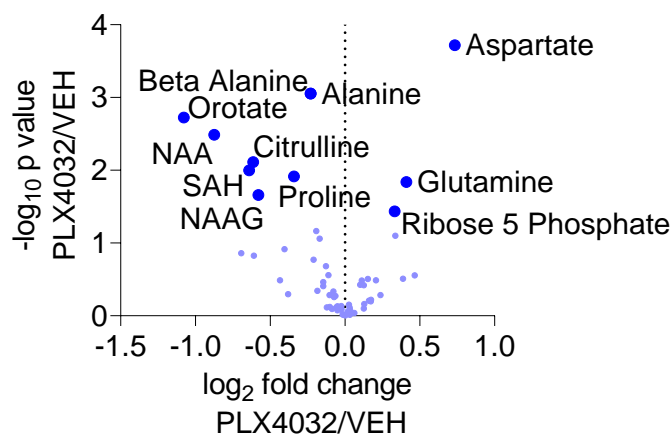


Figure 3.4.2-4: Volcano plot showing the  $\log_2$  fold change and  $-\log_{10}$  p value of a comparison of the levels of 66 metabolites measured in tumour samples between PLX4032 treatment and vehicle treatment. Samples were taken at endpoint and metabolite levels were measured using LC-MS. The comparison was run by performing an unpaired t test between two groups of tumours, for which a metabolite level was generated from an average of 3 tumour fragments in the same tumour ( $n_{\text{tumours}}=6$ ,  $n_{\text{fragments}}=3$ ). Metabolites whose levels are significant ( $p<0.05$ ) are labelled with their identity, including S-adenosyl-homocysteine (SAH), N-acetyl-aspartate (NAA), N-acetyl-aspartyl-glutamate (NAAG).

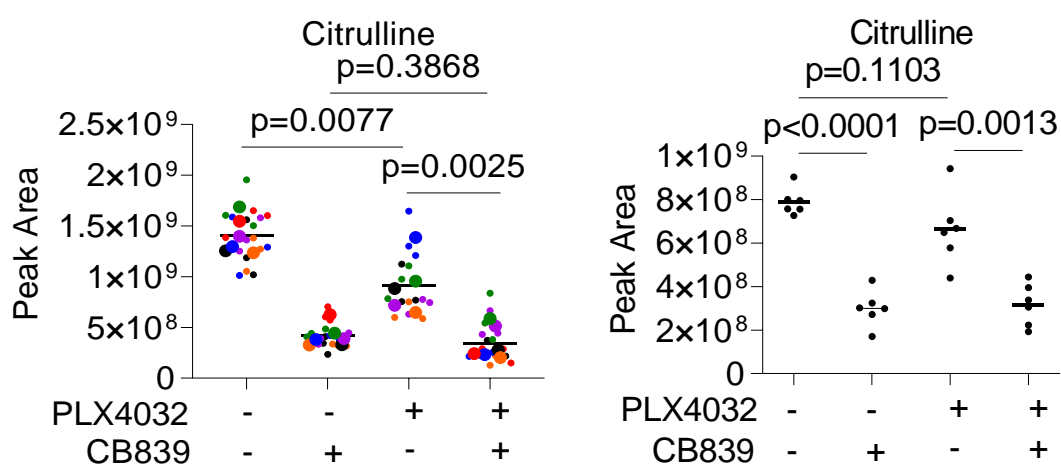


Figure 3.4.2-5: Citrulline levels measured from tumour tissue (left) or serum (right) taken from NSG mice that were subcutaneously injected with A375 cells and treated with PLX4032, CB839 or a combination of the two. Samples were taken at endpoint and metabolite levels were measured using LC-MS. For tumour samples, large points represent one tumour, which was generated from an average of three tumour fragments in the same colour, represented by small points ( $n_{\text{tumours}}=6$ ,  $n_{\text{fragments}}=3$ ). For serum, points represent serum from one mouse ( $n_{\text{mice}}=6$ ). Lines above groups represent the p value from an unpaired t test performed between each tumour or serum sample.

As in non-tumour bearing mice, citrulline levels were significantly decreased in the serum in response to CB839 treatment, but not in response to PLX4032 treatment (Figure 3.4.2-5). This showed that the

changes in citrulline in response to CB839 but not PLX4032 may be at least in part caused by changes in the levels of systemic citrulline. Therefore, this demonstrated that the metabolic rewiring caused by PLX4032 decreased the levels of tumour citrulline. Having shown that PLX4032 and CB839 caused a decrease in citrulline specifically in tumours, we tested whether PLX4032 could affect ammonia metabolism. Thus, we measured the levels of urea cycle intermediates argininosuccinate, arginine and ornithine in the tumours and serum of mice treated with PLX4032 and CB839 (Figure 3.4.2-6).

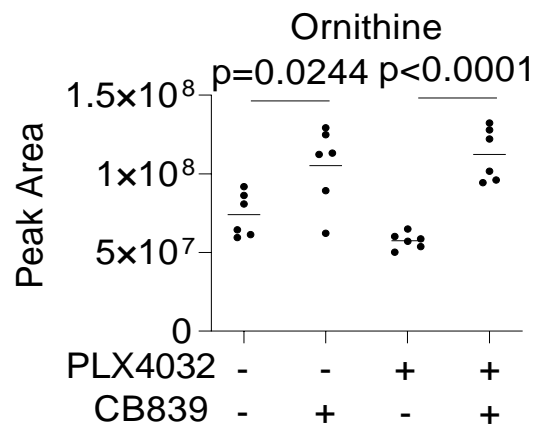
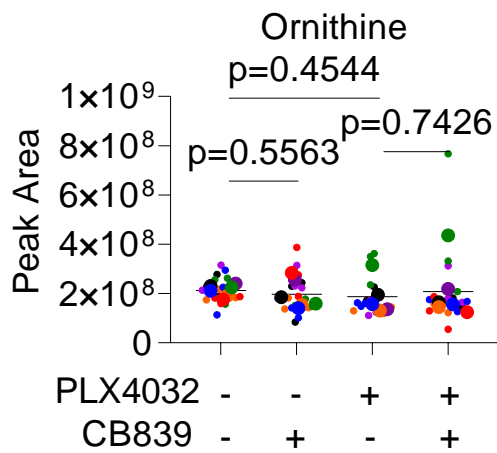
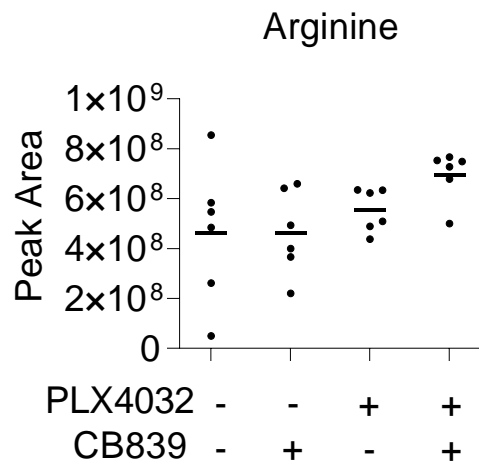
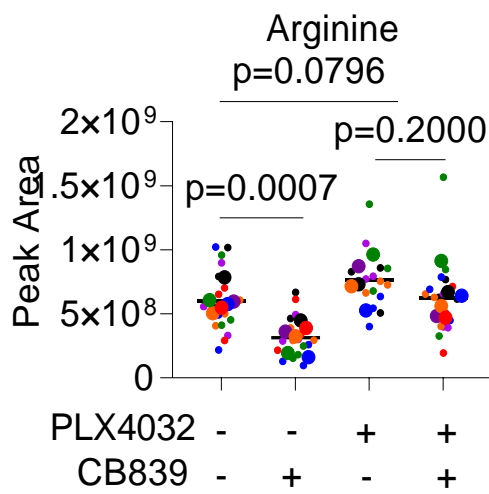
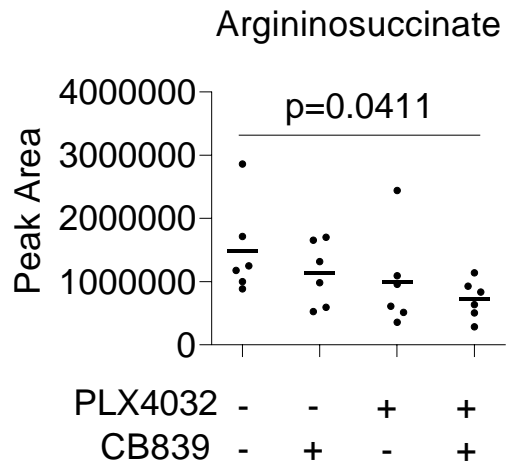
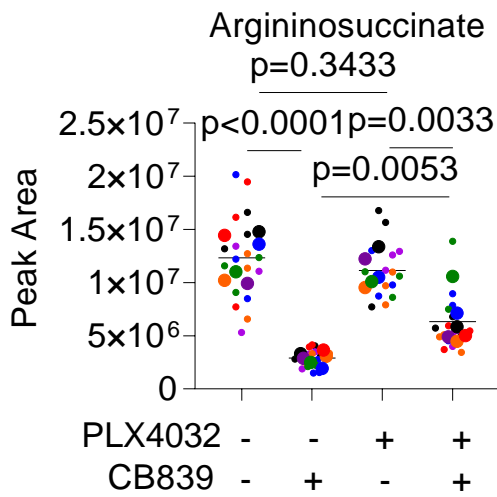


Figure 3.4.2-6: From top to bottom: Ornithine, Arginine and Argininosuccinate levels measured from tumour tissue (left) or serum (right) taken from NSG mice that were subcutaneously injected with A375 cells and treated with PLX4032, CB839 or a combination of the two. Samples were taken at endpoint and metabolite levels were measured using LC-MS. For tumour samples, large points represent one tumour, which was generated from an average of three tumour fragments in the same colour, represented by small points ( $n_{\text{tumours}}=6$ ,  $n_{\text{fragments}}=3$ ). For serum, points represent serum from one mouse ( $n_{\text{mice}}=6$ ). Lines above groups represent the p value from an unpaired t test performed between each tumour or serum sample

The levels of argininosuccinate, and arginine were decreased in response to CB839 treatment in the tumour, but not in the serum. In addition, PLX4032 did not significantly change the levels of any of these three urea cycle intermediates in the tumour. However, addition of PLX4032 to CB839 treatment resulted in significantly higher levels of argininosuccinate than CB839 treatment alone (Figure 3.4.2-6). This showed that PLX4032 could directly affect the levels of citrulline and could also affect the change in the levels of argininosuccinate in response to CB839. These results suggested that the metabolic rewiring caused by PLX4032 may affect the use of the urea cycle.

Given previous reports that the urea cycle enzyme, ASS1 could be epigenetically silenced in melanoma (Li *et al.*, 2016), ASS1 was stained for in A375 derived tumours. This revealed that A375 derived tumours have regions in which cells expressed human ASS1 in the cytosol regardless of PLX4032 and CB839 treatment (Figure 3.4.2-7). There was no clear difference in the area or intensity of ASS1 staining based on treatment across all tumours.

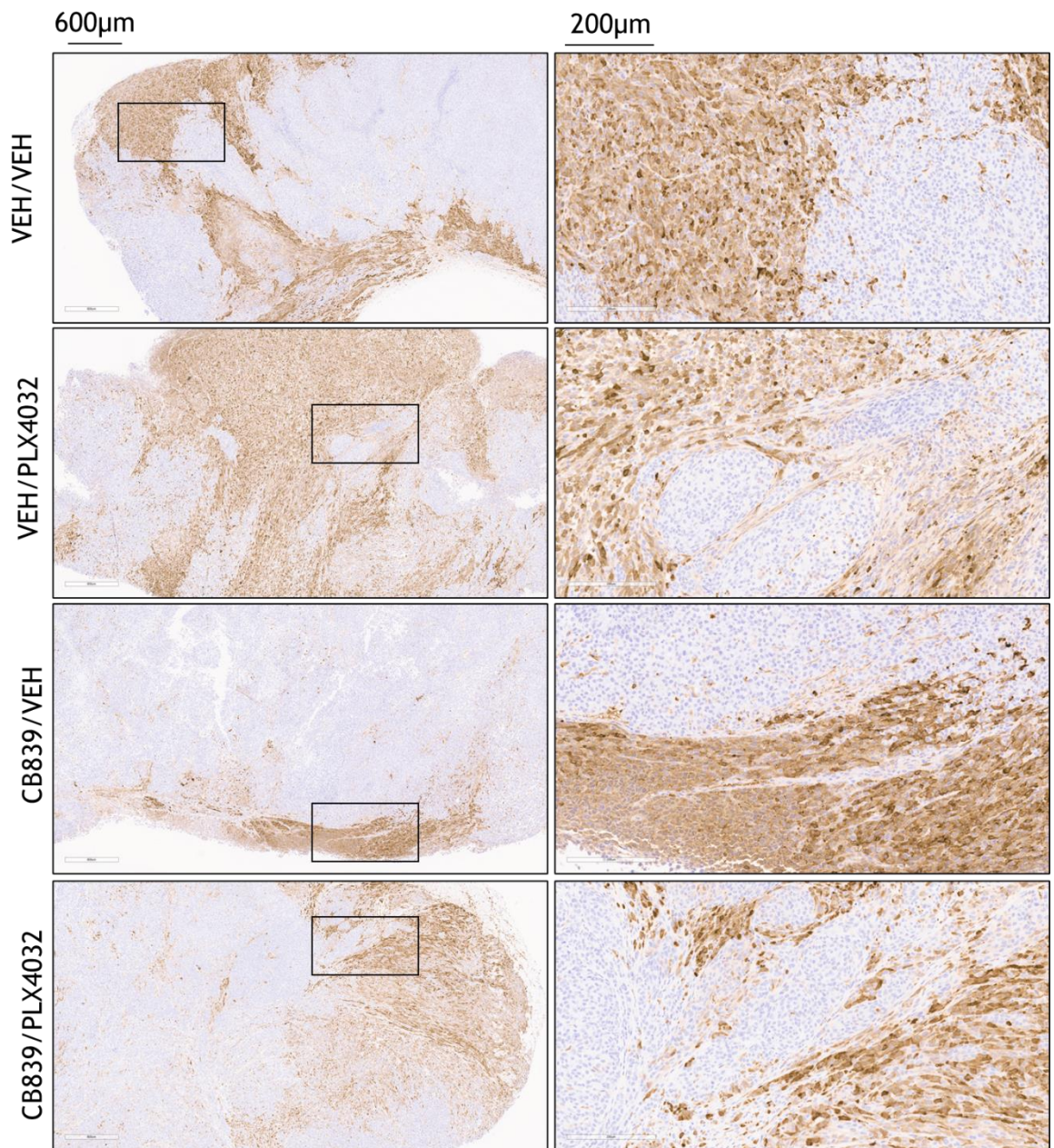


Figure 3.4.2-7: Microscope images of ASS1 immunohistochemical staining in tumours generated from a subcutaneous injection of A375 cells in an NSG mouse and treated with PLX4032, CB839 or a combination of the two. Images are taken at 4x magnification (left) and at 10x magnification (right) with the region of the image taken at 20x outlined within the image taken at 4x. Scale markers are shown at the top of each column of images.

Finally, we measured the levels of ammonia in the serum of mice treated with PLX4032, CB839 and combined PLX4032 and CB839 treatment. The results revealed a trend towards a decrease in the

levels of ammonia in the serum of tumour bearing mice treated with PLX4032. The combination treatment further decreased the levels of circulating ammonia, such that it reached statistical significance compared to vehicle treated controls (Figure 3.4.2-6). Taken together with the reduced level of citrulline specific to tumours, this suggested that PLX4032 could modulate the activity of the urea cycle.

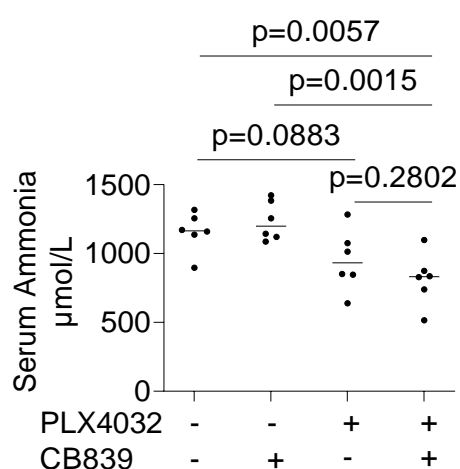


Figure 3.4.2-8: Serum ammonia levels from NSG mice that were subcutaneously injected with A375 cells and treated with PLX4032, CB839 or a combination of the two. Samples were taken at endpoint and aspartate levels were measured using an Arkray ammonia test strip kit. Points represent serum from one mouse, ( $n_{mice}=6$ ). Lines above groups represent the p value from an unpaired t test performed between each serum sample in GraphPad prism 9.4.1.

### 3.4.3 PLX4032 Reduces Expression of HIF1a targets

To complement the metabolomic analysis of A375 derived tumours treated with PLX4032 and CB839, a transcriptomic analysis was carried out on fragments from the same tumours using RNAseq. The analysis measured the reads for 21,508 genes in all tumours from the four treatment groups. Having shown that PLX4032 could change the levels of citrulline and glutamine, we first examined the expression of GLS, GLUD, ASS1 and ASL to see if PLX4032 affected the expression of these enzymes. GLS, GLUD1 and ASS1 expression was not changed by the treatments, but ASL expression was significantly increased by PLX4032, and increased further by the combination treatment ([Figure 3.4.3-1](#)).

A principal component analysis (PCA) was carried out on the 21,508 genes, demonstrating that principal component 1 (PC1) (explaining 50% of variance) separated the tumour samples based on PLX4032 treatment ([Figure 3.4.3-2](#)). On the other hand, tumour samples from mice treated with CB839 clustered with the control mice. Therefore, PLX4032 influenced the transcription of genes to a greater extent than CB839 treatment.

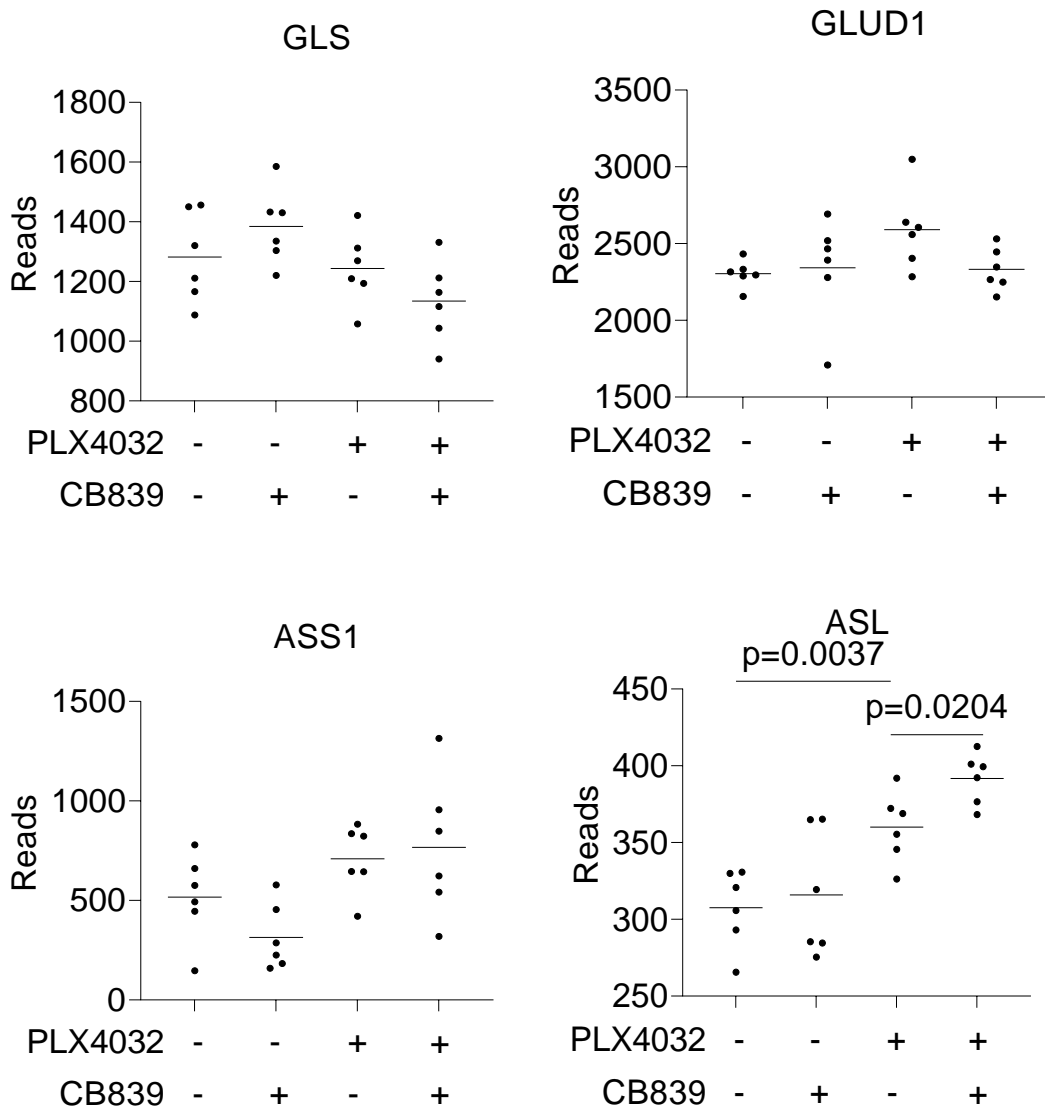


Figure 3.4.3-1: Reads of GLS, GLUD1, ASS1 and ASL as measured by RNAseq in A375 derived tumours treated with the indicated treatment and taken at endpoint. Each point represents one tumour ( $n_{\text{tumours}}=6$ ). Lines above groups represent the p value from an unpaired t test performed between each serum sample

Indeed, a set of differential analyses showed that while PLX4032 caused a significant change in the expression of 2559 genes compared to vehicle treatment, CB839 only significantly changed the expression of 1 gene (Ras responsive element binding protein 1 - RREB1). On the other hand, combination treatment significantly

changed the expression of 4231 genes. Interestingly, only 51% (2165) of which were shared with PLX4032 treatment (Figure 3.4.3-3). A separate comparison of gene expression levels in combination treatment with PLX4032 treatment showed that 43 of these were significantly different (adjusted p value < 0.05 based on the negative binomial distribution using the DESeq2 package version 1.36 (Love, Huber and Anders, 2014)), including pro-growth factors cyclin D1 (CCND1) and an AP1 transcription factor subunit (JUNB) (Figure 3.4.3-4) (Table 3.4.3-1). This demonstrated that CB839 has very little effect on gene expression on its own, but exacerbates the expression of genes regulated by PLX4032, in most cases amplifying the effect of PLX4032 on gene expression.

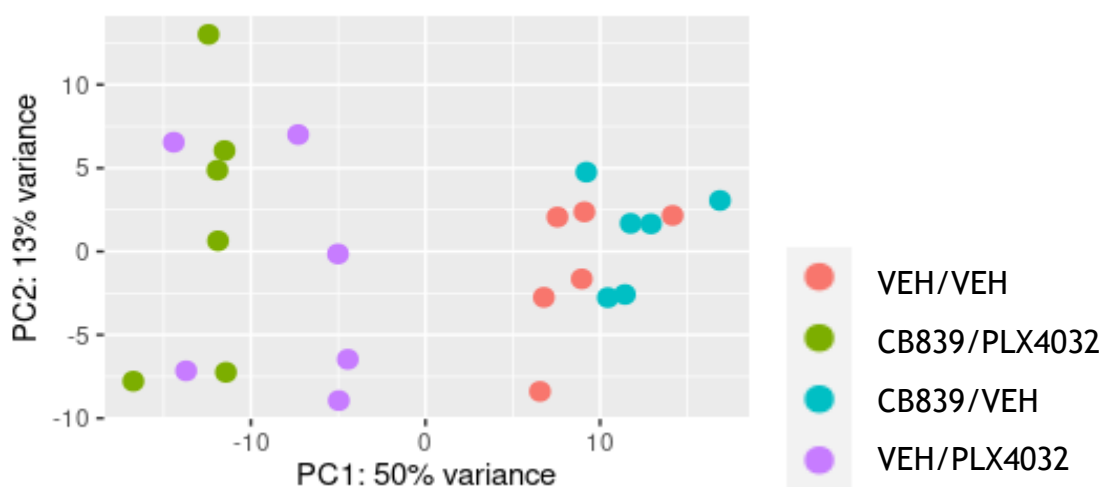


Figure 3.4.3-2: Plot depicting principal component 1 (PC1) and principal component 2 (PC2) of a principal component analysis performed on the reads from 21,508 genes measured in tumours by RNAseq. Tumours were taken from NSG mice that were subcutaneously injected with A375 cells and treated with PLX4032, CB839 or a combination of the two and points are coloured according to treatment.

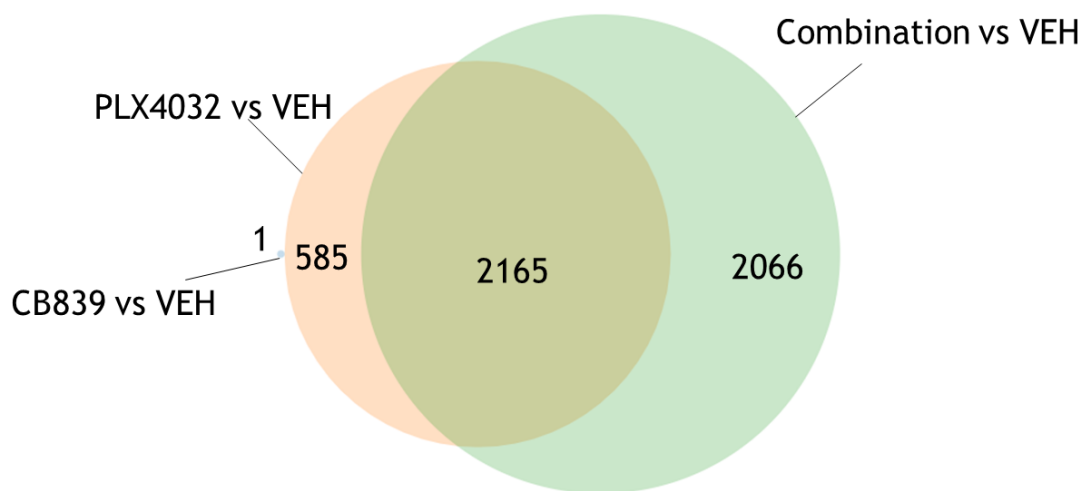


Figure 3.4.3-3: Venn Diagram showing the number of genes that had significantly different (adjusted p value<0.05 based on the negative binomial distribution using the DESeq2 package version 1.36(Love, Huber and Anders, 2014)) expression in the comparison stated. Diagram produced using <https://www.meta-chart.com/venn#/display>.

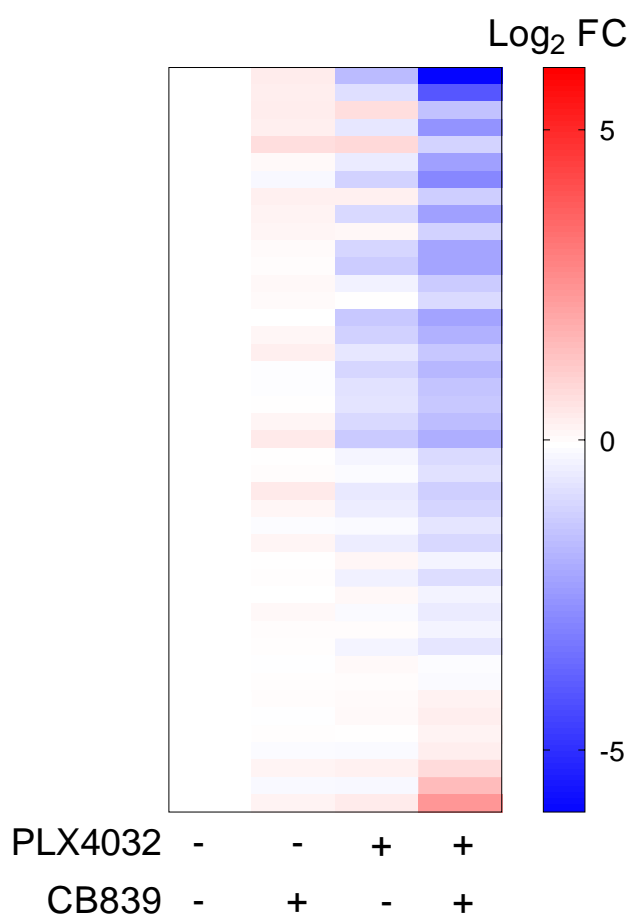


Figure 3.4.3-4: heatmap showing the 43 genes significantly changed in a comparison of combination treatment vs PLX4032 treatment (adjusted p value<0.05 based on the negative binomial distribution using the DESeq2 package version 1.36(Love, Huber and Anders, 2014)). Colours represent the log<sub>2</sub> fold change of the reads for each gene in each sample. Gene names are shown in table 3.4.4-1 in the order in which they appear in the heatmap

| Gene ID         | CB_PLX vs VEH_PLX<br>Fold Change | CB_PLX vs VEH_PLX<br>Adjusted p |
|-----------------|----------------------------------|---------------------------------|
| ENSG00000287430 | -4.3                             | 0.023052                        |
| DCSTAMP         | -3.24                            | 0.027009                        |
| RXRG            | -2.21                            | 0.005918                        |
| CXCL8           | -1.99                            | 0.002769                        |
| COL5A3          | -1.91                            | 0.033003                        |
| EGR3            | -1.78                            | 7.41E-05                        |

|                 |       |          |
|-----------------|-------|----------|
| EGR1            | -1.75 | 0.01861  |
| NR4A1           | -1.52 | 0.005464 |
| EGR2            | -1.35 | 0.012056 |
| PTHLH           | -1.24 | 0.023052 |
| OPRD1           | -1.16 | 0.021693 |
| SPRY4           | -0.94 | 0.01647  |
| BIRC3           | -0.93 | 0.001073 |
| TENT5A          | -0.89 | 0.03683  |
| ABHD17C         | -0.88 | 0.005918 |
| NR4A2           | -0.75 | 0.03683  |
| DUSP5           | -0.75 | 0.040449 |
| SLC20A1         | -0.71 | 0.01706  |
| ICAM1           | -0.71 | 0.023052 |
| SLC5A3          | -0.68 | 0.027009 |
| SH2B3           | -0.67 | 0.03683  |
| ITGB3           | -0.66 | 0.01647  |
| CCND1           | -0.62 | 0.001073 |
| RELB            | -0.62 | 0.03683  |
| COL4A1          | -0.61 | 0.024773 |
| CNKSR3          | -0.57 | 0.040819 |
| MFSD2A          | -0.51 | 0.024705 |
| MCL1            | -0.49 | 0.013932 |
| OSTM1           | -0.48 | 0.025795 |
| JUNB            | -0.47 | 0.005464 |
| B3GNT2          | -0.45 | 0.00747  |
| TNFRSF10B       | -0.36 | 0.046326 |
| XBP1            | -0.34 | 0.002769 |
| YRDC            | -0.33 | 0.03683  |
| DNAJC5          | -0.21 | 0.024773 |
| RPN2            | -0.18 | 0.035689 |
| ENSG00000271254 | 0.2   | 0.016553 |

|           |       |          |
|-----------|-------|----------|
| CNDP2     | 0.261 | 0.023052 |
| AGBL5     | 0.261 | 0.011353 |
| LINC01029 | 0.505 | 0.022328 |
| PCLO      | 0.524 | 0.03683  |
| LIN7A     | 1.782 | 0.021693 |
| CCBE1     | 1.987 | 0.032155 |

Table 3.4.3-1: Table showing the gene names for genes that had a significant difference (adjusted p value < 0.05 based on the negative binomial distribution using the DESeq2 package version 1.36 (Love, Huber and Anders, 2014)) in their expression (n=43) between PLX4032 and combination treatment. The adjusted p value and fold change (calculated based on the adaptive shrinkage model, Apeglm (Zhu, Ibrahim and Love, 2019)) are shown beside each gene.

Having shown that PLX4032 treatment had a profound impact on the expression of global transcription, we sought to determine the groups of genes that PLX4032 affected. An enrichment analysis was carried out by ranking all genes on their  $\pi$ -value (Xiao *et al.*, 2014) ( $\text{Log}_2$  fold change multiplied by  $-\text{Log}_{10}$  adjusted p-value) in a comparison between PLX4032 treatment and vehicle treatment, as well as between combination and vehicle treatment. This found that a gene set associated with the ‘transcription of HIF1 $\alpha$  targets’ was significantly enriched in the genes regulated by PLX4032 treatment ( $-\text{log}_{10}$  adjusted p value=7.11) (Figure 3.4.3-5). This same gene set was even more significantly enriched in the genes regulated by combination treatment ( $-\text{log}_{10}$  adjusted p value=13.14). 29 genes were associated with the enrichment of ‘transcription of HIF1 $\alpha$  targets’ in the combination treatment, 6 of which were increased by PLX4032 and 23 of which were decreased (Figure 3.4.3-6). Among these were included hexokinase (HK2), two glucose transporters (SLC2A1, SLC2A3) and a regulator of pyruvate dehydrogenase (PDK1) which

were all decreased by PLX4032. This demonstrated that PLX4032 decreased the expression of genes involved in glycolytic metabolism, and this effect was exacerbated by the addition of CB839.

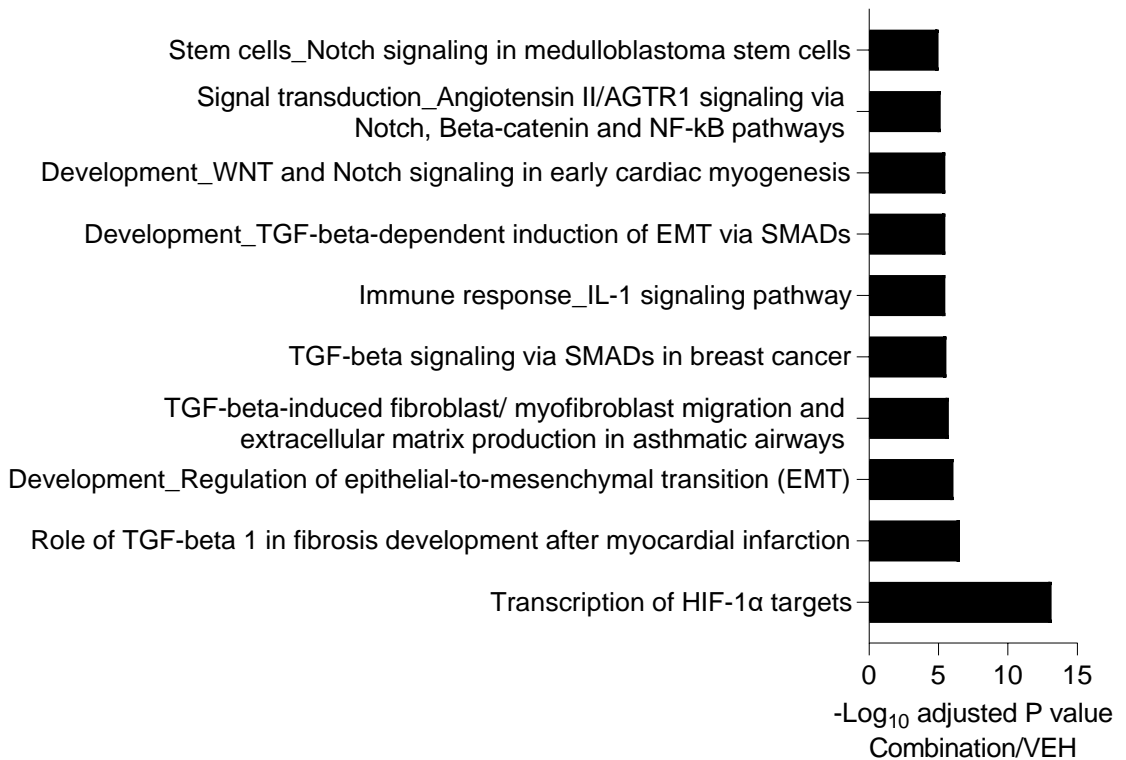
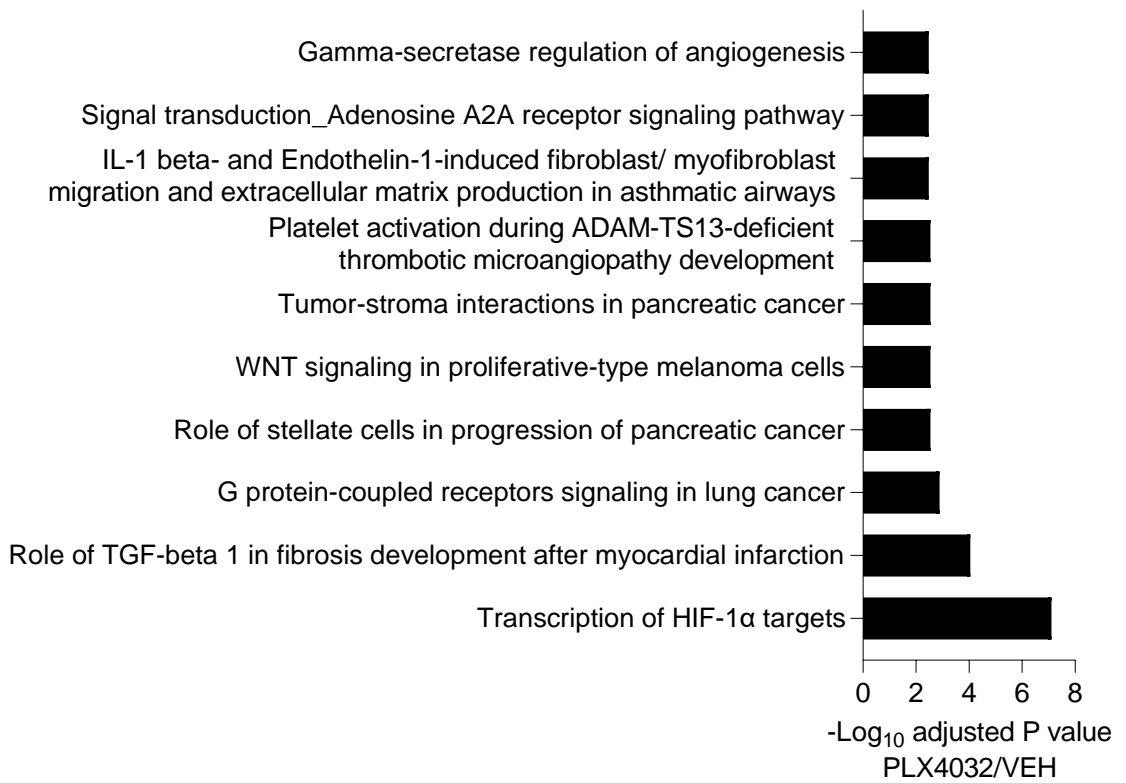


Figure 3.4.3-5: Results of an enrichment analysis performed on genes measured by RNAseq and ranked by their  $\pi$  value in a comparison of PLX4032 against vehicle (above) and combination against vehicle (below) treatment in A375 derived tumours.

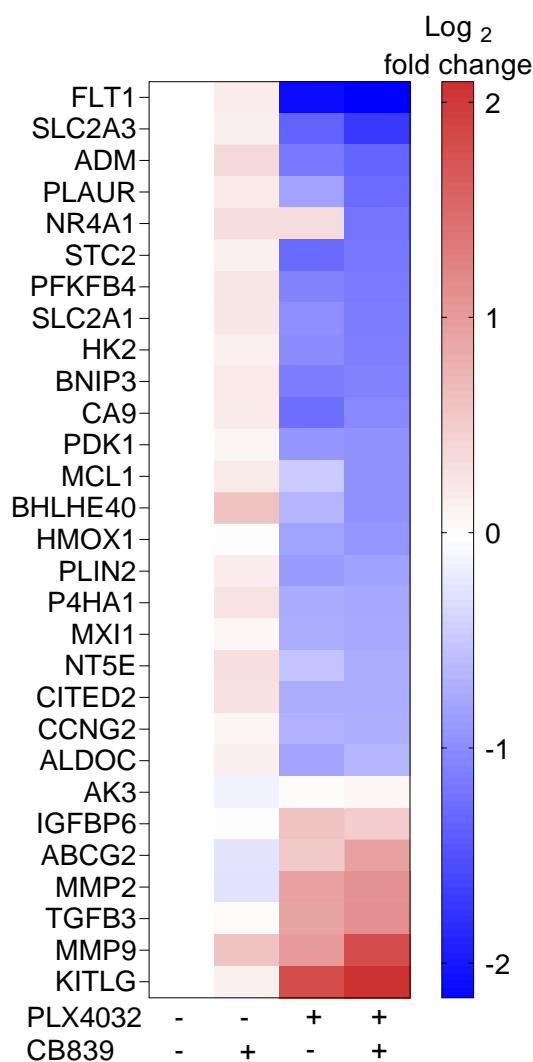


Figure 3.4.3-6: A heatmap of the 29 genes significantly regulated by the combination treatment and attributed to “transcription of HIF1 $\alpha$  targets” in an enrichment analysis. Colours represent average log<sub>2</sub> fold change for the reads of each gene in each treatment group compared to vehicle treated tumours.

Having shown that PLX4032 treatment affected the expression of glycolytic genes, the levels of glucose, glucose-6-phosphate, pyruvate

and lactate were measured in response to PLX4032 and CB839 treatment. These treatments did not significantly change the levels of glucose, glucose-6-phosphate or lactate, but their combination resulted in significant depletion of pyruvate (Figure 3.4.3-7). This demonstrated that the change in expression of glycolytic genes resulted in a decrease in the product of glycolysis - pyruvate.

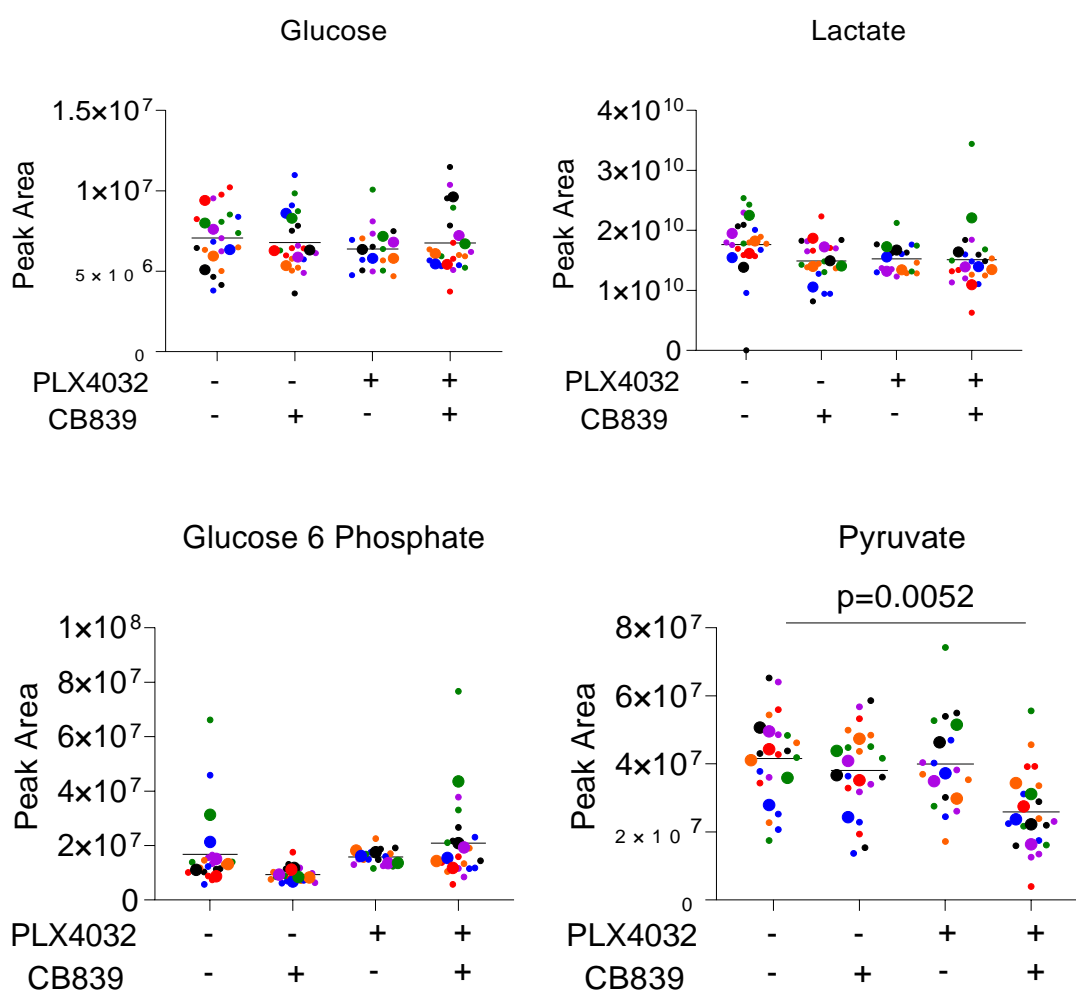


Figure 3.4.3-7: Levels of Glucose, Lactate, Glucose-6-Phosphate and Pyruvate levels measured from tumour tissue taken from NSG mice that were subcutaneously injected with A375 cells and treated with PLX4032, CB839 or a combination of the two. Samples were taken at endpoint and metabolite levels were measured using LC-MS. Large points represent one tumour, which was generated from an average of 3 tumour fragments in the same colour, represented by small points ( $n_{\text{tumours}}=6$ ,  $n_{\text{fragments}}=3$ ). Lines above groups represent the p value from an unpaired t test performed between six tumours in each treatment group.

The reduction in glycolytic genes and in pyruvate suggested a reduction in glycolytic activity. Reduced use of glycolysis would subsequently cause a reduction in ATP generation from the ETC. Thus, to determine if changes in levels of pyruvate resulted in a change in ATP generation, we measured the ratio of ATP/AMP demonstrating that combination treatment reduced the ATP/AMP ratio (Figure 3.4.3-8).

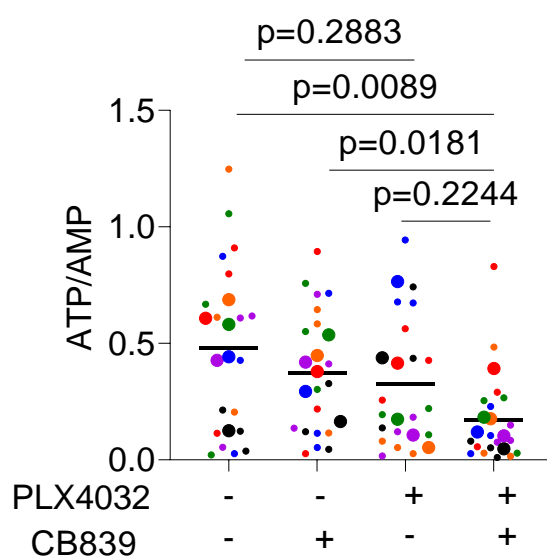


Figure 3.4.3-8: The ratio of ATP to AMP measured from tumour tissue taken from NSG mice that were subcutaneously injected with A375 cells and treated with PLX4032, CB839 or a combination of the two. Samples were taken at endpoint and metabolite levels were measured using LC-MS. Large points represent one tumour, which was generated from an average of 3 tumour fragments in the same colour, represented by small points ( $n_{\text{tumours}}=6$ ,  $n_{\text{fragments}}=3$ ). Lines above groups represent the p value from an unpaired t test performed between the six tumours in each treatment group.

## Chapter 4: Discussion

### 4.1 Inhibition of Glutaminase Causes Greater Growth Inhibition for Cells under BRAF Inhibition

I showed *in vitro* that glutaminase inhibition is more effective at reducing the growth of BRAF inhibitor resistant cells kept in PLX4720, than for their parental counterparts (Figure 3.1.1-3). This effect was maintained in the physiological culture medium, Plasmax™. In addition, BRAF inhibitor resistant cells had increased expression of glutaminase in both DMEM and Plasmax™ (Figure 3.1.1-2), suggesting that these cells have a higher capacity for glutaminase activity. This aligned with the previous experiments, showing that BRAF inhibitor resistant cells maintained in PLX4720 had greater growth inhibition by a first generation glutaminase inhibitor (BPTES), as well as by glutamine starvation (Baenke *et al.*, 2016). Further to this, however, I found that the presence of BRAF inhibition sensitized A375R cells to glutaminase inhibition, even though they had previously been exposed to long term BRAF inhibition (Figure 3.1.1-4). This suggested that in A375R cells, BRAF inhibition directly caused metabolic rewiring that exposed the metabolic vulnerability of glutaminase dependence. Indeed, changes in aspects of the metabolism such as pyrimidine synthesis and one-carbon metabolism were previously shown to occur in response to a short-term exposure to BRAF inhibition in A375 cells (Karki *et al.*, 2021), however other studies investigating the importance of glutamine anaplerosis in the presence of BRAF inhibition have used cells exposed to long-term

BRAF inhibition and have therefore used these models to report findings on BRAF inhibitor resistance (Corazao-Rozas *et al.*, 2013; Baenke *et al.*, 2016; Li *et al.*, 2016).

Results from *in vivo* experiments corroborated this finding by showing that the combination of PLX4032 and CB839 inhibited the growth of A375 and YUMM1.7 derived tumours, compared to PLX4032 treatment alone (Figure 3.3.1-1&3). Therefore, in these models, the addition of a glutaminase inhibitor to BRAF inhibition was therapeutically beneficial. I showed that for A375 derived tumours in the absence of PLX4032, CB839 did not significantly affect tumour growth (Figure 3.3.1-1). In addition, by subjecting xenografted A375 and YUMM1.7 derived tumours to continuous and prolonged treatment with PLX4032 treatment throughout their initial growth phase, I generated tumours that had overcome PLX4032 treatment. This constitutes a model that replicates the growth of BRAF inhibitor resistant melanoma in patients, however I found that these BRAF inhibitor resistant tumours were not sensitized to CB839 treatment (Figure 3.3.2-1&2). Taken together with the *in vitro* results, this demonstrates that the presence of a BRAF inhibitor is required to sensitize BRAF mutant melanoma to glutaminase inhibition. Translationally, these results imply that treatment with glutaminase inhibitors should be given simultaneously with BRAF inhibition to maximize their efficacy. However, it should be noted that in COLO829 derived tumours, growth was inhibited by CB839 regardless of the presence of BRAF inhibition (Figure 3.3.1-2).

## 4.2 *In Vivo* CB839 Treatment Changes Serum Metabolites which has the Potential to Affect its Efficacy

CB839 is currently under clinical trials to determine its efficacy in combination with other targeted and chemotherapeutic agents (Varghese *et al.*, 2021), however its use in combination with PLX4032 had not been investigated. I showed that CB839 treatment could be administered to immunocompromised NSG and immunocompetent C57BL/6 mice in combination with PLX4032 without weight loss or adverse effects (Figure 3.2.2-2). Interestingly, CB839 caused changes in the levels of several amino acids and hexose derivatives in the serum of tumour-free mice, including increased glucose-6-phosphate, fructose-6-phosphate, glutamine, lysine, alanine, proline, asparagine and ornithine (Figure 3.2.1-2). This demonstrated that the effects of CB839 on non-tumour glutaminase, such as that expressed in the kidney (Katt, Lukey and Cerione, 2017) can indirectly change the availability of nutrients available to tumours.

I showed *in vitro*, that changes in the availability of external nutrients may indeed affect the growth response of melanoma to CB839. The commercial media, DMEM which has higher glutamine levels increased the consumption of glutamine and secretion of glutamate (Figure 3.1.2-1). Furthermore, cells in DMEM medium had higher glutaminase activity (Figure 3.1.2-2). Consequentially, culture of A375 cells in DMEM resulted in growth inhibition by CB839, whereas in Plasmax, growth was unaffected (Figure 3.1.1-3).

Therefore, a change in the external availability of metabolites, including increased glutamine, can affect the efficacy of CB839.

Therefore, whilst CB839 was able to exert a significant effect on tumour growth, further consideration of its systemic effects may enable precision medicine to ensure its optimal efficacy. For example, alterations to the diet could counteract the changes caused by CB839 should they be found to constitute a toxicity, or to exacerbate its effects should they be found to increase the efficacy of CB839. In addition, the interaction of the metabolic changes caused by CB839 should be considered when prescribing a combination treatment.

### 4.3 BRAF Inhibition Reduces the Expression of Glycolytic Genes and Increases Dependence on Glutaminolysis

Since BRAF inhibition in combination with glutaminase inhibition could reduce the growth of mutant BRAF melanoma, I investigated how BRAF inhibition affects glutaminase use. I showed that cells under long term BRAF inhibition had higher expression of glutaminase, regardless of the media in which they were cultured (Figure 3.1.1-2). Cells cultured under long term BRAF inhibition did not have a difference in their basal level of glutamine compared to their parental counterparts (Figure 3.1.3-1). However, using glutamine tracing, I showed that cells under long term BRAF inhibition had a lower proportion of glutamate and  $\alpha$ -ketoglutarate directly from glutamine, compared to their parental counterparts (Figure 3.1.3-2&3).

This suggested that cells under long term BRAF inhibition had reduced glutaminase activity.

I showed that cells treated with long-term BRAF inhibition had greater depletion of glutamate and a greater build-up in glutamine under glutaminase inhibition compared to their parental counterparts (Figure 3.1.3-1). Despite this, the proportion of glutamate derived directly from glutamine was significantly reduced by glutaminase inhibition only in COLO829 cells (Figure 3.1.3-2).

Therefore, glutaminase inhibition decreased overall glutamate pools to a greater extent in cells under long term BRAF inhibition. This demonstrates that cells under long term BRAF inhibition are more dependent on glutaminase to maintain their total pools of glutamate and thus TCA cycle intermediates.

*In vivo*, I showed that expression of genes encoding for enzymes and transporters enabling glycolysis were decreased by BRAF inhibition in tumours (Figure 3.4.3-6). Interestingly, the gene signature of HIF1 $\alpha$  expression was made more significant by the addition of glutaminase inhibition (Figure 3.4.3-5). The change in HIF1 $\alpha$  target genes aligns with the fact that expression of HIF1 $\alpha$  is reported to be increased by mutant BRAF in melanoma (Kumar *et al.*, 2007), and thus its inhibition would result in a reduction in HIF1 $\alpha$  activity. In addition, glucose tracing with A375 and COLO829 cells *in vitro* has previously shown the BRAF inhibitor resistant subclones under BRAF inhibition had reduced flux of glucose, although this was for cells cultured in the non-physiological medium, DMEM (Baenke *et al.*, 2016). Indeed, the levels of the glycolytic product, pyruvate and the ratio of ATP/AMP were both decreased *in vivo* by combined PLX4032 and CB839 treatment in tumours (Figure 3.4.3-7&8), suggesting a decrease in glycolytic flux. Whilst I have not demonstrated whether reduced

glycolysis results in increased dependence on glutaminase, a reduced flux of glucose derived carbons into the TCA cycle by BRAF inhibition may indeed exacerbate the need for glutamine anaplerosis (Figure 4.3-1). A reduced flux of glucose derived carbons could not increase the use of the TCA cycle but could increase the dependence on glutamine for oxidative metabolism.

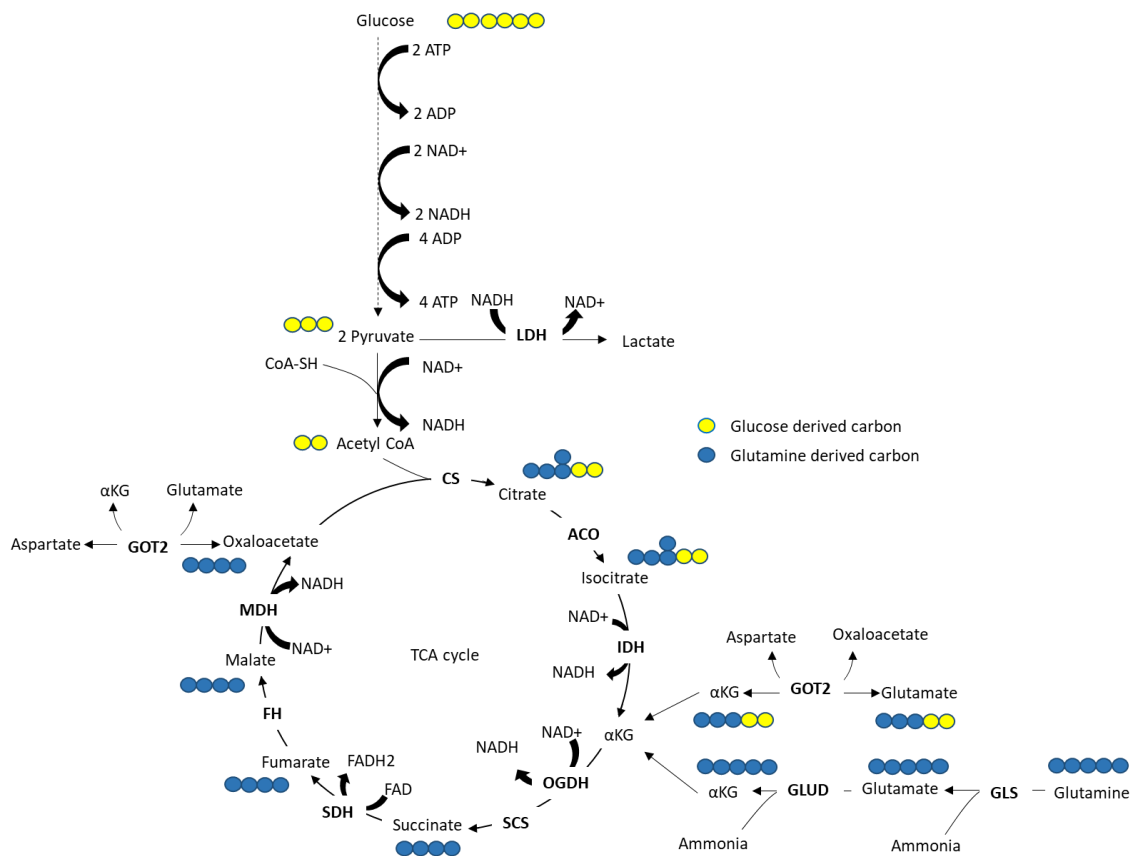


Figure 4.3-1: Diagram depicting how glucose and glutamine derived carbons contribute to the function of the TCA cycle and allow the production of glutamate.

## 4.4 Glutaminase Activity is Required for Aspartate Synthesis and Maintenance of NAD<sup>+</sup>/NADH Homeostasis

I showed that *in vitro* glutaminase inhibition consistently caused a decrease in aspartate more pronounced than in any other proteogenic amino acid (Figure 3.1.4-2). Furthermore, glutamine tracing demonstrated that glutamine derived aspartate was produced in A375, A375R, COLO829 and COLO829R cells, and that it was reduced in response to glutaminase inhibition (Figure 3.1.5-1). I showed that glutaminase inhibition resulted in a reduction in the intermediates of pyrimidine synthesis *in vitro* (Figure 3.1.4-3). This suggested that glutamine derived aspartate was required for nucleotide synthesis. Glutamine derived aspartate has indeed been reported to be essential for malignant cell growth due to its use in nucleotide synthesis (Sullivan *et al.*, 2015; Kodama *et al.*, 2020). Despite this, it was not evident that the synthesis of nucleotides was limiting the proliferation of glutaminase inhibited cells, as indicated by the lack of rescuing activity of exogenously supplied nucleotide precursors (Figure 3.1.4-5).

Nonetheless, 10mM aspartate was able to partially rescue cell growth from glutaminase inhibition (Figure 3.1.5-2). Whilst this is a supraphysiological concentration of aspartate, this amino acid is poorly transported into most mammalian cells (Birsoy *et al.*, 2015; Sullivan *et al.*, 2015). This experiment demonstrated that the reduction in aspartate caused by glutaminase inhibition was detrimental to cell growth. Another function of aspartate is in the malate-aspartate shuttle, which allows the transfer of cytosolic

electrons in the form of NADH (mainly produced by glycolysis) into the mitochondria to be used by the ETC (Alkan *et al.*, 2018). A drop in glutamine derived aspartate may be associated with a lower NAD<sup>+</sup>/NADH ratio through the activity of OGDH and MDH, which require NAD<sup>+</sup> for their activity and are needed to generate glutamine derived oxaloacetate from which to produce aspartate (Figure 4.3-1) (Sullivan *et al.*, 2015; Luengo *et al.*, 2021). In support of this, the NAD<sup>+</sup>/NADH ratio was increased in cells under long term BRAF inhibition and slightly decreased by glutaminase inhibition, suggesting a link between the NAD<sup>+</sup>/NADH ratio and glutaminase activity in A375, A375R, COLO829 and COLO829 cells.

I showed that addition of oxaloacetate and pyruvate could rescue growth from glutaminase inhibition, whereas malate could not. As previously mentioned, oxaloacetate can increase the availability of pyruvate in the medium due to its spontaneous decarboxylation (Tsai, 1967). However, both oxaloacetate and pyruvate are distinct from malate in their ability to rescue the growth from glutaminase inhibition (Figure 3.1.5-4). The link between these two rescuing metabolites, may be due to their ability to regenerate NAD<sup>+</sup> (Figure 4.4-1) although further experiments are required to confirm this. I also showed that pyruvate supplementation rescued growth from glutaminase inhibition, whereas addition of lactate caused an even further growth reduction in some conditions (Figure 3.1.4-5). In addition, I showed that addition of dimethyl- $\alpha$ -ketoglutarate could fully rescue the growth of COLO829R cells from glutaminase inhibition and produce NAD<sup>+</sup> (Figure 3.1.4-6) (Figure 4.4-1).

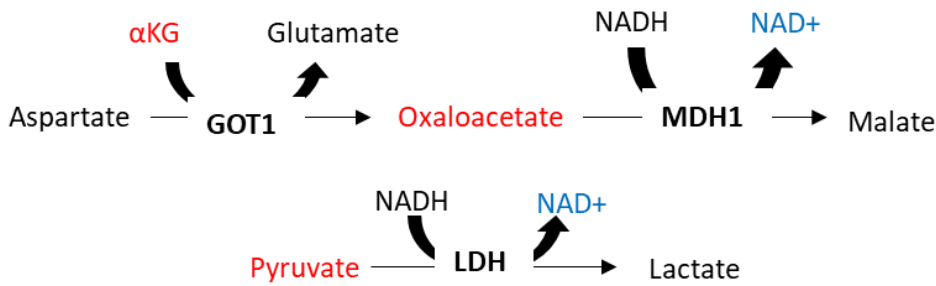


Figure 4.4-1: A diagram depicting the generation of NAD<sup>+</sup> (highlighted in blue) by oxaloacetate, pyruvate, and  $\alpha$ -ketoglutarate ( $\alpha$ KG) (highlighted in red).

Pyruvate, oxaloacetate, and dimethyl- $\alpha$ -ketoglutarate supplementation increased the NAD<sup>+</sup>/NADH ratio but did not increase the intracellular levels of aspartate. Conversely, aspartate supplementation did not increase the ratio of NAD<sup>+</sup>/NADH (Figure 3.1.5-7). These results showed that the essential function of glutaminase is not only in the maintenance of the NAD<sup>+</sup>/NADH ratio in the malate-aspartate shuttle, nor is it solely to increase the NAD<sup>+</sup>/NADH ratio to enable aspartate production. Glutaminase use is required for these two functions, separately though. Given that use of both transamination reactions and redox reactions are closely linked through the activity of the malate aspartate shuttle (Figure 1.3.4-1), the rescuing activities of these supplements may have a common point of convergence in the malate-aspartate shuttle. However, further experiments are required to determine whether these supplements change the uptake or use of glutamine and glutamate to affect the dependence on glutaminase.

## 4.5 BRAF and Glutaminase Inhibition Affect the expression of the Urea Cycle Enzyme, Argininosuccinate Lyase

Having shown that aspartate levels in tumours were responsive to glutaminase inhibition *in vitro* (Figure 3.1.4-2), I measured the levels of aspartate in tumours *in vivo* and showed that glutaminase inhibition did indeed reduce the levels of aspartate, even though it had not caused a significant effect on tumour growth. However, the combination of glutaminase and BRAF inhibition which had significantly reduced tumour growth, increased the levels of aspartate (Figure 3.3.1-1) (Figure 3.4.2-1). I therefore sought to find metabolites whose levels were changed in response to the combination treatment. 41 metabolic features were found whose abundance in tumours changed significantly in response to combination treatment, but not in each of the individual treatments alone. These involved an increase in serine, asparagine and methyl nicotinamide and a decrease in deoxyglucose-6-phosphate, acetylornithine, succinyl-homoserine, myo inositol and hexanoate (Figure 3.4.1-3). Further investigation is required to determine whether the changes in these metabolites are causative of changes in tumour growth.

*In vivo* I showed that BRAF inhibition caused an increase in tumoral glutamine but no change in the levels of tumoral glutamate (Figure 3.4.2-2). Neither glutamine nor glutamate was changed significantly in the serum by BRAF inhibition alone (Figure 3.4.2-3). Together these results indicated that either glutamine catabolism is decreased, or glutamine uptake is increased by BRAF inhibition. These results

contrasted with the findings *In vitro*, which showed that long term BRAF inhibition did not cause changes in basal levels of glutamine or glutamate (Figure 3.1.3-1). However, several changes exist between the *in vitro* and *in vivo* conditions, including a different length of exposure to BRAF inhibition, and a difference in the availability of nutrients in the serum. Further experiments are needed to decipher the cause of the increase in tumour glutamine on BRAF inhibition, however these results show a novel finding that BRAF inhibition alters glutamine metabolism in tumours.

Having shown that glutamine and aspartate levels were changed by BRAF inhibition, I checked the levels of other metabolites using our in-house list of standards which showed that several metabolites were in fact changed by BRAF inhibition (Figure 3.4.2-4). Interestingly, citrulline levels were decreased by BRAF inhibition and by glutaminase inhibition (Figure 3.4.2-5). Given that BRAF inhibition prevents tumour growth by reducing the transcription of genes downstream of the RAS-RAF-MEK-ERK signalling cascade, I theorised that BRAF inhibition might elicit its effects on the metabolism by altering the transcription of metabolic genes. Therefore, I used RNAseq to determine if BRAF inhibition changed the transcription of metabolic genes. I found that *in vivo*, BRAF inhibition increased the transcription of argininosuccinate lyase (ASL) but did not change the expression (Figure 3.4.1-1).

ASL is responsible for the conversion of argininosuccinate to arginine and fumarate, and thus its overexpression could increase the availability of arginine and fumarate (Figure 4.5-1). Silencing of argininosuccinate synthase (ASS1), the enzyme responsible for argininosuccinate synthesis, is reported to occur in BRAF inhibitor resistant melanoma, increasing their dependence on exogenous

arginine(Li *et al.*, 2016, 2017), although ASS1 was expressed in our model (Figure 3.4.3-1 & Figure 3.4.2-7). On the other hand, it has also been reported that increased ASS1 expression results in increased expression of glutaminase and sensitivity to its inhibition in melanoma(Long *et al.*, 2013). Increased expression of ASL in response to BRAF inhibition is not a previously reported phenomenon. However, the reversal of ASL was reported to result in arginine auxotrophy, similar to silencing of ASS1(Zheng *et al.*, 2013). Increased expression of ASL therefore might increase the capacity for production of arginine. Further experiments are required to determine the expression and activity of ARG1 and OTC in tumours, but increased ASL expression may increase the capacity for use of the urea cycle.

Our experiments showed a decrease in systemic ammonia in mice treated with BRAF inhibition (Figure 3.4.2-8), which supports the idea that BRAF inhibition favours ammonia clearance via the urea cycle of inhibits ammonia production. However, the increase in tumour aspartate under BRAF inhibition (Figure 4.4.2-1) was surprising in conjunction with increased ASL expression, given that decreased expression of the upstream ASS1 was reported to conserve aspartate levels(Rabinovich *et al.*, 2015). Increased expression, and activity of ASL in tumours allows the return of aspartate derived carbons back to the TCA cycle, while directing aspartate derived nitrogen toward disposal in urea (Figure 4.5-2). This means that theoretically, increased urea cycle use would result in the disposal of aspartate derived (and by extension glutamine derived) nitrogen in urea, while conserving carbon. This may be disadvantageous if met with a second hit of decreased glutamine derived nitrogen caused by glutaminase inhibition.

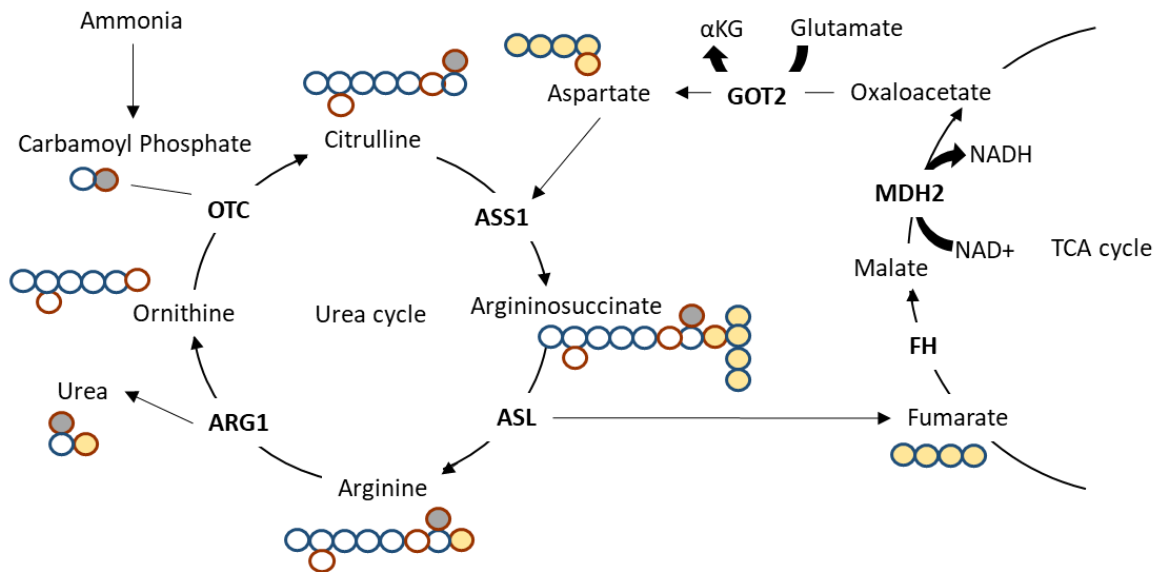


Figure 4.5-2: Diagram depicting the urea cycle and the use of aspartate derived carbon (circled in blue) and nitrogen (circled in brown). Aspartate derived carbon and nitrogen are shown in filled yellow and ammonia derived nitrogen are shown in grey, with carbon and nitrogen from other sources filled in white. The enzymes fumarate hydratase (FH), malate dehydrogenase (MDH2), glutamate-oxaloacetate transaminase (GOT2), Argininosuccinate synthase (ASS1), Argininosuccinate lyase (ASL), Arginase (ARG1) and Ornithine transcarbamylase (OTC) are represented in the diagram.

BRAF inhibition and glutaminase inhibition individually reduced the levels of citrulline (Figure 3.4.2-5). This indicates the urea cycle as a putative point of mechanistic interaction between glutaminase and BRAF inhibition. Circulating citrulline is decreased by glutaminase inhibition, so tumour citrulline may be decreased because of this systemic effect, or alternatively because of reduced ammonia production from glutaminase in the tumours. By reducing citrulline levels, glutaminase inhibition reduces the levels of a key intermediate of the urea cycle. As discussed above, BRAF inhibition increases the expression of ASL, which may increase the activity of

the urea cycle. If this were the case a decrease in citrulline would oppose this change by decreasing levels of the intermediates available for use of the urea cycle.

Further experiments will be needed to demonstrate whether BRAF inhibition is affecting the activity of the urea cycle, as well as whether it is essential for growth or just an artefact of BRAF inhibition. Indeed, silencing of the upstream enzyme ASS1 was reported to increase growth by conserving aspartate derived nitrogen for their contribution to pyrimidine synthesis (Rabinovich *et al.*, 2015). However, in cells with a reduced growth due to BRAF inhibition, an increase in ASL activity might not be detrimental unless coupled with a second metabolic hit i.e. the inhibition of glutaminase. However, pools of aspartate are increased by BRAF inhibition, suggesting that the increased activity of the urea cycle is not imposing any further burden on the pools of aspartate. Further investigation will therefore also be required to determine the significance of increased ASL expression in response to BRAF inhibition. However, the change in levels of urea cycle intermediate, citrulline in response to both PLX4032 and CB839 is a novel finding that may yield further insights into how their combined treatment may cause growth inhibition.

## 4.5 Overview

In this thesis, I investigated the effectiveness of glutaminase as a treatment for mutant BRAF melanoma. Specifically, I used the glutaminase inhibitor CB839, which has been used in phase 1b/2 clinical trials (*ClinicalTrials.gov*, 2022), with the BRAF inhibitors PLX4032 (Vemurafenib) or PLX4720 to assess their effect on growth and metabolism in various *in vitro* and *in vivo* models of mutant BRAF melanoma. To my knowledge this study represents the first in depth assessment of the growth and metabolic effects of these two clinically relevant drugs used in combination.

*In vitro*, I found that glutaminase inhibition resulted in greater growth inhibition and glutamate depletion in cells selected for their resistance to PLX4720. These cells had an increased NAD<sup>+</sup>/NADH ratio as well as increased expression of glutaminase compared to their parental counterparts. Glutaminase inhibition reduced the levels of aspartate in both cell types. Aspartate levels have been reported to limit cell survival under glutamine starvation due to the requirement for aspartate in the malate-aspartate shuttle to maintain redox homeostasis (Furkan Alkan *et al.*, 2018) (Figure 4.5-1). Based on this, I tested the importance of glutamine derived aspartate in melanoma cells and demonstrated that aspartate supplementation as well as supplementation of NAD<sup>+</sup> regenerating compounds could rescue proliferation from CB839.

*In vivo*, I found that CB839 treatment resulted in reduced growth inhibition only when given in combination with PLX4032. Metabolically, CB839 treatment caused depletion of tumour aspartate as it had *in vitro*, however PLX4032 increased tumour

aspartate. BRAF and glutaminase inhibition individually caused an increase in tumour glutamine levels, that was additive in response to the combination. In addition, BRAF and glutaminase inhibition individually decreased tumour citrulline levels. BRAF inhibition also decreased systemic levels of ammonia and increased the mRNA expression of the urea cycle enzyme, ASL. To my knowledge, the depletion of citrulline and increase in glutamine caused by BRAF inhibition are previously unreported. They demonstrate that PLX4032 can cause metabolic rewiring to affect the same metabolites as CB839. I showed that BRAF inhibition decreased the transcription of HIF1 $\alpha$  targets, which also suggested how BRAF inhibition might induce metabolic changes on a large scale through transcription. Together, these findings can inform the use of combined glutaminase inhibition with a BRAF inhibitor in melanoma.

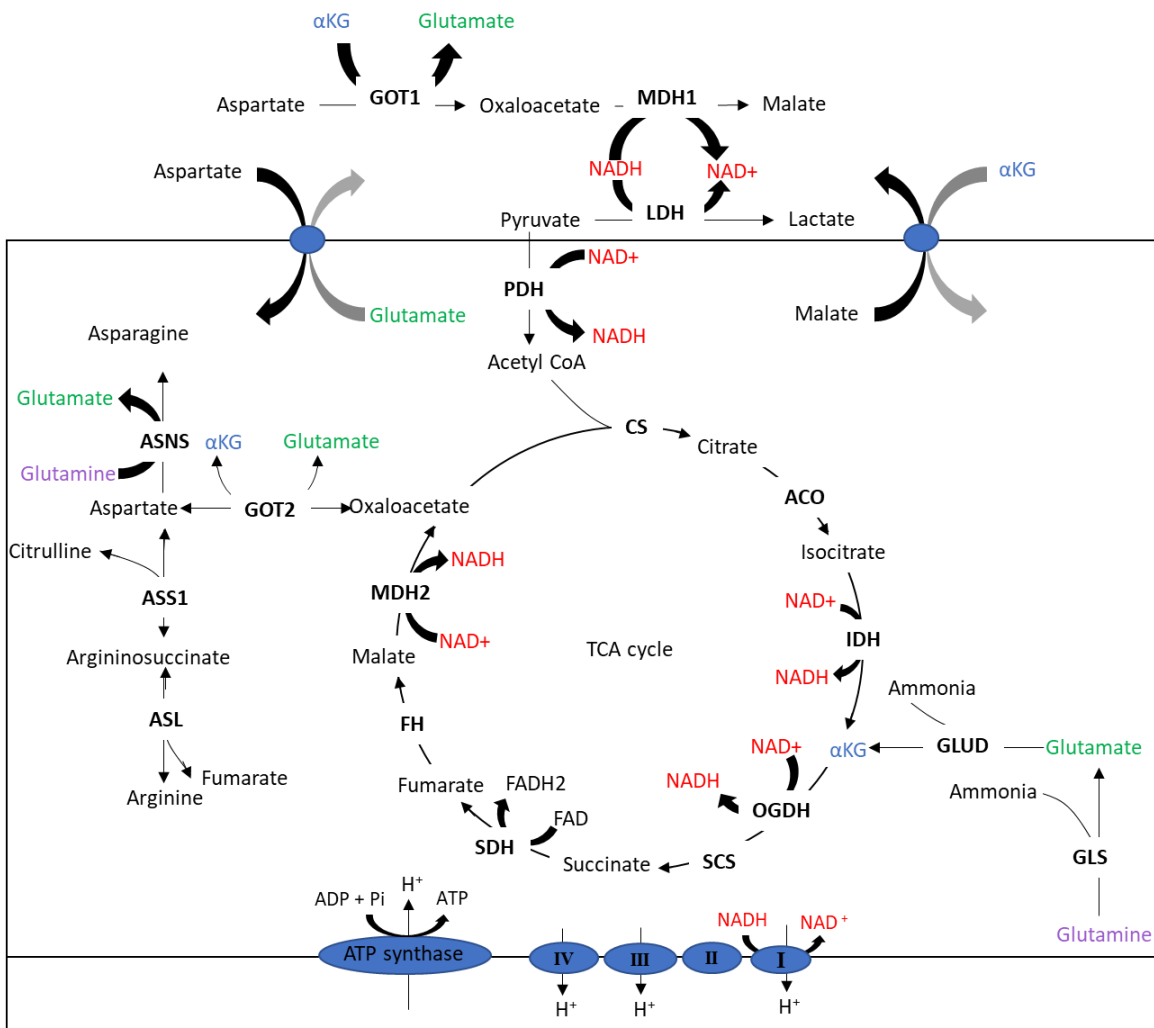


Figure 4.5-1: A diagram showing the links between redox homeostasis and aspartate synthesis.  $\text{NAD}^+$  and  $\text{NADH}$  are highlighted in red, glutamine in purple, glutamate in green, and  $\alpha$ -ketoglutarate in blue to demonstrate the relationship between glutaminolysis and redox homeostasis.

## 4.7 Future work

In this section I propose experiments to follow up on the work carried out in this thesis, that I anticipate will increase our understanding of the therapeutic and metabolic effects of glutaminase and BRAF inhibition in melanoma.

### 4.7.1 Determination of the direct metabolic effects of BRAF inhibition

Cells under long term BRAF inhibition (i.e. BRAF inhibitor resistant) were used for much of this thesis due to their ability to withstand 1 $\mu$ M BRAF inhibition without significantly undergoing a significant amount of cell death. However, I showed that the presence of BRAF inhibitor rather than the acquisition of resistance sensitizes melanoma cells to glutaminase inhibition. Thus, measurement of glutamate levels, as well as glutamine tracing should be compared in BRAF inhibitor resistant cells in the presence and absence of BRAF inhibition, to determine how the direct application of BRAF inhibition is able to affect glutaminase use. This experiment will demonstrate whether the changes in glutaminase activity in cells under long term BRAF inhibition are caused directly by BRAF inhibition.

Furthermore, *in vivo* I showed that glutamine levels are increased by BRAF inhibition. This was a surprising but intriguing result, because BRAF inhibition sensitised cells to glutaminase inhibition. Levels of glutamine in the serum were not changed by Vemurafenib treatment, indicating that the changes in glutamine levels were selective for the tumour. A follow up experiment of glutamine tracing should be performed *in vivo* in the presence of Vemurafenib, as well as during

glutaminase inhibition. This experiment may demonstrate if the presence of BRAF inhibition results in reduced use of glutaminase, or reduced use of another reaction consuming glutamine.

I also showed *in vivo* by RNAseq analysis, that BRAF inhibition changed the expression of HIF1 $\alpha$  targets and that this signature was stronger in combination with CB839 treatment. This result aligned with previously reported finding showing that that expression of HIF1 $\alpha$  is increased by mutant BRAF in melanoma(Kumar *et al.*, 2007). Moreover I showed that BRAF and glutaminase inhibition decreased pyruvate levels and the ratio of ATP/AMP, changes consistent with a decreased activity of glycolysis. To determine the effect of BRAF and glutaminase inhibition on glycolytic flux, glucose tracing should be performed *in vivo* under these treatments.

#### 4.7.2 Determination of the systemic effects of CB839

I showed that CB839 treatment *in vivo* caused a significant change in the level of several metabolites in the serum of mice without tumours. A determination of the changes in serum concentration of key metabolites *in vivo* may allow an *in vitro* determination of whether these changes affect the response of tumour cells to CB839. For example, media could be formulated based on the average concentration of metabolites found in human serum under CB839 treatment, which could be used along with Plasmax<sup>TM</sup> to compare the sensitivity of human cancer cells to CB839. The results of these two experiments may allow the more informed use of CB839 in human patients and may initiate a precision medicine approach to prescribing CB839.

#### 4.7.3 Determination of metabolic changes caused by combined CB839 and PLX4032 treatment

The metabolomic analysis on tumours derived from A375 cells, identified 41 metabolic features whose levels were significantly changed by the combination treatment (PLX0432 and CB839), but not by PLX4032 and CB839 treatment alone. Given that the combination treatment resulted in greater growth inhibition than did either of the treatments alone, it is expected that the metabolites of interest are indicative of the changes caused by the interaction of PLX4032 and CB839. We used in-house generated retention times and MS2 spectra to identify a number of these, however levels of these metabolites in serum have not yet been measured. Therefore, LC-MS should be used to measure the metabolites of interest in respective serum samples. This will elucidate if systemic metabolic changes triggered by CB839 and Vemurafenib can explain the metabolic effects of these drugs observed in tumours of treated mice.

Furthermore, we identified that BRAF and glutaminase inhibition both resulted in decrease in citrulline, and that BRAF inhibition caused an increased ASL expression, which was exacerbated by glutaminase inhibition. Given the effect of both treatments on citrulline, this suggested that it may be a putative point of mechanistic interaction between glutaminase and BRAF inhibition. Therefore, to determine whether urea cycle activity might be feasible in these cells, the expression of other enzymes in the urea cycle - ARG1 and OTC - could be measured in the tumours either by

immunohistochemistry or western blot. Furthermore, the effect of arginine starvation in the presence of BRAF and glutaminase inhibition could be determined *in vitro*, to show whether the increase in ASL expression caused by BRAF and glutaminase inhibition may increase the growth of cells under arginine deprivation.

## References

Porter J *et al* (2022). 'Absolute Quantification of the Lower Abundance Proteome Through Immunoaffinity Depletion of the Twenty Most Abundant Proteins in Human Serum'. Available at: [https://www.sigmaaldrich.com/content/dam/sigma-aldrich/docs/Sigma/General\\_Information/hupoaqua.pdf](https://www.sigmaaldrich.com/content/dam/sigma-aldrich/docs/Sigma/General_Information/hupoaqua.pdf) (Accessed: 12 September 2022).

Ackermann, T. and Tardito, S. (2019) 'Cell Culture Medium Formulation and Its Implications in Cancer Metabolism', *Trends in Cancer*, 5(6), pp. 329-332. Available at: <https://doi.org/10.1016/J.TRECAN.2019.05.004>.

Aderemi, A.V. *et al.* (2021) 'metabolites H OH OH Metabolomics: A Scoping Review of Its Role as a Tool for Disease Biomarker Discovery in Selected Non-Communicable Diseases', 11, p. 418. Available at: <https://doi.org/10.3390/metabo11070418>.

Alkan, H.F. *et al.* (2018) 'Cytosolic Aspartate Availability Determines Cell Survival When Glutamine Is Limiting', *Cell Metabolism*, 28(5), pp. 706-720.e6. Available at: <https://doi.org/10.1016/J.CMET.2018.07.021>.

Allaire, J.J. (2022) 'RStudio: Integrated Development Environment for R'. Available at: <http://www.rstudio.org/> (Accessed: 12 September 2022).

*Babraham Bioinformatics - FastQC A Quality Control tool for High Throughput Sequence Data* (2022). Available at: <https://www.bioinformatics.babraham.ac.uk/projects/fastqc/> (Accessed: 12 September 2022).

Baenke, F. *et al.* (2016) 'Resistance to BRAF inhibitors induces glutamine dependency in melanoma cells', *Molecular Oncology* [Preprint]. Available at: <https://doi.org/10.1016/j.molonc.2015.08.003>.

Bellenghi, M. *et al.* (2020) 'Sex and Gender Disparities in Melanoma', *Cancers*, 12(7), pp. 1-23. Available at: <https://doi.org/10.3390/CANCERS12071819>.

Benjamini, Y. and Hochberg, Y. (1995) 'Controlling the False Discovery Rate: A Practical and Powerful Approach to Multiple Testing', *Journal of the Royal Statistical Society: Series B (Methodological)*, 57(1), pp. 289-300. Available at: <https://doi.org/10.1111/J.2517-6161.1995.TB02031.X>.

Bingol, K. and Brüscheweiler, R. (2015) 'Two elephants in the room: new hybrid nuclear magnetic resonance and mass spectrometry approaches for metabolomics.', *Current opinion in clinical nutrition and metabolic care*, 18(5), pp. 471-7. Available at: <https://doi.org/10.1097/MCO.000000000000206>.

Birsoy, K. *et al.* (2015) 'An Essential Role of the Mitochondrial Electron Transport Chain in Cell Proliferation Is to Enable Aspartate Synthesis', *Cell*, 162(3), pp. 540-551. Available at: <https://doi.org/10.1016/j.cell.2015.07.016>.

Blunt, T. *et al.* (1995) 'Defective DNA-dependent protein kinase activity is linked to V(D)J recombination and DNA repair defects associated with the murine scid mutation', *Cell*, 80(5), pp. 813-823. Available at: [https://doi.org/10.1016/0092-8674\(95\)90360-7](https://doi.org/10.1016/0092-8674(95)90360-7).

Bollag, G. *et al.* (2010) 'Clinical efficacy of a RAF inhibitor needs broad target blockade in BRAF-mutant melanoma', *Nature*, 467(7315), pp. 596-599. Available at: <https://doi.org/10.1038/nature09454>.

Bollag, G. *et al.* (2012) 'Vemurafenib: the first drug approved for BRAF-mutant cancer', *Nature Publishing Group*. Available at: <https://doi.org/10.1038/nrd3847>.

Brash, D.E. (2015) 'UV Signature Mutations', *Photochemistry and photobiology*, 91(1), p. 15. Available at: <https://doi.org/10.1111/PHP.12377>.

Brian J. Altman, Zachary E. Stine and Chi V. Dang (2016) 'From Krebs to clinic: glutamine metabolism to cancer therapy', *Nature Reviews Cancer* 2016 16:10, 16(10), pp. 619-634. Available at: <https://doi.org/10.1038/nrc.2016.71>.

Burke, L. *et al.* (2020) 'The Janus-like role of proline metabolism in cancer', *Cell Death Discovery* 2020 6:1, 6(1), pp. 1-17. Available at: <https://doi.org/10.1038/s41420-020-00341-8>.

Cantor, J.R. *et al.* (2017) 'Physiologic Medium Rewires Cellular Metabolism and Reveals Uric Acid as an Endogenous Inhibitor of UMP Synthase', *Cell*, 169, pp. 258-272.e17. Available at: <https://doi.org/10.1016/j.cell.2017.03.023>.

Cerami *et al.* (2012) 'The cBio Cancer Genomics Portal: An Open Platform for Exploring Multidimensional Cancer Genomics Data.' *Cancer Discovery*. May 2012 2;401.

Chae, Y.K. *et al.* (2017) 'Path toward Precision Oncology: Review of Targeted Therapy Studies and Tools to Aid in Defining "Actionability" of a Molecular Lesion and Patient Management Support', *Molecular Cancer Therapeutics*, 16(12), pp. 2645-2655. Available at: <https://doi.org/10.1158/1535-7163.MCT-17-0597>.

Chapman, P.B. *et al.* (2011) 'Improved survival with vemurafenib in melanoma with BRAF V600E mutation.', *The New England journal of medicine*, 364(26), pp. 2507-16. Available at: <https://doi.org/10.1056/nejmoa1103782>.

Chapman, P.B. (2013) 'Mechanisms of Resistance to RAF Inhibition in Melanomas Harboring a BRAF Mutation', *Am Soc Clin Oncol Educ Book*, (33), pp. e80-e82. Available at: [https://doi.org/10.14694/edbook\\_am.2013.33.E80](https://doi.org/10.14694/edbook_am.2013.33.E80).

Chen, L. *et al.* (2021) 'Metabolite discovery through global annotation of untargeted metabolomics data', *Nature Methods*, 18(11), pp. 1377-1385. Available at: <https://doi.org/10.1038/s41592-021-01303-3>.

Choi, Y.K. and Park, K.G. (2018) 'Targeting Glutamine Metabolism for Cancer Treatment', *Biomolecules & Therapeutics*, 26(1), p. 19. Available at: <https://doi.org/10.4062/biolmolther.2017.178>.

Corazao-Rozas, P. *et al.* (2013) 'Mitochondrial oxidative stress is the Achille's heel of melanoma cells resistant to Braf-mutant inhibitor.', *Oncotarget*. Available at: <https://doi.org/10.18632/oncotarget.1420>.

Polsky, D and Codon-Cardo, C (2003) 'Oncogenes in melanoma', *Oncogene*, 22(20), pp. 3087-3091. Available at: <https://doi.org/10.1038/sj.onc.1206449>.

Dankort, D. *et al.* (2009) 'Braf(V600E) cooperates with Pten loss to induce metastatic melanoma', *Nature genetics*, 41(5), pp. 544-552. Available at: <https://doi.org/10.1038/NG.356>.

Davarinejad, H. (2022) 'Quantifications of Western Blots with ImageJ'. Available at: <http://rsb.info.nih.gov/ij/> (Accessed: 17 September 2022).

Davis, L.E., Shalin, S.C. and Tackett, A.J. (2019) 'Current state of melanoma diagnosis and treatment', *Cancer Biology and Therapy*. Taylor and Francis Inc., pp. 1366-1379. Available at: <https://doi.org/10.1080/15384047.2019.1640032>.

Delage, B. *et al.* (2010) 'Arginine deprivation and argininosuccinate synthetase expression in the treatment of cancer', *International Journal of Cancer*, 126(12), p. 2762-72. Available at: <https://doi.org/10.1002/ijc.25202>.

Desideri, E., Cavallo, A.L. and Baccarini, M. (2015) 'Alike but Different: RAF Paralogs and Their Signaling Outputs', *Cell*, 161(5), pp. 967-970. Available at: <https://doi.org/10.1016/j.cell.2015.04.045>.

Parkin DM, Mesher D and Sasieni P (2011) '13. Cancers attributable to solar (ultraviolet) radiation exposure in the UK in 2010', *British journal of cancer*, 105(Suppl 2), pp. S66-S69. Available at: <https://doi.org/10.1038/bjc.2011.486>.

Dummer, R. *et al.* (2018) 'Encorafenib plus binimetinib versus vemurafenib or encorafenib in patients with BRAF-mutant melanoma

(COLUMBUS): a multicentre, open-label, randomised phase 3 trial', *The Lancet. Oncology*, 19(5), pp. 603-615. Available at: [https://doi.org/10.1016/S1470-2045\(18\)30142-6](https://doi.org/10.1016/S1470-2045(18)30142-6).

Elsó, C.M. *et al.* (2004) 'Leishmaniasis host response loci (Imr1-3) modify disease severity through a Th1/Th2-independent pathway', *Genes and immunity*, 5(2), pp. 93-100. Available at: <https://doi.org/10.1038/sj.gene.6364042>.

Ewels, P. *et al.* (2016) 'MultiQC: summarize analysis results for multiple tools and samples in a single report', *Bioinformatics*, 32(19), pp. 3047-3048. Available at: <https://doi.org/10.1093/bioinformatics/btw354>.

Keung, E Z and Gershenwald, J E (2018) 'The eighth edition American Joint Committee on Cancer (AJCC) melanoma staging system: implications for melanoma treatment and care', *Expert review of anticancer therapy*, 18(8), pp. 775-784. Available at: <https://doi.org/10.1080/14737140.2018.1489246>.

Fernandez-de-Cossio-Diaz, J. and Vazquez, A. (2017) 'Limits of aerobic metabolism in cancer cells', *Scientific Reports*, 7(1), p. 13488. Available at: <https://doi.org/10.1038/s41598-017-14071-y>.

Ferretta, A. *et al.* (2016) 'New insight into the role of metabolic reprogramming in melanoma cells harboring BRAF mutations', *Biochimica et Biophysica Acta (BBA) - Molecular Cell Research*, 1863(11), pp. 2710-2718. Available at: <https://doi.org/10.1016/j.bbamcr.2016.08.007>.

Frederick, D.T. *et al.* (2013) 'BRAF inhibition is associated with enhanced melanoma antigen expression and a more favorable tumor microenvironment in patients with metastatic melanoma', *Clinical*

*cancer research*, 19(5), pp. 1225-1231. Available at:  
<https://doi.org/10.1158/1078-0432.ccr-12-1630>.

Frezza, C. (2019) 'Metabolism and cancer: the future is now', *British Journal of Cancer* 2019 122:2, 122(2), pp. 133-135. Available at:  
<https://doi.org/10.1038/s41416-019-0667-3>.

Furkan Alkan, H. *et al.* (2018) 'Cytosolic Aspartate Availability Determines Cell Survival When Glutamine Is Limiting', *Cell Metabolism*, 28, pp. 706-720.e6. Available at:  
<https://doi.org/10.1016/j.cmet.2018.07.021>.

Gao, S., Zhang, Z.P. and Karnes, H.T. (2005) 'Sensitivity enhancement in liquid chromatography/atmospheric pressure ionization mass spectrometry using derivatization and mobile phase additives', *Journal of Chromatography B*, 825(2), pp. 98-110. Available at: <https://doi.org/10.1016/j.jchromb.2005.04.021>.

Gao *et al.* 'Integrative analysis of complex cancer genomics and clinical profiles using the cBioPortal.' *Sci. Signal.* 6, pl1 (2013)

Garcia-Bermudez, J. *et al.* (2018) 'Aspartate is a limiting metabolite for cancer cell proliferation under hypoxia and in tumours', *Nature Cell Biology* 2018 20:7, 20(7), pp. 775-781. Available at:  
<https://doi.org/10.1038/s41556-018-0118-z>.

Gertsman, I. and Barshop, B.A. (2018) 'Promises and pitfalls of untargeted metabolomics'. *J Inherit Metab Dis.* May;41(3): pp.355-366. Available at: <https://doi.org/10.1007/s10545-017-0130-7>.

Goldstein, A.M. and Tucker, M.A. (2001) 'Genetic Epidemiology of Cutaneous Melanoma: A Global Perspective', *Archives of Dermatology*, 137(11), pp. 1493-1496. Available at:  
<https://doi.org/10.1001/archderm.137.11.1493>.

Gorgoglione, R. *et al.* (2022) 'Glutamine-Derived Aspartate Biosynthesis in Cancer Cells: Role of Mitochondrial Transporters and New Therapeutic Perspectives', *Cancers*, 14(1). Available at: <https://doi.org/10.3390/cancers14010245>.

Gross, M.I. *et al.* (2014) 'Antitumor Activity of the Glutaminase Inhibitor CB-839 in Triple-Negative Breast Cancer', *Molecular Cancer Therapeutics*, 13(4), pp. 890-901. Available at: <https://doi.org/10.1158/1535-7163.mct-13-0870>.

Grulich, A.E. *et al.* (2007) 'Incidence of cancers in people with HIV/AIDS compared with immunosuppressed transplant recipients: a meta-analysis', *The Lancet*, 370(9581), pp. 59-67. Available at: [https://doi.org/10.1016/S0140-6736\(07\)61050-2](https://doi.org/10.1016/S0140-6736(07)61050-2).

Guo, Jinxiu *et al.* (2021) 'Biological Roles and Therapeutic Applications of IDH2 Mutations in Human Cancer', *Frontiers in Oncology*, 11, p. 1344. Available at: <https://doi.org/10.3389/fonc.2021.644857/bibtex>.

Guo, Jian *et al.* (2021) 'ISFrag: De Novo Recognition of In-Source Fragments for Liquid Chromatography-Mass Spectrometry Data', *Analytical Chemistry*, 93(29), pp. 10243-10250. Available at: [https://doi.org/10.1021/acs.analchem.1c01644/asset/images/large/ac1c01644\\_0006.jpeg](https://doi.org/10.1021/acs.analchem.1c01644/asset/images/large/ac1c01644_0006.jpeg).

Gutzmer, R. *et al.* (2020) 'Atezolizumab, vemurafenib, and cobimetinib as first-line treatment for unresectable advanced BRAFV600 mutation-positive melanoma (IMspire150): primary analysis of the randomised, double-blind, placebo-controlled, phase 3 trial', *The Lancet*, 395(10240), pp. 1835-1844. Available at: [https://doi.org/10.1016/s0140-6736\(20\)30934-x/attachment/1dbb8c58-35b9-4c32-adb0-d8448823158d/mmc1.pdf](https://doi.org/10.1016/s0140-6736(20)30934-x/attachment/1dbb8c58-35b9-4c32-adb0-d8448823158d/mmc1.pdf).

Hanahan, D. and Weinberg, R.A. (2011) 'Hallmarks of cancer: The next generation', *Cell*, 144(5), pp. 646-674. Available at: <https://doi.org/10.1016/j.cell.2011.02.013/attachment/3f528e16-8b3c-4d8d-8de5-43e0c98d8475/mmc1.pdf>.

Haq, R., Shoag, J., Andreu-Perez, P., Yokoyama, S., Edelman, H., Rowe, Glenn C., *et al.* (2013) 'Oncogenic BRAF Regulates Oxidative Metabolism via PGC1 $\alpha$  and MITF', *Cancer Cell*, 23(3), pp. 302-315. Available at: <https://doi.org/10.1016/J.CCR.2013.02.003>.

Hartman, M.L. and Czyz, M. (2015) 'MITF in melanoma: mechanisms behind its expression and activity', *Cellular and Molecular Life Sciences*, 72(7), p. 1249. Available at: <https://doi.org/10.1007/S00018-014-1791-0>.

Heiden, M.G.V., Cantley, L.C. and Thompson, C.B. (2009) 'Understanding the warburg effect: The metabolic requirements of cell proliferation', *Science*, 324(5930), pp. 1029-1033. Available at: [https://doi.org/10.1126/science.1160809/asset/c00ca2ce-14f9-4352-ac43-7d1bb04b41d8/assets/graphic/324\\_1029\\_f4.jpeg](https://doi.org/10.1126/science.1160809/asset/c00ca2ce-14f9-4352-ac43-7d1bb04b41d8/assets/graphic/324_1029_f4.jpeg).

Herranz, D. (2017) 'Glutaminolysis gets the spotlight in cancer', *Oncotarget*, 8(7), p. 10761. Available at: <https://doi.org/10.18632/oncotarget.14384>.

Hodis, E., Watson, Ian R, *et al.* (2012) 'A landscape of driver mutations in melanoma.', *Cell*, 150(2), pp. 251-63. Available at: <https://doi.org/10.1016/j.cell.2012.06.024>.

Hodis, E., Watson, Ian R., *et al.* (2012) 'A Landscape of Driver Mutations in Melanoma', *Cell*, 150(2), pp. 251-263. Available at: <https://doi.org/10.1016/j.cell.2012.06.024>.

Hooijkaas, A.I. *et al.* (2012) 'Targeting BRAFV600E in an Inducible Murine Model of Melanoma', *The American Journal of Pathology*, 181(3), pp. 785-794. Available at: <https://doi.org/10.1016/j.ajpath.2012.06.002>.

Horai, H. *et al.* (2010) 'MassBank: a public repository for sharing mass spectral data for life sciences', *Journal of mass spectrometry : JMS*, 45(7), pp. 703-714. Available at: <https://doi.org/10.1002/jms.1777>.

Huber, W. *et al.* (2015) 'Orchestrating high-throughput genomic analysis with Bioconductor', *Nature Methods* 2015 12:2, 12(2), pp. 115-121. Available at: <https://doi.org/10.1038/nmeth.3252>.

Ticher, I. *et al.* (2019) 'A comprehensive evaluation of pathogenic mutations in primary cutaneous melanomas, including the identification of novel loss-of-function variants', *Scientific reports*, 9(1). Available at: <https://doi.org/10.1038/S41598-019-53636-X>.

Iizuka-Ohashi, M. *et al.* (2018) 'Blockage of the mevalonate pathway overcomes the apoptotic resistance to MEK inhibitors with suppressing the activation of Akt in cancer cells', *Oncotarget*. Available at: <https://doi.org/10.18632/oncotarget.24696>.

Illumina (2021) 'Illumina Stranded mRNA Prep, Ligation Reference Guide (1000000124518)'. Available at: [www.illumina.com/company/legal.html](http://www.illumina.com/company/legal.html). (Accessed: 17 September 2022).

de Jager, T.L. *et al.* (2017) 'Ultraviolet Light in Human Health, Diseases and Environment', *Advances in Experimental Medicine and Biology*, 996. Available at: [https://doi.org/10.1007/978-3-319-56017-5\\_2](https://doi.org/10.1007/978-3-319-56017-5_2).

- Jayesh, N. et al (2015) 'Metabolomics: A Tool Ahead for Understanding Molecular Mechanisms of Drugs and Diseases', *Indian Journal of Clinical Biochemistry*. Available at: <https://doi.org/10.1007/s12291-014-0455-z>.
- Jensen, C. and Teng, Y. (2020) 'Is It Time to Start Transitioning From 2D to 3D Cell Culture?', *Frontiers in Molecular Biosciences*, 7, p. 33. Available at: <https://doi.org/10.3389/fmolb.2020.00033/bibtex>.
- Jeremy M Berg, John L Tymoczko and Lubert Stryer (2012) 'Biochemistry', in. Basingstoke: Freeman, pp. 431-432.
- Jhappan, C., Noonan, F.P. and Merlino, G. (2003) 'Ultraviolet radiation and cutaneous malignant melanoma', *Oncogene 2003* 22:20, 22(20), pp. 3099-3112. Available at: <https://doi.org/10.1038/sj.onc.1206450>.
- Johnson, M.O. et al. (2018) 'Distinct Regulation of Th17 and Th1 Cell Differentiation by Glutaminase-Dependent Metabolism', *Cell*, 175(7), pp. 1780-1795.e19. Available at: <https://doi.org/10.1016/j.cell.2018.10.001>.
- Kakavand, H. et al. (2015) 'PD-L1 Expression and Tumor-Infiltrating Lymphocytes Define Different Subsets of MAPK Inhibitor-Treated Melanoma Patients', *Clinical cancer research*, 21(14), pp. 3140-3148. Available at: <https://doi.org/10.1158/1078-0432.ccr-14-2023>.
- Kang, H.B. et al. (2015) 'Metabolic Rewiring by Oncogenic BRAF V600E Links Ketogenesis Pathway to BRAF-MEK1 Signaling', *Molecular Cell*. Available at: <https://doi.org/10.1016/j.molcel.2015.05.037>.
- Kaplan, F.M. et al. (2011) 'Hyperactivation of MEK-ERK1/2 signaling and resistance to apoptosis induced by the oncogenic B-RAF

inhibitor, PLX4720, in mutant N-RAS melanoma cells', *Oncogene*, 30(3), p. 366. Available at: <https://doi.org/10.1038/onc.2010.408>.

Karki, P. *et al.* (2021) 'BRAF-Inhibitor-Induced Metabolic Alterations in A375 Melanoma Cells', *Metabolites*, 11(11). Available at: <https://doi.org/10.3390/metabo11110777>.

Karpievitch, Y. v. *et al.* (2014) 'Metabolomics Data Normalization with EigenMS', *PLoS ONE*, 9(12), p. 116221. Available at: <https://doi.org/10.1371/journal.pone.0116221>.

Katt, W.P., Lukey, M.J. and Cerione, R.A. (2017) 'A tale of two glutaminases: homologous enzymes with distinct roles in tumorigenesis', *Future Medicinal Chemistry*, 9(2), p. 223. Available at: <https://doi.org/10.4155/fmc-2016-0190>.

Kawakami, A. and Fisher, D.E. (2017) 'The master role of microphthalmia-associated transcription factor in melanocyte and melanoma biology', *Laboratory Investigation* 2017 97:6, 97(6), pp. 649-656. Available at: <https://doi.org/10.1038/labinvest.2017.9>.

Kim D *et al.* (2019) 'Graph-based genome alignment and genotyping with HISAT2 and HISAT-genotype.', *Nat Biotechnol*, 37(8), pp. 907-15. Available at: <https://doi.org/10.1038/ncb3272>.

Kluyver, T. *et al.* (2016) 'Jupyter Notebooks - a publishing format for reproducible computational workflows', *Positioning and Power in Academic Publishing: Players, Agents and Agendas - Proceedings of the 20th International Conference on Electronic Publishing, ELPUB 2016*, pp. 87-90. Available at: <https://doi.org/10.3233/978-1-61499-649-1-87>.

Kodama, M. *et al.* (2020) 'A shift in glutamine nitrogen metabolism contributes to the malignant progression of cancer', *Nature*

*Communications* 2020 11:1, 11(1), pp. 1-16. Available at:

<https://doi.org/10.1038/s41467-020-15136-9>.

Krauthammer, M. *et al.* (2012) 'Exome sequencing identifies recurrent somatic RAC1 mutations in melanoma', *Nature genetics*, 44(9), pp. 1006-1014. Available at: <https://doi.org/10.1038/ng.2359>.

Kumar, S.M. *et al.* (2007) 'Mutant V600E BRAF Increases Hypoxia Inducible Factor-1 $\alpha$  Expression in Melanoma', *Cancer Research*, 67(7), pp. 3177-3184. Available at: <https://doi.org/10.1158/0008-5472.can-06-3312>.

Kuryk, L. *et al.* (2020) 'From Conventional Therapies to Immunotherapy: Melanoma Treatment in Review', *Cancers*, 12(10), pp. 1-20. Available at: <https://doi.org/10.3390/cancers12103057>.

Larkin, J. *et al.* (2015) 'Combined Nivolumab and Ipilimumab or Monotherapy in Previously Untreated Melanoma', *The New England journal of medicine*, 373(1), p. 23. Available at: <https://doi.org/10.1056/nejmoa1504030>.

Leonardi, G.C. *et al.* (2018) 'Cutaneous melanoma: From pathogenesis to therapy (Review)', *International Journal of Oncology*, 52(4), pp. 1071-1080. Available at: <https://doi.org/10.3892/ijo.2018.4287>.

Li H *et al.* (2009) 'The Sequence Alignment/Map format and SAMtools', *Bioinforma Oxf Engl*, 25(16), pp. 2078-9. Available at: <https://doi.org/10.1038/nm.4399>.

Li, S. *et al.* (2013) 'Predicting Network Activity from High Throughput Metabolomics', *PLoS Comput Biol*, 9(7), p. 1003123. Available at: <https://doi.org/10.1371/journal.pcbi.1003123>.

- Li, Y.Y. *et al.* (2016) 'BRAF inhibitor resistance enhances vulnerability to arginine deprivation in melanoma', *Oncotarget*, 7(14), pp. 17665-17680. Available at: <https://doi.org/10.18632/oncotarget.6882>.
- Li, Y.Y. *et al.* (2017) 'Degradation of AMPK- $\alpha$ 1 sensitizes BRAF inhibitor-resistant melanoma cells to arginine deprivation', *Molecular Oncology* [Preprint]. Available at: <https://doi.org/10.1002/1878-0261.12151>.
- Liao, Y., Smyth, G.K. and Shi, W. (2014) 'featureCounts: an efficient general purpose program for assigning sequence reads to genomic features', *Bioinformatics (Oxford, England)*, 30(7), pp. 923-930. Available at: <https://doi.org/10.1093/bioinformatics/btt656>.
- Lin, J.Y. and Fisher, D.E. (2007) 'Melanocyte biology and skin pigmentation', *Nature 2007 445:7130*, 445(7130), pp. 843-850. Available at: <https://doi.org/10.1038/nature05660>.
- Lindsay M. Biga *et al.* (2019) *5.1 Layers of the Skin*. OpenStax/Oregon State University. Available at: <https://open.oregonstate.edu/aandp/chapter/5-1-layers-of-the-skin/> (Accessed: 28 January 2022).
- Liu, Y. and Sheikh, M.S. (2014) 'Melanoma: Molecular Pathogenesis and Therapeutic Management', *Molecular and cellular pharmacology*, 6(3), p. 228. Available at: [/pmc/articles/pmc4346328/](https://pubmed.ncbi.nlm.nih.gov/24444444/) (Accessed: 6 August 2021).
- Long, Y. *et al.* (2013) 'Arginine deiminase resistance in melanoma cells is associated with metabolic reprogramming, glucose dependence, and glutamine addiction', *Molecular Cancer Therapeutics*, 12(11), pp. 2581-2590. Available at: <https://doi.org/10.1158/1535-7163.mct-13-0302>.

Lord, S.R. *et al.* (2019) 'Transcriptomic analysis of human primary breast cancer identifies fatty acid oxidation as a target for metformin', *British Journal of Cancer* 2019 122:2, 122(2), pp. 258-265. Available at: <https://doi.org/10.1038/s41416-019-0665-5>.

Love, M.I., Huber, W. and Anders, S. (2014) 'Moderated estimation of fold change and dispersion for RNA-seq data with DESeq2', *Genome Biology*, 15(12), pp. 1-21. Available at: <https://doi.org/10.1186/S13059-014-0550-8/FIGURES/9>.

Lowry, O.H. *et al.* (1951) 'Protein measurement with the Folin phenol reagent.', *The Journal of biological chemistry*, 193(1), pp. 265-275. Available at: [https://doi.org/10.1016/S0021-9258\(19\)52451-6](https://doi.org/10.1016/S0021-9258(19)52451-6).

Luengo, A. *et al.* (2021) 'Increased demand for NAD<sup>+</sup> relative to ATP drives aerobic glycolysis', *Molecular Cell*, 81(4), pp. 691-707.e6. Available at: <https://doi.org/10.1016/j.molcel.2020.12.012>.

MacKay, G.M. *et al.* (2015) *Analysis of Cell Metabolism Using LC-MS and Isotope Tracers*, *Methods in Enzymology*. Available at: <https://doi.org/10.1016/bs.mie.2015.05.016>.

Mantovani, F., Collavin, L. and Sal, G. del (2019) 'Mutant p53 as a guardian of the cancer cell', *Cell Death & Differentiation*, 26, pp. 199-212. Available at: <https://doi.org/10.1038/s41418-018-0246-9>.

'Mass Spectrometry Learning Center - UK' (2022). Available at: <https://www.thermofisher.com/uk/en/home/industrial/mass-spectrometry/mass-spectrometry-learning-center.html> (Accessed: 5 September 2022).

Masters, J.R. (2002) 'HeLa cells 50 years on: the good, the bad and the ugly', *Nature Reviews Cancer* 2002 2:4, 2(4), pp. 315-319. Available at: <https://doi.org/10.1038/nrc775>.

Meeth, K. *et al.* (2016) 'The YUMM lines: a series of congenic mouse melanoma cell lines with defined genetic alterations', *Pigment cell & melanoma research*, 29(5), p. 590. Available at: <https://doi.org/10.1111/pcmr.12498>.

Memon, A. *et al.* (2021) 'Changing epidemiology and age-specific incidence of cutaneous malignant melanoma in England: An analysis of the national cancer registration data by age, gender and anatomical site, 1981-2018', *The Lancet Regional Health - Europe*, 2, p. 100024. Available at: <https://doi.org/10.1016/j.lanep.2021.100024>.

Mihaylova, M.M. and Shaw, R.J. (2011) 'The AMPK signalling pathway coordinates cell growth, autophagy and metabolism.', *Nature cell biology*, 13(9), pp. 1016-23. Available at: <https://doi.org/10.1038/ncb2329>.

Muir, A. *et al.* (2017) 'Environmental cystine drives glutamine anaplerosis and sensitizes cancer cells to glutaminase inhibition', *eLife*, 6. Available at: <https://doi.org/10.7554/ELIFE.27713>.

Mullard, A. (2017) 'FDA approves first-in-class cancer metabolism drug', *Nature reviews. Drug discovery*, 16(9), p. 593. Available at: <https://doi.org/10.1038/nrd.2017.174>.

*Thermo Fisher Scientific - UK* (2022). 'mzCloud Mass Spectral Library' Available at: <https://www.thermofisher.com/uk/en/home/industrial/mass-spectrometry/liquid-chromatography-mass-spectrometry-lc-ms/lc->

ms-software/mass-spectral-libraries/mzcloud-mass-spectral-library.html (Accessed: 11 September 2022).

Natalie H. Matthews *et al.* (2017) 'Epidemiology of Melanoma', *Progress in clinical cancer*, 6, pp. 139-149. Available at: <https://doi.org/10.15586/codon.cutaneoumelanoma.2017.CH1>.

Newman, V. *et al.* (2018) 'The Ensembl Genome Browser: Strategies for Accessing Eukaryotic Genome Data.', *Methods in Molecular Biology (Clifton, N.J.)*, 1757, pp. 115-139. Available at: [https://doi.org/10.1007/978-1-4939-7737-6\\_6](https://doi.org/10.1007/978-1-4939-7737-6_6).

Olivier, M., Hollstein, M. and Hainaut, P. (2010) 'TP53 Mutations in Human Cancers: Origins, Consequences, and Clinical Use', *Cold Spring Harbor Perspectives in Biology*, 2(1). Available at: <https://doi.org/10.1101/cshperspect.A001008>.

Paolo A. Ascierto *et al.* (2012) 'The role of BRAF V600 mutation in melanoma', *Journal of Translational Medicine*, 10(1), p. 85. Available at: <https://doi.org/10.1186/1479-5876-10-85>.

Paraiso, K.H.T. *et al.* (2011) 'PTEN loss confers BRAF inhibitor resistance to melanoma cells through the suppression of BIM expression', *Cancer research*, 71(7), pp. 2750-2760. Available at: <https://doi.org/10.1158/0008-5472.can-10-2954>.

Patel, D. *et al.* (2016) 'Aspartate Rescues S-phase Arrest Caused by Suppression of Glutamine Utilization in KRas-driven Cancer Cells'. Available at: <https://doi.org/10.1074/jbc.M115.710145>.

Perillo, B. *et al.* (2020) 'ROS in cancer therapy: the bright side of the moon', *Experimental & Molecular Medicine* 2020 52:2, 52(2), pp. 192-203. Available at: <https://doi.org/10.1038/s12276-020-0384-2>.

Perna, D. *et al.* (2015) 'BRAF inhibitor resistance mediated by the AKT pathway in an oncogenic BRAF mouse melanoma model', *Proceedings of the National Academy of Sciences of the United States of America*, 112(6), pp. E536-e545. available at: <https://doi.org/10.1073/pnas.1418163112/-/dcsupplemental>.

Pires da Silva, I. *et al.* (2021) 'Ipilimumab alone or ipilimumab plus anti-PD-1 therapy in patients with metastatic melanoma resistant to anti-PD-(L)1 monotherapy: a multicentre, retrospective, cohort study', *The Lancet Oncology*, 22(6), pp. 836-847. Available at: [https://doi.org/10.1016/s1470-2045\(21\)00097-8/attachment/1f01ac5d-2fea-4043-bc59-02fd61b39067/mmc1.pdf](https://doi.org/10.1016/s1470-2045(21)00097-8/attachment/1f01ac5d-2fea-4043-bc59-02fd61b39067/mmc1.pdf).

Pitt, J.J. (2009) 'Principles and Applications of Liquid Chromatography-Mass Spectrometry in Clinical Biochemistry', *The Clinical Biochemist Reviews*, 30(1), p. 19. Available at: </pmc/articles/PMC2643089/> (Accessed: 3 September 2022).

Proietti, I. *et al.* (2020) 'Mechanisms of Acquired BRAF Inhibitor Resistance in Melanoma: A Systematic Review', *Cancers*, 12(10), pp. 1-29. Available at: <https://doi.org/10.3390/cancers12102801>.

*Thermo Fisher Scientific - UK* (2022). 'Q Exactive Orbitrap Mass Spectrometers' Available at: <https://www.thermofisher.com/uk/en/home/industrial/mass-spectrometry/liquid-chromatography-mass-spectrometry-lc-ms/lc-ms-systems/orbitrap-lc-ms/q-exactive-orbitrap-mass-spectrometers.html> (Accessed: 3 September 2022).

*R: a language and environment for statistical computing* (2022). Available at: <https://www.gbif.org/tool/81287/r-a-language-and-environment-for-statistical-computing> (Accessed: 17 September 2022).

Rabinovich, S. *et al.* (2015) 'Diversion of aspartate in ASS1-deficient tumours fosters de novo pyrimidine synthesis', *Nature* [Preprint]. Available at: <https://doi.org/10.1038/nature15529>.

Ratnikov, B.I. *et al.* (2017) 'Metabolic rewiring in melanoma', *Oncogene*. Available at: <https://doi.org/10.1038/onc.2016.198>.

Rebecca, V.W., Somasundaram, R. and Herlyn, M. (2020) 'Pre-clinical modeling of cutaneous melanoma', *Nature Communications* 2020 11:1, 11(1), pp. 1-9. Available at: <https://doi.org/10.1038/s41467-020-15546-9>.

J, Villanueva, *et al.* (2011) 'Resistance to BRAF inhibitors: Unraveling mechanisms and future treatment options' *Cancer Res* 2022 Dec 1;71(23):7137-40. Available at: doi: 10.1158/0008-5472.can-11-1243.

Roesch, A. *et al.* (2013) 'Overcoming intrinsic multi-drug resistance in melanoma by blocking the mitochondrial respiratory chain of slow-cycling JARID1B high cells', *Cancer Cell*, 23(6). Available at: <https://doi.org/10.1016/j.ccr.2013.05.003>.

Rossa, C. and D'silva, N.J. (2019) 'Immune-relevant aspects of murine models of head and neck cancer', *Oncogene* [Preprint]. Available at: <https://doi.org/10.1038/s41388-019-0686-9>.

Rossi, M. *et al.* (2019) 'Familial Melanoma: Diagnostic and Management Implications', *Dermatology Practical & Conceptual*, 9(1), p. 10. Available at: <https://doi.org/10.5826/dpc.0901a03>.

Sakakura, Y. *et al.* (2001) 'Sterol regulatory element-binding proteins induce an entire pathway of cholesterol synthesis', *Biochemical and Biophysical Research Communications*. Available at: <https://doi.org/10.1006/bbrc.2001.5375>.

Schneider, C.A., Rasband, W.S. and Eliceiri, K.W. (2012) 'NIH Image to ImageJ: 25 years of image analysis', *Nature methods*, 9(7), pp. 671-675. Available at: <https://doi.org/10.1038/nmeth.2089>.

Segeritz, C.P. and Vallier, L. (2017) 'Cell Culture: Growing Cells as Model Systems In Vitro', *Basic Science Methods for Clinical Researchers*, p. 151. Available at: <https://doi.org/10.1016/B978-0-12-803077-6.00009-6>.

Merck (2022). 'SeQuant® HILIC HPLC Columns | Analytics and Sample Preparation' Available at: [https://www.merckmillipore.com/GB/en/products/analytics-sample-prep/chromatography-for-analysis/analytical-hplc/sequent-zic-hilic-hplc-columns/wk6b.qb.pm0aaae\\_r\\_z3.lxi,nav](https://www.merckmillipore.com/GB/en/products/analytics-sample-prep/chromatography-for-analysis/analytical-hplc/sequent-zic-hilic-hplc-columns/wk6b.qb.pm0aaae_r_z3.lxi,nav) (Accessed: 5 September 2022).

Shao, Y. and Aplin, A.E. (2010) 'Akt3-Mediated Resistance to Apoptosis in B-RAF-Targeted Melanoma Cells', *Cancer Research*, 70(16), pp. 6670-6681. Available at: <https://doi.org/10.1158/0008-5472.can-09-4471>.

Sheppard, K.E. and McArthur, G.A. (2013) 'The Cell-Cycle Regulator CDK4: An Emerging Therapeutic Target in Melanoma', *Clinical Cancer Research*, 19(19), pp. 5320-5328. Available at: <https://doi.org/10.1158/1078-0432.ccr-13-0259>.

Shifu Chen *et al.* (2021) 'fastp: an ultra-fast all-in-one FASTQ preprocessor', *Bioinformatics*, 34(17), pp. i884-i890. Available at: <https://doi.org/10.1007/S11306-021-01796-1>.

Shin, C.S. *et al.* (2017) 'The glutamate/cystine xCT antiporter antagonizes glutamine metabolism and reduces nutrient flexibility', *Nature Communications* 2017 8:1, 8(1), pp. 1-11. Available at: <https://doi.org/10.1038/ncomms15074>.

Smalley, K.S.M. *et al.* (2008) 'Increased cyclin D1 expression can mediate BRAF inhibitor resistance in BRAF V600E-mutated melanomas', *Molecular cancer therapeutics*, 7(9), pp. 2876-2883. Available at: <https://doi.org/10.1158/1535-7163.mct-08-0431>.

Solit, D.B. *et al.* (2006) 'BRAF mutation predicts sensitivity to MEK inhibition'. *Nature* Jan 19;439(7074):358-62. Available at: <https://doi.org/10.1038/nature04304>.

*ClinicalTrials.gov* (2022). 'Study of CB-839 (Telaglenastat) in Combination With Talazoparib in Patients With Solid Tumors - Study Results' Available at: <https://clinicaltrials.gov/ct2/show/results/NCT03875313?term=CB839&draw=2&rank=8> (Accessed: 14 September 2022).

Sugimoto, M. *et al.* (2012) *Bioinformatics Tools for Mass Spectroscopy-Based Metabolomic Data Processing and Analysis*, *Current Bioinformatics*. Available at: <https://www.ncbi.nlm.nih.gov/pmc/articles/PMC3299976/pdf/CBIO-7-96.pdf> (Accessed: 6 January 2019).

Sullivan, L.B. *et al.* (2015) 'Supporting Aspartate Biosynthesis Is an Essential Function of Respiration in Proliferating Cells', *Cell*, 162(3), pp. 552-563. Available at: <https://doi.org/10.1016/j.cell.2015.07.017>.

Sullivan, L.B. *et al.* (2018) 'Aspartate is an endogenous metabolic limitation for tumour growth', *Nature Cell Biology*, 20(7), pp. 782-788. Available at: <https://doi.org/10.1038/s41556-018-0125-0>.

Swetter S.M. *et al.* (2021) *NCNN Clinical Practice Guidelines in Oncology, Melanoma: Cutaneous*.

- Clancy S (2008) *Mutation, DNA Repair, and DNA Integrity | Learn Science at Scitable, Nature Education*. Available at: <https://www.nature.com/scitable/topicpage/dna-damage-repair-mechanisms-for-maintaining-dna-344/> (Accessed: 5 August 2021).
- Talebi, A. *et al.* (2018) ‘Sustained SREBP-1-dependent lipogenesis as a key mediator of resistance to BRAF-targeted therapy’, *Nature Communications*. Available at: <https://doi.org/10.1038/s41467-018-04664-0>.
- Tanda, E.T. *et al.* (2020) ‘Current State of Target Treatment in BRAF Mutated Melanoma’, *Frontiers in Molecular Biosciences*, 7, p. 154. Available at: <https://doi.org/10.3389/fmolb.2020.00154/bibtex>.
- Tate, J.G. *et al.* (2019) ‘COSMIC: the Catalogue Of Somatic Mutations In Cancer’, *Nucleic Acids Research*, 47(D1), pp. D941-D947. Available at: <https://doi.org/10.1093/nar/gky1015>.
- das Thakur, M. *et al.* (2013) ‘Modelling vemurafenib resistance in melanoma reveals a strategy to forestall drug resistance’, *Nature* 2013 494:7436, 494(7436), pp. 251-255. Available at: <https://doi.org/10.1038/nature11814>.
- Tine, B.A. van *et al.* (2021) ‘Phase II trial of pegylated arginine deiminase in combination with gemcitabine and docetaxel for the treatment of soft tissue sarcoma.’, [https://doi.org/10.1200/jco.2021.39.15\\_suppl.11508](https://doi.org/10.1200/jco.2021.39.15_suppl.11508), 39(15\_suppl), pp. 11508-11508. Available at: [https://doi.org/10.1200/jco.2021.39.15\\_suppl.11508](https://doi.org/10.1200/jco.2021.39.15_suppl.11508).
- Trousil, S. *et al.* (2017) ‘Phenformin Enhances the Efficacy of ERK Inhibition in NF1-Mutant Melanoma’, *Journal of Investigative Dermatology*, 137(5), pp. 1135-1143. Available at: <https://doi.org/10.1016/j.jid.2017.01.013>.

- Tsai, C.S. (1967) 'Spontaneous decarboxylation of oxalacetic acid', *Canadian Journal of Chemistry*, 45, p. 873.
- Tsai, H.J. *et al.* (2017) 'A Phase II Study of Arginine Deiminase (ADI-PEG20) in Relapsed/Refractory or Poor-Risk Acute Myeloid Leukemia Patients', *Scientific Reports* 2017 7:1, 7(1), pp. 1-10. Available at: <https://doi.org/10.1038/s41598-017-10542-4>.
- Tsai, J. *et al.* (2008) 'Discovery of a selective inhibitor of oncogenic B-Raf kinase with potent antimelanoma activity', *Proceedings of the National Academy of Sciences of the United States of America*, 105(8), p. 3041. Available at: <https://doi.org/10.1073/pnas.0711741105>.
- Tyanova, S., Temu, T., Sinitcyn, P. *et al.* (2016) 'The Perseus computational platform for comprehensive analysis of (prote)omics data.' *Nat Methods* 13, 731-740. Available at: <https://doi.org/10.1038/nmeth.3901>
- Tyrell, R. *et al.* (2017) 'Surgical resection of metastatic melanoma in the era of immunotherapy and targeted therapy', *Melanoma Management*, 4(1), p. 61. Available at: <https://doi.org/10.2217/mmt-2016-0018>.
- Varghese, S. *et al.* (2021) 'The glutaminase inhibitor CB-839 (Telaglenastat) enhances the anti-melanoma activity of T cell mediated immunotherapies', *Mol Cancer Ther*, 20(3), pp. 500-511. Available at: <https://doi.org/10.1158/1535-7163.mct-20-0430>.
- Voorde, J. vande *et al.* (2019) 'Improving the metabolic fidelity of cancer models with a physiological cell culture medium', *Science Advances*. Available at: <https://doi.org/10.1126/sciadv.aau7314>.

Wang, Q. *et al.* (2014) 'Targeting glutamine transport to suppress melanoma cell growth', *International Journal of Cancer*, 135(5), pp. 1060-1071. Available at: <https://doi.org/10.1002/ijc.28749>.

Warburg, O. (1956) *SCIENCE Injuring of Respiration On the Origin of Cancer Cells*. Available at: <http://science.sciencemag.org/> (Accessed: 13 November 2018).

Wellbrock, C. and Arozarena, I. (2016) 'The Complexity of the ERK/MAP-Kinase Pathway and the Treatment of Melanoma Skin Cancer', *Frontiers in Cell and Developmental Biology*, 4(APR), p. 33. Available at: <https://doi.org/10.3389/fcell.2016.00033>.

William W Wheaton (2014) Metformin inhibits mitochondrial complex I of cancer cells to reduce tumorigenesis *eLife* 3:e02242.

Wickham, H. *et al.* (2019) 'Welcome to the Tidyverse', *Journal of Open Source Software*, 4(43), p. 1686. Available at: <https://doi.org/10.21105/joss.01686>.

Wingett SW and Andrews S (2018) 'FastQ Screen: A tool for multi-genome mapping and quality control', *F1000 Research*, 7 (1338). Available at: <https://doi.org/10.7554/eLife.02242>

Wise, D.R. and Thompson, C.B. (2010) 'Glutamine Addiction: A New Therapeutic Target in Cancer', *Trends in biochemical sciences*, 35(8), p. 427. Available at: <https://doi.org/10.1016/j.tibs.2010.05.003>.

Wishart, D.S. *et al.* (2022) 'HMDB 5.0: the Human Metabolome Database for 2022', *Nucleic acids research*, 50(D1), pp. D622-D631. Available at: <https://doi.org/10.1093/nar/gkab1062>.

Wolchok, J.D. *et al.* (2013) 'Development of ipilimumab: a novel immunotherapeutic approach for the treatment of advanced

melanoma', *Annals of the New York Academy of Sciences*, 1291(1), p. 1. Available at: <https://doi.org/10.1111/nyas.12180>.

Workman, P. *et al.* (2010) 'Guidelines for the welfare and use of animals in cancer research', *British Journal of Cancer*, 102(11), pp. 1555-1577. Available at: <https://doi.org/10.1038/sj.bjc.6605642>.

Xia, S. *et al.* (2017) 'Prevention of Dietary-Fat-Fueled Ketogenesis Attenuates BRAF V600E Tumor Growth', *Cell Metabolism*, 25(2), pp. 358-373. Available at: <https://doi.org/10.1016/j.cmet.2016.12.010>.

Xiao, W. *et al.* (2018) 'TP53 Mutation as Potential Negative Predictor for Response of Anti-CTLA-4 Therapy in Metastatic Melanoma', *EBioMedicine*, 32, pp. 119-124. Available at: <https://doi.org/10.1016/j.ebiom.2018.05.019>.

Xiao, Y. *et al.* (2014) 'A novel significance score for gene selection and ranking', *Bioinformatics (Oxford, England)*, 30(6), pp. 801-807. Available at: <https://doi.org/10.1093/bioinformatics/btr671>.

Yadav, V. *et al.* (2014) 'The CDK4/6 inhibitor LY2835219 overcomes vemurafenib resistance resulting from MAPK reactivation and cyclin D1 upregulation', *Molecular Cancer Therapeutics*, 13(10), pp. 2253-2263. Available at: <https://doi.org/10.1158/1535-7163.mct-14-0257/175484/am/the-cdk4-6-inhibitor-ly2835219-overcomes>.

Yang, H. *et al.* (2010) 'RG7204 (PLX4032), a Selective BRAFV600E Inhibitor, Displays Potent Antitumor Activity in Preclinical Melanoma Models', *Cancer Research*, 70(13), pp. 5518-5527. Available at: <https://doi.org/10.1158/0008-5472.can-10-0646>.

Yang, X. *et al.* (2018) 'Stem Cell Reports Resource An Immune System-Modified Rat Model for Human Stem Cell Transplantation

Research'. Available at:

<https://doi.org/10.1016/j.stemcr.2018.06.004>.

Yao, S. *et al.* (2021) 'Phase 1 trial of ADI-PEG20 plus cisplatin in patients with pretreated metastatic melanoma or other advanced solid malignancies', *British Journal of Cancer* 2021 124:9, 124(9), pp. 1533-1539. Available at: <https://doi.org/10.1038/s41416-020-01230-8>.

Yoo, H.C. *et al.* (2020) 'A Variant of SLC1A5 Is a Mitochondrial Glutamine Transporter for Metabolic Reprogramming in Cancer Cells', *Cell Metabolism*, 31(2), pp. 267-283.e12. Available at: <https://doi.org/10.1016/j.cmet.2019.11.020>.

Yuan, P. *et al.* (2013) 'Phenformin enhances the therapeutic benefit of BRAF V600E inhibition in melanoma'. Available at: <https://doi.org/10.1073/pnas.1317577110>.

Zhang, J. *et al.* (2014) '<sup>13</sup>C isotope-assisted methods for quantifying glutamine metabolism in cancer cells', *Methods in Enzymology*, 542, pp. 369-389. Available at: <https://doi.org/10.1016/B978-0-12-416618-9.00019-4>.

Zhao, H., Swanson, K.D. and Zheng, B. (2021) 'Therapeutic Repurposing of Biguanides in Cancer', *Trends in Cancer*, 7(8), pp. 714-730. Available at: <https://doi.org/10.1016/j.trecan.2021.03.001>.

Zhao, L. *et al.* (2017) 'HMG-CoA synthase 1 is a synthetic lethal partner of BRAFV600E in human cancers', *The Journal of Biological Chemistry*, 292(24), p. 10142. Available at: <https://doi.org/10.1074/jbc.m117.788778>.

Zheng, B. *et al.* (2009) ‘Oncogenic B-RAF Negatively Regulates the Tumor Suppressor LKB1 to Promote Melanoma Cell Proliferation’, *Molecular Cell*. Available at:  
<https://doi.org/10.1016/j.molcel.2008.12.026>.

Zheng, L. *et al.* (2013) ‘Reversed argininosuccinate lyase activity in fumarate hydratase-deficient cancer cells’, *Cancer & Metabolism* [Preprint]. Available at: <https://doi.org/10.1186/2049-3002-1-12>.

Zhu, A., Ibrahim, J.G. and Love, M.I. (2019) ‘Heavy-tailed prior distributions for sequence count data: removing the noise and preserving large differences’, *Bioinformatics*, 35(12), pp. 2084-2092. Available at: <https://doi.org/10.1093/bioinformatics/bty895>.